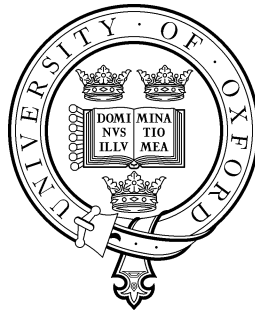


Mass Determination of New Particle States



Mario A Serna Jr
Wadham College
University of Oxford

A thesis submitted for the degree of
Doctor of Philosophy

Trinity 2008

This thesis is dedicated to
my wife
for joyfully supporting me and our daughter while I studied.

Mass Determination of New Particle States

Mario Andres Serna Jr

Wadham College

Thesis submitted for the degree of Doctor of Philosophy
Trinity Term 2008

Abstract

We study theoretical and experimental facets of mass determination of new particle states. Assuming supersymmetry, we update the quark and lepton mass matrices at the grand unification scale accounting for threshold corrections enhanced by large ratios of the vacuum expectation value of the two supersymmetric Higgs fields $v_u/v_d \equiv \tan \beta$. From the hypothesis that quark and lepton masses satisfy a classic set of relationships suggested in some Grand Unified Theories (GUTs), we predict $\tan \beta$ needs to be large, and the gluino's soft mass needs to have the opposite sign to the wino's soft mass. Existing tools to measure the phase of the gluino's mass at upcoming hadron colliders require model-independent, kinematic techniques to determine the masses of the new supersymmetric particle states. The mass determination is made difficult because supersymmetry is likely to have a dark-matter particle which will be invisible to the detector, and because the reference frame and energy of the parton collisions are unknown at hadron colliders. We discuss the current techniques to determine the mass of invisible particles. We review the transverse mass kinematic variable M_{T2} and the use of invariant-mass edges to find relationships between masses. Next, we introduce a new technique to add additional constraints between the masses of new particle states using M_{T2} at different stages in a symmetric decay chain. These new relationships further constrain the mass differences between new particle states, but still leave the absolute mass weakly determined. Next, we introduce the constrained mass variables $M_{2C, LB}$, $M_{2C, UB}$, $M_{3C, LB}$, $M_{3C, UB}$ to provide event-by-event lower-bounds and upper-bounds to the mass scale given mass differences. We demonstrate mass scale determination in realistic case studies of supersymmetry models by fitting ideal distributions to simulated data. We conclude that the techniques introduced in this thesis have precision and accuracy that rival or exceed the best known techniques for invisible-particle mass-determination at hadron colliders.

Declaration

This thesis is the result of my own work, except where reference is made to the work of others, and has not been submitted for other qualification to this or any other university.

Mario Andres Serna Jr

Acknowledgements

I would like to thank my supervisor Graham Ross for his patient guidance as I explored many topics about which I have wanted to learn for a long time. For the many hours of teaching, proofreading, computer time and conversations they have provided me, I owe many thanks to my fellow students Tanya Elliot, Lara Anderson, Babiker Hassanain, Ivo de Medeiros Varzielas, Simon Wilshin, Dean Horton, and the friendly department post-docs James Gray, Yang-Hui He, and David Maybury. I also need to thank Laura Serna, Alan Barr, Chris Lester, John March Russell, Dan Tovey, and Giulia Zanderighi for many helpful comments on my published papers which were forged into this thesis. Next I need to thank Tilman Plehn, Fabio Maltoni and Tim Stelzer for providing us online access to MadGraph and MadEvent tools. I would also like to thank Alex Pinder, Tom Melina, and Elco Makker, with whom I've worked on fourth-year projects this past year, for questions and conversations that have helped my work on this thesis. I also would like to thank my mentors over the years: Scotty Johnson, Leemon Baird, Iyad Dajani, Richard Cook, Alan Guth, Lisa Randall, Dave Cardimona, Sanjay Krishna, Scott Dudley, and Kevin Cahill, and the many others who have offered me valuable advice that I lack the space to mention here. Finally I'd like to thank my family and family-in-law for their support and engaging distractions during these past few years while I've been developing this thesis.

I also acknowledge support from the United States Air Force Institute of Technology. The views expressed in this thesis are those of the author and do not reflect the official policy or position of the United States Air Force, Department of Defense, or the US Government.

Contents

1	Introduction	1
2	Mass Determination in the Standard Model and Supersymmetry	6
2.1	Past Mass Determination and Discovery of New Particle States	7
2.2	Dark Matter: Evidence for New, Massive, Invisible Particle States	16
2.3	Supersymmetry: Predicting New Particle States	21
3	Predictions from Unification and Fermion Mass Structure	35
3.1	Supersymmetric Thresholds and GUT-Scale Mass Relations	37
3.2	Updated fits to Yukawa matrices	43
4	Mass Determination Toolbox at Hadron Colliders	49
4.1	Mass Determination Challenges at Hadron Colliders	49
4.2	Invariant Mass Edge Techniques	53
4.3	Mass Shell Techniques	56
4.4	Transverse Mass Techniques	57
5	Using M_{T2} with Cascade decays	62
5.1	M_{T2} and M_{CT} in this context	62
5.2	Application to symmetric decay chains	64
6	The Variable M_{2C}: Direct Pair Production	67
6.1	An improved distribution from which to determine M_Y	68
6.2	Using M_{T2} to Find M_{2C} and the max M_{T2} Kink	70
6.3	Symmetries and Dependencies of the M_{2C} Distribution	72
6.4	Application of the method: SUSY model examples	76
7	The Variable M_{2C}: Significant Upstream Transverse Momentum	82
7.1	Upper Bounds on M_Y from Recoil against UTM	84
7.2	Modeling and Simulation	87
7.3	Factors for Successful Shape Fitting	89
7.4	Estimated Performance	99
8	The Variable M_{3C}: On-shell Interlineate States	105
8.1	Introducing M_{3C}	106
8.2	How to calculate M_{3C}	108
8.3	Factors for Successful Shape Fitting	111
8.4	Estimated Performance	117
9	Discussions and Conclusions	122

A	Renormalization Group Running	124
A.1	RGE Low-Energy $SU(3)_c \times U(1)_{EM}$ up to the Standard Model	125
A.2	RGE for Standard Model with Neutrinos up to MSSM	126
A.3	RGE for the MSSM with Neutrinos up to GUT Scale	128
A.4	Approximate Running Rules of Thumb	129
B	Hierarchical Yukawa couplings and Observables	130
C	Verifying M_{T2} in Eq(5.4)	133
D	Fitting Distributions to Data	134
E	Uniqueness of Event Reconstruction	137
F	Acronyms List	139

List of Figures

2.1	The states of the $SU(3)$ 10 of $J^P = 3/2^+$ baryons in 1962. Also shown is the $SU(3)$ 27	11
2.2	One Loop Contributions to the Higgs mass self energy. (a) Fermion loop. (b) Higgs loop.	16
2.3	Direct dark matter searches showing the limits from the experiments CDMS, XENON10, and the DAMA signal. Also shown are sample dark-matter cross sections and masses predicted for several supersymmetric models and universal extra dimension models. Figures generated using http://dmttools.berkeley.edu/limitplots/	20
2.4	One Loop Contributions to the supersymmetric Higgs H_u mass self energy. (a) top loop. (b) stop loop.	26
2.5	Gauge couplings for the three non-gravitational forces as a function of energy scale for the (left) Standard Model and (right) MSSM.	29
3.1	Updates to the top-quark mass, strong coupling constant, and bottom-quark mass are responsible for the quantitative stress of the classic GUT relation for y_b/y_τ . .	36
3.2	Updates to the strange-quark mass and V_{cb} are responsible for the quantitative stress of the Georgi-Jarlskog mass relations and the need to update values from Ref. [1].	36
4.1	(Left:) Two body decay and it's associated m_{ll} distribution. (Right:) Three body decay and it's associated m_{ll} distribution.	54
4.2	Cascade decay from Z to Y to X ending in N and visible particle momenta $\alpha_1, \alpha_2, \alpha_3$	56
4.3	Events with the new state Y is pair produced and in which each Y decays through a two-body decay to a massive new state X and a visible state 1 and then where X subsequently decays to a massive state N invisible to the detector and visible particles 2. All previous decay products are grouped into the upstream transverse momentum, k	56
4.4	Events with the new state Y is pair produced and in which each Y decays through a three-body decay to a massive state N invisible to the detector and visible particles 1, 2, 3, and 4. All previous decay products are grouped into the upstream transverse momentum, k	60
4.5	The max $M_{T2}(\chi)$ shows a kink at the true M_N and M_Y . For this simulation, $m_Y = 200$ GeV, and $m_N = 99$ GeV.	61
5.1	Shows constraints from max M_{T2} used with different combinations as described in eqs(5.7,5.8,5.9) and the max m_{12} described in Eq(5.11). Intersection is at the true mass (97 GeV, 144 GeV, 181 GeV) shown by sphere. Events include ISR but otherwise ideal conditions: no background, resolution, or combinatoric error. . .	65

6.1	The distribution of 30000 events in 5 GeV bins with perfect resolution and no background. The three curves represent $M_Y = 200$ GeV (dot-dashed), $M_Y = 150$ GeV (dotted) and $M_Y = 100$ GeV (solid) each with $M_- = 50$ GeV. Each distribution cuts off at the correct M_Y .	71
6.2	The $M_{T2}(\chi)$ curves for four events with $M_N = 50$ GeV and $M_Y = 100$ GeV. Only the events whose curves starts off at $M_{T2}(0) > M_-$ intersect the straight line given by $M_{T2}(\chi) - \chi = M_-$. The M_{T2} at the intersection is M_{2C} for that event.	72
6.3	Effect of this maximally spin correlated process on the M_{2C} distribution. Modeled masses are $M_Y = 200$ GeV and $M_N = 150$ GeV. The solid black distribution is the uncorrelated case and red dotted distribution is maximally spin correlated.	74
6.4	Demonstrates the distribution is independent of the COM energy, angle with which the pair is produced with respect to the beam axis, and the frame of reference.	76
6.5	χ^2 fit of 250 events from model P1 of Ref [2] to the theoretical distributions calculated for different $M_{\chi_2^0}$ values but fixed $M_{\chi_2^0} - M_{\chi_1^0}$. The fit gives $M_{\chi_2^0} = 133 \pm 6$ GeV.	79
6.6	χ^2 fit of 3000 events from model SPS 6 of Ref [3] to the theoretical distributions calculated for different $M_{\chi_2^0}$ values but fixed $M_{\chi_2^0} - M_{\chi_1^0}$. The fit gives $M_{\chi_2^0} = 221 \pm 20$ GeV.	79
7.1	Shows $g(\chi_N)$ for the extreme event in Eq(7.2-7.4) with $M_- = 53$ GeV and $M_N = 67.4$ GeV. The red dotted line has $M_G = 150$ GeV and shows an event providing a lower bound on M_Y . The blue dashed line $M_G = 170$ GeV and shows an event with both a lower bound and an upper-bound on M_Y . The black solid line shows $M_G = \sqrt{M_Y^3/M_N}$ where the lower bound equals the upper bound.	87
7.2	The M_{2C} and $M_{2C,UB}$ distributions of HERWIG events before smearing (to simulate detector resolution) is applied. The distributions' end-points show $M_{\tilde{\chi}_2^0} \approx 120$ GeV. The top thick curve shows the net distribution, the next curve down shows the contribution of only the signal events, and the bottom dashed curve shows the contribution of only background events.	89
7.3	We show the M_{2C} and $M_{2C,UB}$ ideal distributions for five choices of $M_{\tilde{\chi}_2^0}$ assuming the HERWIG generated m_{ll} and UTM distributions.	90
7.4	Dependence of M_{2C} distribution on the m_{ll} distribution. Left: The m_{ll} distributions. Right: The corresponding M_{2C} distributions. The solid curves show the case where the m_{ll} distribution when the three-body decay is dominated by the Z boson channel, and the dashed curves show the case where the m_{ll} distribution is taken directly from the HERWIG simulation.	92
7.5	Left: The UTM distribution observed in the HERWIG simulation. Right: Ideal M_{2C} upper bound and lower bound distribution for a range of upstream transverse momentum (UTM) values ($k_T = 0, 75, 175, 275, 375, 575$ GeV) where $M_N = 70$ GeV and $M_Y = 123$ GeV.	93
7.6	Figure shows that even with large UTM, the distribution is independent of k^2 and the parton collision energy to the numerical accuracies as calculated from 15000 events. Shown are three distributions and their difference. (1) $k_T = 175$ GeV, $k^2 = (100 \text{ GeV})^2$, \sqrt{s} distributed via Eq(7.10). (2) $k_T = 175$ GeV, $k^2 = (2000 \text{ GeV})^2$, \sqrt{s} distributed via Eq(7.10). (3) $k_T = 175$ GeV, $k^2 = (100 \text{ GeV})^2$, $\sqrt{s} = 549$ GeV.	94

7.7	The invariant mass of the OSSF leptons from both branches of forming a Dalitz-like wedgebox analysis. The events outside the $m_{ll} \leq 53$ GeV signal rectangle provide control samples from which we estimate the background shape and magnitude. The dark events are signal, the lighter events are background.	94
7.8	The missing transverse momentum vs M_{2C} values for HERWIG data. This shows that a $\cancel{P}_T > 20$ GeV cut would not affect the distribution for $M_{2C} > 65$ GeV. . .	99
7.9	The result of χ^2 fits to the data with differing assumptions for 100 fb^{-1} (left panel) and 400 fb^{-1} (right panel). The thick line with filled squares shows the final result with all cuts, resolution error, combinatorics, and backgrounds included and estimated in the shape fitting. This gives us $M_{\tilde{\chi}_1^0} = 63.2 \pm 4.1$ GeV with 700 events (signal or background) representing 100 fb^{-1} . After 400 fb^{-1} this improves to $M_{\tilde{\chi}_1^0} = 66.0 \pm 1.8$ GeV. The error-free best case gives $M_{\tilde{\chi}_1^0} = 67.0 \pm 0.9$ GeV. The correct value is $M_{\tilde{\chi}_1^0} = 67.4$ GeV.	100
7.10	HERWIG data for 100 fb^{-1} (thick line) and the smooth ideal expectation assuming $M_{\tilde{\chi}_1^0} = 70$ GeV generated by Mathematica with all resolution, background, and combinatoric effects included (thin line). The χ^2 of this curve to the HERWIG gives the solid-black square on the left frame of Fig. 7.9.	102
8.1	Ideal $M_{3C, LB}$ and $M_{3C, UB}$ distribution for 25000 events in two cases both sharing $\Delta M_{YN} = 100$ GeV and $\Delta M_{XN} = 50$ GeV. The solid, thick line shows $M_Y = 200$ GeV, and the dashed, thin line shows $M_Y = 250$ GeV.	107
8.2	(Left) The M_{3C} distributions before (solid) and after (dashed) introducing the combinatoric ambiguity. (Right) The M_{3C} distributions with and without UTM. The no UTM case ($k_T = 0$) is shown by the solid line; the large UTM case with $k_T = 250$ GeV is shown by the dashed line.	112
8.3	The effect of energy resolution on the M_{3C} distribution. (Left) The dotted line shows the energy resolution has washed out the sharp cut-off. (Right) $M_{3C, LB}$ with perfect energy resolution plotted against the result with realistic energy resolutions.	113
8.4	The dependence of the M_{3C} distributions on the parton collision energy. The solid line shows the collision distributed according to Eq(7.10), and the dashed line shows the collision energy fixed at $\sqrt{s} = 600$ GeV.	114
8.5	The effect of missing transverse momentum cuts on the M_{3C} distributions. (Left) The $M_{3C, LB}$ result versus the \cancel{P}_T . (Right) The difference of the $M_{3C, UB}$ and $M_{3C, LB}$ distributions with and without the cut $\cancel{P}_T > 20$ GeV. The smallest bins of $M_{3C, LB}$ are the only bins to be statistically significantly affected.	115
8.6	Effect of a spin correlated process on the M_{3C} distributions. Modeled masses are $M_Y = 200$ GeV, $M_X = 150$ GeV, and $M_N = 100$ GeV. The thick black and thick blue lines show the distributions of the uncorrelated lower bound and upper bound M_{3C} . The dotted red lines show the distributions of the spin correlated process.	116
8.7	Fit of ideal $M_{3C}(M_{\tilde{\chi}_1^0})$ distributions to the HERWIG generated M_{3C} distributions. Includes combinatoric errors, backgrounds, energy resolution, and \cancel{P}_T cuts. (Left) The observed HERWIG counts versus the expected counts for ideal $M_{\tilde{\chi}_1^0} = 95$ GeV. (Right) The χ^2 fit to ideal distributions of $M_{\tilde{\chi}_1^0} = 80, 85, 90, 95, 100, 105, 110$ GeV. The correct mass is $M_{\tilde{\chi}_1^0} = 96.0$ GeV.	118
8.8	Combined constraint from fitting both $\max m_{ll}$ and M_{3C} with the mass difference as free parameters. We parameterized the difference from the true values in the model by $\Delta M_{YN} = 80.8 \text{ GeV} + \delta \Delta M_{YN}$ and $\Delta M_{XN} = 47.0 \text{ GeV} + \delta \Delta M_{XN}$. We shown the 1, 2, 3σ contours.	119

A.1	The impact of RG running parameter ratios with $M_S = 500$ GeV. These ratios determine χ defined in Eq. A.34. If $M_S = M_Z$, all three are degenerate at small $\tan\beta$	129
E.1	Shows the ellipses defined for p_o and q_o in Eqs(8.13-8.14) using the correct mass scale for an event that nearly saturates the M_{3C} endpoint. For this event, the M_{3C} lies within 1% of the endpoint and reconstructs p and q to within 4%. Perfect error resolution and combinatorics are assumed.	138

Chapter 1

Introduction

In the mid-seventeenth century, a group of Oxford natural philosophers, including Robert Boyle and Robert Hooke, argued for the inclusion of experiments in the natural philosopher’s toolkit as a means of falsifying theories [4]. This essentially marks the beginning of modern physics, which is rooted in an interplay between creating theoretical models, developing experimental techniques, making observations, and falsifying theories¹. This thesis is concerned with mass determination of new particle states in these first two stages: we present a new theoretical observation leading to predictions about particle masses and their relationships, and we develop new experimental analysis techniques to extract the masses of new states produced in hadron collider experiments. The remaining steps of the cycle will follow in the next several years: New high-energy observations will begin soon at the Large Hadron Collider (LHC)², and history will record which theories were falsified and which (if any) were chosen by nature.

No accepted theory of fundamental particle physics claims to be ‘true’, rather theories claim to make successful predictions within a given domain of validity for experiments performed within a range of accuracy and precision. The Standard Model with an extension to include neutrino masses is the best current ‘minimal’ model. Its predictions agree with all the highest-energy laboratory-based observations (1.96 TeV at the Tevatron) to within the best attainable accuracy and precision (an integrated luminosity \mathcal{L} of about $\int dt \mathcal{L} \approx 4 \text{ fb}^{-1}$) [7]³. The Standard Model’s agreement with collider data requires agreement with quantum corrections [8, Ch 10]. The success of the Standard Model will soon be challenged.

¹There are many philosophy of physics subtleties about how physics progress is made [5] or how theories are falsified [6] which we leave for future philosophers. Nevertheless, acknowledging the philosophical interplay between experiment and scientific theory is an important foundational concept for a physics thesis.

²This does not mean that the LHC will observe new particles, but that the LHC will perform experiments with unexplored energies and luminosities that will constrain theories.

³Grossly speaking in particle physics, the domain of validity is given in terms of the energy of the collision, and the precision of the experiment is dictated by the integrated luminosity $\int dt \mathcal{L}$. Multiplying the $\int dt \mathcal{L}$ with the cross-section for a process gives the number of events of that process one expects to occur. The larger the integrated luminosity, the more sensitive one is potentially to processes with small cross sections.

At about the time this thesis is submitted, the Large Hadron Collider (LHC) will (hopefully) begin taking data at a substantially larger collision energy of 10 TeV and soon after at 14 TeV [9]. The high luminosity of this collider ($10^{34} \text{ cm}^{-2} \text{ sec}^{-1}$) [9] enables us to potentially measure processes with much greater precision (hopefully about $\int dt \mathcal{L} = 300 \text{ fb}^{-1}$ after three years). The LHC holds promise to test many candidate theories of fundamental particle physics that make testable claims at these new energy and precision frontiers.

The thesis is arranged in two parts. The first regards theoretical determination of masses of new particle states, and the second regards experimental determination of masses at hadron colliders. Each part begins with a review of important developments relevant to placing the new results of this thesis in context. The content is aimed at recording enough details to enable future beginning graduate students to follow the motivations and, with the help of the cited references, reproduce the work. A full pedagogical explanation of quantum field theory, gauge theories, supersymmetry, grand unified theories (GUTs) and renormalization would require several thousand pages reproducing easily accessed lessons found in current textbooks. Instead we present summaries of key features and refer the reader to the author's favored textbooks or review articles on the subjects for refining details.

Part I of this thesis contains Chapters 2-3. Part II of this thesis contains Chapters 4-8.

Chapter 2 outlines theoretical approaches to mass determination that motivate the principles behind our own work. Exact symmetry, broken symmetry, and fine-tuning of radiative corrections form the pillars of past successes in predicting mass properties of new particle states. By mass properties, we mean both the magnitude and any CP violating phase that cannot be absorbed into redefinition of the respective field operators. We highlight a few examples of the powers of each pillar through the discoveries of the past century. We continue with a discussion of what the future likely holds for predicting masses of new particle states. The observation of dark-matter suggests that nature has a stable, massive, neutral particle that has not yet been discovered. What is the underlying theoretical origin of this dark matter? The answer on which we focus is supersymmetry. SUSY, short for supersymmetry, relates the couplings of current fermions and bosons to the couplings of new bosons and fermions known as superpartners. The masses of the new SUSY particles reflect the origin of supersymmetry breaking. Many theories provide plausible origins of supersymmetry breaking but are beyond the scope of this thesis. We review selected elements of SUSY related to why one might believe it has something to do with nature and to key elements needed for the predictions in the following chapter.

Chapter 3, which is drawn from work published by the author and his supervisor in [10], presents a series of arguments using supersymmetry, unification, and precision measurements of low-energy observables to suggest some mass relationships and phases of the yet undiscovered superpartner masses⁴. In the early 1980s, Georgi and Jarlskog [11] observed that the masses of the quarks and leptons satisfied several properties at the grand unification scale. Because these masses cover six orders of magnitude, these relationships are very surprising. We discover that with updated experimental observations, the Georgi Jarlskog mass relationships can now only be satisfied for a specific class of quantum corrections enhanced by the ratio of the vacuum expectation value of the two supersymmetric Higgs $v_u/v_d \equiv \tan \beta$. We predict that $\tan \beta$ be large ($\gtrsim 20$) and the gluino mass has the sign opposite to the sign of the wino mass.

Chapter 4 reviews the existing toolbox of experimental techniques to determine masses and phases of masses. If the model is known, then determining the masses and phases can be done by fitting a complete simulation of the model to the LHC observations. However, to discover properties of an unknown model, one would like to study mass determination tools that are mostly model-independent⁵. Astrophysical dark-matter observations suggests the lightest new particle states be stable and leave the detector unnoticed. The dark-matter's stability suggests the new class of particles be produced in pairs. The pair-produced final-state invisible particles, if produced, would lead to large missing transverse momentum. Properties of hadron colliders make the task of mass determination of the dark-matter particles more difficult because we do not know the rest frame or energy of the initial parton collision. We review techniques based on combining kinematic edges, and others based on assuming enough on-shell states in one or two events such that the masses can be numerically solved. We continue with the transverse mass M_T which forms a lower-bound on the mass of the new particle which decays into a particle with missing transverse momentum, and was used to measure the mass of the W . The transverse mass M_T has a symmetry under boosts along the beam line. Next we review M_{T2} [12][13] which generalizes this to the case where there are two particles produced where each of them decays to invisible particle states.

Chapter 5 begins the original contributions of this thesis towards more accurate and robust mass determination techniques in the presence of invisible new particle states. We begin by

⁴The phase of a Majorana fermion mass contributes to the degree to which a particle and its antiparticle have distinguishable interactions. The convention is to remove the phase from the mass by redefining the fields such as to make the mass positive. This redefinition sometimes transfers the CP violating phase to the particle's interactions.

⁵By model-independent, we mean techniques that do not rely on the cross section's magnitude and apply generally to broad classes of models.

introducing novel ways to use the kinematic variable M_{T2} to discover new constraints among the masses of new states. We also discuss the relationship of M_{T2} to a recent new kinematic variable called M_{CT} . This work was published by the author in Ref. [14].

Chapter 6 introduces a new kinematic variable $M_{2C}(M_-)$. Most model-independent mass determination approaches succeed in constraining the mass difference $M_- = M_Y - M_N$ between a new states Y and the dark-matter particle N , but leave the mass scale $M_+ = M_Y + M_N$ more poorly determined. $M_{2C}(M_-)$ assume the mass difference, and then provides an event-by-event lower bound on the mass scale. The end-point of the M_{2C} distribution gives the mass M_Y which is equivalent to the mass scale if M_- is known. In this chapter we also discover a symmetry of the M_{2C} distribution which for direct Y pair production, makes the shape of the distribution entirely independent of the unknown collision energy or rest frame. Fitting the shape of the distribution improves our accuracy and precision considerably. We perform some initial estimates of the performance with several simplifying assumptions and find that with 250 signal events we are able to determine M_N with a precision and accuracy of ± 6 GeV for models with $M_Y + M_N/(M_Y - M_N) \approx 3$. This chapters results were published in Ref [15].

Chapter 7, which is based on work published by the author with Alan Barr and Graham Ross in Ref. [16], extends the M_{2C} kinematic variable in two ways. First we discover that in the presence of large upstream transverse momentum (UTM), that we are able to bound the mass scale from above. This upper bound is referred to as $M_{2C,UB}$. Here we perform a more realistic case study of the performance including backgrounds, combinatorics, detector acceptance, missing transverse momentum cuts and energy resolution. The case study uses data provided by Dr Alan Barr created with HERWIG Monte Carlo generator [17, 18, 19] to simulate the experimental data. The author wrote Mathematica codes that predict the shape of the distributions built from properties one can measure with the detector. We find the mass M_N by fitting to the lower-bound distribution M_{2C} and the upper-bound distribution $M_{2C,UB}$ distribution shapes. Our simulation indicates that with 700 events and all anticipated effects taken into consideration that we are able to measure the M_N to ± 4 GeV for models with $M_Y + M_N/(M_Y - M_N) \approx 3$. This indicates that the method described is as good as, if not better than, the other known kinematic mass determination techniques.

Chapter 8, which is based on work published by the author with Alan Barr and Alex Pinder in Ref. [20], extends the constrained mass variables to include two mass differences in the variable M_{3C} . We discuss the properties of the M_{3C} distribution. We observe that although the technique is more sensitive to energy resolution errors, we are still able to determine both the mass scale and

the two mass differences as good if not better than other known kinematic mass determination techniques. For SPS 1a we forecast determining the LSP mass with ± 2.4 GeV with about 3600 events.

Chapter 9 concludes the thesis. We predict the wino's mass will have the opposite sign of the gluino's mass. We develop new techniques to measure the mass of dark-matter particles produced at the LHC. Our techniques work with only two or three new particle states, and have precision and accuracy as good or better than other known kinematic mass determination techniques.

To facilitate identifying the original ideas contained in this thesis for which the author is responsible, we list them here explicitly along with the location in the thesis which elaborates on them:

- **Chapter 3** The updated values of the strong coupling constant, top quark mass, and strange quark mass lead to quantitative disagreement with the Georgi-Jarlskog mass relationships unless one uses $\tan \beta$ enhanced threshold corrections and fix the gluino's mass to be opposite sign of the wino's mass published in Ref [10].
- **Chapter 5** The relationship between Tovey's M_{CT} and Lester, Barr, and Summer's M_{T2} variables published in Ref [14].
- **Chapter 5** Using M_{T2} along intermediate stages of a symmetric cascade decay to discover new constraints among the masses published in Ref [14].
- **Chapter 6 and 7** The definition and use of the variable M_{2C} to determine mass of dark-matter-like new particle states published in Ref [15] and [16].
- **Chapter 7** The ability to obtain an event-by-event upper bound on the mass scale given the mass difference when the mass difference is known and the event has large upstream transverse momentum published in Ref [16].
- **Chapter 8** Complications and advantages to the logical extension variable M_{3C} and their use as a distribution which is published in Ref [20].
- A set of Mathematica Monte Carlo simulations, and M_{T2} calculators used to test the above contributions for M_{2C} , M_{3C} and some C++ codes for M_{2C} and $M_{2C,UB}$ which has not yet been published. The author will be happy to share any codes related to this thesis upon request.

Chapter 2

Mass Determination in the Standard Model and Supersymmetry

Chapter Overview

This chapter highlights three pillars of past successful new-particle state prediction and mass determination, and it shows how these pillars are precedents for the toolbox and concepts employed in Chapter 3's contributions. The three pillars on which rest most demonstrated successful theoretical new-particle-state predictions and mass determinations in particle physics are: (i) Symmetries, (ii) Broken symmetries, and (iii) Fine Tuning of Radiative Corrections. We use the narrative of these pillars to review and introduce the Standard Model and supersymmetry.

The chapter is organized as follows. Section 2.1 gives a few historical examples of these pillars: the positron's mass from Lorentz symmetry and from fine tuning, the Ω^- 's mass from an explicitly broken flavor symmetry, the charm quark's mass prediction from fine tuning, and the W^\pm and Z^0 masses from broken $SU(2)_L \times U(1)_Y$ gauge symmetries of the Standard Model. These historical examples give us confidence that these three pillars hold predictive power and that future employments of these techniques may predict new particle states and their masses. Section 2.2 introduces astrophysical observation of dark-matter which suggests that nature has a stable, massive, neutral particle that has not yet been discovered. Section 2.3 introduces key features of Supersymmetry, a model with promising potential to provide a dark-matter particle and simultaneously address many other issues in particle physics. We discuss reasons why Supersymmetry may describe nature, observational hints like the top-quark mass, anomaly in the muon's magnetic moment $(g - 2)_\mu$, and gauge coupling unification. We also review the classic $SU(5)$ Georgi-Jarlskog mass relations and $\tan \beta$ -enhanced SUSY threshold corrections. Chapter 3 will discuss how updated low-energy data and the Georgi-Jarlskog mass relationships may provide a window on predicting mass relationships of the low-energy supersymmetry.

2.1 Past Mass Determination and Discovery of New Particle States

2.1.1 Unbroken Lorentz Symmetry: Positron Mass

Our first example uses Lorentz symmetry to predict the existence of and mass of the positron. Lorentz symmetry refers to the invariance of physics to the choice of inertial frame of reference. The Lorentz group, which transforms vectors from their expression in one inertial frame to another, is generated by the matrix $M^{\alpha\beta}$. For a spin-1 object (single index 4-vector), the group elements, parameterized by a antisymmetric 4×4 matrix $\theta_{\mu\nu}$, are given by

$$\Lambda(\theta) = \exp(iM^{\mu\nu}\theta_{\mu\nu}) \quad (2.1)$$

where the antisymmetric matrix of generators $M^{\mu\nu}$ satisfies

$$[M^{\mu\nu}, M^{\rho\sigma}] = i(g^{\mu\rho}M^{\nu\sigma} - g^{\nu\rho}M^{\mu\sigma} - g^{\mu\sigma}M^{\nu\rho} + g^{\nu\sigma}M^{\mu\rho}) \quad (2.2)$$

and $g^{\mu\nu} = \text{diag}(1, -1, -1, -1)$ is the Lorentz metric. We emphasize that each entry of $M^{\mu\nu}$ is an operator (generator), where each entry of $\theta_{\mu\nu}$ is a number. The generators of the Poincaré symmetry are the generators of the Lorentz symmetry supplemented with generators for space-time translations P_μ satisfying $[P_\mu, P_\nu] = 0$ and

$$[M_{\mu\nu}, P_\rho] = -i(g_{\mu\rho}P_\nu - g_{\nu\rho}P_\mu). \quad (2.3)$$

Supersymmetry, introduced later in this thesis, is a generalization of the Poincaré symmetry.

In 1928 designing a theory with Lorentz symmetry was a major goal in early quantum mechanics. As Dirac described in his original paper, two problems persisted, (1) preservation of probability in quantum mechanics requires a first order linear equation for time evolution and (2) the presence of positive and negative energy solutions. The Klein-Gordon equation is

$$(D_\mu D^\mu - m^2)\phi = 0 \quad (2.4)$$

where $D_\mu = \partial_\mu - ieA_\mu$. It is invariant under Lorentz transformations but suffers from both problems: the equation is second order in ∂_t , and it has solutions proportional to $\exp(i\omega t)$ and $\exp(-i\omega t)$.

Dirac's 1928 paper on the Dirac equation [21] claims only to solve problem (1). Because problem (2) was not solved, Dirac claimed "The resulting theory is therefore still only an approximation". However, the paper shows how to do Lorentz invariant quantum mechanics of

spin 1/2 fields. Although in different notation, Dirac's paper showed that if one has a set of four matrices γ^μ that satisfy

$$\gamma^\mu \gamma^\nu + \gamma^\nu \gamma^\mu = 2g^{\mu\nu} \quad (2.5)$$

then the system of equations

$$(i\gamma^\mu D_\mu - m)\psi = 0 \quad (2.6)$$

transforms covariantly under Lorentz transformations if we define a new class of transforms $\Lambda_{1/2} = \exp(i\theta_{\mu\nu}(M_{1/2})^{\mu\nu})$ where the group is generated by

$$(M_{1/2})^{\mu\nu} = \frac{i}{2}(\gamma^\mu \gamma^\nu - \gamma^\nu \gamma^\mu). \quad (2.7)$$

The new generators $M_{1/2}$ satisfy Eq(2.2) so they form a representation of the Lorentz group specific to spin 1/2. The Dirac field transforms as $\psi' = \Lambda_{1/2}\psi$ and the γ^μ matrices transform as $\Lambda_{1/2}^\mu \gamma^\nu = \Lambda_{1/2}^{-1} \gamma^\mu \Lambda_{1/2}$.

Dirac interprets that the negative-energy solutions to the equations will behave as if they have the opposite charge but same mass in the presence of a background electromagnetic field. The formation of a relativistic quantum mechanics which still possesses negative energy solutions suggests that this alternative solution with negative energy and the opposite charge and same mass may be a prediction of relativistic quantum mechanics. Indeed, Anderson observed the negative energy version of the electron in 1933 [22]¹. The positron has the opposite charge of the electron but the same mass.

Today the Dirac equation is interpreted in terms of quantum field theory where all energies are always considered positive. With hindsight we see that Dirac's motivation was partially wrong, and the Klein-Gordon equation provides just as good an argument for antiparticles.

2.1.2 Renormalization, Fine Tuning and the Positron

The next example is not the historical origin of the positron's prediction, but could have been if physicists in the early 1900s understood the world with today's effective field theory tools. The electron's self-energy poses another problem which effective quantum field theory and the existence of the positron solve [23].

If we divide up the electron's charge into two pieces², we ask how much energy is stored in the system in the process of bringing the two halves together from infinity? At what distance

¹Anderson's first paper makes no reference to Dirac. However, he does introduce the term positron and suggests renaming the electron the negatron.

²The choice of two pieces is arbitrary and simplifies the calculations to illuminate the fine-tuning concept trying to be communicated.

apart will the ‘self energy’ of the electron be equal to the mass energy of the electron? This is approximately the classical electron radius³, and the answer is around ten times bigger than atomic nuclei at around $r_e = 7 \times 10^{-14}$ m. Electron-electron scattering can probe closer than this for collisions with $\sqrt{s} \approx 2$ MeV. Also electrons are emitted from nuclei during β decay suggesting the electron must be smaller than the nucleus. We now break the mass up into two quantities: the bare mass m_{e_o} and the ‘self-energy’ mass δm with the observed mass equalling $m_e = m_{e_o} + \delta m_e$. Phrasing self energy in terms of a cut-off one finds

$$\delta m_e \approx \frac{\Lambda}{4} \quad (2.8)$$

and the cut off Λ indicates the energy needed to probe the minimum distance within which two pieces of the electrons mass and charge must be contained. At the Plank scale, this requires a cancelation between the bare mass m_{e_o} and the self energy δm_e to more than 22 decimal places to end up with the observed mass $m_e = 0.511$ MeV! Fine tuning is where large cancelations between terms are needed to give an observable quantity. This large cancelation could be perceived as an indication of missing physics below the scale of about 2 MeV where we would have had a cancelation of the same size as the observable quantity m_e .

The effective quantum field theory used to describe electromagnetism introduces the positron with the same mass as the electron. The positron acts to moderate this “self-energy”. In QFT, the self energy of the electron is partly due to electron interaction with electron, but also partly due to electron interaction with a virtual positron. This is because the two interaction vertices x and y are integrated over $\int d^4x d^4y$ so the interaction The resulting self energy, in terms of a cut off Λ , is

$$\frac{\delta m_e}{m_e} \approx \frac{\alpha}{4\pi} \ln \frac{\Lambda^2}{m_e^2} \quad (2.9)$$

where $\alpha = e^2/4\pi$. Weisskopf and Furry were the first to discover that quantum field theory with both positrons and electrons leads to only a logarithmic divergence [24, 25]. Now we see that taking the cut off Λ to the Plank scale only gives a 6% correction. There is no longer a cancelation of two large terms, an issue solved by introducing new physics below the scale at which the low-energy effective theory became fine tuned.

2.1.3 Broken Flavor Symmetry: Ω^- Mass

The next example brings us to the early 1960s when Murray Gell-mann [26] and Yuval Ne’eman [27]⁴ were both studying broken $SU(3)$ flavor symmetry as a way to understand the zoo of par-

³The classical electron radius is $4\times$ this value.

⁴Yuval Ne’eman, like the author of this thesis, was a member of the military while studying for his PhD [28].

ticles being discovered in the 1950s and 1960s. Their study led to the theoretical determination of mass of the Ω^- baryon before it was observed.

To place the $SU(3)$ flavor symmetry in context, we begin first with the $SU(2)$ isospin symmetry. Isospin symmetry postulates that protons p and neutrons n are indistinguishable if one ignores electromagnetism. Therefore, the equations and forces governing p and n interactions should have a symmetry on rotating the proton's complex field p into the neutron's complex field n with an $SU(2)$ rotation. The symmetry is explicitly broken by the electromagnetic force and to a lesser extent the quark masses, and a special direction is singled out. We can label the eigenvalues along this broken direction. The eigenvalues of I_3 isospin generator label the states along the broken isospin axis: $I_3 = 1/2$ denotes a proton, and $I_3 = -1/2$ denotes a neutron. Today we can trace the isospin symmetry to the presence of up and down quarks with nearly the same mass. Isospin symmetry is broken both by electromagnetism and by the up and down quark mass difference.

Next we wish to understand how $SU(3)_f$ symmetry predicted the mass of the Ω^- . The $SU(3)$ flavor symmetry is an extension of isospin symmetry. It can be understood in modern language as the existence of three light quarks. The symmetry is broken because the strange quark is considerably more massive ($\approx 103 \pm 12$ GeV) than the up and down quark ($m_u \approx 2.7 \pm 0.5$ GeV, and $m_d = 5.7 \pm 0.5$ GeV)⁵. The group $SU(3)$ has isospin $SU(2)$ as a supgroup so I_3 remains a good quantum number; in addition $SU(3)$ states are also specified by the hypercharge Y . Quarks and anti-quarks are given the following charge assignments (I_3, Y) : $u = (1/2, 1/3)$, $d = (-1/2, 1/3)$, $s = (0, -2/3)$, $\bar{u} = (-1/2, -1/3)$, $\bar{d} = (1/2, -1/3)$, $\bar{s} = (0, 2/3)$. Representations of $SU(3)$ are formed by tensors of the fundamental its conjugate with either symmetrized or antisymmetrized indices and with traces between upper and lower indices removed. Representations are named by the number of independent components that tensor possesses and shown by bold numbers like **3**, **8**, **10**, **27** etc.

Gell-mann and Ne'eman did not know what representation of $SU(3)$ was the correct one to describe the many baryons and mesons being discovered; to describe the spin 3/2 light baryons, they were each considering the **10** and the **27**. The representation **10** is formed by B^{abc} where a, b , and c are indexes that run over u , d , and s , and where the tensor B^{abc} is symmetric on interchanges of the three indices. The states are displayed as the red dots in Fig. 2.1 where the conserved quantum numbers of I_3 is plotted against hypercharge Y . The **27** is given by a tensor B_{cd}^{ab} where (ab) is symmetrized, (cd) is symmetrized, and the 9 traces $B_{cd}^{ac} = 0$ are removed.

⁵Quark masses are very difficult to define because they are not free particles. Here we quote the current quark masses at an \overline{MS} renormalization scheme scale of $\mu = 2$ GeV as fit to observations in Chapter 3.

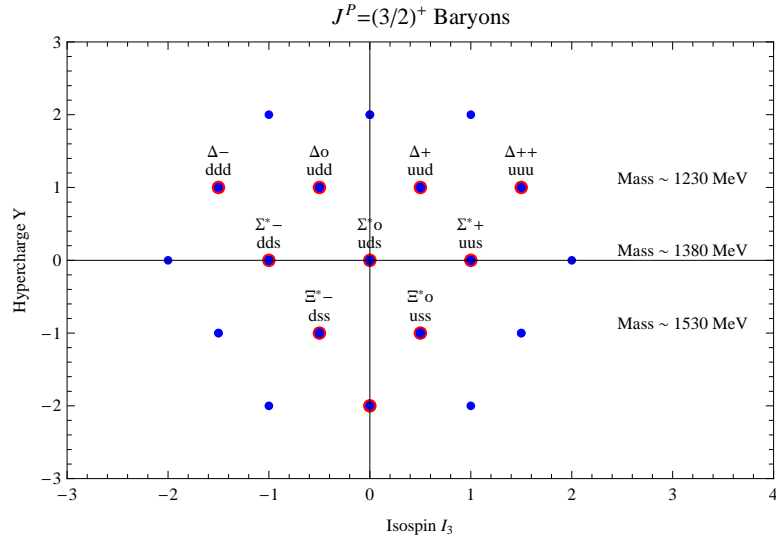


Figure 2.1: The states of the $SU(3)$ **10** of $J^P = 3/2^+$ baryons in 1962. Also shown is the $SU(3)$ **27**.

The **27** is shown by the smaller blue dots. The particles and the observed masses as of 1962 are shown in the Fig 2.1.

In July 1962, both Gell-mann and Ne'eman went to the 11th International Conference on High-Energy Physics at CERN. Ne'eman learned from Sulamith and Gerson Goldhaber (a husband and wife pair) that $K^+(\bar{u}s, I_3 = +1/2, Y = 1)$ vs $N(du, I_3 = -1/2, Y = 1)$ scattering did not lead to a resonance at $(I_3 = 0, Y = 2)$ with a mass range near 1000 MeV as one would expect if the pattern followed was that of the **27** [29]. Gell-mann had also learned of the Goldhabers' negative result, now known as the Goldhaber gap. During the discussion after the next talk at the conference, Gell-mann and Ne'eman both planned on announcing their observation; Gell-mann was called on first, and announced that one should discover the Ω^- with a mass near 1680 GeV. The Ω^- was first seen in 1964 at Brookhaven [30] with a mass of $M_{\Omega^-} = 1686 \pm 12$ MeV. Amazingly the spin of Ω^- was not experimentally verified until 2006 [31].

The broken $SU(3)_F$ flavor symmetry successfully predicted and explained the masses of the Ω^- and many other baryons and mesons. The general formula for the masses in terms of the broken symmetry was developed both by Gell-mann and by Okubo and is known as the Gell-mann-Okubo mass formula [32].

Despite this success (and many others) the quark-model theoretical description used here is still approximate; the strong force is only being parameterized. The quarks here classify the hadrons, but the masses of the quarks do not add up to the mass of the hadron. Quark masses that are thought of as being about 1/3 the mass of the baryon are called “constituent quark masses”. These are not the quark masses that are most often referenced in particle physics. A

consistent definition of quark mass and explanation of how these quarks masses relate to hadron masses will wait for the discovery of color $SU(3)_c$. In $SU(3)_c$ the masses of the quarks are defined in terms of Chiral Perturbation Theory (χ PT) and are called “current” quark masses. We will be using current quark masses as a basis for the arguments in Chapter 3.

Another important precedent set here is that of arranging the observed particles in a representation of a larger group that is broken. This is the idea behind both the Standard Model and the Grand Unified Theories to be discussed later. The particle content and the forces are arranged into representations of a group. When the group is broken, the particles distinguish themselves as those we more readily observe.

2.1.4 Charm Quark Mass Prediction and Fine Tuning of Radiative Corrections

In the non-relativistic quark model, the neutral K^0 is a bound state of d and \bar{s} and \bar{K}^0 is a bound state of s and \bar{d} . The Hamiltonian for this system is given by ⁶

$$H_{K,\bar{K}} = \begin{pmatrix} K^0 & \bar{K}^0 \end{pmatrix} \begin{pmatrix} M_o^2 & \delta^2 \\ \delta^2 & M_o^2 \end{pmatrix} \begin{pmatrix} K^0 \\ \bar{K}^0 \end{pmatrix}. \quad (2.10)$$

A non-zero coupling δ between the two states leads to two distinct mass eigenstates. For $\delta \ll M_o$, the two mass eigenstates have almost equal mixtures of K^0 and \bar{K}^0 and are called K_1 and K_2 . Experimentally the mass splitting between the two eigenstates is $M_{K_2} - M_{K_1} = 3.5 \times 10^{-6}$ eV.

During the 1960s, a combination of chiral four-Fermi interactions with the approximate chiral symmetry $SU(3)_L \times SU(3)_R$ of the three lightest quarks was proving successful at describing many hadronic phenomena; however, it predicted δ was non zero. Let’s see why. The effective weak interaction Lagrangian that was successful in atomic decays and Kaon decays [33][34] was given by

$$\mathcal{L} = \frac{2G_F}{\sqrt{2}} J^\mu J_\mu^\dagger \quad \text{where} \quad J^\mu = J_{(L)}^\mu + J_{(H)}^\mu \quad (2.11)$$

and

$$J_{(L)}^\mu = \bar{\nu}_e \gamma^\nu \frac{1}{2} (1 - \gamma^5) e + \bar{\nu}_\mu \gamma^\nu \frac{1}{2} (1 - \gamma^5) \mu \quad (2.12)$$

$$J_{(H)}^\mu = \bar{u} \gamma^\nu \frac{1}{2} (1 - \gamma^5) d \cos \theta_c + \bar{u} \gamma^\nu \frac{1}{2} (1 - \gamma^5) s \sin \theta_c. \quad (2.13)$$

and θ_c is the Cabibbo angle. Using a spontaneously broken $SU(3)_L \times SU(3)_R$ [35] one can calculate the loops connecting $u\bar{s}$ to $\bar{u}s$. These loops are responsible for the Kaon mass splitting

⁶In this Hamiltonian, we’re neglecting the CP violating features.

and give

$$M_{K_2} - M_{K_1} = \frac{\delta^2}{M_K} \approx \frac{\cos^2 \theta_c \sin \theta_c}{4\pi^2} f_K^2 M_K G_F (G_F \Lambda^2) \quad (2.14)$$

where Λ is the cut off on the divergent loop and $f_K \approx 180$ GeV [36][37][35][33]. Using this relation, the cut-off cannot be above 2 GeV without exceeding the observed Kaon mass splitting. There are higher order contributions, each with higher powers of $G_F \Lambda^2$, that may cancel to give the correct answer. Indeed Glashow, Ilioupoulos, and Maiani (GIM) [37] observe in a footnote “Of course there is no reason that one cannot exclude *a priori* the possibility of a cancelation in the sum of the relevant perturbation expansion in the limit $\Lambda \rightarrow \infty$ ”. The need for an extremely low cut off was a problem of fine tuning and naturalness with respect to radiative corrections.

This solution to the unnaturally low scale of Λ suggested by the mass splitting $M_{K_2} - M_{K_1}$ holds foreshadowing for supersymmetry ⁷. GIM proposed a new broken quark symmetry $SU(4)$ which required the existence of the charm quark, and also discuss its manifestation in terms of a massive intermediate vector boson W^+ , W^- . They introduce a unitary matrix U , which will later be known as the CKM matrix. We place group the quarks into groups: $d^i = d, s, \dots$ and $u^i = u, c, \dots$; then the matrix U_{ij} links up-quark i to down-quark j to the charged current

$$(J_{(H)})^\mu = \bar{u}^i \gamma^\mu \frac{1}{2} (1 - \gamma^5) d^j U_{ij}. \quad (2.15)$$

The coupling of the Kaon to the neutral current formed by the pair of W^+ with W^- . In the limit of exact $SU(4)$ (all quark masses equal) the coupling of the Kaon to the neutral current is proportional to $\mathcal{A} \propto (\sum_{j=u,c,\dots} U_{dj} U_{js}^\dagger) = \delta_{ds} = 0$. The coupling δ^2 between K^o and \bar{K}^o is proportional to \mathcal{A}^2 . This means that in the limit of $SU(4)$ quark symmetry, there would be no coupling to enable K_1 and K_2 mass splitting.

However, the observed K_1 K_2 mass splitting is non-zero, and $SU(4)$ is not an exact symmetry; it is broken by the quark masses. The mass splitting is dominated by the mass of the new quark m_c . GIM placed a limit on $m_c \lesssim 3$ GeV. One might think of the proposed $SU(4)$ symmetry becoming approximately valid above scale $\Lambda \approx m_c$. The new physics (in this case the charm quark) was therefore predicted and found to lie at the scale where fine tuning could be avoided.

2.1.5 The Standard Model: Broken Gauge Symmetry: W^\pm , Z^o Bosons Mass

The Standard Model begins with a gauge symmetry $SU(3)_c \times SU(2)_L \times U(1)_Y$ that gets spontaneously broken to $SU(3)_c \times U(1)_{EM}$. For a more complete pedagogical introduction, the author has found useful Refs. [38, 39, 40] and the PDG [41, Ch 10].

⁷I have learned from Alan Barr that Maiani also sees the GIM mechanism as a precedent in favor of supersymmetry.

Field	Lorentz ⁸	$SU(3)_c$	$SU(2)_L$	$U(1)_Y$
$(L)^i$	$(2, 0)$	1	2	-1
$(e^c)^i$	$(2, 0)$	1	1	2
$(\nu^c)^i$	$(2, 0)$	1	1	0
$(Q)^i$	$(2, 0)$	3	2	1/3
$(u^c)^i$	$(2, 0)$	$\bar{3}$	1	-4/3
$(d^c)^i$	$(2, 0)$	$\bar{3}$	1	2/3
H	1	1	2	+1
B_μ	4	1	1	0^\ddagger
W_μ	4	1	3^\ddagger	0
G_μ	4	8^\ddagger	1	0

Table 2.1: Standard Model field's transformation properties. [‡] Indicates the field does not transform covariantly but rather transform as a connection⁹.

The field content of the Standard Model with its modern extensions for our future use is given in Table 2.1. The i indexes the three generations. The fermions are all represented as 2-component Weyl left-handed transforming states⁸. The gauge bosons do not transform covariantly under the gauge group, rather they transform as connections⁹. In 1967 [42], Weinberg set the stage with a theory of leptons which consisted of the left-handed leptons which form $SU(2)$ doublets L^i , the right-handed charged leptons which form $SU(2)$ singlets $(e^c)^i$, and the Higgs fields H which is an $SU(2)$ doublet. Oscar Greenberg first proposed 3-color internal charges of $SU(3)_c$ in 1964 [43]¹⁰. It was not until Gross and Wilczek and Politzer discovered asymptotic freedom in the mid 1970s that $SU(3)_c$ was being taken seriously as a theory of the strong nuclear force [45][46]. The hypercharge in the SM is not the same hypercharge as in the previous subsection¹¹. The $U(1)_Y$ hypercharge assignments Y are designed to satisfy $Q = \sigma^3/2 + Y/2$ where Q is the electric charge operator and $\sigma^3/2$ is with respect to the $SU(2)_L$ doublets (if it has a charge under $SU(2)_L$ otherwise it is 0).

The gauge fields have the standard Lagrangian

$$\mathcal{L}_{W,B,G} = \frac{-1}{4}B_{\mu\nu}B^{\mu\nu} + \frac{-1}{2}\text{Tr}W_{\mu\nu}W^{\mu\nu} + \frac{-1}{2}\text{Tr}G_{\mu\nu}G^{\mu\nu} \quad (2.16)$$

where $B_{\mu\nu} = \frac{i}{g'}[D_\mu, D_\nu]$ when D_μ is the covariant derivative with respect to $U(1)$: $D_\mu = \partial_\mu - ig'B_\mu$. Likewise $W_{\mu\nu} = \frac{i}{g}[D_\mu, D_\nu]$ with $D_\mu = \partial_\mu - ig\frac{\sigma^a}{2}W_\mu^a$ and $G_{\mu\nu} = \frac{i}{g_3}[D_\mu, D_\nu]$ with $D_\mu = \partial_\mu - ig_3\frac{\lambda^a}{2}G_\mu^a$ with $\sigma/2$ and $\lambda/2$ the generators of $SU(2)$ and $SU(3)$ gauge symmetry

⁸ The $(2, 0)$ is the projection of Eq(2.7) onto left handed states with $P_L = 1/2(1 - \gamma^5)$. In a Weyl basis, Eq(2.7) is block diagonal so one can use just the two components that survive P_L . If e^c transforms as a $(2, 0)$ then $i\sigma^2(e^c)^*$ transforms as $(0, 2)$.

⁹The gauge fields transform as connections under gauge transformations: $W'_\mu = UW_\mu U^{-1} + (i/g)U\partial_\mu U^{-1}$.

¹⁰Greenberg, like the author, also has ties to the US Air Force. Greenberg served as a Lieutenant in the USAF from 1957 to 1959. A discussion of the history of $SU(3)_c$ can be found in Ref. [44].

¹¹In the SM, the d and s (both left-handed or right-handed) have the same hypercharge, but in flavor $SU(3)_f$ (2.1.3) they have different hypercharge.

respectively. The $1/g$ factors in these definitions give the conventional normalization of the field strength tensors. At this stage, $SU(2)$ gauge symmetry prevents terms in the Lagrangian like $\frac{1}{2}M_W^2 W_\mu W^\mu$ which would give W a mass.

The leptons and quarks acquire mass through the Yukawa sector given by

$$\mathcal{L}_Y = Y_{ij}^e L^i (i\sigma^2 H^*) (e^c)^j + Y_{ij}^d Q^i (i\sigma^2 H^*) (d^c)^j + Y_{ij}^u Q^i H (u^c)^j + h.c. \quad (2.17)$$

where we have suppressed all but the flavor indices¹². Because H and $i\sigma_2 H^*$ both transform as a **2** (as opposed to a $\bar{\mathbf{2}}$), these can be used to couple a single Higgs field to both up-like and down-like quarks and leptons. If neutrinos have a Dirac mass then Eq(2.17) will also have a term $Y_{ij}^\nu L^i H (\nu^c)^j$. If the right-handed neutrinos have a Majorana mass, there will also be a term $M_{R_{jk}} (\nu^c)^j (\nu^c)^k$.

With these preliminaries, we can describe how the W boson's mass was predicted. The story relies on the Higgs mechanism that enables a theory with an exact gauge symmetry to give mass to gauge bosons in such a way that the gauge symmetry is preserved, although hidden. The Higgs sector Lagrangian is

$$\mathcal{L}_H = D_\mu H^\dagger D^\mu H - \mu^2 H^\dagger H - \lambda (H^\dagger H)^2 \quad (2.18)$$

where the covariant derivative coupling to H is given by $D_\mu = \partial_\mu - ig\frac{\sigma^a}{2}W_\mu^a - ig'B_\mu$. The gauge symmetry is spontaneously broken if $\mu^2 < 0$, in which case H develops a vacuum expectation value (VEV) which by choice of gauge can be chosen to be along $\langle H \rangle = (0, v/\sqrt{2})$. The gauge boson's receive an effective mass due to the coupling between the vacuum state of H and the fluctuations of W and B :

$$\langle \mathcal{L}_H \rangle = \frac{g^2 v^2}{8} ((W^1)_\mu^2 + (W^2)_\mu^2) + \frac{v^2}{8} (g'B_\mu + g(W^3)_\mu)^2. \quad (2.19)$$

From this expression, one can deduce W_μ^1 and W_μ^2 have a mass of $M_W^2 = g^2 v^2/4$, and the linear combination $Z_\mu = (g^2 + g'^2)^{-1/2} (g'B_\mu + g(W^3)_\mu)$ has a mass $M_Z^2 = (g^2 + g'^2) v^2/4$. The massless photon A_μ is given by the orthogonal combination $A_\mu = (g^2 + g'^2)^{-1/2} (gB_\mu - g'(W^3)_\mu)$. The weak mixing angle θ_W is given by $\sin \theta_W = g'/(g^2 + g'^2)^{1/2}$, and electric charge coupling e is given by $e = g \sin \theta_W$.

Before W^\pm or Z^0 were observed, the value of v and $\sin^2 \theta_W$ could be extracted from the rate of neutral current weak processes, and through left right asymmetries in weak process experiments [47]. At tree-level, for momentum much less than M_W , the four-Fermi interaction

¹²Because both H and L transform as **2** their contraction to form an invariant is done like $L^a H^b \epsilon_{ab}$ where ϵ_{ab} is the antisymmetric tensor.

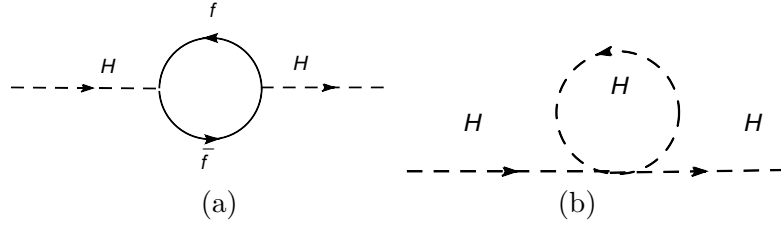


Figure 2.2: One Loop Contributions to the Higgs mass self energy. (a) Fermion loop. (b) Higgs loop.

can be compared to predict $M_W^2 = \sqrt{2}e^2/(8G_F \sin^2 \theta_W)$. By 1983 when the W boson was first observed, the predicted mass including quantum corrections was given by $M_W = 82 \pm 2.4$ GeV to be compared with the UA1 Collaboration's measurement $M_W = 81 \pm 5$ GeV [48]. A few months later the Z^0 boson was observed [49]. Details of the W boson's experimental mass determination will be discussed in Section 4.4 as it is relevant for this thesis's contributions in Chapters 5 - 8.

The Standard Model described in here has one serious difficulty regarding fine tuning of the Higgs mass radiative corrections. The Higgs field has two contributions to the mass self-energy shown in Fig. 2.2. The physical mass m_H is given by

$$m_H^2 \approx m_{o,H}^2 - \sum_{f=u,d,e} \frac{\text{Tr}(Y^f (Y^f)^\dagger)}{8\pi^2} \Lambda^2 + \frac{\lambda}{2\pi^2} \Lambda^2 \quad (2.20)$$

where $m_{o,H}$ is the bare Higgs mass, Λ is the cut off energy scale, $Y^u Y^d Y^e$ are the three Yukawa coupling matrices, third term is from the Higgs loop. Assuming the physical Higgs mass m_H is near the electo-weak scale (≈ 100 GeV)¹³ and Λ is at the Plank scale means that these terms need to cancel to some 34 orders of magnitude. If we make the cut off at $\Lambda \approx 1$ TeV the corrections from either Higgs-fermion loop¹⁴ are equal to a physical Higgs mass of $m_H = 100$ GeV. Once again there is no reason that we cannot exclude *a priori* the possibility of a cancelation between terms of this magnitude. However, arguing that such a cancelation is unnatural has successfully predicted the charm quark mass in Sec 2.1.4. Arguing such fine-tuning is unnatural in the Higgs sector suggests new physics should be present below around 1 TeV.

2.2 Dark Matter: Evidence for New, Massive, Invisible Particle States

Astronomical observations also point to a something missing in the Standard Model. Astronomers see evidence for 'dark matter' in galaxy rotation curves, gravitational lensing, the

¹³We use 100 GeV as a general electroweak scale. The current fits to Higgs radiative corrections suggest $m_H = 95 \pm 35$ GeV [8, Ch10], but the direct search limits require $m_H \gtrsim 115$ GeV.

¹⁴We use the fermion loop because the Higgs loop depends linearly on the currently unknown quartic Higgs self coupling λ .

cosmic microwave background (CMB), colliding galaxy clusters, large-scale structure, and high red-shift supernova. Some recent detailed reviews of astrophysical evidence for dark-matter can be found in Bertone *et.al*[50] and Baer and Tata [51]. We discuss the evidence for dark matter below.

• Galactic Rotation Curves

Observations of the velocity of stars normal to the galactic plane of the Milky Way led Jan Oort [52] in 1932 to observe the need for ‘dark matter’. The 1970s saw the beginning of using doppler shifts of galactic centers versus the periphery. Using a few ideal assumptions, we can estimate how the velocity should trend with changing r . The 21 cm HI line allows rotation curves of galaxies to be measured far outside the visible disk of a galaxy [53] To get a general estimate of how to interpret the observations, we assume spherical symmetry and circular orbits. If the mass responsible for the motion of a star at a radius r from the galactic center is dominated by a central mass M contained in $R \ll r$, then the tangential velocity is $v_T \approx \sqrt{G_N M/r}$ where G_N is Newton’s constant. If instead the star’s motion is governed by mass distributed with a uniform density ρ then $v_T = r \sqrt{4 G_N \rho \pi/3}$. Using these two extremes, we can find when the mass of the galaxy has been mostly bounded by seeking the distance r where the velocity begins to fall like \sqrt{r} . The observations [53, 54] show that for no r does v_T fall as $\sqrt{1/r}$. Typically v_T begins to rise linearly with r and then for some $r > R_o$ it stabilizes at $v_T = \text{const.}$. In our galaxy the constant v_T is approximately 220km/sec. The flat v_T vs r outside the optical disk of the galaxy implies $\rho(r) \propto r^{-2}$ for the dark matter. The density profile of the dark matter near the center is still in dispute. The rotation curves of the galaxies is one of the most compelling pieces of evidence that a non-absorbing, non-luminous, source of gravitation permeates galaxies and extends far beyond the visible disk of galaxies.

• Galaxy clusters

In 1937 Zwicky [55] published research showing that galaxies within clusters of galaxies were moving with velocities such that they could not have been bound together without large amounts of ‘dark matter’. Because dark matter is found near galaxies, a modified theory of newtonian gravity (MOND) [56] has been shown to agree with the galactic rotation curves of galaxies. A recent observation of two clusters of galaxies that passed through each other, known as the bullet cluster, shows that the dark matter is separated from the luminous matter of the galaxies[57]. The dark matter is measured through the gravitational lensing effect on the shape

of the background galaxies. The visible ‘pressureless’ stars and galaxies pass right through each other during the collision of the two galaxy clusters. The dark matter lags behind the visible matter. This separation indicates that the excess gravitation observed in galaxies and galaxy clusters cannot be accounted for by a modification of the gravitation of the visible sector, but requires a separate ‘dark’ gravitational source not equal to the luminous matter that can lag behind and induce the observed gravitational lensing. The bullet cluster observation is a more direct, empirical observation of dark matter.

The dark matter seen in the rotation curves and galaxy clusters could not be due to H gas (the most likely baryonic candidate) because it would have been observed in the 21 cm HI observations and is bounded to compose no more than 1% of the mass of the system [58]. Baryonic dark matter through MAssive Compact Halo Objects (MACHOs) is bounded to be $\lesssim 40\%$ of the total dark matter [8, Ch22]

• Not Baryonic: The Anisotropy of the Cosmic Microwave Background and Nucleosynthesis

The anisotropy of the cosmic microwave background radiation provides an strong constraint on both the total energy density of the universe, but also on the dark-matter and the baryonic part of the dark matter. Here is a short explanation of why.

The anisotropy provides a snapshot of the density fluctuations in the primordial plasma at the time the universe cools enough so that the protons finally ‘recombine’ with the electrons to form neutral hydrogen. The initial density fluctuations imparted by inflation follow a simple power law. The universe’s equation-of-state shifts from radiation dominated to matter dominated before the time of recombination. Before this transition the matter-photon-baryon system oscillates between gravitational collapse and radiation pressure. After matter domination, the dark matter stops oscillating and only collapses, but the baryons and photons remain linked and oscillating. The peaks are caused by the number of times the baryon-photon fluid collapses and rebounds before recombination.

The first peak of the CMB anisotropy power spectrum requires the total energy density of the universe to be very close to the critical density $\Omega = 1$. This first peak is the scale where the photon-baryon plasma is collapsing following a dark-matter gravitational well, reaches its peak density, but doesn’t have time to rebound under pressure before recombination. This attaches a length scale to the angular scale observed in the CMB anisotropy in the sky. The red-shift attaches a distance scale to the long side of an isosceles triangle. We can determine the geometry

from the angles subtended at vertex of this isosceles triangle with all three sides of fixed geodesic length. The angle is larger for such a triangle on a sphere than on a flat surface. By comparing the red-shift, angular scale, and length scale allows one to measure the total spatial curvature of space-time [59] to be nearly the critical density $\Omega = 1$.

We exclude baryonic matter as being the dark matter both from direct searches of H and MACHOs and from cosmological measurement of Ω_M vs Ω_b . Ω_M is the fraction of the critical density that needs to obey a cold-matter equation of state and Ω_b is the fraction of the critical density that is composed of baryons. Ω_Λ is the fraction of the critical density with a vacuum-like equation of state (dark energy). The anisotropy of the Cosmic Microwave Background (CMB) provides a constraint the reduced baryon density ($h^2\Omega_b$) and reduced matter density ($h^2\Omega_b$).

As the dark-matter collapses, the baryon-photon oscillates within these wells. The baryons however have more inertia than the photons and therefore ‘baryon-load’ the oscillation. The relative heights of the destructive and constructive interference positions indicate how much gravitational collapse due to dark matter occur during the time of a baryon-photon oscillation cycle. The relative heights of different peaks measure the baryon loading. Therefore, the third peak provides data about the dark matter density as opposed to the photon-baryon density.

Using these concepts, the WMAP results give estimates of the baryonic dark-matter: $\Omega_b h^2 = 0.0224 \pm 0.0009$ and the dark-matter plus baryonic matter $\Omega_M h^2 = 0.135 \pm 0.008$ [50]. The CMB value for Ω_b agrees with the big-bang nucleosynthesis (BBN) value $0.018 < \Omega_b h^2 < 0.023$. The dark-matter abundance is found to be $\Omega_M = 0.25$ using $h = 0.73 \pm 0.03$ [8, Ch21]. Combining the CMB results with supernova observations with baryon acoustic oscillations (BAO) compared to the galaxy distribution on large scales all lead to a three-way intersection on Ω_M vs Ω_Λ that give $\Omega_M = 0.245 \pm 0.028$, $\Omega_\Lambda = 0.757 \pm 0.021$, $\Omega_b = 0.042 \pm 0.002$ [60]. This is called the concordance model or the Λ CDM model.

Because all these tests confirm $\Omega_b \ll \Omega_M$, we see that the cosmological observations confirm the non-baryonic dark matter observed in galactic rotation curves.

• Dark Matter Direct Detection and Experimental Anomalies

First we assume a local halo density of the dark matter of $0.3 \text{ GeV}/\text{cm}^3$ as extracted from Ω_M and galaxy simulations. For a given mass of dark matter particle, one can now find a number density. The motion of the earth through this background number density creates a flux. Cryogenic experiments shielded deep underground with high purity crystals search for interactions of this dark matter flux with nucleons. Using the lack of a signal they place bounds on the cross

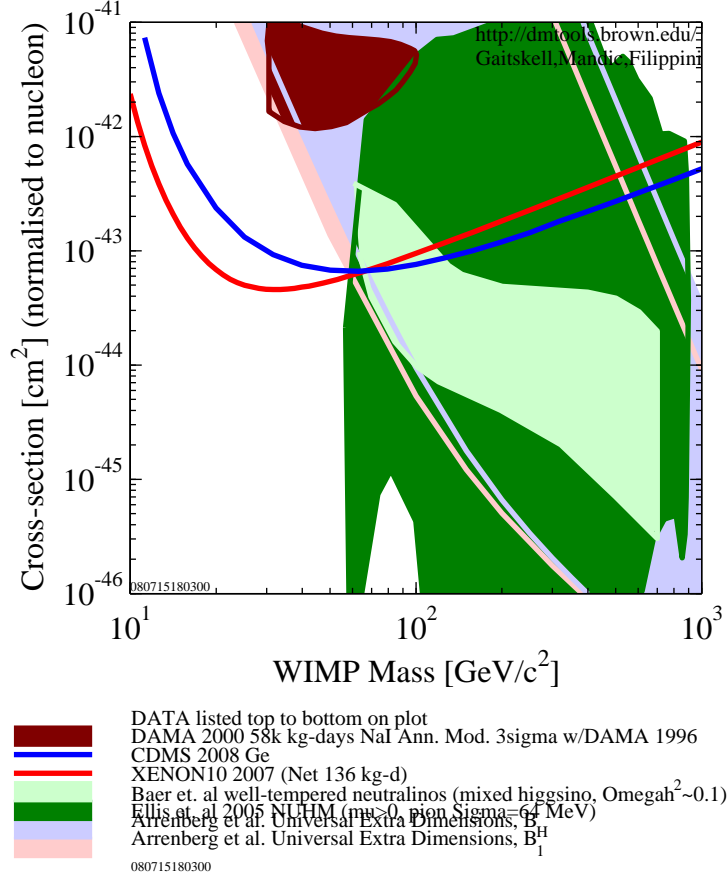


Figure 2.3: Direct dark matter searches showing the limits from the experiments CDMS, XENON10, and the DAMA signal. Also shown are sample dark-matter cross sections and masses predicted for several supersymmetric models and universal extra dimension models. Figures generated using <http://dmttools.berkeley.edu/limitplots/>.

section as a function of the mass of the dark matter particle which can be seen in Fig. 2.3. This figure shows direct dark-matter limits from the experiments CDMS (2008)[61], XENON10 (2007)[62], and the DAMA anomaly (1999) [63][64]. Also shown are sample dark-matter cross sections and masses predicted for several supersymmetric models [65][66] and universal extra dimension models [67]. This shows that the direct searches have not excluded supersymmetry as a viable source for the dark matter.

Although direct searches have no confirmed positive results, there are two anomalies of which we should be aware. The first is an excess in gamma rays observed in the EGRET experiment [68] which points to dark matter particle annihilation with the dark-matter particles mass between $50 \text{ GeV} < M_N < 100 \text{ GeV}$. The uncertainties in the background gamma ray sources could also explain this excess. The second anomaly is an annual variation observed in the DAMA experiment [63]. The annual variation could reflect the annual variation of the dark

matter flux as the earth orbits the sun. The faster and slower flux of dark-matter particles triggering the process would manifest as an annual variation. Unfortunately, CDMS did not confirm DAMA's initial results [69][61]. This year the DAMA/LIBRA experiment released new results which claim to confirm their earlier result[64] with an 8σ confidence. Until another group's experiment confirms the DAMA result, the claims will be approached cautiously.

• Dark matter Candidates

There are many models that provide possible dark-matter candidates. To name a few possibilities that have been considered we list: R -parity conserving supersymmetry, Universal Extra Dimensions (UED), axions, degenerate massive neutrinos [70], stable black holes. In Chapter 3 we focus on Supersymmetry as the model framework for explaining the dark-matter, but our results in Chapters 6 - 8 apply to any model where new particle states are pair produced and decay to two semi-stable dark matter particles that escape the detector unnoticed.

The pair-produced nature of dark-matter particles is relatively common trait of models with dark matter. For example the UED models [71, 72, 73] can also pair produced dark-matter particles at a collider. The lightest Kaluza-Klein particle (LKP) is also a dark-matter candidate. In fact UED and SUSY have very similar hadron collider signatures [74].

2.3 Supersymmetry: Predicting New Particle States

Supersymmetry will be the theoretical frame-work for new-particle states on which this thesis focuses. Supersymmetry has proven a very popular and powerful framework with many successes and unexpected benefits: Supersymmetry provides a natural dark-matter candidate. As a fledgling speculative theory, supersymmetry showed a preference for a heavy top-quark mass. In a close analogy with the GIM mechanism, Supersymmetry's minimal phenomenological implementation eliminates a fine-tuning problem associated with the Higgs boson in the Standard Model. Supersymmetry illuminates a coupling constant symmetry (Grand Unification) among the three non-graviational forces at an energy scale around 2×10^{16} GeV. Supersymmetry is the only extension of Poincaré symmetry discussed in 2.1.1 allowed with a graded algebra [75]. It successfully eliminates the tachyon in String Theory through the GSO projection [76]. Last, it is a candidate explanation for the 3σ deviation of the muons magnetic moment known as the $(g - 2)_\mu$ anomaly [77].

These successes are exciting because they follow many of the precedents and clues described earlier in this chapter that have successfully predicted new-particle states in the past. SUSY,

short for supersymmetry, relates the couplings of the Standard-Model fermions and bosons to the couplings of new bosons and fermions known as superpartners. SUSY is based on an extension of the Poincaré-symmetry (Sec 2.1.1). In the limit of exact Supersymmetry, the Higgs self-energy problem (Sec 2.1.5) vanishes. In analogy to the GIM mechanism (Sec 2.1.4), the masses of the new SUSY particles reflect the breaking of supersymmetry. There are many theories providing the origin of supersymmetry breaking which are beyond the scope of this thesis. The belief that nature is described by Supersymmetry follows from how SUSY connects to the past successes in predicting new-particle states and their masses from symmetries, broken-symmetries, and fine-tuning arguments.

Excellent introductions and detailed textbooks on Supersymmetry exist, and there is no point to reproduce these textbooks here. Srednicki provides a very comprehensible yet compact introduction to supersymmetry via superspace at the end of Ref [39]. Reviews of SUSY that have proved useful in developing this thesis are Refs [78, 79, 80, 81, 82, 83]. In this introduction, we wish to highlight a few simple parallels to past successes in new-particle state predictions. We review supersymmetric radiative corrections to the coupling constants and to the Yukawa couplings. These radiative corrections can be summarized in the renormalization group equations (RGE). The RGE have surprising predictions for Grand Unification of the non-gravitational forces and also show evidence of a quark lepton mass relations suggested by Georgi and Jarlskog which we refer to as mass matrix unification. The mass matrix unification predictions can be affected by potentially large corrections enhanced by the ratio of the vacuum expectation value of the two supersymmetric Higgs particles $v_u/v_d = \tan \beta$. Together, these renormalization group equations and the large $\tan \beta$ enhanced corrections provide the basis for the new contributions this thesis presents in Chapter 3.

2.3.1 Supersymmetry, Radiative Effects, and the Top Quark Mass

Supersymmetry extends the Poincaré symmetry used in 2.1.1. The super-Poincaré algebra involves a graded Lie algebra which has generators that anticommute as well as generators that commute. One way of understanding Supersymmetry is to extend four space-time coordinates to include two complex Grassmann coordinates which transform as two-component spinors. This extended space is called superspace. In the same way that P_μ generates space-time translations, we introduce one supercharge¹⁵ Q that generates translations in θ and $\bar{\theta}$. The graded super-

¹⁵We will only consider theories with one supercharge.

Poincaré algebra includes the Poincaré supplemented by

$$[Q_a^\dagger, P^\mu] = [Q_a, P^\mu] = 0 \quad (2.21)$$

$$\{Q_a, Q_b\} = \{Q_a^\dagger, Q_b^\dagger\} = 0 \quad (2.22)$$

$$[Q_a, M^{\mu\nu}] = \frac{i}{2}(\bar{\sigma}^\mu \sigma^\nu - \bar{\sigma}^\nu \sigma^\mu)_a^c Q_c^\dagger \quad (2.23)$$

$$[Q_a^\dagger, M^{\mu\nu}] = \frac{i}{2}(\sigma^\mu \bar{\sigma}^\nu - \sigma^\nu \bar{\sigma}^\mu)_{\dot{a}}^{\dot{c}} Q_{\dot{c}}^\dagger \quad (2.24)$$

$$\{Q_a, Q_{\dot{a}}^\dagger\} = 2\sigma_{a\dot{a}}^\mu P_\mu. \quad (2.25)$$

where M are the boost generators satisfying Eq(2.3), $\{, \}$ indicate anticommutation, a, b, \dot{a}, \dot{b} are spinor indices, $\sigma_\mu = (1, \vec{\sigma})$ and $\bar{\sigma}_\mu = (1, -\vec{\sigma})$. Eq(2.21) indicates that the charge Q is conserved by space-time translations. Eq(2.22) indicates that no more than states of two different spins can be connected by the action of a supercharge. Eq(2.23-2.24) indicate that Q and Q^\dagger transform as left and right handed spinors respectively. Eq(2.25) indicates that two supercharge generators can generate a space-time translation.

In relativistic QFT, we begin with fields $\phi(x)$ that are functions of space-time coordinates x^μ and require the Lagrangian to be invariant under a representation of the Poincaré group acting on the space-time and the fields. To form supersymmetric theories, we begin with superfields $\hat{\Phi}(x, \theta, \bar{\theta})$ that are functions of space-time coordinates x^μ and the anticommuting Grassmann coordinates θ_a and $\bar{\theta}_{\dot{a}}$ and require the Lagrangian to be invariant under a representation of the super-Poincaré symmetry acting on the superspace and the superfields. The procedure described here is very tedious: defining a representation of the super-Poincaré algebra, and formulating a Lagrangian that is invariant under actions of the group involves many iterations of trial and error. Several short-cuts have been discovered to form supersymmetric theories very quickly. These shortcuts involve studying properties of superfields.

Supersymmetric theories can be expressed as ordinary relativistic QFT by expressing the superfield $\hat{\Phi}(x, \theta, \bar{\theta})$ in terms of space-time fields like $\phi(x)$ and $\psi(x)$. The superfields, which we denote with hats, can be expanded as a Taylor series in θ and $\bar{\theta}$. Because $\theta_a^2 = \bar{\theta}_{\dot{a}}^2 = 0$, the superfield expansions consist of a finite number of space-time fields (independent of θ or $\bar{\theta}$); some of which transform as scalars, and some transform as spinors, vectors, or higher level tensors. A supermultiplet is the set of fields of different spin interconnected because they are part of the same superfield. If supersymmetry were not broken, then these fields of different spin would be indistinguishable. The fields of a supermultiplet share the same quantum numbers (including mass) except spin.

Different members of a supermultiplet are connected by the action of the supercharge operator Q or Q^\dagger : roughly speaking $Q|\text{boson}\rangle = |\text{fermion}\rangle$ and $Q|\text{fermion}\rangle = |\text{boson}\rangle$. Because $Q_a^2 = (Q_a^\dagger)^2 = 0$ a supermultiplet only has fields of two different spins. Also because it is a symmetry transformation, the fields of different spin within a supermultiplet need to have equal numbers of degrees of freedom¹⁶. A simple type of superfield is a chiral superfield. A chiral superfield consists of a complex scalar field and a chiral fermion field each with 2 degrees of freedom. Another type of superfield is the vector superfield $\hat{V} = \hat{V}^\dagger$ which consists of a vector field and a Weyl fermion field. Magically vector superfields have natural gauge transformations, the spin-1 fields transform as connections under gauge transformation whereas the superpartner spin-1/2 field transforms covariantly in the adjoint of the gauge transformation¹⁷.

The shortcuts to form Lagrangians invariant under supersymmetry transformations are based on three observations: (1) the products of several superfields is again a superfield (2) the term in an expansion of a superfield (or product of superfields) proportional to $\theta_a \theta_b \epsilon^{ab}$ is invariant under supersymmetry transformations up to a total derivative (called an F -term), and (3) the term in an expansion of a superfield (or product of superfields) proportional to $\theta_a \theta_b \epsilon^{ab} \bar{\theta}_{\dot{a}} \bar{\theta}_{\dot{b}} \epsilon^{\dot{a}\dot{b}}$ is invariant under supersymmetry transformations up to a total derivative (called a D -term).

These observations have made constructing theories invariant under supersymmetry a relatively painless procedure: the D -term of $\hat{\Psi}^\dagger e^{-\hat{V}} \hat{\Psi}$ provides supersymmetrically invariant kinetic terms. A superpotential \hat{W} governs the Yukawa interactions among chiral superfields. The F -term of \hat{W} gives the supersymmetrically invariant interaction Lagrangian. The F -term of \hat{W} can be found with the following shortcuts: If we take all the chiral superfields in \hat{W} to be enumerated by i in $\hat{\Psi}_i$ then the interactions follow from two simple calculations: The scalar potential is given by $\mathcal{L} \supset -(\sum_j |\partial \hat{W} / \partial \hat{\Psi}_j|^2)$ where $\hat{\Psi}_j$ is a the superfield and all the superfields inside $()$ are replaced with their scalar part of their chiral supermultiplet. The fermion interactions with the scalars are given by $\mathcal{L} \supset -\sum_{i,j} (\partial^2 \hat{W} / \partial \hat{\Psi}_i \partial \hat{\Psi}_j) \psi_i \psi_j$. where the superfields in $()$ are replaced with the scalar part of the chiral supermultiplet and ψ_i and ψ_j are the 2-component Weyl fermions that are part of their chiral supermultiplet $\hat{\Psi}_j$. Superpotential terms must be gauge invariant just as one would expect for terms in the Lagrangian and must be holomorphic function of the superfields¹⁸. Another way to express the interaction Lagrangian is by

¹⁶There are auxiliary fields in supermultiplets that, while not dynamical, preserve the degrees of freedom when virtual states go off mass shell.

¹⁷ Although this seems very unsymmetric, Wess and Bagger[81] show a supersymmetric differential geometry with tetrads that illuminate the magic of how the spin-1 fields transform as connections but the superpartners transform covariantly in the adjoint representation.

¹⁸By holomorphic we mean the superpotential can only be formed from unconjugated superfields $\hat{\Psi}$ and not the conjugate of superfields like $\hat{\Psi}^*$.

Field	Lorentz	$SU(3)_c$	$SU(2)_L$	$U(1)_Y$
$(L)^i$	$(2, 0)$	1	2	-1
$(\tilde{L})^i$	0	1	2	-1
$(e^c)^i$	$(2, 0)$	1	1	2
$(\tilde{e}^c)^i$	0	1	1	2
$(\nu^c)^i$	$(2, 0)$	1	1	0
$(\tilde{\nu}^c)^i$	0	1	1	0
$(Q)^i$	$(2, 0)$	3	2	1/3
$(\tilde{Q})^i$	0	3	2	1/3
$(u^c)^i$	$(2, 0)$	$\bar{3}$	1	-4/3
$(\tilde{u}^c)^i$	0	$\bar{3}$	1	-4/3
$(d^c)^i$	$(2, 0)$	3	1	2/3
$(\tilde{d}^c)^i$	0	3	1	2/3
H_u	1	1	2	+1
\tilde{H}_u	$(2, 0)$	1	2	+1
H_d	1	1	2	-1
\tilde{H}_d	$(2, 0)$	1	2	-1
B_μ	4	1	1	0^\pm
\tilde{B}	$(2, 0)$	1	1	0
W_μ	4	1	3^\pm	0
\tilde{W}	$(2, 0)$	1	3	0
g_μ	4	8^\pm	1	0
\tilde{g}	$(2, 0)$	8	1	0

Table 2.2: Minimal Supersymmetric Standard Model (MSSM) field's transformation properties. Fields grouped together are part of the same supermultiplet. $^\pm$ Indicated fields transform as a connection as opposed to covariantly¹⁷.

$\mathcal{L}_W = \int d\theta^2 \hat{W} + \int d\bar{\theta}^2 W^\dagger$ where the integrals pick out the F terms of the superpotential \hat{W} .

In addition to supersymmetry preserving terms, we also need to add ‘soft’ terms which parameterize the breaking of supersymmetry. ‘Soft’ refers to only SUSY breaking terms which do not spoil the fine-tuning solution discussed below.

To form the minimal supersymmetric version of the Standard Model, known as the MSSM, we need to identify the Standard Model fields with supermultiplets. The resulting list of fields is given in Table 2.2. Supersymmetry cannot be preserved in the Yukawa sector with just one Higgs field because the superpotential which will lead to the F -terms in the theory must be holomorphic so we cannot include both \hat{H} and \hat{H}^* superfields in the same superpotential; instead the MSSM has two Higgs fields $H_u = (h_u^+, h_u^0)$ and $H_d = (h_d^0, h_d^-)$. The neutral component of each Higgs will acquire a vacuum expectation value (VEV): $\langle h_u^0 \rangle = v_u$ and $\langle h_d^0 \rangle = v_d$. The parameter $\tan \beta = v_u/v_d$ is ratio of the VEV of the two Higgs fields.

The structure of the remaining terms can be understood by studying a field like a right-handed up quark. The (u^c) transforms as a $\mathbf{3}$ under $SU(3)$ so its superpartner must be also transform as a $\mathbf{3}$ but have spin 0 or 1. No Standard Model candidate exists that fits either option. A spin-1 superpartner is excluded because the fermion component of a vector superfield transforms as a connection in the adjoint of the gauge group; not the fundamental representation

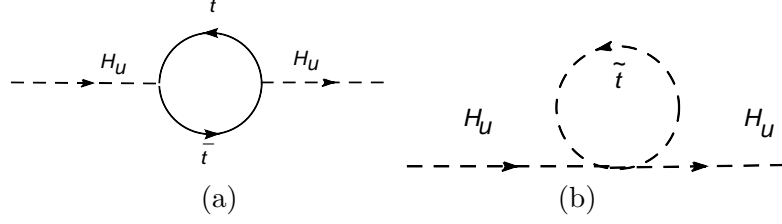


Figure 2.4: One Loop Contributions to the supersymmetric Higgs H_u mass self energy. (a) top loop. (b) stop loop.

like a quark. If (u^c) is part of a chiral superfield, then there is an undiscovered spin-0 partner. Thus the (u^c) is part of a chiral supermultiplet with a scalar partner called a right-handed squark \tilde{u}^c ¹⁹.

The remaining supersymmetric partner states being predicted in Table 2.2 can be deduced following similar arguments. The superpartners are named after their SM counterparts with preceding ‘s’ indicating it is a scalar superpartner of a fermion or affixing ‘ino’ to the end indicating it is a fermionic partner of a boson: for example selectron, smuon, stop-quark, Higgsino, photino, gluino, etc.

Supersymmetry solves the fine-tuning problem of the Higgs self energy. The superpotential describing the Yukawa sector of the MSSM is given by

$$\hat{W} = Y_{ij}^e \hat{L}^i \hat{H}_d (\hat{e}^c)^j + Y_{ij}^d \hat{Q}^i \hat{H}_d (\hat{d}^c)^j + Y_{ij}^u \hat{Q}^i \hat{H}_u (\hat{u}^c)^j + \mu \hat{H}_u \hat{H}_d \quad (2.26)$$

where the fields with hats like \hat{L} , $\hat{H}_{u,d}$, \hat{Q} , etc. are all superfields. In the limit of exact supersymmetry the fine-tuning problem is eliminated because the resulting potential and interactions lead to a cancelation of the quadratic divergences between the fermion and scalar loops in Fig 2.4. The self-energy of the neutral Higgs $H_u = (h_u^+, h_u^o)$ is now approximately given by

$$m_{h_u^o}^2 \approx |\mu_o|^2 - \frac{\text{Tr}(Y^u(Y^u)^\dagger)}{8\pi^2} \Lambda^2 + \frac{\text{Tr}(Y^u(Y^u)^\dagger)}{8\pi^2} \Lambda^2 \quad (2.27)$$

where $|\mu_o|^2$ is the modulus squared of the bare parameter in the superpotential which must be positive, the second term comes from the fermion loop and therefore has a minus sign, and the third term comes from the scalar loop. Both divergent loops follow from the MSSM superpotential: the first loop term follows from the fermion coupling $\partial^2 W / \partial t \partial t^c = y_t h_u^o t t^c$ and the second loop term follows from the scalar potential $|\partial W / \partial t^c|^2 = y_t^2 |h_u^o|^2 |\tilde{t}|^2$ and $|\partial W / \partial t|^2 = y_t^2 |h_u^o|^2 |\tilde{t}^c|^2$ where we assume the top-quark dominates the process. Exact supersymmetry ensures these two quadratically divergent loops cancel. However two issues remain and share a common solution: supersymmetry is not exact, and the Higgs mass squared must go negative to trigger

¹⁹The right-handed refers to which fermion it is a partner with. The field is a Lorentz scalar.

spontaneous symmetry breaking (SSB). In the effective theory well above the scale where all superpartners are energetically accessible the cancelation dominates. The fine-tuning arguments in Sec. 2.1.5 suggest that if $\mu_o \approx 100$ GeV ²⁰ this cancelation should dominate above about 1 TeV. In an effective theory between the scale of the top-quark mass and the stop-quark mass only the fermion loop (Fig 2.4 a) will contribute significantly. In this energy-scale region we neglect the scalar loop (Fig 2.4 b). With only the fermion loop contributing significantly and if y_t is large enough then the fermion loop will overpower μ_o^2 then the mass squared $m_{h_u}^2$ can be driven negative.

In this way the need for SSB without fine tuning in the MSSM prefers a large top-quark mass and the existence of heavier stop scalar states. Assuming $\mu_o \approx 100$ GeV predicts \tilde{t} and \tilde{t}^c below around 1 TeV²¹. This phenomena for triggering SSB is known as radiative electroweak symmetry breaking (REWSB). We have shown a very coarse approach to understanding the major features; details can be found in a recent review [84] or any of the supersymmetry textbooks listed above.

The detailed REWSB [85] technology was developed in the early 1980s, and predicted $M_t \approx 55 - 200$ GeV [86][87]; a prediction far out of the general expectation of $M_t \approx 15 - 40$ GeV of the early 1980s ²² and closer to the observed value of $M_t = 170.9 \pm 1.9$ GeV. If supersymmetric particles are observed at the LHC, the large top-quark mass may be looked at as the first confirmed prediction of supersymmetry.

The MSSM provides another independent reason to prefer a large top quark mass. The top Yukawa coupling's radiative corrections are dominated by the difference between terms proportional to g_3^2 and y_t^2 . If the ratio of these two terms is fixed, then y_t will remain fixed [92]. For the standard model this gives a top quark mass around 120 GeV. However for the MSSM, assuming $\alpha_3 = g_3^2/4\pi = 0.12$ then one finds a top quark mass around 180 GeV assuming a moderate $\tan\beta$ [93]. Our observations of the top quark mass very near this fixed point again points to supersymmetry as a theory describing physics at scalars above the electroweak scales.

2.3.2 Dark Matter and SUSY

Supersymmetry is broken in nature. The masses of the superpartners reflect this breaking. Let's assume the superpartner masses are at a scale that avoids bounds set from current searches yet still solve the fine-tuning problem. Even in this case there are still problems that need to be

²⁰Again we choose 100 GeV as a generic electroweak scale.

²¹As fine tuning is an aesthetic argument, there is a wide range of opinions on the tolerable amount of fine tuning acceptable. There is also a wide range of values for μ that are tolerable.

²²Raby [88] Glashow [89] and others [90] [91] all made top-quark mass predictions in the range of 15 – 40 GeV.

resolved ²³. There are many couplings allowed by the charge assignments displayed in Table 2.2 that would immediately lead to unobserved phenomena. For example the superpotential could contain superfield interactions $\hat{u}^c \hat{u}^c \hat{d}^c$ or $\hat{Q} \hat{L} \hat{d}^c$ or $\hat{L} \hat{L} \hat{e}^c$ or $\kappa \hat{L} \hat{H}_u$ where κ is a mass scale. Each of these interactions is invariant under the $SU(3)_c \times SU(2)_L \times U(1)_Y$ charges listed in Table 2.2. These couplings, if allowed with order 1 coefficients, would violate the universality of the four-Fermi decay, lead to rapid proton decay, lepton and baryon number violation, etc.

These couplings can be avoided in several ways. We can require a global baryon number or lepton number $U(1)$ on the superpotential; in the Standard Model these were accidental symmetries. However, successful baryogenesis requires baryon number violation so imposing it directly is only an approximation. Another option is to impose an additional discrete symmetry on the Lagrangian; a common choice is R -parity

$$R = (-1)^{2j+3B+L} \quad (2.28)$$

where j is the spin of the particle. This gives the Standard Model particles $R = 1$ and the superpartners $R = -1$. Each interaction of the MSSM Lagrangian conserves R -parity. The specific choice of how to remove these interactions is more relevant for GUT model building. The different choices lead to different predictions for proton decay lifetime.

The R -Parity, which is needed to effectively avoid these unobserved interactions at tree level, has the unexpected benefit of also making stable the lightest supersymmetric particle (LSP). A stable massive particle that is non-baryonic is exactly what is needed to provide the dark matter observed in the galactic rotation curves of Sec. 2.2.

2.3.3 Renormalization Group and the Discovered Supersymmetry Symmetries

Unification of $SU(3)_c \times SU(2)_L \times U(1)_Y$ coupling constants

Up until now, the divergent loops have been treated with a UV cut off. Renormalization of non-abelian gauge theories is more easily done using dimensional regularization where the dimensions of space-time are taken to be $d = 4 - 2\epsilon$. The dimensionless coupling constants g pick up a dimensionfull coefficient $g\mu^{-\epsilon}$ where μ is an arbitrary energy scale. The divergent term in loops diagrams is now proportional to $1/\epsilon$, and the counter-terms can be chosen to cancel these divergent parts of these results. By comparison with observable quantities, all the parameters in the theory are measured assuming a choice of μ . The couplings with one choice of μ can be related to an alternative choice of μ by means of a set of differential equation known as the

²³There is also a flavor changing neutral current (FCNC) problem not discussed here.

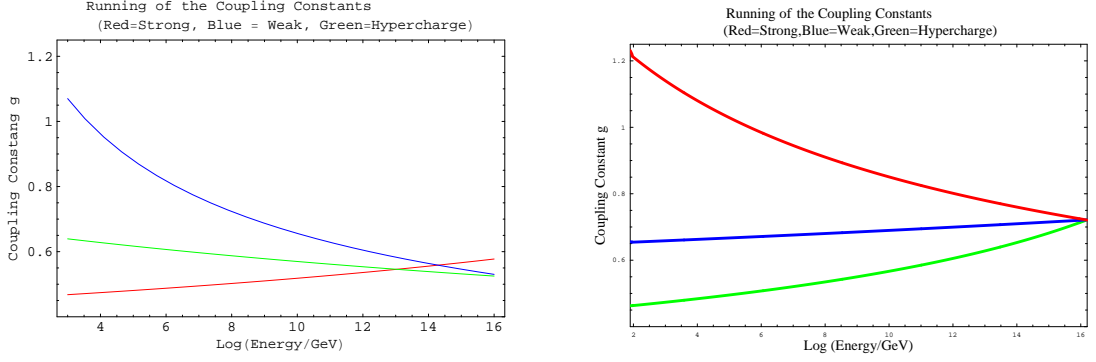


Figure 2.5: Gauge couplings for the three non-gravitational forces as a function of energy scale for the (left) Standard Model and (right) MSSM.

renormalization group equations (RGE). The choice of μ is similar to the choice of the zero of potential energy; in principle any choice will do, but in practice some choices are easier than others. Weinberg shows how this arbitrary scale can be related to the typical energy scale of a process [34].

The renormalization group at one loop for the coupling constant g of an $SU(N)$ gauge theory coupled to fermions and scalars is

$$\frac{\partial}{\partial \log \mu} g = \frac{g^3}{16\pi^2} \left[\frac{11}{3} C(G) - \frac{2}{3} n_F S(R_F) - \frac{1}{3} n_S S(R_S) \right] \quad (2.29)$$

where n_F is the number of 2-component fermions, n_S is the number of complex scalars, $S(R_{F,S})$ is the Dynkin index for the representation of the fermions or scalars respectively. Applying this to our gauge groups in the MSSM $C(G) = N$ for $SU(N)$ and $C(G) = 0$ for $U(1)$. For the fundamental $SU(N)$ we have $S(R) = 1/2$; for the adjoint $S(R) = N$; for $U(1)$ we have $S(R)$ equal to the $\sum (Y/2)^2$ over all the scalars (which accounts for the number of scalars). When the $SU(3)_c \times SU(2)_L \times U(1)_Y$ is embedded in a larger group like $SU(5)$, the $U(1)_Y$ coupling g' is rescaled to the normalization appropriate to the $SU(5)$ generator that becomes hypercharge. This rescaling causes us to work with $g_1 = \sqrt{5/3} g'$ ²⁴.

Applying this general formula to both the Standard Model (SM) and the MSSM leads to

$$\frac{\partial}{\partial \log \mu} g_i = \frac{g_i^3}{16\pi^2} b_i \quad (2.30)$$

$$\text{SM} \begin{cases} b_1 = n_G 4/3 + n_H 1/10 \\ b_2 = -22/3 + n_G 4/3 + n_H 1/6 \\ b_3 = -11 + n_G 4/3 \end{cases} \quad \text{MSSM} = \begin{cases} b_1 = n_G 2 + n_H 3/10 \\ b_2 = -6 + n_G 2 + n_H 1/2 \\ b_3 = -9 + n_G 2 \end{cases}$$

where $n_G = 3$ is the number of generations and n_H is the number of Higgs doublets ($n_H = 1$ in SM and $n_H = 2$ in MSSM). A miracle is shown in Fig. 2.5. The year 1981 saw a flurry of

²⁴Eq(2.29) is for g' and one must substitute the definition of g_1 to arrive at Eq(2.30).

papers from Dimopoulos, Ibanez, Georgi, Raby, Ross, Sakai and Wilczek who were detailing the consequences of this miracle [94][95][96][97]. There is one degree of freedom in terms of where to place an effective supersymmetry scale M_S where Standard Model RG running turns into MSSM RG running. At one-loop order, unification requires $M_S \approx M_Z$; at two-loop order $200 \text{ GeV} < M_S < 1 \text{ TeV}$ ²⁵.

The MSSM was not designed for this purpose, but the particle spectrum gives this result effortlessly²⁶. A symmetry among the coupling of the three forces is discovered through the RG equations. If the coupling unify, they may all originate from a common grand-unified force that is spontaneously broken at $\mu \approx 2 \times 10^{16} \text{ GeV}$.

There are several possibilities for SUSY GUT theories: $SU(5)$ [100] or $SO(10)$ or $SU(4) \times SU(2)_L \times SU(2)_R$ [101] to list just a few. $SU(5)$, although the minimal version is now excluded experimentally, is the prototypical example with which we work. A classic review of GUT theories can be found in [102]

Georgi-Jarlskog Factors

It is truly miraculous that the three coupling constants unify (to within current experimental errors) with two-loop running when adjusted to an $SU(5)$ grand unified gauge group and when the SUSY scale is placed in a region where the fine-tuning arguments suggest new-particle states should exist. Let's now follow the unification of forces arguments to the next level. Above the unification scale, there is no longer a distinction between $SU(3)_c$ and $U(1)_Y$. If color and hypercharge are indistinguishable, what distinguishes an electron from a down-quark? The Yukawa couplings, which give rise to the quark and lepton masses, are also functions of the scale μ and RG equations relate the low-energy values to their values at the GUT scale. Appendix A gives details of the RG procedure used in this thesis to take the measured low-energy parameters and use the RG equations to relate them to the predictions at the GUT scale. Do the mass parameters also unify?

With much more crude estimates for the quark masses, strong force, and without the knowledge of the value of the top quark mass Georgi and Jarlskog (GJ) [11] noticed that at the GUT

²⁵This range comes from a recent study [98] which assumes $\alpha_S(M_Z) = 0.122$. If we assume $\alpha_S(M_Z) = 0.119$, then we find $2 \text{ TeV} < M_S < 6 \text{ TeV}$. Current PDG [8, Ch 10] SM global fits give $\alpha_S = 0.1216 \pm 0.0017$.

²⁶Very close coupling constant unification can also occur in non-supersymmetric models. The Standard Model with six Higgs doublets is one such example [99], but the unification occurs at too low a scale $\approx 10^{14} \text{ GeV}$. GUT-scale gauge-bosons lead to proton decay. Such a low scale proton decay at a rate in contradiction with current experimental bounds.

scale the masses satisfied the approximate relations ²⁷:

$$m_\tau \approx m_b \quad m_\mu \approx 3m_s \quad 3m_e \approx m_d. \quad (2.31)$$

This is a very non-trivial result. The masses of the quarks and charged leptons span more than 5 orders of magnitude. The factor 3 is coincidentally equal to the number of colors. At the scale of the Z^0 -boson's mass $\mu = M_Z$ the ratios look like $m_\mu \approx 2m_s$, and $1.6m_\tau \approx m_b$ so the factor of three is quite miraculous. Using this surprising observation, GJ constructed a model where this relation followed from an $SU(5)$ theory with the second generation coupled to a Higgs in a different representation.

In the $SU(5)$ model the fermions are arranged into a $\bar{\mathbf{5}}$ (ψ_i^a) and a $\mathbf{10}$ ($\psi_{ab i}$) where a, b, c, \dots are the $SU(5)$ indexes and i, j, \dots are the family indexes. The particle assignments are

$$\psi_a^i = (d^c \quad d^c \quad d^c \quad \nu \quad e)^i \quad (2.32)$$

$$\psi^{abj} = \frac{1}{\sqrt{2}} \begin{pmatrix} 0 & u^c & -u^c & -u & -d \\ -u^c & 0 & u^c & -u & -d \\ u^c & -u^c & 0 & -u & -d \\ u & u & u & 0 & -e^c \\ d & d & d & e^c & 0 \end{pmatrix}^j \quad (2.33)$$

where c indicates the conjugate field. There are also a $\bar{\mathbf{5}}$ Higgs fields $(H_d)_a$ and a $\mathbf{5}$ Higgs field $(H_u)^a$. The key to getting the mass relations hypothesized in Eq(2.31) is coupling only the second generation to a $\mathbf{45}$ Higgs ²⁸. The VEVs of the Higgs fields are $H_u = (0, 0, 0, 0, v_u)$, $H_d = (0, 0, 0, 0, v_d)$ and $(H_{45,d})_{b5}^a = v_{45}(\delta_b^a - 4\delta^{a4}\delta_{b4})$. The coupling to matter that gives mass to the down-like states is

$$W_{Yd} = Y_{d\bar{5}ij} \psi^{ab i} \psi_a^j (H_d)_b + Y_{d45ij} \psi^{ab i} \psi_c^j (H_{d,45})_{ab}^c \quad (2.34)$$

and that give mass to the up-like states

$$W_{Yu} = Y_{5u ij} \psi^{ab i} \psi^{cd j} (H_u)^e \epsilon_{abcde}. \quad (2.35)$$

Georgi and Jarlskog do not concern themselves with relating the neutrino masses to the up-quark masses, so we will focus on the predictions for the down-like masses. The six masses of both the down-like quarks and the charged leptons may now be satisfied by arranging for

$$Y_{d45} = \begin{pmatrix} 0 & 0 & 0 \\ 0 & C & 0 \\ 0 & 0 & 0 \end{pmatrix} \quad Y_{d\bar{5}} = \begin{pmatrix} 0 & A & 0 \\ A & 0 & 0 \\ 0 & 0 & B \end{pmatrix} \quad (2.36)$$

²⁷To the best of my knowledge, the $b = \tau$ relations were first noticed by Buras *et.al*[103].

²⁸In tensor notation the $\mathbf{45}$ representation is given by $(H_{d,45})_{ab}^c$ where ab are antisymmetric and the five traces $(H_{d,45})_{ab}^a = 0$ are removed.

and fitting the three parameters A , B , and C . The fitting will create the hierarchy $B \gg C \gg A$. Coupling these Yukawa matrices to the Eq(2.34) gives the factor of $-3C$ for the (2,2) entry of the leptons mass matrix relative to the (2,2) entry of the down-like quark mass matrix. Because $B \gg C \gg A$, the equality of the (3,3) entry leads to $m_b/m_\tau \approx 1$. The (2,2) entry dominates the mass of the second generation so $m_\mu/m_s \approx 3$. The determinant of the resulting mass matrix is independent of C so at the GUT scale the product of the charged lepton masses is predicted to equal the product of the down-like quark masses.

These results have been generalized to other GUT models like the Pati-Salam model ²⁹. Family symmetries have been used to arrange the general structure shown here [104]. The continued validity of the Georgi-Jarlskog mass relations is one of the novel contributions of the thesis presented in Chapter 3.

2.3.4 $\tan\beta$ Enhanced Threshold Effects

The Appelquist Carazzone [105] decoupling theorem indicates that particle states heavier than the energy scales being considered can be integrated out and decoupled from the low-energy effective theory. A good review of working with effective theories and decoupling relations is found in Pich [106]. The parameters we measure are in some cases in an effective theory of $SU(3)_c \times U(1)_{EM}$; in other cases we measure the parameters with global fits to the Standard Model. At the energy scale of the sparticles, we need to match onto the MSSM effective theory. Finally at the GUT scale we need to match onto the GUT effective theory.

As a general rule, matching conditions are needed to maintain the order of accuracy of the results. If we are using one-loop RG running, we can use trivial matching conditions at the interface of the two effective theories. If we are using two-loop RG running, we should use one-loop matching conditions at the boundaries. This is to maintain the expected order of accuracy and precision of the results. There is an important exception to this general rule relevant to SUSY theories with large $\tan\beta$.

At tree level the VEV of H_u gives mass to the up-like states (t,c,u) and the neutrinos. At tree-level the VEV of H_d gives mass to the down-like states (b, s, d, τ , μ , e). However ‘soft’ interactions which break supersymmetry allow the VEV of H_u to couple to down-like Yukawa couplings through loop diagrams. Two such soft terms are the trilinear couplings $\mathcal{L} \supset y_t A^t H_u \tilde{t} \tilde{t}^c$ where A_t is a mass parameter and the gluino mass $\mathcal{L} \supset \tilde{g} \tilde{g} M_3$ where M_3 is the gluino’s soft mass parameter.

²⁹In Pati-Salam the $\mathbf{45}$ ’s VEV is such that one has a factor of 3 and not -3 for the charged leptons vs the down-like quark Yukawa coupling.

The matching conditions for two effective theories are deduced by expressing a common observable in terms of the two effective theories. For example the Pole mass M_b of the bottom quark ³⁰ would be expressed as

$$M_b \approx \begin{array}{c} b_L \xrightarrow{\quad} y_b \xrightarrow{\quad} b_R \\ | \\ H \end{array} + \begin{array}{c} b_L \xrightarrow{\quad} g_3 \xrightarrow{\quad} y_b \xrightarrow{\quad} g_3 \xrightarrow{\quad} b_R \\ | \\ H \end{array} + \dots$$

where H takes on the vacuum expectation value, $y_b(\mu)$ and $g_3(\mu)$ are the QFT parameters which depends on an unphysical choice of scale μ . The same observable expressed in MSSM involves new diagrams

$$M_b \approx \begin{array}{c} b_L \xrightarrow{\quad} y_b \xrightarrow{\quad} b_R \\ | \\ Hd \end{array} + \begin{array}{c} b_L \xrightarrow{\quad} g_3 \xrightarrow{\quad} y_b \xrightarrow{\quad} g_3 \xrightarrow{\quad} b_R \\ | \\ Hd \end{array} + \begin{array}{c} Hu \\ | \\ \tilde{b} \xrightarrow{\quad} y_b^\mu \xrightarrow{\quad} \tilde{b} \\ | \\ M_3 \end{array} + \begin{array}{c} Hu \\ | \\ \tilde{\tau} \xrightarrow{\quad} y_t A^t \xrightarrow{\quad} \tilde{\tau} \\ | \\ \mu \end{array} + \dots$$

$\begin{array}{c} b_L \xrightarrow{\quad} g_3 \xrightarrow{\quad} \tilde{g} \xrightarrow{\quad} g_3 \xrightarrow{\quad} b_R \\ | \\ \tilde{g} \end{array}$
 $\begin{array}{c} b_L \xrightarrow{\quad} y_t \xrightarrow{\quad} \tilde{h} \xrightarrow{\quad} \tilde{h} \xrightarrow{\quad} y_b \xrightarrow{\quad} b_R \\ | \\ \mu \end{array}$

The parameters $y_b^{SM}(\mu), g_3^{SM}(\mu)$ are not equal to the parameters $y_b^{MSSM}(\mu), g_3^{MSSM}(\mu)$. By expressing $y_b^{MSSM} = y_b^{SM} + \delta y_b$ and likewise for $g_3^{MSSM} = g_3^{SM} + \delta g_3$, we find many common graphs which cancel. We are left with an expression for δy_b equal to the graphs not common between the two effective theories.

$$-(\delta y_b)v_d = \begin{array}{c} Hu \\ | \\ \tilde{b} \xrightarrow{\quad} y_b^\mu \xrightarrow{\quad} \tilde{b} \\ | \\ M_3 \end{array} + \begin{array}{c} Hu \\ | \\ \tilde{\tau} \xrightarrow{\quad} y_t A^t \xrightarrow{\quad} \tilde{\tau} \\ | \\ \mu \end{array} + \dots \quad (2.37)$$

$\begin{array}{c} b_L \xrightarrow{\quad} g_3 \xrightarrow{\quad} \tilde{g} \xrightarrow{\quad} g_3 \xrightarrow{\quad} b_R \\ | \\ \tilde{g} \end{array}$
 $\begin{array}{c} b_L \xrightarrow{\quad} y_t \xrightarrow{\quad} \tilde{h} \xrightarrow{\quad} \tilde{h} \xrightarrow{\quad} y_b \xrightarrow{\quad} b_R \\ | \\ \mu \end{array}$

The two graphs in this correction are proportional to the VEV of $\langle h_u^0 \rangle = v_u$. However the y_b Yukawa coupling is the ratio of m_b to $\langle h_d^0 \rangle = v_d$. This makes the correction $\delta y_b/y_b$ due to the two loops shown proportional to $v_u/v_d = \tan \beta$. If $\tan \beta$ were small $\lesssim 5$, then the loop result times the $\tan \beta$ would remain small and the effect would be only relevant at two-loop accuracy. However when $\tan \beta \gtrsim 10$ then the factor of $\tan \beta$ makes the contribution an order of magnitude bigger and the effect can be of the same size as the one-loop running itself.

³⁰If it existed as a free state.

These $\tan\beta$ enhanced SUSY threshold corrections can have a large effect on the GUT-scale parameters. More precise observations of the low-energy parameters have driven the Georgi-Jarlskog mass relations out of quantitative agreement. However there is a class of $\tan\beta$ enhanced corrections that can bring the relations back into quantitative agreement. Chapter 3 of this thesis makes predictions for properties of the SUSY mass spectrum by updating the GUT-scale parameters to the new low-energy observations and considering properties of $\tan\beta$ enhanced SUSY threshold corrections needed to maintain the quantitative agreement of the Georgi Jarlskog mass relations.

Chapter Summary

In this chapter we have introduced the ingredients of the Standard Model and its supersymmetric extension and given examples of how symmetries, broken symmetries, and fine-tuning arguments have successfully predicted the mass of the positron, the Ω^- , the charm quark, and the W^\pm and Z^0 bosons. We have introduced astrophysical evidence that indicate a significant fraction of the mass-energy density of the universe is in a particle type yet to be discovered. We have introduced supersymmetry as a plausible framework for solving the fine-tuning of the Higgs self energy, for explaining the top-quarks large mass, and for providing a dark-matter particle. In addition we have discussed how SUSY predicts gauge coupling unification, and a framework for mass-matrix unification. Last we have introduced potentially large corrections to the RG running of the mass matrices.

Chapter 3

Predictions from Unification and Fermion Mass Structure

Chapter Overview

Grand Unified Theories predict relationships between the GUT-scale quark and lepton masses. Using new data in the context of the MSSM, we update the values and uncertainties of the masses and mixing angles for the three generations at the GUT scale. We also update fits to hierarchical patterns in the GUT-scale Yukawa matrices. The new data shows that not all the classic GUT-scale mass relationships remain in quantitative agreement at small to moderate $\tan\beta$. However, at large $\tan\beta$, these discrepancies can be eliminated by finite, $\tan\beta$ -enhanced, radiative, threshold corrections if the gluino mass has the opposite sign to the wino mass. This chapter is based on work first published by the author and his supervisor in Ref. [10].

Explaining the origin of fermion masses and mixings remains one of the most important goals in our attempts to go beyond the Standard Model. In this, one very promising possibility is that there is an underlying stage of unification relating the couplings responsible for the fermion masses. However we are hindered by the fact that the measured masses and mixings do not directly give the structure of the underlying Lagrangian both because the data is insufficient unambiguously to reconstruct the full fermion mass matrices and because radiative corrections can obscure the underlying structure. In this chapter we will address both these points in the context of the MSSM.

We first present an analysis of the measured mass and mixing angles continued to the GUT scale. The analysis updates Ref [1] using the precise measurements of fermion masses and mixing angles from the b-factories and the updated top-quark mass from CDF and D0. The resulting data at the GUT scale allows us to look for underlying patterns which may suggest a unified origin. We also explore the sensitivity of these patterns to $\tan\beta$ -enhanced, radiative threshold

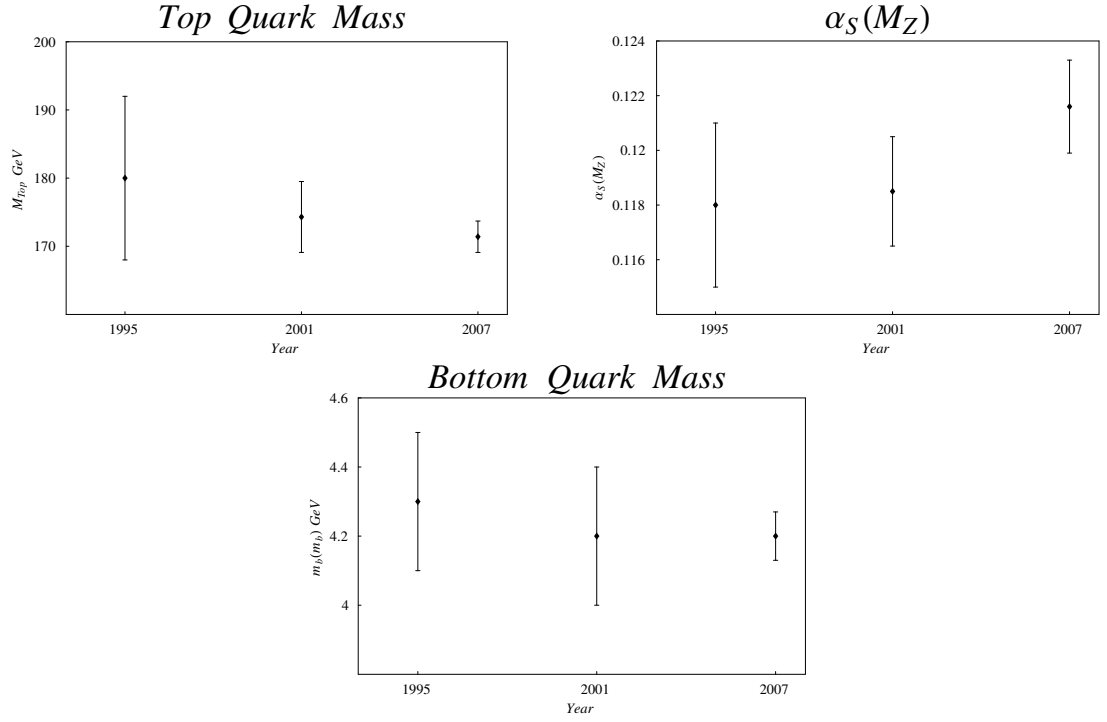


Figure 3.1: Updates to the top-quark mass, strong coupling constant, and bottom-quark mass are responsible for the quantitative stress of the classic GUT relation for y_b/y_τ .

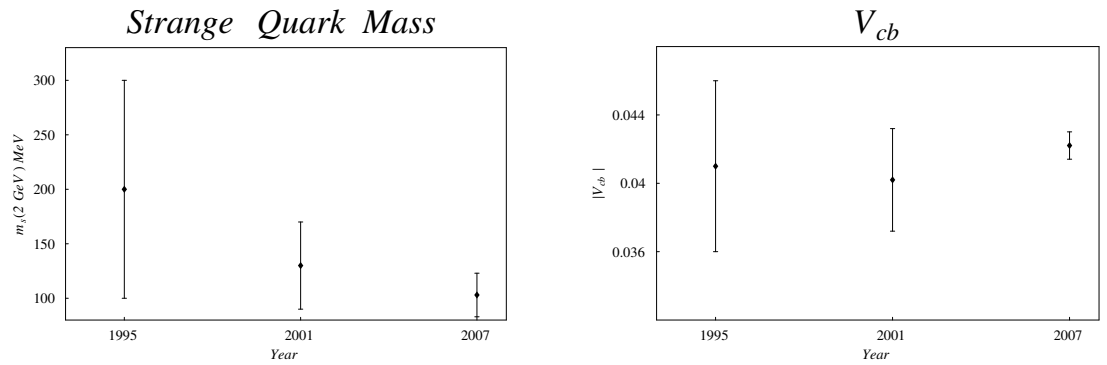


Figure 3.2: Updates to the strange-quark mass and V_{cb} are responsible for the quantitative stress of the Georgi-Jarlskog mass relations and the need to update values from Ref. [1].

corrections.

We next proceed to extract the underlying Yukawa coupling matrices for the quarks and leptons. There are two difficulties in this. The first is that the data cannot, without some assumptions, determine all elements of these matrices. The second is that the Yukawa coupling matrices are basis dependent. We choose to work in a basis in which the mass matrices are hierarchical in structure with the off-diagonal elements small relative to the appropriate combinations of on-diagonal matrix elements. Appendix B, Eq(B.1) defines this basis more precisely. This is the basis we think is most likely to display the structure of the underlying theory, for example that of a spontaneously broken family symmetry in which the hierarchical structure is ordered by the (small) order parameter breaking the symmetry. With this structure to leading order the observed masses and mixing angles determine the mass matrix elements on and above the diagonal, and our analysis determines these entries, again allowing for significant $\tan \beta$ enhanced radiative corrections. The resulting form of the mass matrices provides the “data” for developing models of fermion masses such as those based on a broken family symmetry.

3.1 Supersymmetric Thresholds and GUT-Scale Mass Relations

The data set used is summarized in Table 3.1. Since the fit of reference [1] (RRRV) to the Yukawa texture was done, the measurement of the Standard-Model parameters has improved considerably. Figs 3.1 and 3.2 highlight a few of the changes in the data since: The top-quark mass has gone from $M_t = 174.3 \pm 5$ GeV to $M_t = 170.9 \pm 1.9$ GeV. In 2000 the Particle Data Book reported $m_b(m_b) = 4.2 \pm 0.2$ GeV [109] which has improved to $m_b(m_b) = 4.2 \pm 0.07$ GeV today. In addition each higher order QCD correction pushes down the value of $m_b(M_Z)$ at the scale of the Z bosons mass. In 1998 $m_b(M_Z) = 3.0 \pm 0.2$ GeV [110] and today it is $m_b(M_Z) = 2.87 \pm 0.06$ GeV [111]. The most significant shift in the data relevant to the RRRV fit is a downward revision to the strange-quark mass at the scale $\mu_L = 2$ GeV from $m_s(\mu_L) \approx 120 \pm 50$ MeV [109] to today’s value $m_s(\mu_L) = 103 \pm 20$ MeV. We also know the CKM unitarity triangle parameters better today than six years ago. For example, in 2000 the Particle Data book reported $\sin 2\beta = 0.79 \pm 0.4$ [109] which is improved to $\sin 2\beta = 0.69 \pm 0.032$ in 2006 [41]. Figures 3.1 and 3.2 show these updates visually. The $\sin 2\beta$ value is about 1.2σ off from a global fit to all the CKM data [112], our fits generally lock onto the global-fit data and exhibit a 1σ tension for $\sin 2\beta$. Together, the improved CKM matrix observations add stronger constraints to the textures compared to data from several years ago.

Low-Energy Parameter	Value(Uncertainty in last digit(s))	Notes and Reference
$m_u(\mu_L)/m_d(\mu_L)$	0.45(15)	PDB Estimation [41]
$m_s(\mu_L)/m_d(\mu_L)$	19.5(1.5)	PDB Estimation [41]
$m_u(\mu_L) + m_d(\mu_L)$	[8.8(3.0), 7.6(1.6)] MeV	PDB, Quark Masses, pg 15 [41]. (Non-lattice, Lattice)
$Q = \sqrt{\frac{m_s^2 - (m_d + m_u)^2/4}{m_d^2 - m_u^2}}$	22.8(4)	Martemyanov and Sopov [107]
$m_s(\mu_L)$	[103(20), 95(20)] MeV	PDB, Quark Masses, pg 15 [41]. [Non-lattice, lattice]
$m_u(\mu_L)$	3(1) MeV	PDB, Quark Masses, pg 15 [41]. Non-lattice.
$m_d(\mu_L)$	6.0(1.5) MeV	PDB, Quark Masses, pg 15 [41]. Non-lattice.
$m_c(m_c)$	1.24(09) GeV	PDB, Quark Masses, pg 16 [41]. Non-lattice.
$m_b(m_b)$	4.20(07) GeV	PDB, Quark Masses, pg 16,19 [41]. Non-lattice.
M_t	170.9 (1.9) GeV	CDF & D0 [108] Pole Mass
(M_e, M_μ, M_τ)	(0.511(15), 105.6(3.1), 1777(53)) MeV	3% uncertainty from neglecting Y^e thresholds.
A Wolfenstein parameter	0.818(17)	PDB Ch 11 Eq. 11.25 [41]
$\bar{\rho}$ Wolfenstein parameter	0.221(64)	PDB Ch 11 Eq. 11.25 [41]
λ Wolfenstein parameter	0.2272(10)	PDB Ch 11 Eq. 11.25 [41]
$\bar{\eta}$ Wolfenstein parameter	0.340(45)	PDB Ch 11 Eq. 11.25 [41]
$ V_{CKM} $	$\begin{pmatrix} 0.97383(24) & 0.2272(10) & 0.00396(09) \\ 0.2271(10) & 0.97296(24) & 0.04221(80) \\ 0.00814(64) & 0.04161(78) & 0.999100(34) \end{pmatrix}$	PDB Ch 11 Eq. 11.26 [41]
$\sin 2\beta$ from CKM	0.687(32)	PDB Ch 11 Eq. 11.19 [41]
Jarlskog Invariant	$3.08(18) \times 10^{-5}$	PDB Ch 11 Eq. 11.26 [41]
$v_{Higgs}(M_Z)$	246.221(20) GeV	Uncertainty expanded. [41]
$(\alpha_{EM}^{-1}(M_Z), \alpha_s(M_Z), \sin^2 \theta_W(M_Z))$	(127.904(19), 0.1216(17), 0.23122(15))	PDB Sec 10.6 [41]

Table 3.1: Low-energy observables. Masses in lower-case m are \overline{MS} running masses. Capital M indicates pole mass. The light quark's (u, d, s) mass are specified at a scale $\mu_L = 2$ GeV. V_{CKM} are the Standard Model's best fit values.

We first consider the determination of the fundamental mass parameters at the GUT scale in order simply to compare to GUT predictions. The starting point for the light-quark masses at low scale is given by the χ^2 fit to the data of Table 3.1

$$m_u(\mu_L) = 2.7 \pm 0.5 \text{ MeV} \quad m_d(\mu_L) = 5.3 \pm 0.5 \text{ MeV} \quad m_s(\mu_L) = 103 \pm 12 \text{ MeV}. \quad (3.1)$$

Using these as input we determine the values of the mass parameters at the GUT scale for various choices of $\tan \beta$ but not including possible $\tan \beta$ enhanced threshold corrections. We do this using numerical solutions to the RG equations. The one-loop and two-loop RG equations for the gauge couplings and the Yukawa couplings in the Standard Model and in the MSSM that we use in this study come from a number of sources [110][113][40][114] and are detailed in Appendix A. The results are given in the first five columns of Table 3.2. These can readily be compared to expectations in various Grand Unified models. The classic prediction of $SU(5)$ with third generation down-quark and charged-lepton masses given by the coupling $B \bar{5}_f.10_f.5_H^1$ is

¹ $\bar{5}_f$, 10_f refer to the $SU(5)$ representations making up a family of quarks and leptons while 5_H is a five

$m_b(M_X)/m_\tau(M_X) = 1$ [103]. This ratio is given in Table 3.2 where it may be seen that the value agrees at a special low $\tan\beta$ value but for large $\tan\beta$ it is some 25% smaller than the GUT prediction². A similar relation between the strange quark and the muon is untenable and to describe the masses consistently in $SU(5)$ Georgi and Jarlskog [11] proposed that the second generation masses should come instead from the coupling $C \bar{5}_f.10_f.45_H$ leading instead to the relation $3m_s(M_X)/m_\mu(M_X) = 1$. As may be seen from Table 3.2 in all cases this ratio is approximately 0.69(8). The prediction of Georgi and Jarlskog for the lightest generation masses follows from the relation $\text{Det}(M^d)/\text{Det}(M^l) = 1$. This results from the form of their mass matrix which is given by³

$$M^d = \begin{pmatrix} 0 & A' & \\ A & C & \\ & & B \end{pmatrix}, \quad M^l = \begin{pmatrix} 0 & A' & \\ A & -3C & \\ & & B \end{pmatrix} \quad (3.2)$$

in which there is a $(1,1)$ texture zero⁴ and the determinant is given by the product of the $(3,3)$, $(1,2)$ and $(2,1)$ elements. If the $(1,2)$ and $(2,1)$ elements are also given by $\bar{5}_f.10_f.5_H$ couplings they will be the same in the down-quark and charged-lepton mass matrices giving rise to the equality of the determinants. The form of Eq(3.2) may be arranged by imposing additional continuous or discrete symmetries. One may see from Table 3.2 that the actual value of the ratio of the determinants is quite far from unity disagreeing with the Georgi Jarlskog relation.

In summary the latest data on fermion masses, while qualitatively in agreement with the simple GUT relations, has significant quantitative discrepancies. However the analysis has not, so far, included the SUSY threshold corrections which substantially affect the GUT mass relations at large $\tan\beta$ [116]. A catalog of the full SUSY threshold corrections is given in [117]. The particular finite SUSY thresholds discussed in this letter do not decouple as the superpartners become massive. We follow the approximation described in Blazek, Raby, and Pokorski (BRP) for threshold corrections to the CKM elements and down-like mass eigenstates [118]. The finite threshold corrections to Y^e and Y^u and are generally about 3% or smaller

$$\delta Y^u, \delta Y^d \lesssim 0.03 \quad (3.3)$$

and will be neglected in our study. The logarithmic threshold corrections are approximated by using the Standard-Model RG equations from M_Z to an effective SUSY scale M_S .

dimensional representation of Higgs scalars.

²We'd like to thank Ilja Dorsner for pointing out that the $\tan\beta$ dependence of $m_b/m_\tau(M_X)$ is more flat than in previous studies (e.g. ref. [115]). This change is mostly due to the higher effective SUSY scale M_S , the higher value of $\alpha_s(M_Z)$ found in global standard model fits, and smaller top-quark mass M_t .

³The remaining mass matrix elements may be non-zero provided they do not contribute significantly to the determinant.

⁴Below we discuss an independent reason for having a $(1,1)$ texture zero.

Parameters	Input SUSY Parameters					
$\tan \beta$	1.3	10	38	50	38	38
γ_b	0	0	0	0	-0.22	+0.22
γ_d	0	0	0	0	-0.21	+0.21
γ_t	0	0	0	0	0	-0.44
Parameters	Corresponding GUT-Scale Parameters with Propagated Uncertainty					
$y^t(M_X)$	6_{-5}^{+1}	0.48(2)	0.49(2)	0.51(3)	0.51(2)	0.51(2)
$y^b(M_X)$	$0.0113_{-0.01}^{+0.0002}$	0.051(2)	0.23(1)	0.37(2)	0.34(3)	0.34(3)
$y^\tau(M_X)$	0.0114(3)	0.070(3)	0.32(2)	0.51(4)	0.34(2)	0.34(2)
$(m_u/m_c)(M_X)$	0.0027(6)	0.0027(6)	0.0027(6)	0.0027(6)	0.0026(6)	0.0026(6)
$(m_d/m_s)(M_X)$	0.051(7)	0.051(7)	0.051(7)	0.051(7)	0.051(7)	0.051(7)
$(m_e/m_\mu)(M_X)$	0.0048(2)	0.0048(2)	0.0048(2)	0.0048(2)	0.0048(2)	0.0048(2)
$(m_c/m_t)(M_X)$	$0.0009_{-0.00006}^{+0.001}$	0.0025(2)	0.0024(2)	0.0023(2)	0.0023(2)	0.0023(2)
$(m_s/m_b)(M_X)$	0.014(4)	0.019(2)	0.017(2)	0.016(2)	0.018(2)	0.010(2)
$(m_\mu/m_\tau)(M_X)$	0.059(2)	0.059(2)	0.054(2)	0.050(2)	0.054(2)	0.054(2)
$A(M_X)$	$0.56_{-0.01}^{+0.34}$	0.77(2)	0.75(2)	0.72(2)	0.73(3)	0.46(3)
$\lambda(M_X)$	0.227(1)	0.227(1)	0.227(1)	0.227(1)	0.227(1)	0.227(1)
$\bar{\rho}(M_X)$	0.22(6)	0.22(6)	0.22(6)	0.22(6)	0.22(6)	0.22(6)
$\bar{\eta}(M_X)$	0.33(4)	0.33(4)	0.33(4)	0.33(4)	0.33(4)	0.33(4)
$J(M_X) \times 10^{-5}$	$1.4_{-0.2}^{+2.2}$	2.6(4)	2.5(4)	2.3(4)	2.3(4)	1.0(2)
Parameters	Comparison with GUT Mass Ratios					
$(m_b/m_\tau)(M_X)$	$1.00_{-0.4}^{+0.04}$	0.73(3)	0.73(3)	0.73(4)	1.00(4)	1.00(4)
$(3m_s/m_\mu)(M_X)$	$0.70_{-0.05}^{+0.8}$	0.69(8)	0.69(8)	0.69(8)	0.9(1)	0.6(1)
$(m_d/3m_e)(M_X)$	0.82(7)	0.83(7)	0.83(7)	0.83(7)	1.05(8)	0.68(6)
$(\frac{\det Y^d}{\det Y^e})(M_X)$	$0.57_{-0.26}^{+0.08}$	0.42(7)	0.42(7)	0.42(7)	0.92(14)	0.39(7)

Table 3.2: The mass parameters continued to the GUT-scale M_X for various values of $\tan \beta$ and threshold corrections $\gamma_{t,b,d}$. These are calculated with the 2-loop gauge coupling and 2-loop Yukawa coupling RG equations assuming an effective SUSY scale $M_S = 500$ GeV.

The finite, $\tan \beta$ -enhanced Y^d SUSY threshold corrections are dominated by the a sbottom-gluino loop, a stop-higgsino loop, and a stop-chargino loop. Integrating out the SUSY particles at a scale M_S leaves the matching condition at that scale for the Standard-Model Yukawa couplings:

$$\delta m_{sch} Y^{u SM} = \sin \beta Y^u \quad (3.4)$$

$$\delta m_{sch} Y^{d SM} = \cos \beta U_L^{d\dagger} \left(1 + \Gamma^d + V_{CKM}^\dagger \Gamma^u V_{CKM} \right) Y_{\text{diag}}^d U_R^d \quad (3.5)$$

$$Y^{e SM} = \cos \beta Y^e. \quad (3.6)$$

All the parameters on the right-hand side take on their MSSM values in the \overline{DR} scheme. The factor δm_{sch} converts the quark running masses from \overline{MS} to \overline{DR} scheme. Details about this scheme conversion are listed in Appendix A.3. The β corresponds to the ratio of the two Higgs VEVs $v_u/v_d = \tan \beta$. The U matrices decompose the MSSM Yukawa couplings at the scale M_S : $Y^u = U_L^{u\dagger} Y_{\text{diag}}^u U_R^u$ and $Y^d = U_L^{d\dagger} Y_{\text{diag}}^d U_R^d$. The matrices Y_{diag}^u and Y_{diag}^d are diagonal and

correspond to the mass eigenstates divided by the appropriate VEV at the scale M_S . The CKM matrix is given by $V_{CKM} = U_L^u U_L^{d\dagger}$. The left-hand side involves the Standard-Model Yukawa couplings. The matrices Γ^u and Γ^d encode the SUSY threshold corrections.

If the squarks are diagonalized in flavor space by the same rotations that diagonalize the quarks, the matrices Γ^u and Γ^d are diagonal: $\Gamma^d = \text{diag}(\gamma_d, \gamma_d, \gamma_b)$, $\Gamma^u = \text{diag}(\gamma_u, \gamma_u, \gamma_t)$. In general the squarks are not diagonalized by the same rotations as the quarks but provided the relative mixing angles are reasonably small the corrections to flavour conserving masses, which are our primary concern here, will be second order in these mixing angles. We will assume Γ^u and Γ^d are diagonal in what follows.

Approximations for Γ^u and Γ^d based on the mass insertion approximation are found in [119][120][121]:

$$\gamma_t \approx y_t^2 \mu A^t \frac{\tan \beta}{16\pi^2} I_3(m_{\tilde{t}_1}^2, m_{\tilde{t}_2}^2, \mu^2) \sim y_t^2 \frac{\tan \beta}{32\pi^2} \frac{\mu A^t}{m_t^2} \quad (3.7)$$

$$\gamma_u \approx -g_2^2 M_2 \mu \frac{\tan \beta}{16\pi^2} I_3(m_{\chi_1}^2, m_{\chi_2}^2, m_u^2) \sim 0 \quad (3.8)$$

$$\gamma_b \approx \frac{8}{3} g_3^2 \frac{\tan \beta}{16\pi^2} M_3 \mu I_3(m_{\tilde{b}_1}^2, m_{\tilde{b}_2}^2, M_3^2) \sim \frac{4}{3} g_3^2 \frac{\tan \beta}{16\pi^2} \frac{\mu M_3}{m_b^2} \quad (3.9)$$

$$\gamma_d \approx \frac{8}{3} g_3^2 \frac{\tan \beta}{16\pi^2} M_3 \mu I_3(m_{\tilde{d}_1}^2, m_{\tilde{d}_2}^2, M_3^2) \sim \frac{4}{3} g_3^2 \frac{\tan \beta}{16\pi^2} \frac{\mu M_3}{m_d^2} \quad (3.10)$$

where I_3 is given by

$$I_3(a^2, b^2, c^2) = \frac{a^2 b^2 \log \frac{a^2}{b^2} + b^2 c^2 \log \frac{b^2}{c^2} + c^2 a^2 \log \frac{c^2}{a^2}}{(a^2 - b^2)(b^2 - c^2)(a^2 - c^2)}. \quad (3.11)$$

In these expressions \tilde{q} refers to superpartner of q . χ^j indicate chargino mass eigenstates. μ is the coefficient to the $H^u H^d$ interaction in the superpotential. M_1, M_2, M_3 are the gaugino soft breaking terms. A^t refers to the soft top-quark trilinear coupling. The mass insertion approximation breaks down if there is large mixing between the mass eigenstates of the stop or the sbottom. The right-most expressions in Eqs(3.7,3.9,3.10) assume the relevant squark mass eigenstates are nearly degenerate and heavier than M_3 and μ . These expressions (eqs 3.7 - 3.10) provide an approximate mapping from a supersymmetric spectra to the γ_i parameters through which we parameterize the threshold corrections; however, with the exception of Column A of Table 3.4, we do not specify a SUSY spectra but directly parameterize the thresholds corrections through γ_i .

The separation between γ_b and γ_d is set by the lack of degeneracy of the down-like squarks. If the squark masses for the first two generations are not degenerate, then there will be a corresponding separation between the (1,1) and (2,2) entries of Γ^d and Γ^u . If the sparticle

spectra is designed to have a large A^t and a light stop, γ_t can be enhanced and dominate over γ_b . Because the charm Yukawa coupling is so small, the scharm-higgsino loop is negligible, and γ_u follows from a chargino squark loop and is also generally small with values around 0.02 because of the smaller g_2 coupling. In our work, we approximate $\Gamma_{22}^u \sim \Gamma_{11}^u \sim 0$. The only substantial correction to the first and second generations is given by γ_d [116].

As described in BRP, the threshold corrections leave $|V_{us}|$ and $|V_{ub}/V_{cb}|$ unchanged to a good approximation. Threshold corrections in Γ^u do affect the V_{ub} and V_{cb} at the scale M_S giving

$$\frac{V_{ub}^{SM} - V_{ub}^{MSSM}}{V_{ub}^{MSSM}} \simeq \frac{V_{cb}^{SM} - V_{cb}^{MSSM}}{V_{cb}^{MSSM}} \simeq -(\gamma_t - \gamma_u). \quad (3.12)$$

The threshold corrections for the down-quark masses are given approximately by

$$\begin{aligned} m_d &\simeq m_d^0 (1 + \gamma_d + \gamma_u)^{-1} \\ m_s &\simeq m_s^0 (1 + \gamma_d + \gamma_u)^{-1} \\ m_b &\simeq m_b^0 (1 + \gamma_b + \gamma_t)^{-1} \end{aligned}$$

where the superscript 0 denotes the mass without threshold corrections. Not shown are the nonlinear effects which arise through the RG equations when the bottom Yukawa coupling is changed by threshold effects. These are properly included in our final results obtained by numerically solving the RG equations.

Due to our assumption that the squark masses for the first two generations are degenerate, the combination of the GUT relations given by $(\det M^l / \det M^d) (3 m_s / m_\mu)^2 (m_b / m_\tau) = 1$ is unaffected up to nonlinear effects. Thus we cannot simultaneously fit all three GUT relations through the threshold corrections. A best fit requires the threshold effects given by

$$\gamma_b + \gamma_t \approx -0.22 \pm 0.02 \quad (3.13)$$

$$\gamma_d + \gamma_u \approx -0.21 \pm 0.02. \quad (3.14)$$

giving the results shown in the penultimate column of Table 3.2, just consistent with the GUT predictions. The question is whether these threshold effects are of a reasonable magnitude and, if so, what are the implications for the SUSY spectra which determine the γ_i ? From Eqs(3.9,3.10), at $\tan \beta = 38$ we have

$$\frac{\mu M_3}{m_{\tilde{b}}^2} \sim -0.5, \quad \frac{m_{\tilde{b}}^2}{m_{\tilde{d}}^2} \sim 1.0$$

The current observation of the muon's $(g-2)_\mu$ is 3.4σ [122] away from the Standard-Model prediction. If SUSY is to explain the observed deviation, one needs $\tan \beta > 8$ [123] and $\mu M_2 > 0$ [77]. With this sign we must have μM_3 negative and the \tilde{d}, \tilde{s} squarks only lightly split from the \tilde{b}

squarks. M_3 negative is characteristic of anomaly mediated SUSY breaking [124] and is discussed in [125][126][121][127]. Although we have deduced $M_3 < 0$ from the approximate Eqs(3.9,3.10), the correlation persists in the near exact expression found in Eq(23) of Ref [118]. Adjusting to different squark splitting can occur in various schemes [128]. However the squark splitting can readily be adjusted without spoiling the fit because, up to nonlinear effects, the solution only requires the constraints implied by Eq(3.13), so we may make $\gamma_b > \gamma_d$ and hence make $m_b^2 < m_d^2$ by allowing for a small positive value for γ_t . In this case A^t must be positive.

It is of interest also to consider the threshold effects in the case that μM_3 is positive. This is illustrated in the last column of Table 3.2 in which we have reversed the sign of γ_d , consistent with positive μM_3 , and chosen $\gamma_b \simeq \gamma_d$ as is expected for similar down squark masses. The value of γ_t is chosen to keep the equality between m_b and m_τ . One may see that the other GUT relations are not satisfied, being driven further away by the threshold corrections. Reducing the magnitude of γ_b and γ_d reduces the discrepancy somewhat but still limited by the deviation found in the no-threshold case (the fourth column of Table 3.2).

At $\tan \beta$ near 50 the non-linear effects are large and $b - \tau$ unification requires $\gamma_b + \gamma_t \sim -0.1$ to -0.15 . In this case it is possible to have $t - b - \tau$ unification of the Yukawa couplings. For $\mu > 0, M_3 > 0$, the “Just-so” Split-Higgs solution of references [129, 130, 131, 132] can achieve this while satisfying both $b \rightarrow s \gamma$ and $(g - 2)_\mu$ constraints but only with large γ_b and γ_t and a large cancellation in $\gamma_b + \gamma_t$. In this case, as in the example given above, the threshold corrections drive the masses further from the mass relations for the first and second generations because $\mu M_3 > 0$. It is possible to have $t - b - \tau$ unification with $\mu M_3 < 0$, satisfying the $b \rightarrow s \gamma$ and $(g - 2)_\mu$ constraints in which the GUT predictions for the first and second generation of quarks is acceptable. Examples include Non-Universal Gaugino Mediation [133] and AMSB; both have some very heavy sparticle masses ($\gtrsim 4$ TeV) [121]. Minimal AMSB with a light sparticle spectra ($\lesssim 1$ TeV), while satisfying $(g - 2)_\mu$ and $b \rightarrow s \gamma$ constraints, requires $\tan \beta$ less than about 30 [77].

3.2 Updated fits to Yukawa matrices

We turn now to the second part of our study in which we update previous fits to the Yukawa matrices responsible for quark and lepton masses. As discussed above we choose to work in a basis in which the mass matrices are hierarchical with the off-diagonal elements small relative to the appropriate combinations of on-diagonal matrix elements defined in Eq(B.1). This is the basis we think is most likely to display the structure of the underlying theory, for example

Parameter	2001 RRRV	Fit A0	Fit B0	Fit A1	Fit B1	Fit A2	Fit B2
$\tan \beta$	Small	1.3	1.3	38	38	38	38
a'	$\mathcal{O}(1)$	0	0	0	0	-2.0	-2.0
ϵ_u	0.05	0.030(1)	0.030(1)	0.0491(16)	0.0491(15)	0.0493(16)	0.0493(14)
ϵ_d	0.15(1)	0.117(4)	0.117(4)	0.134(7)	0.134(7)	0.132(7)	0.132(7)
$ b' $	1.0	1.75(20)	1.75(21)	1.05(12)	1.05(13)	1.04(12)	1.04(13)
$\arg(b')$	90°	$+93(16)^\circ$	$-93(13)^\circ$	$+91(16)^\circ$	$-91(13)^\circ$	$+93(16)^\circ$	$-93(13)^\circ$
a	1.31(14)	2.05(14)	2.05(14)	2.16(23)	2.16(24)	1.92(21)	1.92(22)
b	1.50(10)	1.92(14)	1.92(15)	1.66(13)	1.66(13)	1.70(13)	1.70(13)
$ c $	0.40(2)	0.85(13)	2.30(20)	0.78(15)	2.12(36)	0.83(17)	2.19(38)
$\arg(c)$	$-24(3)^\circ$	$-39(18)^\circ$	$-61(14)^\circ$	$-43(14)^\circ$	$-59(13)^\circ$	$-37(25)^\circ$	$-60(13)^\circ$

Table 3.3: Results of a χ^2 fit of eqs(3.15,3.16) to the data in Table 3.2 in the absence of threshold corrections. We set a' as indicated and set $c' = d' = d = 0$ and $f = f' = 1$ at fixed values.

that of a spontaneously broken family symmetry, in which the hierarchical structure is ordered by the (small) order parameter breaking the symmetry. With this structure to leading order in the ratio of light to heavy quarks the observed masses and mixing angles determine the mass matrix elements on and above the diagonal provided the elements below the diagonal are not anomalously large. This is the case for matrices that are nearly symmetrical or for nearly Hermitian as is the case in models based on an $SO(10)$ GUT.

For convenience we fit to symmetric Yukawa coupling matrices but, as stressed above, this is not a critical assumption as the data is insensitive to the off-diagonal elements below the diagonal and the quality of the fit is not changed if, for example, we use Hermitian forms. For comparison Appendix B gives the observables in terms of Yukawa matrix entries following a general hierarchical texture. We parameterize a set of general, symmetric Yukawa matrices as:

$$Y^u(M_X) = y_{33}^u \begin{pmatrix} d' \epsilon_u^4 & b' \epsilon_u^3 & c' \epsilon_u^3 \\ b' \epsilon_u^3 & f' \epsilon_u^2 & a' \epsilon_u^2 \\ c' \epsilon_u^3 & a' \epsilon_u^2 & 1 \end{pmatrix}, \quad (3.15)$$

$$Y^d(M_X) = y_{33}^d \begin{pmatrix} d \epsilon_d^4 & b \epsilon_d^3 & c \epsilon_d^3 \\ b \epsilon_d^3 & f \epsilon_d^2 & a \epsilon_d^2 \\ c \epsilon_d^3 & a \epsilon_d^2 & 1 \end{pmatrix}. \quad (3.16)$$

Although not shown, we always choose lepton Yukawa couplings at M_X consistent with the low-energy lepton masses. Notice that the f coefficient and ϵ_d are redundant (likewise in Y^u). We include f to be able to discuss the phase of the (2,2) term. We write all the entries in terms of ϵ so that our coefficients will be $\mathcal{O}(1)$. We will always select our best ϵ parameters such that $|f| = 1$.

RRRV noted that all solutions, to leading order in the small expansion parameters, only

depend on two phases ϕ_1 and ϕ_2 given by

$$\phi_1 = (\phi'_b - \phi'_f) - (\phi_b - \phi_f) \quad (3.17)$$

$$\phi_2 = (\phi_c - \phi_a) - (\phi_b - \phi_f) \quad (3.18)$$

where ϕ_x is the phase of parameter x . For this reason it is sufficient to consider only b' and c as complex with all other parameters real.

As mentioned above the data favours a texture zero in the $(1, 1)$ position. With a symmetric form for the mass matrix for the first two families, this leads to the phenomenologically successful Gatto Sartori Tonin [134] relation

$$V_{us}(M_X) \approx |b\epsilon_d - |b'|e^{i\phi_{b'}}\epsilon_u| \approx \left| \sqrt{\left(\frac{m_d}{m_s}\right)_0} - \sqrt{\left(\frac{m_u}{m_c}\right)_0} e^{i\phi_1} \right|. \quad (3.19)$$

This relation gives an excellent fit to V_{us} with $\phi_1 \approx \pm 90^\circ$, and to preserve it we take d, d' to be zero in our fits. As discussed above, in $SU(5)$ this texture zero leads to the GUT relation $Det(M^d)/Det(M^l) = 1$ which, with threshold corrections, is in good agreement with experiment. In the case that c is small it was shown in RRRV that ϕ_1 is to a good approximation the CP violating phase δ in the Wolfenstein parameterization. A non-zero c is necessary to avoid the relation $V_{ub}/V_{cb} = \sqrt{m_u/m_c}$ and with the improvement in the data, it is now necessary to have c larger than was found in RRRV⁵. As a result the contribution to CP violation coming from ϕ_2 is at least 30%. The sign ambiguity in ϕ_1 gives rise to an ambiguity in c with the positive sign corresponding to the larger value of c seen in Tables 3.3 and 3.4.

Table 3.3 shows results from a χ^2 fit of Eqs(3.15,3.16) to the data in Table 3.2 in the absence of threshold corrections. The error, indicated by the term in brackets, represent the widest axis of the 1σ error ellipse in parameter space. The fits labeled ‘A’ have phases such that we have the smaller magnitude solution of $|c|$, and fits labeled ‘B’ have phases such that we have the larger magnitude solution of $|c|$. As discussed above, it is not possible unambiguously to determine the relative contributions of the off-diagonal elements of the up and down Yukawa matrices to the mixing angles. In the fit A2 and B2 we illustrate the uncertainty associated with this ambiguity, allowing for $O(1)$ coefficients a' . In all the examples in Table 3.3, the mass ratios, and Wolfenstein parameters are essentially the same as in Table 3.2.

The effects of the large $\tan\beta$ threshold corrections are shown in Table 3.4. The threshold corrections depend on the details of the SUSY spectrum, and we have displayed the effects

⁵As shown in ref. [135], it is possible, in a basis with large off-diagonal entries, to have an Hermitian pattern with the $(1,1)$ and $(1,3)$ zero provided one carefully orchestrates cancelations among Y^u and Y^d parameters. We find this approach requires a strange-quark mass near its upper limit.

Parameter	A	B	C	B2	C2
$\tan\beta$	30	38	38	38	38
γ_b	0.20	-0.22	+0.22	-0.22	+0.22
γ_t	-0.03	0	-0.44	0	-0.44
γ_d	0.20	-0.21	+0.21	-0.21	+0.21
a'	0	0	0	-2	-2
ϵ_u	0.0495(17)	0.0483(16)	0.0483(18)	0.0485(17)	0.0485(18)
ϵ_d	0.131(7)	0.128(7)	0.102(9)	0.127(7)	0.101(9)
$ b' $	1.04(12)	1.07(12)	1.07(11)	1.05(12)	1.06(10)
$\arg(b')$	90(12) ^o	91(12) ^o	93(12) ^o	95(12) ^o	95(12) ^o
a	2.17(24)	2.27(26)	2.30(42)	2.03(24)	1.89(35)
b	1.69(13)	1.73(13)	2.21(18)	1.74(10)	2.26(20)
$ c $	0.80(16)	0.86(17)	1.09(33)	0.81(17)	1.10(35)
$\arg(c)$	-41(18) ^o	-42(19) ^o	-41(14) ^o	-53(10) ^o	-41(12) ^o
Y_{33}^u	0.48(2)	0.51(2)	0.51(2)	0.51(2)	0.51(2)
Y_{33}^d	0.15(1)	0.34(3)	0.34(3)	0.34(3)	0.34(3)
Y_{33}^e	0.23(1)	0.34(2)	0.34(2)	0.34(2)	0.34(2)
$(m_b/m_\tau)(M_X)$	0.67(4)	1.00(4)	1.00(4)	1.00(4)	1.00(4)
$(3m_s/m_\mu)(M_X)$	0.60(3)	0.9(1)	0.6(1)	0.9(1)	0.6(1)
$(m_d/3m_e)(M_X)$	0.71(7)	1.04(8)	0.68(6)	1.04(8)	0.68(6)
$\left \frac{\det Y^d(M_X)}{\det Y^e(M_X)} \right $	0.3(1)	0.92(14)	0.4(1)	0.92(14)	0.4(1)

Table 3.4: A χ^2 fit of Eqs(3.15,3.16) including the SUSY threshold effects parameterized by the specified γ_i .

corresponding to a variety of choices for this spectrum. Column A corresponds to a “standard” SUGRA fit - the benchmark Snowmass Points and Slopes (SPS) spectra 1b of ref([3]). Because the spectra SPS 1b has large stop and sbottom squark mixing angles, the approximations given in Eqns(3.7-3.10) break down, and the value for the correction γ_i in Column A need to be calculated with the more complete expressions in BRP [118] . In the column A fit and the next two fits in columns B and C, we set a' and c' to zero. Column B corresponds to the fit given in the penultimate column of Table 3.2 which agrees very well with the simple GUT predictions. It is characterized by the “anomaly-like” spectrum with M_3 negative. Column C examines the M_3 positive case while maintaining the GUT prediction for the third generation $m_b = m_\tau$. It corresponds to the “Just-so” Split-Higgs solution. In the fits A, B and C the value of the parameter a is significantly larger than that found in RRRV. This causes problems for models based on non-Abelian family symmetries, and it is of interest to try to reduce a by allowing a' , b' and c' to vary while remaining $\mathcal{O}(1)$ parameters. Doing this for the fits B and C leads to the fits B2 and C2 given in Table 3.4 where it may be seen that the extent to which a can be reduced is quite limited. Adjusting to this is a challenge for the broken family-symmetry models.

Although we have included the finite corrections to match the MSSM theory onto the Standard Model at an effective SUSY scale $M_S = 500$ GeV, we have not included finite corrections from matching onto a specific GUT model. Precise threshold corrections cannot be rigorously

calculated without a specific GUT model. Here we only estimate the order of magnitude of corrections to the mass relations in Table 3.2 from matching the MSSM values onto a GUT model at the GUT scale. The $\tan \beta$ enhanced corrections in Eq(3.7-3.10) arise from soft SUSY breaking interactions and are suppressed by factors of M_{SUSY}/M_{GUT} in the high-scale matching. Allowing for $\mathcal{O}(1)$ splitting of the mass ratios of the heavy states, one obtains corrections to y^b/y^τ (likewise for the lighter generations) of $\mathcal{O}(\frac{g^2}{(4\pi)^2})$ from the X and Y gauge bosons and $\mathcal{O}(\frac{y_b^2}{(4\pi)^2})$ from colored Higgs states. Because we have a different Higgs representations for different generations, these threshold correction will be different for correcting the $3m_s/m_\mu$ relation than the m_b/m_τ relation. These factors can be enhanced in the case there are multiple Higgs representation. For an $SU(5)$ SUSY GUT these corrections are of the order of 2%. Planck scale suppressed operators can also induce corrections to both the unification scale [136] and may have significant effects on the masses of the lighter generations [137]. In the case that the Yukawa texture is given by a broken family symmetry in terms of an expansion parameter ϵ , one expects model dependent corrections of order ϵ which may be significant.

Chapter Summary

In summary, in the light of the significant improvement in the measurement of fermion mass parameters, we have analyzed the possibility that the fermion mass structure results from an underlying supersymmetric GUT at a very high-scale mirroring the unification found for the gauge couplings. Use of the RG equations to continue the mass parameters to the GUT scale shows that, although qualitatively in agreement with the GUT predictions coming from simple Higgs structures, there is a small quantitative discrepancy. We have shown that these discrepancies may be eliminated by finite radiative threshold corrections involving the supersymmetric partners of the Standard-Model states. The required magnitude of these corrections is what is expected at large $\tan \beta$, and the form needed corresponds to a supersymmetric spectrum in which the gluino mass is negative with the opposite sign to the wino mass. We have also performed a fit to the recent data to extract the underlying Yukawa coupling matrices for the quarks and leptons. This is done in the basis in which the mass matrices are hierarchical in structure with the off-diagonal elements small relative to the appropriate combinations of on-diagonal matrix elements, the basis most likely to be relevant if the fermion mass structure is due to a spontaneously broken family symmetry. We have explored the effect of SUSY threshold corrections for a variety of SUSY spectra. The resulting structure has significant differences from previous

fits, and we hope will provide the “data” for developing models of fermion masses such as those based on a broken family symmetry.

Since this work was first published, its conclusions have been confirmed by studies of other research groups [138]. The updated fits to the Yukawa textures and viability of the Georgi-Jarlskog relations have been used in numerous string theory and family symmetry models.

Chapter 4

Mass Determination Toolbox at Hadron Colliders

Chapter Overview

In the previous chapter, we presented arguments that predict the sign of the gluino mass relative to the wino mass and relationships between these masses needed to satisfy classic Georgi-Jarlskog mass relationships at the GUT scale.

This chapter and the remaining chapters discuss mostly model-independent experimental techniques to determine the mass of a pair-produced dark-matter particle. As a test case, we take the dark-matter to be the lightest supersymmetric particle (LSP) which we assume is the neutralino $\tilde{\chi}_1^0$ ¹. Determining the mass of the dark-matter particle is a necessary prerequisite to determining the entire mass spectrum of the new particle states and to determining the sign of the gluino's mass (given that supersymmetry is the correct model) predicted in the previous chapter.

This chapter reviews challenges of hadron-collider mass-determination and mostly model-independent techniques to address these challenges existent in the literature. In the subsequent chapters of this thesis, we will improve on these techniques and develop new techniques that can perform precision measurements of the dark-matter's mass with only a few assumptions about the underlying model.

4.1 Mass Determination Challenges at Hadron Colliders

Measuring all the masses and phases associated with the predictions in Chapter 3 or the predictions of any of the many competing models depends on the successful resolution of several challenges present at any hadron collider. First to avoid selection bias and because of the large

¹The four neutralinos are superpositions of the two Higgsinos, the bino, and the neutral wino ($\tilde{h}_u^0, \tilde{h}_d^0, \tilde{B}, \tilde{W}^3$). They are numbered from 1 having the smallest mass to 4 having the largest mass.

number of possible models, we would prefer kinematic model-independent techniques to measure parameters like the mass instead of model-dependent techniques. Kinematic techniques are made complicated because of the possibility of producing dark matter in the collider which would lead to new sources (beyond neutrinos) of missing transverse momentum. Kinematic techniques are also made complex because the reference frame and center-of-mass energy of the parton collision is only known statistically ². Last our particle detector has fundamental limitations on the shortest track that can be observed leading to combinatoric ambiguities identifying decay products from new particle states that are created and decay at the “effective” vertex of the collision.

4.1.1 Kinematic versus Model-Dependent Mass Determination

Any new physics discovered will come with unknown couplings, mixing angles, spins, interactions, and masses. One approach is to assume a model and fit the model parameters to the observed data. However, we have hundreds of distinct anticipated theories possessing tens of new particle states with differing spins and couplings each with tens of parameters. Global fits to approximately 10^9 events recorded per year are an enormous amount of work, and assume that the ‘correct model’ has been anticipated.

We would like to measure the particle properties with minimal model assumptions. The term ‘model-independent’ technique is misleading because we are always assuming some model. When we say model-independent, we mean that we assume broadly applicable assumptions such as special relativity. We also try to ensure that our techniques are largely independent of *a priori* unknown coupling coefficients and model parameters. For this reason our desire for model-independence constrains our toolbox to kinematic properties of particle production and decay.

If we are able to determine the mass of the dark-matter particle, other properties follow more easily. Knowing the dark-matter particle’s mass, the remaining mass spectrum follows from kinematic edges. If we know the dark-matter’s mass and gluino’s mass, then the sign of the gluino’s mass predicted in Chapter 3 can be determined from the distribution of the invariant mass of jet pairs from the decay of gluino pair production [139]. Another avenue to the sign of the gluino’s mass requires measuring the masses of the gluino and the two stop squarks and the measuring the decay width of gluino to these states [140, Appendix B]. In addition,

²To the extent we understand the uncertainties in the measured parton distribution functions.

the measurement of spin correlations, a study that can contribute to spin determination, has historically relied on knowing the masses to reconstruct the event kinematics [141].

In short, mass determination is a key part to identifying the underlying theory which lies beyond the Standard Model. Newly discovered particles could be Kaluza-Klein (KK) states from extra-dimensions, supersymmetric partners of known states, technicolor hadrons, or something else that we have not anticipated. Models predict relationships between parameters. Supersymmetry relates the couplings of current fermions to the couplings of new bosons, and the supersymmetric particle masses reflect the origin of supersymmetry breaking. Masses of KK states tell us about the size of the extra dimensions. If these parameters, such as the masses and spins, can be measured without assuming the model, then these observations exclude or confirm specific models. In general, mass determination of new particle states is central to discerning what lies beyond the Standard Model.

4.1.2 Dark matter: particle pairs carrying missing transverse momentum

If dark matter is produced at a hadron collider, the likely signature will be missing transverse momentum. The lightest supersymmetric particle (LSP) or lightest Kaluza-Klein particle (LKP) is expected to be neutral, stable, and invisible to the particle detectors. The astrophysical dark matter appears to be stable. Whatever symmetry makes dark matter stable and / or distinguishes superpartners from their Standard-Model cousins will likely also require that dark matter particles be pair produced. Therefore, events with supersymmetric new particle states are expected to end in two LSP's leaving the detector unnoticed. Events with Kaluza-Klein particles are expected to end with two LKP's leaving the detector unnoticed. The presence of two invisible particles prevents complete reconstruction of the kinematics of any single event and leads to missing transverse momentum in the events.

4.1.3 Reference frame unknown due to colliding hadrons

At a hadron collider, because the partons colliding each carry an unknown fraction of the hadron's momentum we do not know the reference frame of the collision. Although the individual parton momentum is unknown, the statistical distribution of the parton's momentum can be measured from deep inelastic scattering [142]. The measured parton distribution functions (PDFs) $f_i^H(x, Q)$ give the distribution of parton i within the hadron H carrying x fraction of the hadron's momentum when probed by a space-like momentum probe q^μ with $Q^2 = -q^2$. Q is also the factorization scale at which one cuts off collinear divergences. The dominant parton types i are u , d , s , their antiparticles \bar{u} , \bar{d} , \bar{s} , and gluons g .

The events produced in the collider follow from a convolution of the cross section over the parton distribution functions. If the two colliding protons have 4-momentum $p_1 = \sqrt{s_{LHC}}(1, 0, 0, 1)/2$ and $p_2 = \sqrt{s_{LHC}}(1, 0, 0, -1)/2$, then for example the u and \bar{u} quarks colliding would have 4-momentum $x_u p_1$ and $x_{\bar{u}} p_2$. The spatial momentum of the collision along the beam axis is given by $(x_u - x_{\bar{u}})\sqrt{s_{LHC}}/2$, and the center-of-mass energy of the parton collision is $\sqrt{x_u x_{\bar{u}} s_{LHC}}$. Because x_u and $x_{\bar{u}}$ are only known statistically, any individual collision has an unknown center-of-mass energy and an unknown momentum along the beam axis.

LHC processes are calculated by convolutions over the PDFs as in

$$\sigma = \int dx_u dx_{\bar{u}} f_u^p(x_u, Q) f_{\bar{u}}^p(x_{\bar{u}}, Q) \sigma(x_u x_{\bar{u}} s_{LHC}, Q)_{u\bar{u} \rightarrow final} \quad (4.1)$$

where $\sigma(s, Q)_{u\bar{u} \rightarrow final}$ is the total cross section for a given parton collision center-of-mass squared s , factorization scale Q , and $\sqrt{s_{LHC}}$ is the center-of-mass collision energy of the protons colliding at the LHC. The region of integration of x_u and $x_{\bar{u}}$ is based on the kinematically allowable regions. The factorization scale Q is chosen to minimize the size of the logarithms associated with regulating collinear divergences in the cross section. See Ref [143] for a recent review on choosing the factorization scale.

Calculating these input cross sections even at tree level is an arduous process that has been largely automated. Performing these convolutions over experimentally determined PDFs adds even further difficulties. Monte-Carlo generators typically perform these calculations. The calculations in subsequent chapters made use of MadGraph and MadEvent [144], HERWIG[17], CompHEP [145].

Despite this automation, the author has found it useful to reproduce these tools so that we can deduce and control what aspects of the observed events are caused by what assumptions. For this purpose, parton distributions can be downloaded³ from [146]. Analytic cross sections for processes can be produced by CompHEP[145].

These review studies have led to an appreciation of uncertainties in the parton distribution functions, uncertainties about the correct Q to use⁴, and uncertainties in the process of hadronization of the outgoing partons. All these uncertainties contribute to significant uncertainties in the background of which new physics must be discovered, and to uncertainties underlying model-dependent, cross-section-dependent determinations of particle masses.

³One should also look for the Les Houches Accord PDF Interface (LHAPDFs) interfaces to interface PDFs to different applications (<http://projects.hepforge.org/lhapdf/>).

⁴Ref [140] suggests using $Q \approx 2M_{SUSY}$ or whatever energy scale is relevant to the particles being produced.

4.1.4 Detector Limitations

Particle detectors have finite capabilities which limit what we can learn. We will discuss the effects of finite energy resolution later in this thesis. Here I focus on the lack of the traditional tracks one sees in event representations.

The early history of particle physics shows beautiful bubble chamber tracks of particles. Studies of Pions and Kaons relied on tracks left in bubble chambers or modern digitized detectors. In the case of the K_S the lifetime is $\tau = 0.9 \times 10^{-10}$ seconds or $c\tau = 2.7$ cm, or equivalently the decay width is $\Gamma = 7 \times 10^{-6}$ eV. A particle with a width of $\Gamma = 1$ eV has a lifetime of $\tau = 6 \times 10^{-16}$ seconds with $c\tau = 0.2\mu\text{m}$. The more massive known states of W^\pm , Z^0 bosons and the top quark have widths of $\Gamma_W = 2.141$ GeV, $\Gamma_Z = 2.50$ GeV, and $\Gamma_t \approx 1.5$ GeV. These decay widths give these states tracks with $c\tau \approx 0.1$ fm or about 1/10 the size of an atomic nuclei.

Most supersymmetric states, depending on the model, have decay widths between around 1 MeV and 2 GeV⁵. These observations, while trivial, make us realize that new physics discoveries will most likely need to deduce properties of the new states from their decay products only. The fact that all events effectively occur at the origin creates combinatoric problems because we cannot know the order in which the visible particles came off of a decay chain or even to which decay chain they belong.

4.2 Invariant Mass Edge Techniques

We now turn to existent tools to overcome the challenges inherent in mass determination at hadron colliders in the presence of missing transverse momentum.

4.2.1 Invariant Mass Edges

Lorentz invariant distributions are optimal for making a distribution independent of the unknown frame of reference. Fig 4.1 shows a two-body decay and a three-body decay. The decay products from Y in both cases involve a dark-matter particle N and two visible states with 4-momenta α_1 and α_2 ; we will abbreviate $\alpha = \alpha_1 + \alpha_2$. The Lorentz invariant mass of these two visible states is defined as

$$m_{12}^2 = \alpha^2 = (\alpha_1 + \alpha_2)^2. \quad (4.2)$$

Assuming no spin correlation between α_1 and α_2 , the distribution for the two-body decay looks more like a right-triangle whereas the three-body decay case looks softer. Spin correlations

⁵This is not a universal statement. Some viable models have long lived charged states ($c\tau \gg 1$ cm) [147, 148, 149].

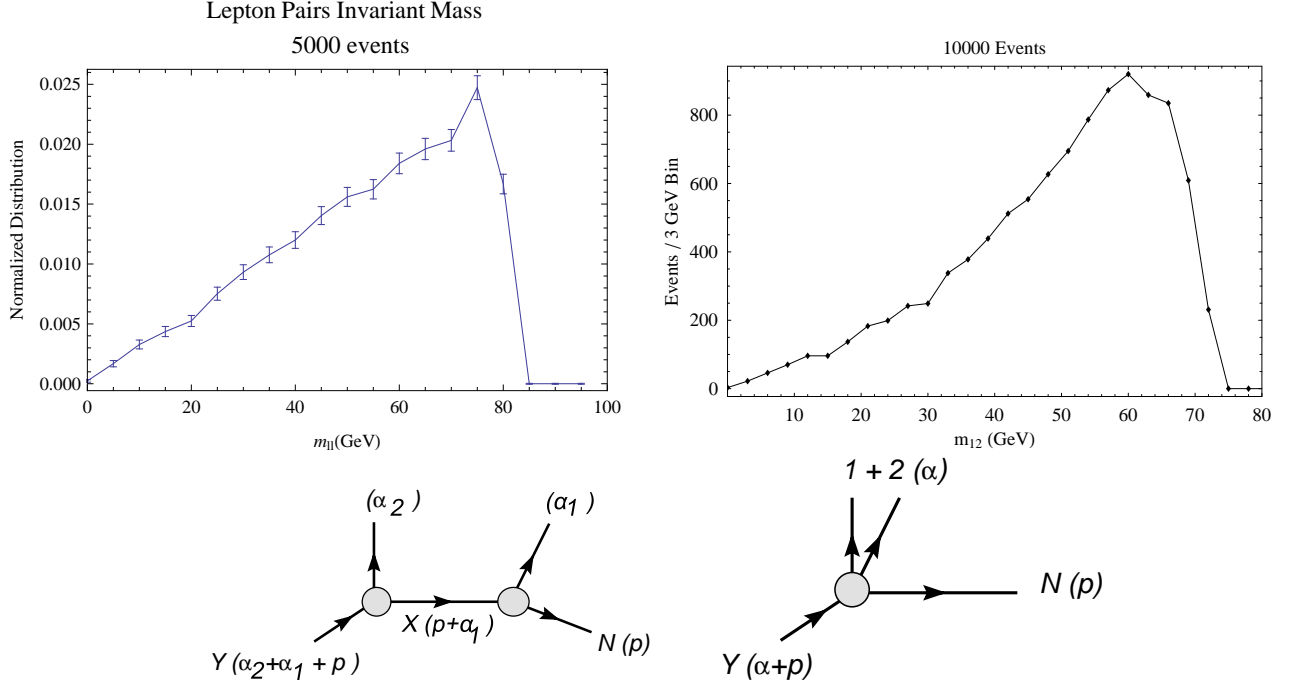


Figure 4.1: **(Left:)** Two body decay and it's associated m_{ll} distribution. **(Right:)** Three body decay and it's associated m_{ll} distribution.

between these states may change the shape and might be used to measure spin in some cases [150]. The distribution shape can also be affected by competing processes in the three-body decay. For example, the degree of interference with the slepton can push the peak to a smaller value[151].

The end-point of the distribution gives information about the masses of the new particle states. In the two-body decay case the endpoint gives

$$\max m_{12}^2 = \frac{(M_Y^2 - M_X^2)(M_X^2 - M_N^2)}{M_X^2}, \quad (4.3)$$

and in the three-body decay case

$$\max m_{12} = M_Y - M_N. \quad (4.4)$$

These edges in invariant mass combinations provide information about mass differences or mass squared differences but not about the mass-scale itself. Measuring these edges requires some model of the events creating the distribution in order to simulate the effect of the detectors energy resolution. For this reason, even end-point techniques, although mostly model-independent, still require some estimate of the distribution near the end point to get an accurate end-point measurement. Radiative corrections also play a role in shifting this endpoint slightly[152].

These techniques have been studied to select a model if one assumes a particular set of starting models [153]. They have also been used with Bayesian techniques to measure the mass difference between slepton states [154].

4.2.2 Constraints from Cascade Decays

If there are many new particle states produced at the collider, then we can use edges from cascade decays between these new states to provide constraints between the masses. Given some luck regarding the relative masses, these constraints may be inverted to obtain the mass scale. Fig 4.2 shows a cascade decay from Z to Y to X ending in N and visible particle momenta $\alpha_1, \alpha_2, \alpha_3$.

There are four unknown masses and potentially four linearly-independent endpoints. In addition to Eq(4.3), we also have [155, 153]

$$\max m_{32}^2 = (M_Z^2 - M_Y^2)(M_Y^2 - M_X^2)/M_Y^2, \quad (4.5)$$

and

$$\max m_{123}^2 = \begin{cases} (M_Z^2 - M_Y^2)(M_Y^2 - M_N^2)/M_Y^2 & \text{iff } M_Y^2 < M_N M_Z \\ (M_Z^2 - M_X^2)(M_X^2 - M_N^2)/M_X^2 & \text{iff } M_N M_Z < M_X^2 \\ (M_Z^2 M_X^2 - M_Y^2 M_N^2)(M_Y^2 - M_X^2)/(M_Y^2 M_X^2) & \text{iff } M_X^2 M_Z < M_N M_Y^2 \\ (M_Z - M_N)^2 & \text{otherwise.} \end{cases} \quad (4.6)$$

The fourth endpoint is

$$\max m_{13}^2 = (M_Z^2 - M_Y^2)(M_X^2 - M_N^2)/M_X^2. \quad (4.7)$$

Depending on whether we can distinguish visible particles 1, 2 and 3 from each other, some of these endpoints may be obscured by combinatorics problems. If the visible particles and the masses are such that these four can be disentangled from combinatoric problems, and if the masses are such that these four end-points provide independent constraints, and if there is sufficient statistics to measure the endpoints well-enough, then we can solve for the mass spectrum.

This technique has been studied in [156, 155, 153] and subsequently by many others. In some cases, there is more than one solution to the equations. This degeneracy can be lifted by using the shape of these distributions [157, 158, 159]. Using the Supersymmetric benchmark point SPS 1a, this technique has been shown to determine the LSP mass to ± 3.4 GeV with about 500 thousand events from 300 fb^{-1} . They are able to determine the mass difference to $\sigma_{M_{\tilde{\chi}_2^0} - M_{\tilde{\chi}_1^0}} = 0.2 \text{ GeV}$ and $\sigma_{M_{\tilde{t}_R} - M_{\tilde{\chi}_1^0}} = 0.3 \text{ GeV}$ [157].

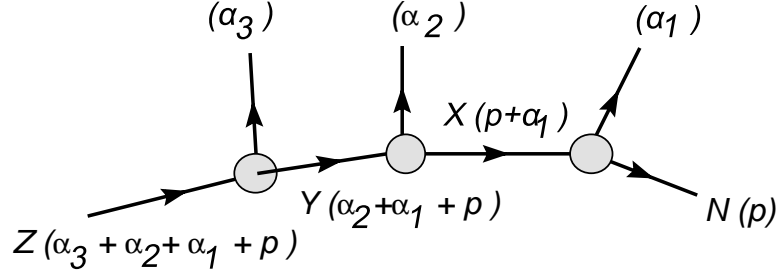


Figure 4.2: Cascade decay from Z to Y to X ending in N and visible particle momenta $\alpha_1, \alpha_2, \alpha_3$.

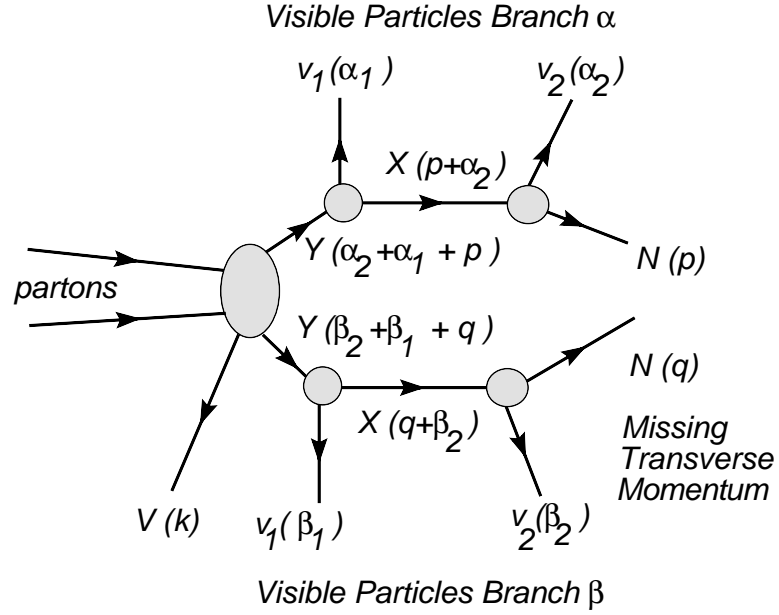


Figure 4.3: Events with the new state Y is pair produced and in which each Y decays through a two-body decay to a massive new state X and a visible state 1 and then where X subsequently decays to a massive state N invisible to the detector and visible particles 2. All previous decay products are grouped into the upstream transverse momentum, k .

4.3 Mass Shell Techniques

What if there are not as many new-states accessible at the collider, or what if the masses arrange themselves to not enable a solution to the four invariant mass edges listed above? There is also a series of approaches called Mass Shell Techniques (MST)⁶ where assumption are used about the topology and on-shell conditions to solve for the unknown masses.

An MST was used in the early 1990s by Goldstein, Dalitz (GD) [161], and Kondo, Chikamatsu, Kim (KCK)[162] as a suggested method to measure the mass of the top quark. The top-quark pair production and decay has the topology shown in Fig 4.3. Here $Y = t$ or \bar{t} , $X = W^\pm$, (1) = b , (2) = e and $N = \nu_e$. In each event, one measures $\alpha_{1,2}$, $\beta_{1,2}$, and the

⁶The title MST is suggested in Ref. [160].

missing transverse momentum $\not{p}_T = (p + q)_T$. The resulting mass shell and missing momentum equations are

$$M_N^2 = p^2 = q^2, \quad (4.8)$$

$$M_X^2 = (p + \alpha_2)^2 = (q + \beta_2)^2, \quad (4.9)$$

$$M_Y^2 = (p + \alpha_1 + \alpha_2)^2 = (q + \beta_1 + \beta_2)^2, \quad (4.10)$$

$$\not{p}_T = (p + q)_T. \quad (4.11)$$

If we assume a mass for M_Y , then we have 8 unknowns (the four components of each p and q) and 8 equations. The equations can be reduced to the intersection of two ellipses which have between zero and four distinct solutions. In GD and KCK, they supplemented these solutions with some data from the cross section and used Bayes' theorem to create a likelihood function for the unknown mass of the top quark. The approach has a systematic bias [163][164] that must be removed by modeling [165]⁷.

A modern reinvention of this MST is found in Cheng, Gunion, Han, Marandella and McElrath (CHGMM) [166] where they assume a symmetric topology with an on-shell intermediate state such as in Fig 4.3. This reinvention assumes $Y = \tilde{\chi}_2^0$, $X = \tilde{l}$ and $N = \tilde{\chi}_1^0$. CHGMM do a test of each event's compatibility with all values of (M_Y, M_X, M_N) . Using this approach, they find that with 300 fb^{-1} of events that they can determine the LSP mass to $\pm 12 \text{ GeV}$. Unlike GD and KCK, CHGMM make no reference to Bayesian techniques.

Another MST assumes a longer symmetric decay chain and assumes the masses in two events must be equal [167]. This results in enough equations to equal the number of unknowns to solve for the masses directly. For SPS 1a after 300 fb^{-1} , they reach $\pm 2.8 \text{ GeV}$ using 700 events satisfying their cuts but have a 2.5 GeV systematic bias that needs modeling to remove.

Finally there is a suggestion for hybrid MST where one combines on-shell conditions with the information from the many edges in cascade decays [168]. The M_{2C} variable introduced in Chapters 6 is a simple example of such a hybrid technique that predated their suggestion.

4.4 Transverse Mass Techniques

4.4.1 M_T and Measuring M_W

The invariant mass distributions are Lorentz invariant. In events with one invisible particle, like the neutrino, leaving the detector unnoticed, we only know the neutrino's transverse momentum inferred from the missing transverse momentum. If a parent particle X decays into a visible

⁷Details of this bias are discussed more in Section 8.2.1

particle with observed 4-momentum α_1 and an invisible particle p , then what progress can be made in mass determination? There is a class of techniques which, although not Lorentz invariant, is invariant with respect to longitudinal boosts along the beam line. The 4-momentum $p_\mu = (p_0, p_x, p_y, p_z)$ is cast in new coordinates

$$\eta(p) = \frac{1}{2} \ln \frac{p_0 + p_z}{p_0 - p_z} \quad (4.12)$$

$$E_T(p) = \sqrt{m_p^2 + p_x^2 + p_y^2} \quad (4.13)$$

$$p_\mu = (E_T \cosh \eta, p_x, p_y, E_T \sinh \eta) \quad (4.14)$$

where $m_p^2 = p^2$. The mass of X in the decay $X(\alpha_1 + p) \rightarrow N(p) + 1(\alpha_1)$ in Fig. 4.1 is

$$M_X^2 = (p + \alpha_1)^2 = M_N^2 + M_1^2 + 2p \cdot \alpha_1 \quad (4.15)$$

$$= M_N^2 + M_1^2 + 2E_T(p)E_T(\alpha_1) \cosh(\eta(p) - \eta(\alpha_1)) - 2p_T \cdot (\alpha_1)_T. \quad (4.16)$$

We observe the 4-momentum α_1 in the detector. From the missing transverse momentum, we can deduce the transverse components p_x and p_z . The components p_o and p_z remain unknown. If we know the mass of N , we can bound the unknown mass of X from below by minimizing with respect to the unknown rapidity $\eta(p)$. The minimum

$$M_X^2 \geq M_T^2(p, \alpha_1) \equiv M_N^2 + M_1^2 + 2E_T(p)E_T(\alpha_1) - 2p_T \cdot (\alpha_1)_T \quad (4.17)$$

is at $\eta(p) = \eta(\alpha_1)$ and is guaranteed to be less than the true mass of X . This lower bound is called the transverse mass M_T .

This technique is used to measure the W^\pm boson's mass with the identification $X = W^\pm$, $N = \nu_e$, and $(1) = e^\pm$. The first observation of the W^\pm was reported in 1983 at UA1 Collaboration at Super Proton Synchrotron (SPS) collider at CERN[48]. They used M_T to bound $M_W \geq 73$ GeV at the 90% confidence level. Assuming the Standard Model and fitting the data to the model with M_W as a free parameter gave the UA1 collaboration the measurement $M_W = 81 \pm 5$ GeV, which agreed with the prediction described by Llewellyn Smith and Wheater [47]. M_T is still used even for the more recent 2002 D0-Collaboration model-independent measurement of $M_W = 80.483 \pm 0.084$ GeV [169].

4.4.2 The Stransverse Mass Variable M_{T2}

If a hadron collider pair produces dark-matter particles, then there are two sources of missing transverse momentum, each with the same unknown mass. The 'stransverse mass' m_{T2}

introduced by Lester and Summers [12, 13] adapts the transverse mass m_T to this task. M_{T2} techniques have become widely used with Refs. [12, 13] having more than 45 citations.

The transverse mass is used to determine the mass *difference* between a parent particle and a dark-matter candidate particle given an assumed mass for the dark-matter candidate based on a topology similar to Figs 4.4 or 4.3. The variable m_{T2} accepts three inputs: χ_N (an assumed mass of the two particles carrying away missing transverse momenta), α and β (the visible momenta of each branch), and $\not{P}_T = (p+q)_T$ (the missing transverse momenta two-vector). We can define m_{T2} in terms of the transverse mass of each branch where we minimize the maximum of the two transverse masses over the unknown split between p and q of the overall missing transverse momenta:

$$M_{T2}^2(\chi_N, \alpha, \beta, \not{P}_T) = \min_{p_T+q_T=\not{P}_T} [\max \{M_T^2(\alpha, p), M_T^2(\beta, q)\}]. \quad (4.18)$$

In this expression χ_N is the assumed mass of N , α and β are the four momenta of the visible particles in the two branches, the transverse mass is given by $M_T^2(\alpha, p) = m_\alpha^2 + \chi_N^2 + 2(E_T(p)E_T(\alpha) - p_T \cdot \alpha_T)$ and the transverse energy $E_T(\alpha) = \sqrt{p_T^2 + \chi_N^2}$ is determined from the transverse momentum of p and the assumed mass of p . The M_T here is identical to Eq(4.17) with M_N replaced by the assumed mass χ_N . An analytic formula for the case with no transverse upstream momentum k_T can be found in the appendix of [170]. For each event, the quantity $M_{T2}(\chi_N = m_N, \alpha_1 + \alpha_2, \beta_1 + \beta_2, \not{P}_T)$ gives the smallest mass for the parent particle compatible with the event's kinematics. Under ideal assumptions, the mass of the parent particle Y is given by the end-point of the distribution of this m_{T2} parameter over a large number of events like Figs. 4.4 or 4.3. Because a priori we do not know M_N , we need some other mechanism to determine M_N . We use χ to distinguish assumed values of the masses (χ_Y, χ_X, χ_N) from the true values for the masses (m_Y, m_X, m_N). Because of this dependence on the unknown mass, we should think of $\max m_{T2}$ as providing a relationship or constraint between the mass of Y and the mass of N . This forms a surface in the (χ_Y, χ_X, χ_N) space on which the true mass will lie. We express this relationship as $\chi_Y(\chi_N)$ ⁸.

In addition to invariance with respect to longitudinal boosts, M_{T2} , in the limit where $k_T = 0$, is also invariant with respect to back-to-back boosts of the parent particle pair in the transverse plane [171].

M_{T2} is an ideal tool for top-mass determination at the LHC [172]. M_{T2} would apply to events where both pair-produced top quarks decay to a b quark and a W^\pm and where in both branches

⁸In principle this surface would be considered a function of $\chi_Y(\chi_X, \chi_N)$, but m_{T2} makes no reference to the mass of X and the resulting constraints are therefore independent of any assumed value of the mass of X .

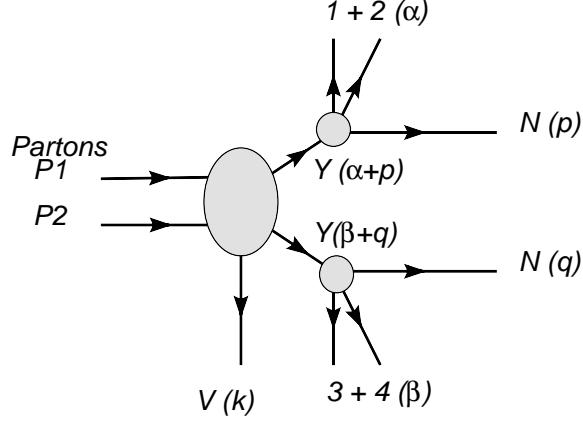


Figure 4.4: Events with the new state Y is pair produced and in which each Y decays through a three-body decay to a massive state N invisible to the detector and visible particles 1, 2, 3, and 4. All previous decay products are grouped into the upstream transverse momentum, k .

the W^\pm decays leptonically to l and ν_l . To use M_{T2} to find the mass of the parent particle, a value must be assumed for $\chi_N = M_N$. For a ν we approximate $\chi_N = 0$. However, even in models of new physics where new invisible particles are nearly massless (like the gravitino studied in [173]), we would rather not just assume the mass of the lightest supersymmetric particle (LSP), which is needed as an input to the traditional m_{T2} analysis, without measuring it in some model independent way.

4.4.3 Max M_{T2} Kink Technique

M_{T2} assumes a mass χ_N for N . Is there any way that one can determine M_N from M_{T2} alone? At the same time as the author was completing work on M_{2C} described in Chapter 6, Cho, Choi Kim, Park (CCKP) [174, 171] published an observation on how the mass could be deduced from M_{T2} alone. If Y is pair produced and each undergoes a three-body decay⁹ to N as shown in Fig. 4.4, then a ‘kink’ in the $\max m_{T2}$ [12, 13], will occur at a position which indicates the invisible particle mass. This ‘kink’ is corroborated in Refs. [176, 177]. Fig 4.5 shows the ‘kink’ in $\max m_{T2}$ in an idealized simulation where $M_Y = 800$ GeV and $M_N = 100$ GeV. In the CCKP example, they study a mAMSB senario where a gluino decays via a three-body decay to the LSP and quarks. In this case, they determined the LSP’s mass to ± 1.7 GeV. The difficulty in mass determination with this technique scales as $(M_+/M_-)^2 = (M_Y + M_N)^2 / (M_Y - M_N)^2$. For CCKP’s example $M_+/M_- = 1.3$; we will consider examples where $M_+/M_- \approx 3$. The $(M_+/M_-)^2$ scaling behavior follows by propagating error in M_- to position of the intersection of the two curves that form the kink.

⁹The presence of a ≥ 3 -body decay is a sufficient but not necessary condition. Two-body decays can also display kinks [175, 176] provided the decaying particles have sufficiently large transverse boosts.

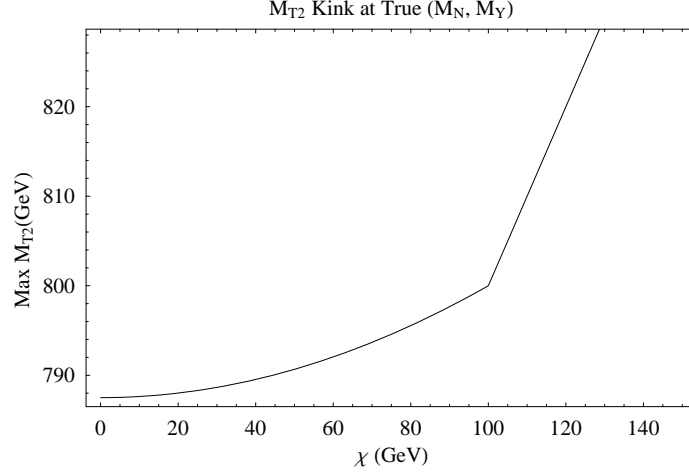


Figure 4.5: The $\max M_{T2}(\chi)$ shows a kink at the true M_N and M_Y . For this simulation, $m_Y = 200$ GeV, and $m_N = 99$ GeV.

This kink is quantified by the constrained mass variable m_{2C} [15][16] that is the subject of later chapters of this thesis. We will be applying it to a case about 5 or 6 times more difficult because $M_+/M_- \approx 3$ for the neutralino studies on which we choose to focus.

Chapter Summary

In this chapter, we have introduced the need for making mass measurements in a model independent manner of collider-produced dark matter. We have outlined many approaches based on edges of invariant mass distributions, mass shell techniques, and transverse mass techniques. Each technique has distinct domains of validity and requirements. In the remaining chapters of this thesis, we introduce and test new model-independent techniques to determine mass of dark-matter particles. Which approach turns out to be best is likely to depend on what scenario nature hands us, since the various techniques involve different assumptions. Having different approaches also offers the advantage of providing a system of redundant checks.

Chapter 5

Using M_{T2} with Cascade decays

Chapter Overview

Recently, a paper by Tovey[178] introduced a new variable, M_{CT} , with the powerful concept of extracting mass information from intermediate stages of a symmetric decay chain. In this chapter, we compare M_{T2} with M_{CT} . The variable M_{CT} is new but shares many similarities and differences with M_{T2} . We briefly define M_{CT} and explain when it gives identical results to M_{T2} and when it gives different results. We comment on benefits of each variable in its intended applications. We find that for massless visible particles M_{CT} equals M_{T2} in a particular limit, but M_{T2} has better properties when there is initial state radiation (ISR) or upstream transverse momentum (UTM)¹. We argue that M_{T2} is a more powerful tool for extracting mass information from intermediate stages of a symmetric decay chain. This chapter is based on work first published by the author in Ref. [14].

5.1 M_{T2} and M_{CT} in this context

Both M_{T2} and M_{CT} assume a pair-produced new-particle state followed by each branch decaying symmetrically to visible states and dark-matter candidates which escape detection and appear as missing transverse momentum. Fig 4.3 is the simplest example on-which we can meaningfully compare the two kinematic quantities. The figure shows two partons colliding and producing some observed initial state radiation (ISR) or upstream transverse momentum (UTM) with four momenta k and an on-shell, pair-produced new state Y . On each branch, Y decays to on-shell states X and v_1 with masses M_X and m_{v_1} , and X then decays to on-shell states N and v_2 with masses M_N and m_{v_2} . The four-momenta of v_1 , v_2 and N are respectively α_1 , α_2 and p on one

¹ISR and UTM both indicate $k_T \neq 0$. We take ISR to mean the case when k_T is small compared to the energy scales involved in the collision.

branch and β_1, β_2 and q in the other branch. The missing transverse momenta \cancel{p}_T is given by the transverse part of $p + q$.

Tovey [178] recently defined a new variable M_{CT} which has many similarities to M_{T2} . The variable is defined as

$$M_{CT}^2(\alpha_1, \beta_1) = (E_T(\alpha_1) + E_T(\beta_1))^2 - (\alpha_{1T} - \beta_{1T})^2. \quad (5.1)$$

Tovey's goal is to identify another constraint between masses in the decay chain. He observes that in the rest frame of Y the momentum of the back-to-back decay products X and v_1 is given by

$$(k_*(M_Y, M_X, m_{v_1}))^2 = \frac{(M_Y^2 - (m_{v_1} + M_X)^2)(M_Y^2 - (m_{v_1} - M_X)^2)}{4M_Y^2} \quad (5.2)$$

where k_* is the two-body excess-momentum parameter (2BEMP)². In the absence of transverse ISR ($k_T = 0$) and if the visible particles are effectively massless ($m_{v_1} = 0$), Tovey observes that $\max M_{CT}(\alpha_1, \beta_1)$ is given by $2k_*$; this provides an equation of constraint between M_Y and M_X . Tovey observes that if we could do this analysis at various stages along the symmetric decay chain, then all the masses in principle could be determined.

The big advantage of M_{CT} is in its computational simplicity. It is a simple one line formula to evaluate. Also, M_{CT} is intended to only be calculated once per event instead of at a variety of choices of the hypothetical LSP mass χ . In contrast, M_{T2} is a more computationally intensive parameter to compute; but this is aided by the use of a common repository of community tested C++ libraries found at [179].

How are these two variables similar? Both M_{CT} and M_{T2} , in the limit of $k_T = 0$, are invariant under back-to-back boosts of the parent particles momenta [171]. The variable M_{CT} equals M_{T2} in the special case where $\chi = 0$, and the visible particles are massless ($\alpha_1^2 = \beta_1^2 = 0$), and there is no transverse ISR or UTM ($k_T = 0$)

$$M_{CT}(\alpha_1, \beta_1) = M_{T2}(\chi = 0, \alpha_1, \beta_1, \cancel{p}_T = (p + q + \alpha_2 + \beta_2)_T) \quad \text{if } \alpha_1^2 = \beta_1^2 = 0. \quad (5.3)$$

$$= 2(\alpha_{1T} \cdot \beta_{1T} + |\alpha_{1T}| |\beta_{1T}|). \quad (5.4)$$

The M_{CT} side of the equation is straight forward. The M_{T2} side of the expression can be derived analytically using the formula for M_{T2} given in [170]; we also show a short proof in Appendix C. Eq(5.3) uses a M_{T2} in a unconventional way; we group the observed momenta of the second decay products into the missing transverse momenta. In this limit, both share an endpoint of

²Tovey refers to this as the 2-body mass parameter \mathcal{M}_i . We feel calling this a mass is a bit misleading so we are suggesting 2BEMP.

$2k_* = (M_Y^2 - M_X^2)/M_Y$. To the best of our knowledge, this endpoint was first pointed out by CCKP [174]³. We find it surprising that a physical relationship between the masses follows from M_{T2} evaluated at a non physical χ . In the presence of ISR or UTM, Eq(5.3) is no longer an equality. Furthermore in the presence of ISR or UTM, the end point of the distribution given by either side of Eq(5.3) exceeds $2k_*$. In both cases, we will need to solve a combinatoric problem of matching visible particles to their decay order and branch of the event which we leave for future research.

In the case where the visible particle v_1 is massive, the two parameters give different endpoints

$$\max M_{CT}(\alpha_1, \beta_1) = \frac{M_Y^2 - M_X^2}{M_Y} + \frac{m_{v_1}^2}{M_Y}, \text{ and} \quad (5.5)$$

$$\max M_{T2}(\chi = 0, \alpha_1, \beta_1, \not{P}_T = (p + q + \alpha_2 + \beta_2)_T) = \sqrt{m_{v_1}^2 + 2(k_*^2 + k_* \sqrt{k_*^2 + m_{v_1}^2})} \quad (5.6)$$

where k_* is given by Eq(5.2). Unfortunately, there is no new information about the masses in these two endpoints. If we solve Eq(5.5) for M_X and substitute this into Eq(5.6) and (5.2), all dependence on M_Y is eliminated.

5.2 Application to symmetric decay chains

Tovey's idea of analyzing the different steps in a symmetric decay chain to extract the masses is powerful. Up to now, we have been analyzing both variables in terms of the first decay products of Y . This restriction is because M_{CT} requires no transverse ISR to give a meaningful endpoint. If we were to try and use α_2 and β_2 to find a relationship between M_X and M_N , then we would need to consider the transverse UTM to be $(k + \alpha_1 + \beta_1)_T$, which is unlikely to be zero.

We suggest M_{T2} is a better variable with which to implement Tovey's idea of analyzing the different steps in a symmetric decay chain because of its ISR properties. With and without ISR, M_{T2} 's endpoint gives the correct mass of the parent particle when we assume the correct value of the missing-energy-particle's mass⁴. For this reason, $\max M_{T2}$ gives a meaningful relationship between masses (M_Y, M_X, M_N) for all three symmetric pairings of the visible particles across the two branches. A relationship between M_Y and M_X is given by

$$\chi_Y(\chi_X) = \max M_{T2}(\chi_X, \alpha_1, \beta_1, \not{P}_T = (p + q + \alpha_2 + \beta_2)_T). \quad (5.7)$$

³The endpoint given by CCKP is violated for non-zero ISR at $\chi_N < M_N$ and $\chi_N > M_N$.

⁴In principle we could plot the $\max M_{T2}(\chi_X, \alpha_1, \beta_1, \not{P}_T = (\alpha_2 + \beta_2 + p + q)_T)$ vs χ_X as a function of transverse ISR and the value of χ_X at which the end point is constant would give the correct value of M_X ; at which point the distributions end point would give the correct M_Y . In practice we probably will not have enough statistics of ISR events.

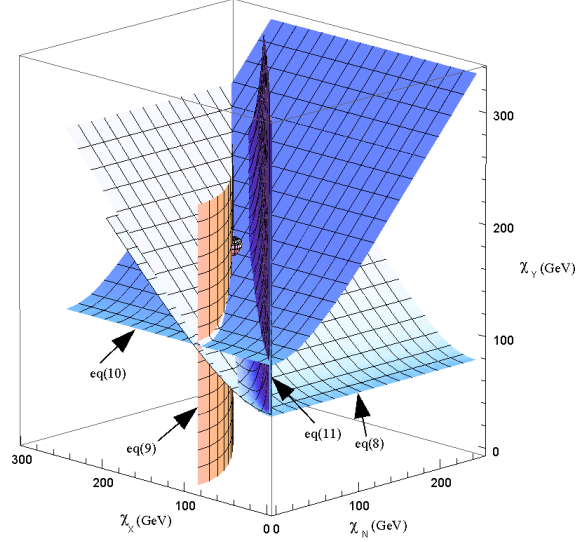


Figure 5.1: Shows constraints from $\max M_{T2}$ used with different combinations as described in eqs(5.7,5.8,5.9) and the $\max m_{12}$ described in Eq(5.11). Intersection is at the true mass (97 GeV, 144 GeV, 181 GeV) shown by sphere. Events include ISR but otherwise ideal conditions: no background, resolution, or combinatoric error.

A relationship between M_X and M_N can be found by computing

$$\chi_X(\chi_N) = \max M_{T2}(\chi_N, \alpha_2, \beta_2, \not{P}_T = (p+q)_T) \quad (5.8)$$

where we have grouped $\alpha_1 + \beta_1$ with the k as a part of the ISR. A relationship between M_Y and M_N can be found by using M_{T2} in the traditional manner giving

$$\chi_Y(\chi_N) = \max M_{T2}(\chi_N, \alpha_1 + \alpha_2, \beta_1 + \beta_2, \not{P}_T = (p+q)_T). \quad (5.9)$$

Lastly, we can form a distribution from the invariant mass of the visible particles on each branch $m_{12}^2 = (\alpha_1 + \alpha_2)^2$ or $m_{12}^2 = (\beta_1 + \beta_2)^2$. The endpoint of this distribution gives a relationship between M_Y , M_X , and M_N given by

$$\max m_{12}^2 = \frac{(M_Y^2 - M_X^2)(M_X^2 - M_N^2)}{M_X^2}. \quad (5.10)$$

Solving this expression for M_Y gives the relationship

$$\chi_Y^2(\chi_N, \chi_X) = \frac{\chi_X^2((\max m_{12}^2) + \chi_X^2 - \chi_N^2)}{\chi_X^2 - \chi_N^2}. \quad (5.11)$$

Fig 5.1 shows the constraints from Eqs(5.7, 5.8, 5.9, 5.11) in an ideal simulation using ($M_Y = 181$ GeV, $M_X = 144$ GeV, $M_N = 97$ GeV), 1000 events, and massless visible particles, and ISR added with an exponential distribution with a mean of 50 GeV. These four surfaces in principle intersect at a single point (M_Y, M_X, M_N) given by the sphere in the figure 5.1. Unfortunately,

all these surfaces intersect the correct masses at a shallow angles so we have a sizable uncertainty along the direction of the sum of the masses and tight constraints in the perpendicular directions. In other words, the mass differences are well-determined but not the mass scale. From here one could use a shape fitting technique like that described in Chapters 6 - 8. to find a constraint on the sum of the masses. Tovey's suggestion for extracting information from these intermediate stages of a symmetric cascade chain clearly provides more constraints to isolate the true mass than one would find from only using the one constraint of Eq(5.9) as described in [174]. However, Tovey's suggestion is more feasible using the M_{T2} rather than M_{CT} because the constraint surfaces derived from M_{T2} intersect the true masses even with UTM.

Chapter summary

In summary, we have compared and contrasted M_{CT} with M_{T2} . The variable M_{CT} is a special case of M_{T2} given by Eq(5.3) when ISR can be neglected and when the visible particles are massless. In this case, the end-point of this distribution gives $2k_*$, twice the two-body excess momentum parameter (2BEMP). If $m_{v_1} \neq 0$, the two distributions have different endpoints but no new information about the masses. In the presence of ISR the two functions are not equal; both have endpoints that exceed $2k_*$. Because of its better properties in the presence of UTM or ISR, M_{T2} is a better variable for the task of extracting information for each step in the decay chain. Extracting this information requires solving combinatoric problems which are beyond the scope of this chapter.

Chapter 6

The Variable M_{2C} : Direct Pair Production

Chapter Overview

In this chapter, we propose an improved method for hadron-collider mass determination of new states that decay to a massive, long-lived state like the LSP in the MSSM. We focus on pair-produced new states which undergo three-body decay to a pair of visible particles and the new invisible long-lived state. Our approach is to construct a kinematic quantity which enforces all known physical constraints on the system. The distribution of this quantity calculated for the observed events has an endpoint that determines the mass of the new states. However we find it much more efficient to determine the masses by fitting to the entire distribution and not just the end point. We consider the application of the method at the LHC for various models under the ideal assumption of effectively direct production with minimal ISR and demonstrate that the method can determine the masses within about 6 GeV using only 250 events. This implies the method is viable even for relatively rare processes at the LHC such as neutralino pair production.

This chapter, which is based on work first published by the author and his supervisor in Ref. [15], concentrates on mass determination involving the production of only two new states. Our particular concern is to use the available information as effectively as possible to reduce the number of events needed to make an accurate determination of M_Y and M_N . The main new ingredient of the method proposed is that it does not rely solely on the events close to the kinematic boundary but makes use of all the events. Our method constrains the unobserved energy and momentum such that all the kinematical constraints of the process are satisfied including the mass difference, Eq(4.4), which can be accurately measured from the ll spectrum discussed in Sec 4.2.1. This increases the information that events far from the kinematic bound-

ary can provide about M_Y and significantly reduces the number of events needed to obtain a good measurement of the overall mass scale. We develop the method for the case where Y is directly pair produced in the parton collision with minimal ISR and where each Y decays via a three-body decay to a on-shell final states $N + l^+ + l^-$. Its generalization to other processes is straightforward and considered later in this thesis¹.

The chapter is structured as follows: In Section 6.1, we introduce the M_{2C} distribution whose endpoint gives M_Y , and whose distribution can be fitted away from the endpoint to determine M_Y and M_N before we have enough events to saturate the endpoint. Section 6.2 discusses the relationship between our distribution and the kink in $M_{T2}(\chi)$ of CCKP and how this relationship can be used to calculate M_{2C} in a computationally efficient manner. We then in 6.3 discuss symmetries and dependencies of the M_{2C} distribution. Section 6.4 estimates the performance for a few SUSY models where we include approximate detector resolution effects and where we expect backgrounds to be minimal but where we assume ($k_T \approx 0$). Finally we summarize the chapter's findings.

6.1 An improved distribution from which to determine M_Y

We consider the event topology shown in Fig 4.4. The new state Y is pair produced. Each branch undergoes a three-body decay to the state N with 4-momentum p (q) and two visible particles $1 + 2$ ($3 + 4$) with 4-momentum α (β). The invariant mass m_{12} (m_{34}) of the particles $1 + 2$ ($3 + 4$) will have an upper edge from which we can well-determine M_- . Other visible particles not involved can be grouped into V with 4-momentum k . In general we refer to any process that creates non-zero k_T as upstream transverse momentum (UTM). One type of UTM is initial state radiation (ISR), which tends to be small compared to the mass scales involved in SUSY processes. Another type of UTM would be decays of heavier particles earlier in the decay chain. In the analysis presented in this chapter, we tested the concepts against both $k = 0$ and $k \lesssim 20$ GeV commiserate with what we might expect for ISR.

We adapt the concept from M_{T2} of minimizing the transverse mass over the unknown momenta to allow for the incorporation of all the available information about the masses. To do this we form a new variable M_{2C} which we define as the minimum mass of the second to lightest

¹We note that the on-shell intermediate case studied by CGHMM is also improved by including the relationship measured by the edge in the ll distribution on each event's analysis. The Y decay channel with an on-shell intermediate state X has an edge in the ll invariant mass distribution which provides a good determination of the relationship $\max m_{ll}^2 = (M_Y^2 - M_X^2)(M_X^2 - M_N^2)/M_X^2$. This relationship forms a surface in M_N, M_X, M_Y space that only intersects the allowed points of CGHMM's Fig 3 near the actual masses. We will investigate this case in Chapter 8.

new state in the event M_Y constrained to be compatible with the observed 4-momenta of Y 's visible decay products with the observed missing transverse energy, with the four-momenta of Y and N being on shell, and with the constraint that $M_- = M_Y - M_N$ is given by the value determined by the end point of the m_{12} distribution. The minimization is performed over the eight relevant unknown parameters which may be taken as the 4-momenta p and q of the particle N . We neglect any contributions from unobserved initial state radiation (ISR). Thus we have

$$M_{2C}^2 = \min_{p,q} (p + \alpha)^2 \quad (6.1)$$

subject to the 5 constraints

$$(p + \alpha)^2 = (q + \beta)^2, \quad (6.2)$$

$$p^2 = q^2, \quad (6.3)$$

$$\cancel{P}_T = (p + q)_T \quad (6.4)$$

$$\sqrt{(p + \alpha)^2} - \sqrt{p^2} = M_- \quad (6.5)$$

where \cancel{P}_T is the missing transverse momentum and $(p + q)_T$ are the transverse components of $p + q$. Although we can implement the minimization numerically or by using Lagrange multipliers, we find the most computationally efficient approach is to modify the M_{T2} analytic solution from Lester and Barr [170]. Details regarding implementing M_{2C} and the relation of M_{2C} to M_{T2} and the approach of CCKP are in Sec. 6.2.

Errors in the determined masses propagated from the error in the mass difference in the limit of $k = 0$ are given by

$$\delta M_Y = \frac{\delta M_-}{2} \left(1 - \frac{M_+^2}{M_-^2} \right) \quad \delta M_N = -\frac{\delta M_-}{2} \left(1 + \frac{M_+^2}{M_-^2} \right) \quad (6.6)$$

where δM_- is the error in the determination of the mass difference M_- . To isolate this source of error from those introduced by low statistics, we assume we know the correct M_- , and we should consider the error described in Eq(6.6) as a separate uncertainty from that reported in our initial performance estimates in the Section 6.4.

Because the true p, q are in the domain over which we are minimizing, M_{2C} will always satisfy $M_{2C} \leq M_Y$. The equality is reached for events with either m_{12} or m_{34} smaller than M_- , with $p_z/p_o = \alpha_z/\alpha_o$, and $q_z/q_o = \beta_z/\beta_o$, and with the transverse components of α parallel to the transverse components of β . When $m_{12} = m_{34} = M_-$ the event only gives information about about the mass difference.

The events that approximately saturate the bound have the added benefit that they are approximately reconstructed (p and q are known). We present a proof of this in Appendix E. If

Y is produced near the end of a longer cascade decay, then this reconstruction would allow us to determine the masses of all the parent states in the event. The reconstruction of several such events may also aid in spin-correlation studies [141].

In order to determine the distribution of M_{2C} for the process shown in Fig 4.4, we computed it for a set of events generated using the theoretical cross section and assuming perfect detector resolution and no background. Figure 6.1 shows the resulting distribution for three cases: $M_Y = 200$ GeV, $M_Y = 150$ GeV and $M_Y = 100$ GeV each with $M_- = 50$ GeV. Each distribution was built from 30000 events. Note that the minimum M_Y for an event is M_- . The three examples each have endpoints that give the mass scale, and we are able to distinguish between different M_Y for a given M_- . The end-point for $M_Y = 100$ GeV is clear, and the endpoint for $M_Y = 150$ GeV and $M_Y = 200$ GeV becomes more difficult to observe. The shape of the distribution exhibits a surprising symmetry discussed in Sec 6.3.

We can also see that as M_+/M_- becomes large, the M_Y determination will be hindered by the small statistics available near the endpoint or backgrounds. To alleviate this, we should instead fit to the entire distribution. It is clear that events away from the endpoint also contain information about the masses. For this reason we propose to fit the entire distribution of M_{2C} and compare it to the ‘ideal’ distribution that corresponds to a given value of the masses. As we shall discuss this allows the determination of M_Y with a significant reduction in the number of events needed. This is the most important new aspect of the method proposed here.

6.2 Using M_{T2} to Find M_{2C} and the max M_{T2} Kink

The calculation of M_{2C} is greatly facilitated by understanding its relation to M_{T2} . The variable M_{T2} , which was introduced in by Lester and Summers [12], is equivalent to

$$M_{T2}^2(\chi) = \min_{p,q} (p + \alpha)^2 \tag{6.7}$$

subject to the 5 constraints

$$(p + \alpha)^2 = (q + \beta)^2, \tag{6.8}$$

$$p^2 = q^2 \tag{6.9}$$

$$\not{P}_T = (p + q)_T \tag{6.10}$$

$$p^2 = \chi^2. \tag{6.11}$$

As is suggested in the simplified example of [175], the minimization over the longitudinal frame of reference and center-of-mass energy is equivalent to assuming p and α have equal rapidity

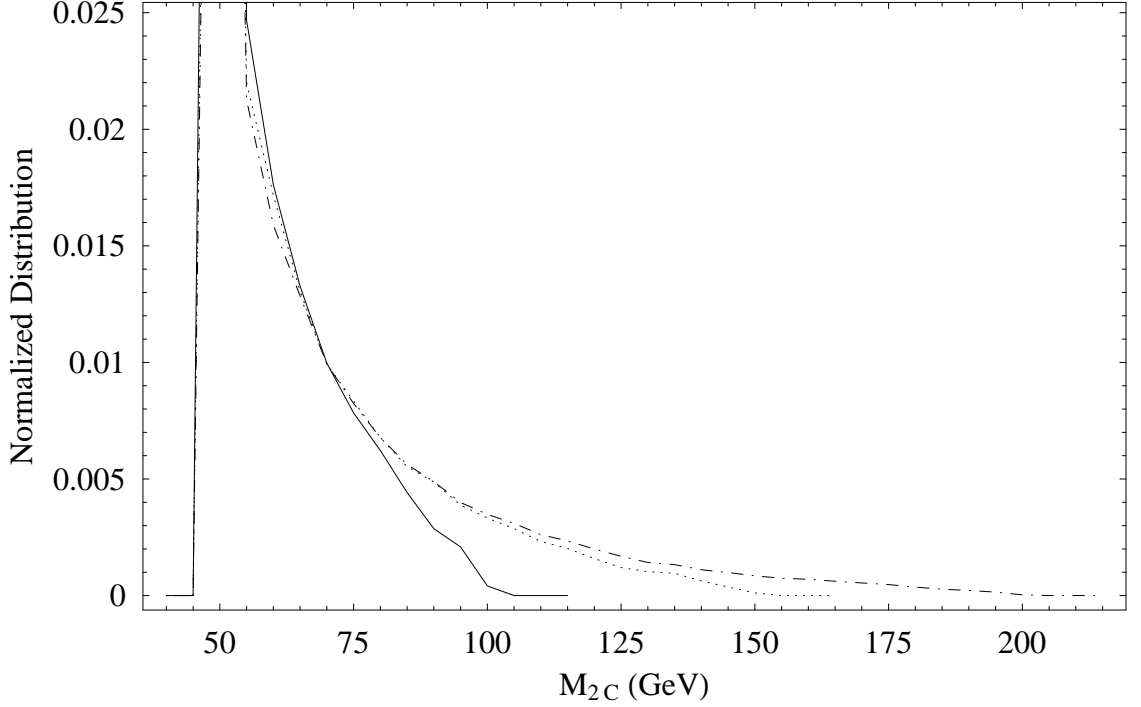


Figure 6.1: The distribution of 30000 events in 5 GeV bins with perfect resolution and no background. The three curves represent $M_Y = 200$ GeV (dot-dashed), $M_Y = 150$ GeV (dotted) and $M_Y = 100$ GeV (solid) each with $M_- = 50$ GeV. Each distribution cuts off at the correct M_Y .

and q and β have equal rapidity. Implementing this Eq(6.7) reduces to the traditional definition of the Cambridge transverse mass ².

By comparing $M_{T2}(\chi)$ as defined above to M_{2C} defined in Eq(6.1), we can see that they are very similar with the exception that the constraint Eq(6.5) is replaced by the constraint Eq(6.11). M_{2C} can be found by scanning $M_{T2}(\chi)$ for the χ value that such that the constraint in Eq(6.5) is also satisfied. At the value of χ that satisfies $M_{T2}(\chi) - \chi = M_-$, both Eq(6.5) and Eq(6.11) are satisfied.

We can see the M_{2C} and M_{T2} relationship visually. Each event provides a curve $M_{T2}(\chi)$; Fig 6.2 shows curves for four events with $M_N = 50$ GeV and $M_Y = 100$ GeV. For all events $M_{T2}(\chi)$ is a continuous function of χ . CCKP point that out that at $\chi > M_N$ and at $k = 0$ the *maximum* $M_{T2}(\chi)$ approaches $\chi + M_-$. At $\chi < M_N$ and at $k = 0$ the *maximum* $M_{T2}(\chi)$ approaches

$$\max M_{T2}(\chi) = k^* + \sqrt{(k^*)^2 + \chi^2} \quad (6.12)$$

where $k^* = (M_Y^2 - M_N^2)/2M_Y$ is the 2BEMP. This maximum occurs for events with $\alpha^2 = \beta^2 = 0$. Putting this together, if $M_{T2}(\chi = 0) > M_-$, as is true for two of the four events depicted in

²We have only tested and verified this equivalence numerically for events satisfying $M_{T2}(\chi = 0) > M_-$.

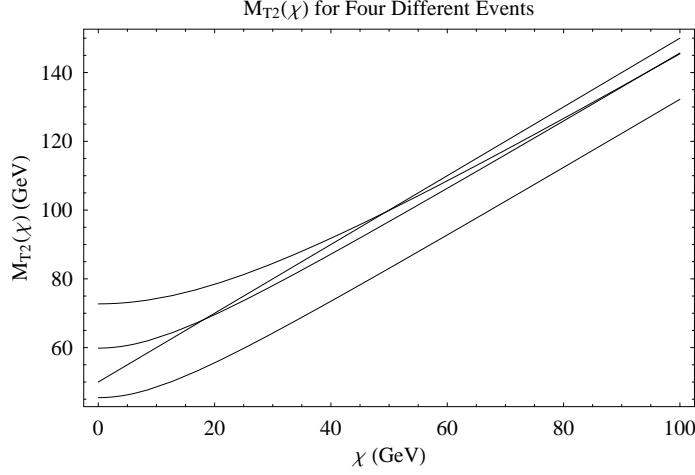


Figure 6.2: The $M_{T2}(\chi)$ curves for four events with $M_N = 50$ GeV and $M_Y = 100$ GeV. Only the events whose curves starts off at $M_{T2}(0) > M_-$ intersect the straight line given by $M_{T2}(\chi) - \chi = M_-$. The M_{T2} at the intersection is M_{2C} for that event.

Fig. 6.2, then because the event is bounded above by Eq(6.12) and is continuous, then it must cross $\chi + M_-$ at $\chi \leq M_N$. At this intersection there is a solution to $M_{T2}(\chi) = \chi + M_-$ where $M_{T2}(\chi) = \min M_Y|_{\text{Constraints}} \equiv M_{2C}$. Equivalently

$$M_{2C} = M_{T2} \text{ at } \chi \text{ where } M_{T2}(\chi) = \chi + M_- \text{ if } M_{T2}(\chi = 0) > M_- \quad (6.13)$$

$$= M_- \text{ otherwise.} \quad (6.14)$$

Assuming $k = 0$, the maximum χ of such an intersection occurs for $\chi = M_N$ which is why the endpoint of M_{2C} occurs at the correct M_Y and why this corresponds to the kink of CCKP. Because Barr and Lester have an analytic solution to M_{T2} in Ref. [170] in the case $k = 0$, this is computationally very efficient as a definition. We will study the intersection of these two curves when $k_T \neq 0$ in Chapter 7.

6.3 Symmetries and Dependencies of the M_{2C} Distribution

All transverse mass variables M_T and M_{T2} are invariant under longitudinal boosts. M_{T2} has an additional invariance. CCKP [171] prove that if $k_T = 0$ then M_{T2} is invariant under back to back boosts of the parent particle pair in the plane perpendicular to the beam direction. This means that for any event of the topology in Fig. 4.4 with $k_T = 0$ and barring spin correlation effects, the M_{T2} distribution will be the same for a fixed center-of-mass energy as it is for a mixed set of collision energies. We now verify this argument numerically.

In order to numerically determine the distribution of M_{2C} for the processes shown in Fig 4.4, it is necessary to generate a large sample of “ideal” events corresponding to the physical process

shown in the figure. We assume $k_T = 0$ where we expect the back-to-back boost invariance to lead to a symmetry of the distribution under changes in the \sqrt{s} of the collision. We assume each branch decays via an off-shell Z^o -boson as this is what could be calculated quickly and captures the essential elements to provide an initial estimate of our approach's utility.

Even under these assumptions without knowing about the invariance of M_{T2} under back-to-back boosts, we might expect that the shape of the distribution depends sensitively on the parton distribution and many aspects of the differential cross section and differential decay rates. This is not the case; in the case of direct pair production the shape of the distribution depends sensitively only on two properties:

(i) the shape of the m_{12} (or equivalently m_{34}) distributions. In the examples studied here for illustration, we calculate the m_{12} distribution assuming it is generated by a particular supersymmetric extension of the Standard Model, but in practice we should use the measured distribution which is accessible to accurate determination. The particular shape of m_{12} does not greatly affect the ability to determine the mass of N and Y so long as we can still find the endpoint to determine $M_Y - M_N$ and use the observed m_{ll} distribution to model the shape of the M_{2C} distribution.

(ii) the angular dependence of the N 's momenta in the rest frame of Y . In the preliminary analysis presented here we assume that in the rest frame of $\tilde{\chi}_2^o$, $\tilde{\chi}_1^o$'s momentum is distributed uniformly over the 4π steradian directions. While this assumption is not universally true it applies in many cases and hence is a good starting point for analyzing the efficacy of the method.

Under what conditions is the uniform distribution true? Note that the $\tilde{\chi}_2^o$'s spin is the only property of $\tilde{\chi}_2^o$ that can break the rotational symmetry of the decay products. For $\tilde{\chi}_2^o$'s spin to affect the angular distribution there must be a correlation of the spin with the momentum which requires a parity violating coupling. Consider first the Z^o contribution. Since we are integrating over the lepton momenta difference³, the parity violating term in the cross section coming from the lepton- Z^o vertex vanishes and a non-zero correlation requires that the parity violating coupling be associated with the neutralino vertex. The Z^o -boson neutralino vertex vanishes as the Z^o interaction is proportional to $\bar{\tilde{\chi}}_2^o \gamma^5 \gamma^\mu \tilde{\chi}_1^o Z_\mu^o$ or $\bar{\tilde{\chi}}_2^o \gamma^\mu \tilde{\chi}_1^o Z_\mu^o$ depending on the relative sign of $M_{\tilde{\chi}_2^o}$ and $M_{\tilde{\chi}_1^o}$ eigenvalues. However if the decay has a significant contribution from an intermediate slepton there are parity violating couplings and there will be spin correlations. In this case there will be angular correlations but it is straightforward to modify the method to take account of correlations⁴.

³ M_{2C} only depends on the sum of the two OSSF lepton momenta that follow from a decay of Y .

⁴Studying and exploiting the neutralino spin correlations is discussed further in Refs [180, 181, 182].

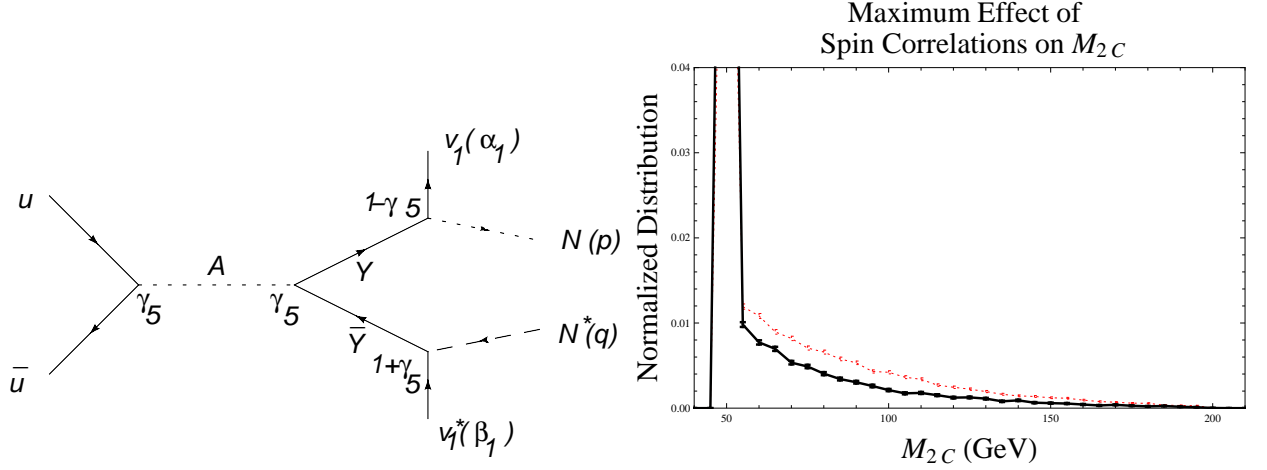


Figure 6.3: Effect of this maximally spin correlated process on the M_{2C} distribution. Modeled masses are $M_Y = 200$ GeV and $M_N = 150$ GeV. The solid black distribution is the uncorrelated case and red dotted distribution is maximally spin correlated.

How big an effect could spin correlations have on the shape of the M_{2C} distribution? To demonstrate, we modeled a maximally spin-correlated direct production process. Fig 6.3 show the spin-correlated process that we consider, and the M_{2C} distributions from this process compared to the M_{2C} distribution from the same topology and masses but without spin correlations. The modeled case has perfect energy resolution, $m_{v_1} = 0$ GeV, $M_Y = 200$ GeV, and $M_N = 150$ GeV. Our maximally spin-correlated process involves pair production of Y through a pseudoscalar A . The fermion Y in both branches decays to a complex scalar N and visible fermion v_1 through a purely chiral interaction. The production of the pseudoscalar ensures that the Y and \bar{Y} are in a configuration $\sqrt{2}^{-1}(|\uparrow\downarrow\rangle + |\downarrow\uparrow\rangle)$. The Y then decays with N preferentially aligned with the spin. The \bar{Y} decays with N^* preferentially aligned against the spin. This causes the two sources of missing transverse momentum to be preferentially parallel and pushes M_{2C} closer to the endpoint. For this reason the spin-correlated distribution (red dotted distribution) is above the uncorrelated distribution (solid thick distribution) in Fig. 6.3. For the remainder of the chapter we assume no such spin correlations are present as is true for neutralino pair production and decay to leptons through a Z^0 boson.

How likely will we have no spin correlations in supersymmetric LHC events? We showed earlier that Z^0 -boson dominated three-body decays lack spin correlations. Even in the case that the slepton contribution is significant the correlations may still be largely absent. Because we are worried about a distribution, the spin correlation is only of concern to our assumption if a mechanism aligns the spin's of the $\tilde{\chi}_2^0$ s in the two branches. Table 6.2 shows that most of the $\tilde{\chi}_2^0$ s that we expect follow from decay chains involving a squark, which being a scalar should

make uncorrelated the spin of the $\tilde{\chi}_2^o$ in the two branches. We would then average over the spin states of $\tilde{\chi}_2^o$ and recover the uniform angular distribution of $\tilde{\chi}_1^o$'s momentum in $\tilde{\chi}_2^o$'s rest frame.

Once we have fixed the dependencies (i) and (ii) above, the shape of the distribution is essentially independent of the remaining parameters. We calculate the “ideal” distributions for M_{2C} assuming that $k = 0$ and that in the rest frame of Y there is an equal likelihood of N going in any of the 4π steradian directions. The observable invariant α^2 is determined according to the differential decay probability of χ_2^o to $e^+ e^-$ and χ_1^o through a Z^o -boson mediated three-body decay. Analytic expressions for cross sections were obtained from the Mathematica output options in CompHEP [145] To illustrate the symmetry with respect to changes in \sqrt{s} and the angle of Y 's production, we show in Fig 6.4 two cases:

(1) The case that the collision energy and frame of reference and angle of the produced Y with respect to the beam axis are distributed according to the calculated cross section for the process considered in Section 6.4 in which $\tilde{\chi}_2^o$ decays via Z^o exchange to the three-body state $l^+ + l^- + \tilde{\chi}_1^o$, convoluted with realistic parton distribution functions.

(2) The case that the angle of the produced Y with respect to the beam axis is arbitrarily fixed at $\theta = 0.2$ radians, the azimuthal angle ϕ fixed at 0 radians, and the center-of-mass energy set to $\sqrt{s} = 500$ GeV.

The left plot of Fig 6.4 shows the two distributions intentionally shifted by 0.001 to allow us to barely distinguish the two curves. On the right side of Fig 6.4 we show the difference of the two distributions with the 2σ error bars within which we expect 95% of the bins to overlap 0 if the distributions are identical.

Analytically, this symmetry is because both the M_{T2} and M_{2C} are invariant under back to back boosts when $k_T = 0$. This symmetry implies that the distributions (1) and (2) above should be the same which has been verified numerically in Fig 6.4. In this way we have identified both the mathematical origin of the symmetry and numerically verified the symmetry. Thus the M_{2C} distribution has a symmetry with respect to changes in \sqrt{s} when $k_T = 0$.

In addition to tests with $k_T = 0$, we also tested that $k \lesssim 20$ GeV does not change the shape of the distribution to within our numerical uncertainties. We constructed events with $M_Y = 150$ GeV, $M_N = 100$ GeV, $\sqrt{k^2}$ uniformly distributed between 2 and 20 GeV, $\vec{k}/k_o = 0.98$, and with uniform angular distribution. We found the M_{2C} distribution agreed with the distribution shown in Fig. 6.4 within the expected error bars after 10000 events. Scaling this down to the masses studied in model $P1$ we trust these results remain unaffected for $k_T \lesssim 20$ GeV. Introduction of

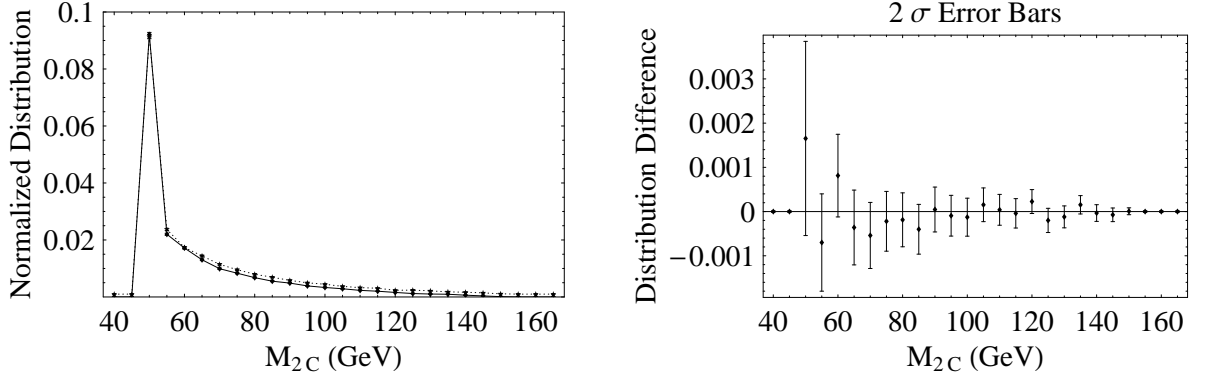


Figure 6.4: Demonstrates the distribution is independent of the COM energy, angle with which the pair is produced with respect to the beam axis, and the frame of reference.

cuts on missing transverse energy and very large UTM ($k_T \gtrsim M_-$) changes the shape of the distribution. These effects will be studied in Chapter 7.

Inclusion of backgrounds also changes the shape. Backgrounds that we can anticipate or measure, like di- τ s or leptons from other neutralino decays observed with different edges can be modeled and included in the ideal shapes used to perform the mass parameter estimation. A more complete study of the background effects also follows in Chapter 7.

6.4 Application of the method: SUSY model examples

To illustrate the power of fitting the full M_{2C} distribution, we now turn to an initial estimate of our ability to measure M_Y in a few specific supersymmetry scenarios. Our purpose here is to show that fitting the M_{2C} distribution can determine M_Y and M_N with very few events. We include detector resolution effects and assume $k = 0$ (equivalent to assuming direct production), but neglect backgrounds until Chapter 7. We calculate M_{2C} for the case where the analytic M_{T2} solution of Barr and Lester can be used to speed up the calculations as described in Sec 6.2. We make the same modeling assumptions described in Sec. 6.3.

Although fitting the M_{2C} distribution could equally well be applied to the gluino mass studied in CCKP, we explore its applications to pair-produced $\tilde{\chi}_2^0$. We select SUSY models where $\tilde{\chi}_2^0$ decays via a three-body decay to $l^+ + l^- + \tilde{\chi}_1^0$. The four momenta $\alpha = p_{l^+} + p_{l^-}$ for the leptons in the top branch, and the four momenta $\beta = p_{l^+} + p_{l^-}$ for the leptons in the bottom branch.

The production and decay cross section estimates in this section are calculated using MadGraph/MadEvent [144] and using SUSY mass spectra inputs from SuSpect [183]. We simulate the typical LHC detector lepton energy resolution [9, 184] by scaling the α and β four vectors

by a scalar normally distributed about 1 with the width of

$$\frac{\delta\alpha_0}{\alpha_0} = \frac{0.1}{\sqrt{\alpha_o(\text{GeV})}} + \frac{0.003}{\alpha_o(\text{GeV})} + 0.007. \quad (6.15)$$

The missing transverse momentum is assumed to be whatever is missing to conserve the transverse momentum after the smearing of the leptons momenta. We do not account for the greater uncertainty in missing momentum from hadrons or from muons which do not deposit all their energy in the calorimeter and whose energy resolution is therefore correlated to the missing momentum. Including such effects is considered in Chapter 7. These finite resolution effects are simulated in both the determination of the ideal distribution and in the small sample of events that is fit to the ideal distribution to determine M_Y and M_N . We do not expect expanded energy resolutions to greatly affect the results because the resolution effects are included in both the simulated events and in the creation of the ideal curves which are then fit to the low statistics events to estimate the mass.

We consider models where the three-body decay channel for $\tilde{\chi}_2^0$ will dominate. These models must satisfy $M_{\tilde{\chi}_2^0} - M_{\tilde{\chi}_1^0} < M_Z$ and must have all slepton masses greater than the $M_{\tilde{\chi}_2^0}$. The models considered are shown in Table 6.1. The Min-Content model assumes that there are no other SUSY particles accessible at the LHC other than $\tilde{\chi}_2^0$ and $\tilde{\chi}_1^0$ and we place $M_{\tilde{\chi}_1^0}$ and $M_{\tilde{\chi}_2^0}$ at the boundary of the PDG Live exclusion limit [41]. SPS 6, P1, and γ are models taken from references [3], [2], and [185] respectively. Each has the $\tilde{\chi}_2^0$ decay channel to leptons via a three-body decay kinematically accessible. We will only show simulation results for the masses in model P1 and SPS 6 because they have the extreme values of M_+/M_- with which the performance scales. The Min-Content model and the γ model are included to demonstrate the range of the masses and production cross sections that one might expect.

Bisset, Kersting, Li, Moortgat, Moretti, and Xie (BKLMMX) [186] have studied the four lepton with missing transverse momentum Standard-Model background for the LHC. They included contributions from jets misidentified as leptons and estimated about 190 background events at a $\mathcal{L} = 300 \text{ fb}^{-1}$ which is equivalent to 0.6 fb. Their background study made no reference to the invariant mass squared of the four leptons, so we only expect a fraction of these to have both lepton pairs to have invariant masses less than M_- . Their analysis shows the largest source of backgrounds will most likely be other supersymmetric states decaying to four leptons. Again, we expect only a fraction of these to have both lepton pairs with invariant masses within the range of interest. The background study of BKLMMX is consistent with a study geared towards a 500 GeV $e^+ e^-$ linear collider in Ref. [187] which predicts 0.4 fb for the standard model

Model	Min Content (ref [41])	SPS 6 (ref [3])	P1 (ref [2])	γ (Ref. [185])
Definition	$\tilde{\chi}_1^o$ and $\tilde{\chi}_2^o$ are the only LHC accessible SUSY States with smallest allowed masses.	Non Universal Gaugino Masses $m_o = 150$ GeV $m_{1/2} = 300$ GeV $\tan\beta = 10$ $\text{sign}(\mu) = +$ $A_o = 0$ $M_1 = 480$ GeV $M_2 = M_3 = 300$ GeV	mSUGRA $m_o = 350$ GeV $m_{1/2} = 180$ GeV $\tan\beta = 20$ $\text{sign}(\mu) = +$ $A_o = 0$	Non-Universal Higgs Model $m_o = 330$ GeV $m_{1/2} = 240$ GeV $\tan\beta = 20$ $\text{sign}(\mu) = +$ $A_o = 0$ $H_u^2 = -(242 \text{ GeV})^2$ $H_d^2 = +(373 \text{ GeV})^2$
$M_{\tilde{\chi}_1^o}$	46 GeV	189 GeV	69 GeV	95 GeV
$M_{\tilde{\chi}_2^o}$	62.4 GeV	219 GeV	133 GeV	178 GeV
M_+/M_-	6.6	13.6	3.2	3.3

Table 6.1: Models with $\tilde{\chi}_2^o$ decaying via a three-body decay to leptons. We only show simulation results for the masses in model P1 and SPS 6 because they have the extreme values of M_+/M_- with which the performance scales.

Model	$\sigma_{\tilde{\chi}_2^o \tilde{\chi}_2^o}$ Direct $\sigma_{\tilde{\chi}_2^o \tilde{\chi}_2^o}$ Via \tilde{g} or \tilde{q}	$\text{BR}_{\tilde{\chi}_2^o \rightarrow l + \bar{l} + \tilde{\chi}_1^o}$ $\text{BR}_{\tilde{\chi}_2^o \rightarrow q + \bar{q} + \tilde{\chi}_1^o}$	Events with 4 leptons + E_T missing + possible extra jets $\mathcal{L} = 300 \text{ fb}^{-1}$
Min Content	2130 fb N/A	0.067 0.69	2893
SPS 6	9.3 fb 626 fb	0.18 0.05	6366
P1	35 fb 12343 fb	0.025 0.66	2310
γ	17 fb 4141 fb	0.043 0.64	2347

Table 6.2: The approximate breakdown of signal events.

contribution to 4 leptons and missing transverse momentum. The neutralino decay to τ leptons also provide a background because the τ decay to a light leptons $l = e, \mu$ ($\Gamma_{\tau \rightarrow l \bar{\nu}_l} / \Gamma \approx 0.34$) cannot be distinguished from prompt leptons. The neutrinos associated with these light leptons will be new sources of missing transverse momentum and will therefore be a background to our analysis. The di- τ events will only form a background when both opposite sign same flavor $\tau\tau$ decay to the same flavor of light lepton which one expects about 6% of the time.

Table 6.2 breaks down the LHC production cross section for pair producing two $\tilde{\chi}_2^o$ in each of these models. In the branching ratio to leptons, we only consider e and μ states as the τ will decay into a jet and a neutrino introducing more missing transverse momentum. Direct pair production of $\tilde{\chi}_2^o$ has a rather modest cross section, but production via a gluino or squark has a considerably larger cross section but will be accompanied by additional QCD jets. We do expect to be able to distinguish QCD jets from τ jets [188]. The events with gluinos and jets will lead to considerable k_T . In this chapter we assume $k_T \lesssim 20$ GeV, but we take up the case of large k_T in the following chapter.

We now estimate how well we may be able to measure $M_{\tilde{\chi}_1^o}$ and $M_{\tilde{\chi}_2^o}$ in these models under these simplifying ideal assumptions. Figures 6.5 and 6.6 show a χ^2 fit⁵ of the M_{2C} distribution

⁵See Appendix D for details of how χ^2 is calculated.

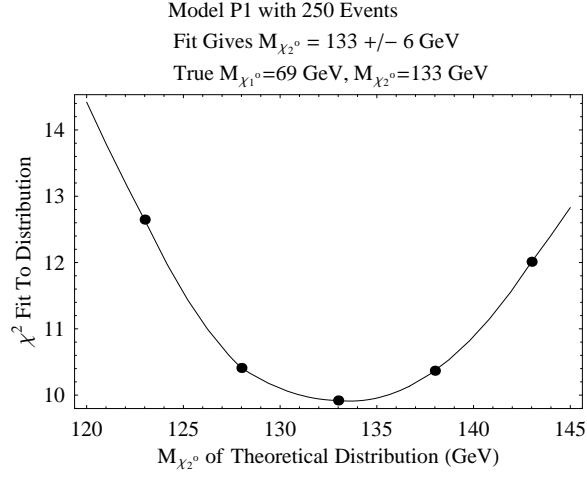


Figure 6.5: χ^2 fit of 250 events from model P1 of Ref [2] to the theoretical distributions calculated for different $M_{\chi_2^0}$ values but fixed $M_{\chi_2^0} - M_{\chi_1^0}$. The fit gives $M_{\chi_2^0} = 133 \pm 6$ GeV.

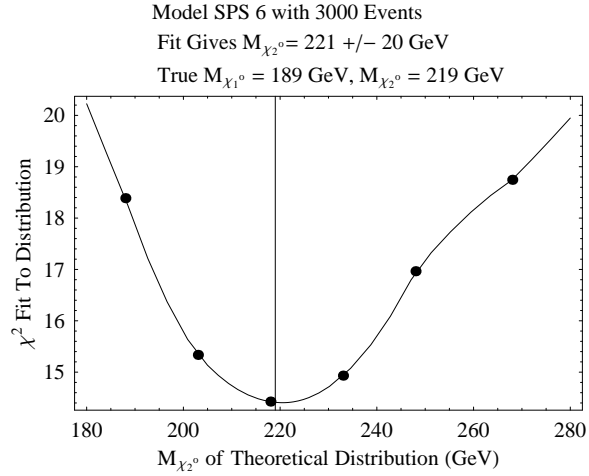


Figure 6.6: χ^2 fit of 3000 events from model SPS 6 of Ref [3] to the theoretical distributions calculated for different $M_{\chi_2^0}$ values but fixed $M_{\chi_2^0} - M_{\chi_1^0}$. The fit gives $M_{\chi_2^0} = 221 \pm 20$ GeV.

from the observed small set of events to ‘ideal’ theoretical M_{2C} distributions parameterized by $M_{\tilde{\chi}_2^0}$. The ‘ideal’ theoretical distributions are calculated for the observed value of M_- using different choices for $M_{\tilde{\chi}_2^0}$. A second-order interpolation is then fit to these points to estimate the value for $M_{\tilde{\chi}_2^0}$. The 1σ uncertainty for $M_{\tilde{\chi}_2^0}$ is taken to be the points where the χ^2 increases from its minimum by one.

The difficulty of the mass determination from the distribution grows with the ratio M_+/M_- . Figures 6.5 and 6.6 show the two extremes among the cases we consider. For the model P1 $M_+/M_- = 3.2$, and for model γ $M_+/M_- = 3.3$. Therefore these two models can have the mass of $M_{\tilde{\chi}_2^0}$ and $M_{\tilde{\chi}_1^0}$ determined with approximately equal accuracy with equal number of signal events. Figure 6.5 shows that we may be able to achieve ± 6 GeV resolution after about 30 fb^{-1} . Model SPS 6 shown in Fig 6.6 represents a much harder case because $M_+/M_- = 13.6$. In this scenario we can only achieve ± 20 GeV resolution with 3000 events corresponding to approximately 150 fb^{-1} . In addition to these uncertainties, we need to also consider the error propagated from δM_- in Eq(6.6).

Chapter Summary

We have proposed a method to extract the masses of new pair-produced states based on a kinematic variable, M_{2C} , which incorporates all the known kinematic constraints on the observed process and whose endpoint determines the new particle masses. However the method does not rely solely on the endpoint but uses the full data set, comparing the observed distribution for M_{2C} with the ideal distribution that corresponds to a given mass. As a result the number of events needed to determine the masses is very significantly reduced so that the method may be employed at the LHC event for processes with electroweak production cross sections.

This chapter is an initial feasibility study of the method for several supersymmetric models. We have made many idealized assumptions which amount to conditions present if the new particle states are directly produced. We have included the effect of detector resolution but not backgrounds, or cuts. Our modeling assumed that $k = 0$. We demonstrated that for some of the models studied we are able to determine the masses to within 6 GeV from only 250 events. This efficiency is encouraging, a study including more of the real-world complications follows in Chapter 7.

The constrained mass variables we advocate here can be readily extended to other processes. By incorporating all the known kinematical constraints, the information away from kinematical end-points can, with some mild process-dependent information, be used to reduce the number

of events needed to get mass measurements. We shall illustrate an extension to three on-shell states in Chapter 8.

Chapter 7

The Variable M_{2C} : Significant Upstream Transverse Momentum

Chapter Overview

In the previous chapter, we introduced the M_{2C} kinematic variable which gives an event-by-event lower bound on the dark-matter particle's absolute mass given the mass difference between the dark matter candidate and its parent. The previous chapter focused on direct pair production with minimal initial state radiation (ISR). In this chapter, we introduce a complementary variable $M_{2C,UB}$ which gives an event-by-event *upper* bound on the same absolute mass. The complementary variable is only relevant in the presence of large upstream transverse momentum (UTM). Our study shows that the technique presented is as good if not better than other model-independent invisible-particle mass determination techniques in precision and accuracy.

In this chapter, which is based on work first published by Barr, Ross, and the author in Ref [16], we demonstrate the use of the variable M_{2C} and $M_{2C,UB}$ in LHC conditions. The variables $M_{2C}(M_-)$ and $M_{2C,UB}(M_-)$ give an event-by-event lower-bound and upper-bound respectively on the mass of Y assuming the topology in Fig. 4.4 and the mass difference $M_- = M_Y - M_N$. To get the mass difference, we use events where Y decays into N and two visible states via a three-body decay in which we can easily determine the mass difference from the end point of the visible-states invariant-mass distribution, m_{12}^2 . One might also conceive of a situation with M_{2C} supplementing an alternative technique that gives a tight constraint on the mass difference but may have multiple solutions or a weaker constraint on the mass scale [157][14]. Given this mass difference and enough statistics, M_{2C} 's endpoint gives the mass of Y . However the main advantage of the M_{2C} method is that it does not rely simply on the position at the endpoint but it uses the additional information contained in events which lie far from the endpoint. As a result it gives a mass determination using significantly fewer events and is less

sensitive to energy resolution and other errors.

To illustrate the method, in this chapter we study in detail the performance of the M_{2C} constrained mass variable in a specific supersymmetric model. We study events where each of the two branches have decay chains that end with a $\tilde{\chi}_2^0$ decaying to a $\tilde{\chi}_1^0$ and a pair of opposite-sign same-flavor (OSSF) leptons. Thus the final states of interest contain four isolated leptons (made up of two OSSF pairs) and missing transverse momentum. Fig 4.4 defines the four momentum of the particle states with $Y = \tilde{\chi}_2^0$, $N = \tilde{\chi}_1^0$, and the OSSF pairs forming the visible particles 1–4. Any decay products early in the decay chains of either branch are grouped into k which we generically refer to as upstream transverse momentum (UTM). Nonzero k could be the result of initial state radiation (ISR) or decays of heavier particles further up the decay chain. Events with four leptons and missing transverse momentum have a very small Standard-Model background. To give a detailed illustration of the M_{2C} methods, we have chosen to analyze the benchmark point P1 from [2] which corresponds to mSUGRA with $m_o = 350$ GeV, $m_{1/2} = 180$ GeV, $\tan\beta = 20$, $\text{sign}(\mu) = +$, $A_o = 0$. Our SUSY particle spectrum was calculated with ISAJET [189] version 7.63. We stress that the analysis technique employed applies generically to models involving decays to a massive particle state that leaves the detector unnoticed.

A powerful feature of the M_{2C} distribution is that, with some mild assumptions, the shape away from the endpoint can be entirely determined from the unknown mass scale and quantities that are measured. The ideal shape fit against early data therefore provides an early mass estimate for the invisible particle. This study is meant to be a guide on how to overcome difficulties in establishing and fitting the shape: difficulties from combinatoric issues, from differing energy resolutions for the leptons, hadrons, and missing transverse momentum, from backgrounds, and from large upstream transverse momentum (UTM) ¹. As we shall discuss, UTM actually provides surprising benefits.

The chapter is structured as follows: In Section 7.1, we review M_{2C} and introduce the new observation that, in addition to an event-by-event lower bound on M_Y , large recoil against UTM enables one also to obtain an event-by-event *upper* bound on M_Y . We call this quantity $M_{2C,UB}$. Section 7.2 describes the modeling and simulation employed. Section 7.3 discusses the implications of several effects on the shape of the distribution including the m_{12} (in our case m_{ll}) distribution, the UTM distribution, the backgrounds, combinatorics, energy resolution, and missing transverse momentum cuts. In Section 7.4, we put these factors together and

¹Our references to UTM correspond to the Significant Transverse Momentum (SPT), pair production category in [176] where SPT indicates that the relevant pair of parent particles can be seen as recoiling against a significant transverse momentum.

estimate the performance. We conclude in Section 7.4 with a discussion about the performance in comparison to previous work.

7.1 Upper Bounds on M_Y from Recoil against UTM

We will now review the definition of M_{2C} as providing an event-by-event lower bound on M_Y . In generalizing this framework, we find a new result that one can also obtain an upper bound on the mass M_Y when the two parent particles Y recoil against some large upstream transverse momentum k_T .

7.1.1 Review of the Lower Bound on M_Y

Fig 4.4 gives the relevant topology and the momentum assignments. The visible particles 1 and 2 and invisible particle N are labeled with momentum α_1 and α_2 (which we group into $\alpha = \alpha_1 + \alpha_2$) and p , respectively $\beta = \beta_1 + \beta_2$ and q in the other branch. We assume that the parent particle Y is the same in both branches so $(p + \alpha)^2 = (q + \beta)^2$. Any earlier decay products of either branch are grouped into the upstream transverse momentum (UTM) 4-vector momentum, k .

In the previous chapter we showed how to find an event-by-event lower bound on the true mass of M_N and M_Y . We assume that the mass difference $M_- = M_Y - M_N$ can be accurately measured from the invariant mass edges $\max m_{12}$ or $\max m_{34}$. For each event, the variable M_{2C} is the minimum value of the mass of Y (the second lightest state) after minimizing over the unknown division of the missing transverse momentum \vec{p}_T between the two dark-matter particles N as described in Eq(6.1-6.5).

One way of calculating M_{2C} for an event is to use $M_{T2}(\chi_N)$ [12, 13, 15], which provides a lower bound on the mass of Y for an assumed mass χ_N of N . The true mass of Y lies along the line $\chi_Y(\chi_N) = M_- + \chi_N$ where we use χ_Y to denote the possible masses of Y and to distinguish it from the true mass of Y denoted with M_Y . In other words M_{T2} provides the constraint $\chi_Y(\chi_N) \geq M_{T2}(\chi_N)$. Thus we can see that for χ_N to be compatible with an event, we must have $M_{T2}(\chi_N) \leq \chi_Y(\chi_N) = \chi_N + M_-$.

For a given event, if one assumes a mass χ_N for N , and if the inequality $M_{T2}(\chi_N) \leq \chi_N + M_-$ is satisfied, then there is no contradiction, and the event is compatible with this value of χ_N . If however, $M_{T2}(\chi_N) > M_- + \chi_N$, then we have a contradiction, and the event excludes this value χ_N as a viable mass of N . Using this observation, M_{2C} can be found for each event by seeking

the intersection between $M_{T2}(\chi_N)$ and $\chi_N + M_-$ [15]. Equivalently, the lower bound on M_Y is given by $M_Y \geq M_- + \chi_N^o$ where χ_N^o is the zero of

$$g(\chi_N) = M_{T2}(\chi_N) - \chi_N - M_-$$

$$\text{with } g'(\chi_N^o) < 0. \quad (7.1)$$

In the case $k = 0$, the extreme events analyzed in CCKP [174] demonstrate that $g(\chi)$ will only have one positive zero or no positive zeros, and the slope at a zero will always be negative. For no positive zeros, the lower bound is the trivial lower bound given by M_- . Note that a lower bound on the value of M_Y corresponds to a lower bound on the value of M_N . The Appendix in Ref. [15] shows that at the zeros of $g(\chi_N)$ which satisfy Eq(7.1), the momenta satisfy Eqns(6.2-6.5).

7.1.2 A New Upper Bound on M_Y

If there is large upstream transverse momentum (UTM) ($k_T \gtrsim M_-$) against which the system recoils, then we find a new result. Using the M_{T2} method to calculate M_{2C} gives one the immediate ability to see that M_Y can also have an upper bound when requiring Eqns(6.2-6.5). This follows because for large UTM the function $g(\chi_N)$ may have two zeros² which provides both an upper and a lower bound for M_Y from a single event. We have also found regions of parameter space where $g(\chi)$ has a single zero but $g'(\chi_N^o) > 0$ corresponding to an upper bound on the true mass of M_N (and M_Y) and only the trivial lower bound of $M_N \geq 0$.

We can obtain some insight into the cases in which events with large UTM provides upper bounds on the mass by studying a class of extreme event with two hard jets, j_α and j_β against which Y recoils ($k = j_\alpha + j_\beta$). We will describe this extreme event and solve for the regions of parameter space for which one can analytically see the intersection points giving a lower bound and/or an upper bound. The event is extremal in that $M_{T2}(\chi_N)$, which gives a lower bound on M_Y , actually gives the true value of M_Y when one selects χ_N equal to the true mass M_N .

The ideal event we consider is where a heavier state G is pair-produced on shell at threshold. For simplicity we assume the lab-frame is the collision frame. Assume that the G s, initially at rest, decay into visible massless jets j_α, j_β and the two Y states with the decay product momenta $\alpha + p$ and $\beta + q$. Both jets have their momenta in the same transverse plane along the negative \hat{x} -axis, and both Y 's momentum are directed along the \hat{x} -axis. Finally, in the rest frame of the two Y s, both decay such that the decay products visible states have their momentum α and β

²There may be regions in parameter space where function $g(\chi)$ has more than two zeros, but we have not encountered such cases in our simulations.

along the \hat{x} -axis and both invisible massive states N have their two momenta along the negative \hat{x} -axis. In the lab frame, the four-vectors are given by

$$j_\alpha = j_\beta = \frac{M_G}{2} \left(1 - \frac{M_Y^2}{M_G^2} \right) \{1, -1, 0, 0\} \quad (7.2)$$

$$\alpha = \beta = \frac{M_G}{2} \left(1 - \frac{M_N^2}{M_Y^2} \right) \{1, 1, 0, 0\} \quad (7.3)$$

$$p = q = \frac{M_G}{2} \left\{ \left(\frac{M_N^2}{M_Y^2} + \frac{M_Y^2}{M_G^2} \right), \left(\frac{M_N^2}{M_Y^2} - \frac{M_Y^2}{M_G^2} \right), 0, 0 \right\}. \quad (7.4)$$

For the event given by Eqns(7.2-7.4), we can exactly calculate $M_{T2}(\chi_N)$:

$$\begin{aligned} M_{T2}^2(\chi_N) = & \chi_N^2 + \frac{(M_N^2 - M_Y^2)(M_N^2 M_G^2 - M_Y^4)}{2 M_Y^4} \\ & + \frac{(M_Y^2 - M_N^2) \sqrt{4 M_G^2 \chi_N^2 M_Y^4 + (M_Y^4 - M_N^2 M_G^2)^2}}{2 M_Y^4}. \end{aligned} \quad (7.5)$$

This is found by calculating the transverse mass for each branch while assuming χ_N to be the mass of N . The value of p_x is chosen so that the transverse masses of the two branches are equal. Substituting this value back into the transverse mass of either branch gives $M_{T2}(\chi_N)$.

Fig 7.1 shows $g(\chi_N)$, given in Eq(7.1), for several choices of M_G for the process described by Eqns(7.2-7.4) with $M_- = 53$ GeV and $M_N = 67.4$ GeV. Because G is the parent of Y , we must have $M_G > M_Y$. If $M_Y < M_G < 2M_Y^2/(M_N + M_Y)$, then $M_{T2}(\chi_N < M_N)$ is larger than $\chi_N + M_-$ up until their point of intersection at $\chi_N = M_N$. In this case their point of intersection provides a lower bound as illustrated by the dotted line in Fig. 7.1 for the case with $M_G = 150$ GeV. For $2M_Y^2/(M_N + M_Y) < M_G < \sqrt{M_Y^3/M_N}$ there are two solutions

$$\chi_{N,\text{Min}} = M_N \quad (7.6)$$

$$\chi_{N,\text{Max}} = \frac{(M_N - M_Y)(-2M_Y^4 + M_N M_G^2 M_Y + M_N^2 M_G^2)}{(M_N M_G + (M_G - 2M_Y)M_Y)(M_N M_G + M_Y(M_G + 2M_Y))}. \quad (7.7)$$

When $M_G = \sqrt{M_Y^3/M_N}$, the function $g(\chi_N)$ has only one zero with the lower bound equalling the upper bound at M_N . The solid line in Fig. 7.1 shows this case. Between $\sqrt{M_Y^3/M_N} < M_G < \sqrt{6}M_Y^2/\sqrt{(M_N + M_Y)(2M_N + M_Y)}$ we again have two solutions but this time with

$$\chi_{N,\text{Min}} = \frac{(M_N - M_Y)(-2M_Y^4 + M_N M_G^2 M_Y + M_N^2 M_G^2)}{(M_N M_G + (M_G - 2M_Y)M_Y)(M_N M_G + M_Y(M_G + 2M_Y))} \quad (7.8)$$

$$\chi_{N,\text{Max}} = M_N. \quad (7.9)$$

The dashed line in Fig. 7.1 shows this case with $M_G = 170$ GeV. For M_G greater than this, we have $\chi_{N,\text{Max}} = M_N$ and $\chi_{N,\text{Min}} = 0$.

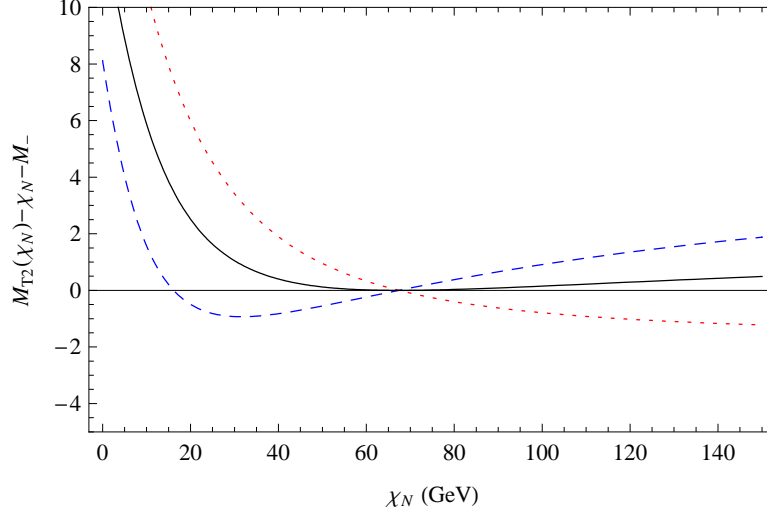


Figure 7.1: Shows $g(\chi_N)$ for the extreme event in Eq(7.2-7.4) with $M_- = 53$ GeV and $M_N = 67.4$ GeV. The red dotted line has $M_G = 150$ GeV and shows an event providing a lower bound on M_Y . The blue dashed line $M_G = 170$ GeV and shows an event with both a lower bound and an upper-bound on M_Y . The black solid line shows $M_G = \sqrt{M_Y^3/M_N}$ where the lower bound equals the upper bound.

This example illustrates how M_{2C} can provide both a lower-bound and an upper-bound on the true mass for those events with large UTM. The upper-bound distribution provides extra information that can also be used to improve early mass determination, and in what follows we will refer to the upper bound as $M_{2C,UB}$. We now move on to discuss modeling and simulation of this new observation.

7.2 Modeling and Simulation

As a specific example of the application of the M_{2C} method, we have chosen a supersymmetry model mSUGRA, $m_o = 350$ GeV, $m_{1/2} = 180$ GeV, $\tan \beta = 20$, $\text{sign}(\mu) = +$, $A_o = 0$ ³. The spectrum used in the simulation has $M_{\tilde{\chi}_1^0} = 67.4$ GeV and $M_{\tilde{\chi}_2^0} = 120.0$ GeV. We have employed two simulation packages. One is a Mathematica code that creates the ‘ideal’ distributions based only on very simple assumptions and input data. The second is HERWIG [17, 18, 19] which simulates events based on a SUSY spectrum, MSSM cross sections, decay chains, and appropriate parton distribution functions. If the simple Mathematica simulator predicts ‘ideal’ shapes that agree with HERWIG generator, then we have reason to believe that all the relevant factors relating to the shape are identified in the simple Mathematica simulation. This is an important check in validating the benefits of fitting the M_{2C} and $M_{2C,UB}$ distribution shape as a method to measure the mass of new invisible particles produced at hadron colliders.

³ This was model P1 from [2] which we also used in [15].

7.2.1 Generation of “Ideal” Distributions

Our ‘ideal’ distributions are produced from a home-grown Monte Carlo event generator written in Mathematica. This generator serves to ensure that we understand the origin of the distribution shape. It also ensures that we have control over measuring the parameters needed to determine the mass without knowing the full model, coupling coefficients, or parton distribution functions. We also use this simulation to determine on what properties the ideal distributions depends.

The simulator is used to create events satisfying the topology shown in Fig 4.4 for a set of specified masses. We take as given the previously measured mass difference $M_{\tilde{\chi}_2^0} - M_{\tilde{\chi}_1^0} = 52.6$ GeV, which we use in this chapter’s simulations. We neglect finite widths of the particle states as most are in the sub GeV range for the model we are considering. We neglect spin correlations between the two branches. We perform the simulations in the center-of-mass frame because M_{2C} and $M_{2C,UB}$ are transverse observables and are invariant under longitudinal boosts. The collision energy \sqrt{s} is distributed according to normalized distribution

$$\rho(\sqrt{s}) = 12 M_{\tilde{\chi}_2^0}^2 \frac{\sqrt{s - 4 M_{\tilde{\chi}_2^0}^2}}{s^2} \quad (7.10)$$

unless otherwise specified. The $\tilde{\chi}_2^0$ is produced with a uniform angular distribution, and all subsequent decays have uniform angular distribution in the rest frame of the parent. The UTM is simulated by making k_T equal to the UTM with $k^2 = (100 \text{ GeV})^2$ (unless otherwise specified), and boosting the other four-vectors of the event such that the total transverse momentum is zero. As we will show, these simple assumptions capture the important elements of the process. Being relatively model independent, they provide a means of determining the mass for various production mechanisms. If one were to assume detailed knowledge of the production process, it would be possible to obtain a better mass determination by using a more complete simulation like **HERWIG** to provide the ‘ideal’ distributions against which one compares with the data. Here we concentrate on the more model independent simulation to demonstrate that it predicts the M_{2C} and $M_{2C,UB}$ distributions well-enough to perform the mass determination that we demonstrate in this case-study.

7.2.2 HERWIG “Data”

In order to obtain a more realistic estimate of the problems associated with collision data, we generate samples of unweighted inclusive supersymmetric particle pair production, using the **HERWIG** Monte Carlo program with LHC beam conditions. These samples produce a more realistic simulation of the event structure that would be obtained for the supersymmetric model

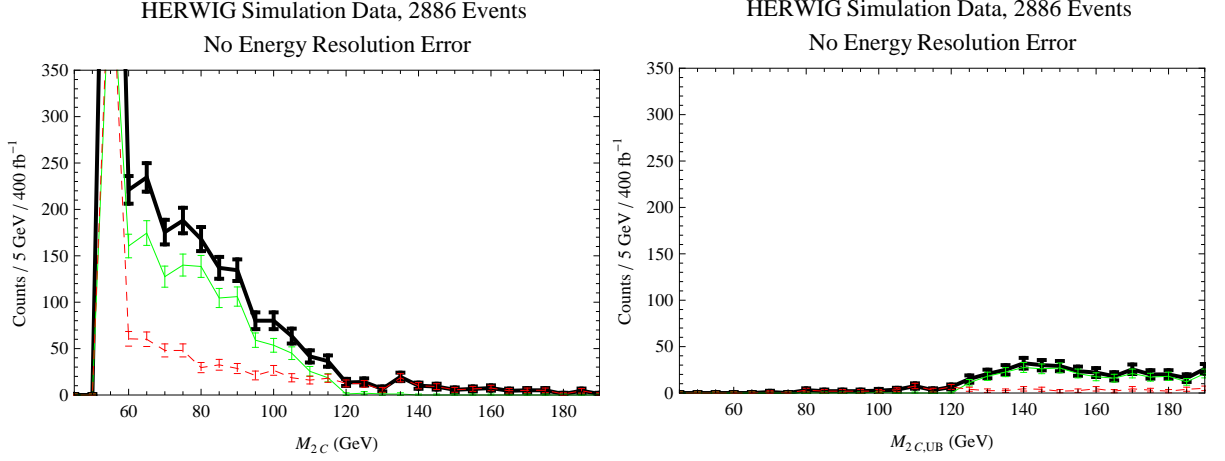


Figure 7.2: The M_{2C} and $M_{2C,UB}$ distributions of HERWIG events before smearing (to simulate detector resolution) is applied. The distributions' end-points show $M_{\tilde{\chi}_2^0} \approx 120$ GeV. The top thick curve shows the net distribution, the next curve down shows the contribution of only the signal events, and the bottom dashed curve shows the contribution of only background events.

studied here, including the (leading order) cross sections and parton distributions. It includes all supersymmetric processes and so contains the relevant background processes as well as the particular decay chain that we wish to study. Figure 7.2 shows the M_{2C} and $M_{2C,UB}$ distributions of a sample of HERWIG generated signal and background events.

Charged leptons (e^\pm and μ^\pm) produced in the decay of heavy objects (SUSY particles and W and Z bosons) were selected for further study provided they satisfied basic selection criteria on transverse momentum ($p_T > 10$ GeV) and pseudorapidity ($|\eta| < 2.5$). Leptons coming from hadron decays are usually contained within hadronic jets and so can be experimentally rejected with high efficiency using energy or track isolation criteria. This latter category of leptons was therefore not used in this study. The acceptance criterion used for the hadronic final state was $|\eta| < 5$. The detector energy resolution functions used are described in Section 7.3.2.

7.3 Factors for Successful Shape Fitting

There are several factors that control or affect the shape of the M_{2C} and $M_{2C,UB}$ distributions. We divide the factors into those that affect the in-principle distribution and the factors that affect the observation of the distribution by the detector like energy resolution and selection cuts.

The in-principle distribution of these events is influenced by the presence or absence of spin-correlations between the branches, the m_{ll} distribution of the visible particles, any significant upstream transverse momentum (UTM) against which the system is recoiling (*e.g.* gluinos or

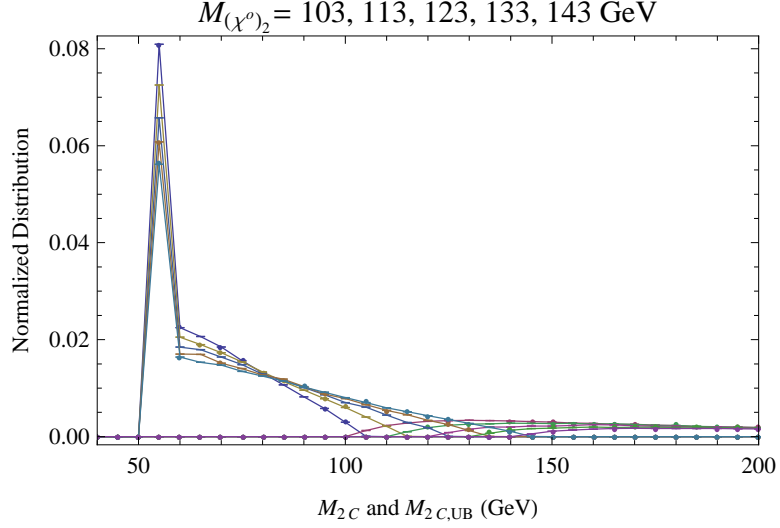


Figure 7.3: We show the M_{2C} and $M_{2C,UB}$ ideal distributions for five choices of $M_{\tilde{\chi}_2^0}$ assuming the HERWIG generated m_{ll} and UTM distributions.

squarks decaying further up the decay chain), and background coming from other new-physics processes or the Standard Model. As all these processes effectively occur at the interaction vertex, there are some combinatoric ambiguities. These are the factors that influence the in-principle distribution of events that impinges on the particle detector.

The actual distribution recorded by the detector will depend on further factors. Some factors we are able to regulate – for example cuts on the missing transverse momentum. Other factors depend on how well we understand the detector’s operation – such as the energy resolution and particle identification.

Where the effect of such factors is significant, for example for the m_{12} , k_T , and background distributions, our approach has been to model their effect on the ideal distributions by using appropriate information from the ‘data’, much as one would do in a real LHC experiment. For the present our ‘data’ are provided by HERWIG, rather than LHC events, but the principle is the same.

7.3.1 Factors Affecting the In-principle Distribution

- **Mass Difference and Mass Scale**

The end-point of M_{2C} and $M_{2C,UB}$ distributions give the mass of $\tilde{\chi}_2^0$. Therefore the mass scale, $M_{\tilde{\chi}_2^0}$, is a dominant factor in the shape of the ‘ideal’ distribution. This is the reason we can use these distributions to determine the mass scale. Fig 7.3 shows the M_{2C} and $M_{2C,UB}$ distributions for five choices of $M_{\tilde{\chi}_2^0}$ assuming the HERWIG generated m_{ll} and UTM distributions.

How does the shape change with mass scale? The shape is typically sharply peaked at $M_{2C} = M_-$ followed by a tail that ends at the mass of $M_{\tilde{\chi}_2^0}$. The peak at M_- is due to events that are compatible with $M_{\tilde{\chi}_1^0} = 0$. We say these events give the trivial constraint. Because we bin the data, the height of the first bin depends on the bin size. As $M_+/M_- = (M_{\tilde{\chi}_2^0} + M_{\tilde{\chi}_1^0})/(M_{\tilde{\chi}_2^0} - M_{\tilde{\chi}_1^0})$ becomes larger, then the non-trivial events are distributed over a wider range and the endpoint becomes less clear. In general if all other things are equal, the larger the mass, the more events in the first bin and the longer and flatter the tail.

The distribution also depends on the mass difference M_- which we assume has been determined. We expect that experimentally one should be able to read off the mass difference from the m_{ll} kinematic end-point with very high precision. Gjelsten, Miller, and Osland estimate this edge can be measured to better than 0.08 GeV [157, 159] using many different channels that lead to the same edge, and after modeling energy resolution and background.

Errors in the mass determination propagated from the error in the mass difference in the limit of $k_T = 0$ are given approximately by

$$\delta M_{\tilde{\chi}_2^0} = \frac{\delta M_-}{2} \left(1 - \frac{M_+^2}{M_-^2} \right) \quad \delta M_{\tilde{\chi}_1^0} = -\frac{\delta M_-}{2} \left(1 + \frac{M_+^2}{M_-^2} \right) \quad (7.11)$$

where δM_- is the error in the determination of the mass difference M_- . An error in M_- will lead to an M_{2C} distribution with a shape and endpoint above or below the true mass in the direction indicated by Eq(7.11).

To isolate this source of error from the uncertainty in the fit, we assume that the mass difference is known exactly in our stated results. In our case an uncertainty of $\delta M_- = 0.08$ GeV would lead to an additional $\delta M_{\tilde{\chi}_1^0} = \pm 0.5$ GeV to be added in quadrature to the error from fitting.

• Spin Correlations Between Branches

The potential impact of spin correlation between branches on M_{2C} were studied in Sec 6.3. There are also no spin correlations if the $\tilde{\chi}_2^0$ parents are part of a longer decay chain which involves a scalar at some stage as is the case in most of the events in the model we study here. In the simple Mathematica simulations, we have assumed no spin dependence in the production of the hypothetical ideal distribution.

• Input m_{12} Distributions

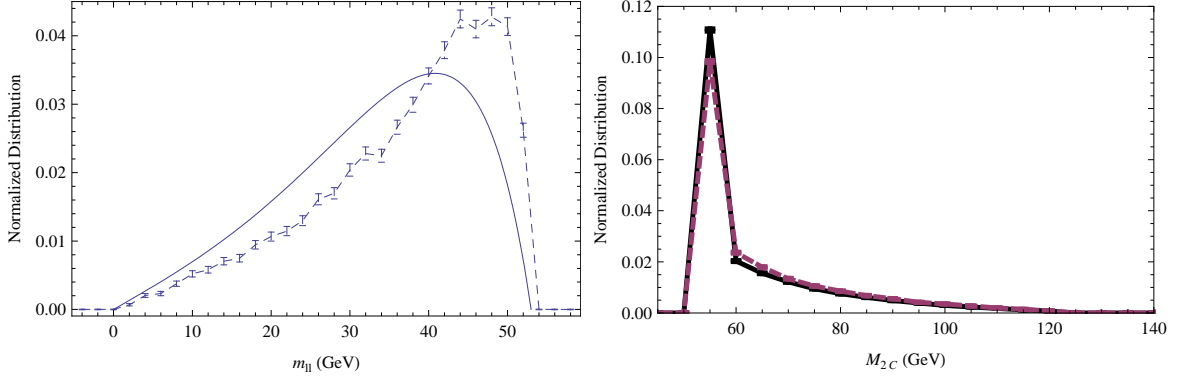


Figure 7.4: Dependence of M_{2C} distribution on the m_{ll} distribution. **Left:** The m_{ll} distributions. **Right:** The corresponding M_{2C} distributions. The solid curves show the case where the m_{ll} distribution when the three-body decay is dominated by the Z boson channel, and the dashed curves show the case where the m_{ll} distribution is taken directly from the HERWIG simulation.

The m_{ll} distribution affects the M_{2C} distribution. Fig 7.4 shows two m_{ll} distributions and the corresponding M_{2C} distributions with $k_T = 0$ (no UTM). The solid lines show the case where the three-body decay from $\tilde{\chi}_2^0$ to $\tilde{\chi}_1^0$ is completely dominated by a Z boson. The dashed line shows the case where the m_{ll} distribution is extracted from the ‘realistic’ HERWIG simulation. We can see that the M_{2C} distribution is affected most strongly in the first several non-zero bins. If we were to determine the mass only from the shape of these first several bins using only the Z contribution for the m_{ll} difference, we would estimate of the mass to be about 4 GeV below the true mass. This can be understood because the shape change of the m_{ll} distribution effectively took events out of the first bin and spread them over the larger bins simulating the effect of a smaller mass.

- **Input Upstream Transverse Momentum Distribution**

As we discussed in Section 7.1, if there is a large upstream transverse momentum (UTM) against which the two $\tilde{\chi}_2^0$ ’s recoil, then we have both an upper and lower bound on the mass scale. The left frame of Fig. 7.5 shows the UTM distribution observed in the ‘realistic’ HERWIG data. The right frame of Fig. 7.5 shows the M_{2C} and $M_{2C,UB}$ distributions for fixed UTM (k_T) of 0, 75, 175, 275, 375, and 575 GeV all with $k^2 = (100 \text{ GeV})^2$. As we discuss under the next bullet, we also find the distribution is not sensitive to the value of k^2 . For $k_T > 275$ GeV, these curves begin to approach a common shape. These are ideal M_{2C} upper and lower bound distributions where $M_N = 70$ GeV and $M_Y = 123$ GeV. Notice that there is no upper-bound curve for the case with zero k_T UTM. The UTM makes the distribution have a sharper endpoint

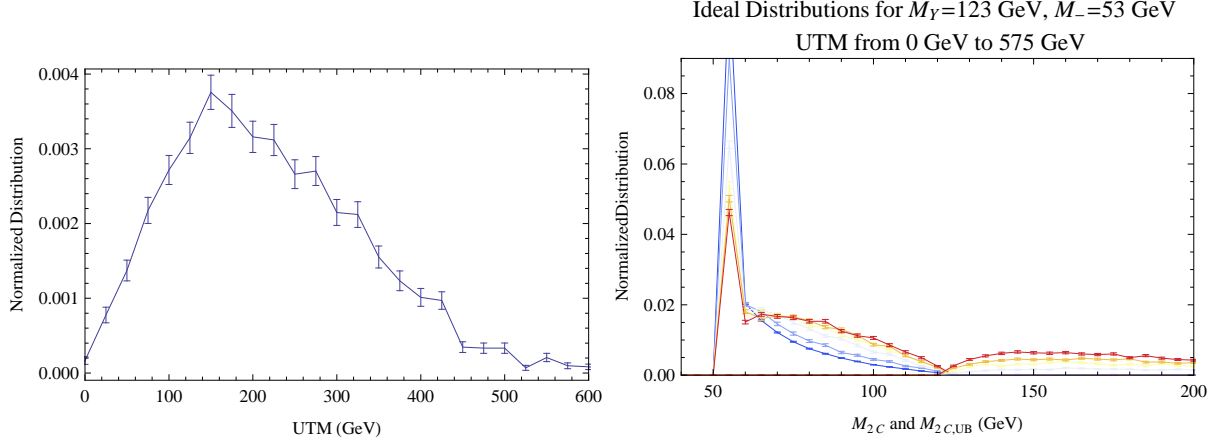


Figure 7.5: **Left:** The UTM distribution observed in the HERWIG simulation. **Right:** Ideal M_{2C} upper bound and lower bound distribution for a range of upstream transverse momentum (UTM) values ($k_T = 0, 75, 175, 275, 375, 575$ GeV) where $M_N = 70$ GeV and $M_Y = 123$ GeV.

and thereby make the mass easier to determine. This is equivalent to having a sharper kink in $\max M_{T2}$ in the presence of large UTM [176].

How do we determine k_T from the data? Because we demand exactly four leptons (two OSSF pairs), we assume all other activity, basically the hadronic activity, in the detector is UTM. The shape used in the ‘ideal’ distribution is a superposition of the different fixed UTM distributions, shown on right frame of Fig. 7.5, weighted by the observed UTM distribution, shown on the left frame of Fig. 7.5. Equivalently, we obtain the ideal distribution by selecting k_T in the Mathematica Monte Carlo according to the observed UTM distribution.

- **Shape Largely Independent of Parton Distributions and Collision Energy**

In the limit where there is no UTM, then M_{2C} is invariant under back-to-back boosts of the parent particles; therefore, M_{2C} is also invariant to changes in the parton distribution functions.

How much of this invariance survives in the presence of large UTM? The answer is that it remains largely independent of the parton collision energy and largely independent of the mass k^2 as shown in Fig 7.6 numerically. On the left frame, we show three distributions and in the right frame their difference with 2σ error bars calculated from 15000 events. The first distribution assumes $k_T = 175$ GeV, $k^2 = (100 \text{ GeV})^2$, \sqrt{s} distributed via Eq(7.10). The second distribution assumes $k_T = 175$ GeV, $k^2 = (2000 \text{ GeV})^2$, \sqrt{s} distributed via Eq(7.10). The third distribution assumes $k_T = 175$ GeV, $k^2 = (100 \text{ GeV})^2$, and a fixed collision energy of $\sqrt{s} = 549$ GeV.

- **Backgrounds**

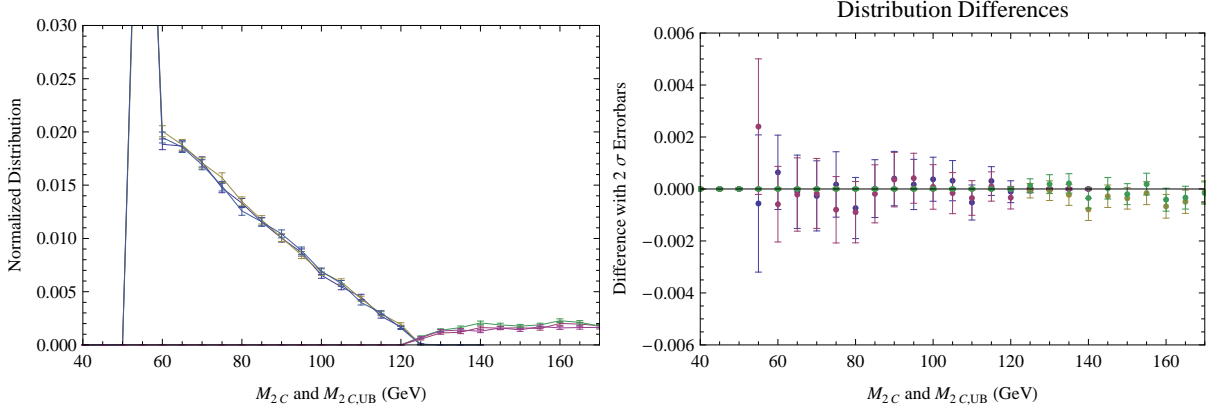


Figure 7.6: Figure shows that even with large UTM, the distribution is independent of k^2 and the parton collision energy to the numerical accuracies as calculated from 15000 events. Shown are three distributions and their difference. (1) $k_T = 175$ GeV, $k^2 = (100 \text{ GeV})^2$, \sqrt{s} distributed via Eq(7.10). (2) $k_T = 175$ GeV, $k^2 = (2000 \text{ GeV})^2$, \sqrt{s} distributed via Eq(7.10). (3) $k_T = 175$ GeV, $k^2 = (100 \text{ GeV})^2$, $\sqrt{s} = 549$ GeV.

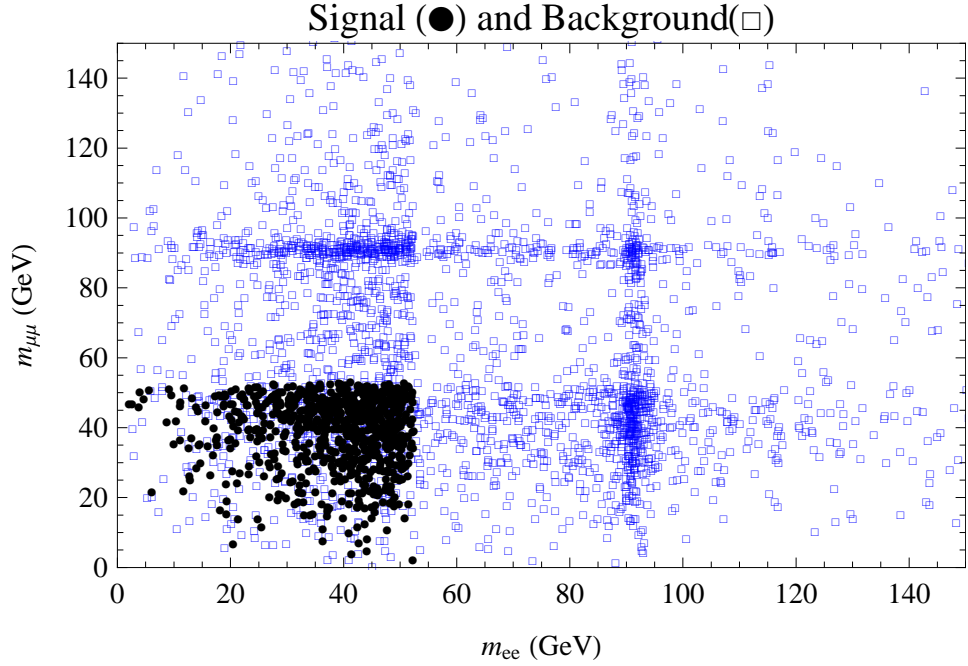


Figure 7.7: The invariant mass of the OSSF leptons from both branches of forming a Dalitz-like wedgebox analysis. The events outside the $m_{ll} \leq 53$ GeV signal rectangle provide control samples from which we estimate the background shape and magnitude. The dark events are signal, the lighter events are background.

Backgrounds affect the shape and, if not corrected for, could provide a systematic error in the estimated mass. In Section 7.4 we will see that the position of the minimum χ^2 in a fit to $M_{\tilde{\chi}_1^0}$ is barely affected by the background. The main effect of the background is to shift the parabola up, giving a worse fit. To improve the fit, we may be able to estimate the M_{2C} and $M_{2C,UB}$ distribution and magnitude of the background from the data itself. We first discuss the sources of background, and then we describe a generic technique using a Dalitz-like wedgebox analysis to estimate a background model which gives approximately the correct shape and magnitude of the background.

One reason we study the four-lepton with missing transverse momentum channel is because of the very-low Standard-Model background [187, 186]. A previous study [186] estimates about 120 Standard-Model four-lepton events (two OSSF pairs) for 100 fb⁻¹ with a $\cancel{P}_T > 20$ GeV cut. They suggest that we can further reduce the Standard-Model background by requiring several hadronic jets. Because we expect very-little direct $\tilde{\chi}_2^0$ pair production, this would have very little effect on the number of signal events. Also, because Z^0 s are a part of the intermediate states of these background processes, very few of these events will have m_{ll} significantly different from M_Z .

What is the source of these Standard-Model backgrounds? About 60% is from Z -pair production events with no invisible decay products, in which the missing transverse momentum can only arise from experimental particle identification and resolution errors. This implies that a slightly stronger \cancel{P}_T cut could further eliminate this background. Another 40% are due to t, \bar{t}, Z production. Not explicitly discussed in their study but representing another possible source of backgrounds are events containing heavy baryons which decay leptonically. If we assume b -quark hadrons decay to isolated leptons with a branching ratio of 0.01, then LHC t, \bar{t} production will lead to about 10 events passing these cuts for 100 fb⁻¹ where both OSSF leptons pairs have $m_{ll} < M_Z$.

Tau decays also provide a background for our specific process of interest. The process $\tilde{\chi}_2^0 \rightarrow \tau^+ \tau^- \tilde{\chi}_1^0$ will be misidentified as $e^- e^+$ or $\mu^+ \mu^-$ about 3% of the time (6% total). Because the τ decays introduce new sources of missing transverse momentum (ν_τ), these events will distort the M_{2C} calculation. This suggests that the dominant background to the $\tilde{\chi}_2^0, \tilde{\chi}_2^0 \rightarrow 4l + \cancel{P}_T +$ hadrons will be from other SUSY processes.

We now create a crude background model from which we estimate the magnitude and distribution of the background using the ‘true’ HERWIG data as a guide. We follow the suggestion of Ref. [160, 186] and use a wedgebox analysis plotting the invariant mass m_{ee} against $m_{\mu\mu}$

to supplement our knowledge of the background events mixed in with our signal events. This wedgebox analysis, seen in Fig. 7.7 for our **HERWIG** simulation, shows patterns that tell about other SUSY states present. The presence of the strips along 91 GeV indicate that particle states are being created that decay to two leptons via an on-shell Z . The observation that the intensity changes above and below $m_{\mu\mu} = 53$ GeV shows that many of the states produced have one branch that decays via a $\tilde{\chi}_2^0$ and the other branch decays via an on-shell Z . The lack of events immediately above and to the right of the (53 GeV, 53 GeV) coordinate but below and to the left of (91 GeV, 91 GeV) coordinate suggest that symmetric process are not responsible for this background.

We also see the density of events in the block above 53 GeV and to the right of 53 GeV suggest a cascade decay with an endpoint near enough to 91 GeV that it is not distinguishable from M_Z . Following this line of thinking, we model the background with a guess of an asymmetric set of events where one branch has new states G , X and N with masses such that the m_{ll} endpoint is

$$\max m_{ll}^2(\text{odd branch}) = \frac{(M_G^2 - M_X^2)(M_X^2 - M_N^2)}{M_X^2} = (85 \text{ GeV})^2 \quad (7.12)$$

and the other branch is our $\tilde{\chi}_2^0$ decay. The masses one chooses to satisfy this edge did not prove important so long as the mass differences were reasonably sized; we tried several different mass triplets ending with the LSP, and all gave similar answers.

We now describe the background model used in our fits. One branch starts with a massive state with $M_G = 160$ GeV which decays to a lepton and a new state $M_X = 120$ GeV which in-turn decays to a lepton and the LSP. The second branch has our signal decay with the $\tilde{\chi}_2^0$ decaying to $\tilde{\chi}_1^0$ and two leptons via a three-body decay. We added UTM consistent with that observed in the events.

By matching the number of events seen outside the $m_{ll} < 53$ GeV region, we estimate the number of the events within the signal cuts that are due to backgrounds. We estimate 0.33 of the events with both OSSF pairs satisfying $m_{ll} < 53$ GeV are background events. The model also gives a reasonable distribution for these events. Inspecting the actual **HERWIG** results showed that actual fraction of background events was 0.4. If we let the fraction be free and minimize the χ^2 with respect to the background fraction, we found a minimum at 0.3.

Our background model is simplistic and does not represent the actual processes, but it does a good job of accounting for the magnitude and the shape of the background mixed into our signal distribution. Most of the **HERWIG** background events came from W and charginos which introduce extra sources of missing transverse momentum. Never the less, the shape fits very

accurately and the performance is discussed in Section 7.4. It is encouraging that our estimate of the background shape and magnitude is relatively insensitive to details of the full spectrum. Even ignoring the background, as we will see in Section 7.4, still leads to a minimum χ^2 at the correct mass.

- **Combinatoric Ambiguities**

If we assume that the full cascade effectively occurs at the primary vertex (no displaced vertices), then the combinatoric question is a property of the ideal distribution produced in the collisions. There are no combinatoric issues if the two opposite-sign same-flavor lepton pairs are each different flavors (*e.g.* the four leptons are e^+ , e^- , μ^+ and μ^-). However if all four leptons are the same flavor, we have found that we can still identify unique branch assignments 90% of the time. The unique identification comes from the observation that both pairs must have an invariant mass m_{ll} less than the value of the $\max m_{ll}$ edge. In 90% of the events, there is only one combination that satisfies this requirement. This allows one to use 95% of the four lepton events without ambiguity. The first 50% are identified from the two OSSF pairs being of different flavors and 90% of the remaining can be identified by requiring that both branches of OSSF lepton for an event's combinatoric pairing satisfy $m_{ll, \text{Event}} < \max_{\text{All Events}} m_{ll}$. The events which remain ambiguous have two possible assignments, both of which are included with a weight of 0.5 in the distribution.

7.3.2 Factors Affecting Distribution Recorded by the Detector

As just described, the ‘ideal’ in-principle distribution is created from the observed m_{ll} distribution and the observed UTM distribution. We include combinatoric effects from events with four leptons of like flavors. Last, we can estimate the magnitude of background events and their M_{2C} and $M_{2C,UB}$ shape. We now modify the in-principle distribution to simulate the effects of the particle detector to form our final ‘ideal’ distribution that includes all anticipated effects. The two main effects on the M_{2C} and $M_{2C,UB}$ distributions are the energy resolution and the \cancel{p}_T cuts.

- **Shape Dependence on Energy Resolution**

Energy resolution causes the M_{2C} and $M_{2C,UB}$ distributions to be smeared. Here we assume the angular resolution is negligible. For both the Mathematica Monte Carlo model and

the HERWIG events we simulate the detector's energy resolution by scaling the four vectors for electrons, muons, and hadrons by

$$\frac{\delta E_e}{E_e} = \frac{0.1}{\sqrt{E_e}} + \frac{0.003}{E_e} + 0.007 \quad (7.13)$$

$$\frac{\delta E_\mu}{E_\mu} = 0.03 \quad (7.14)$$

$$\frac{\delta E_H}{E_H} = \frac{0.58}{\sqrt{E_H}} + \frac{0.018}{E_H} + 0.025 \quad (7.15)$$

respectively [190][9]. The muon energy resolution is different because they are typically not contained by the calorimeter. A more detailed detector simulation is of course possible, but since we do not know the true behavior of any LHC detector until the device begins taking data, a more sophisticated treatment would be of limited value here. In practice the dependence of the ideal distribution shapes on the missing transverse momentum resolution should reflect the actual estimated uncertainty of the missing transverse momentum of the observed events.

Smearing of the distributions decreases the area difference between two normalized distributions, thereby decreasing the precision with which one can determine the mass from a given number of signal events. This expanded uncertainty can be seen in Section 7.4.

The M_{2C} calculations depend on the mass difference, the four-momenta of the four leptons, and the missing transverse momentum. As the lepton energy resolution is very tight, the missing transverse momentum's energy resolution is dominated by the hadronic energy resolution. We model the energy resolution of the UTM as a hadronic jet. This significantly increases the uncertainty in the missing transverse momentum because hadrons have about five times the energy resolution error.

In our Mathematica model, we represent the UTM as a single four-vector k , but in reality it will be the sum of many four-vectors. Because we apply the energy resolution smearing to k , if k is small the simple Mathematica model will have a smaller missing transverse momentum resolution error. However, an events with almost 0 UTM could have a large missing momentum energy resolution if it has a lot of hadronic jets whose transverse momentum mostly cancels. Fig 7.5 shows that most of the time we have considerable hadronic UTM, so this effect is a minor correction on our results.

• Shape Dependence on Missing Transverse Momentum Cuts

A key distinguishing feature of these events is missing transverse momentum. To eliminate the large number of Standard Model events with four-lepton and with no \cancel{p}_T , we will need to cut

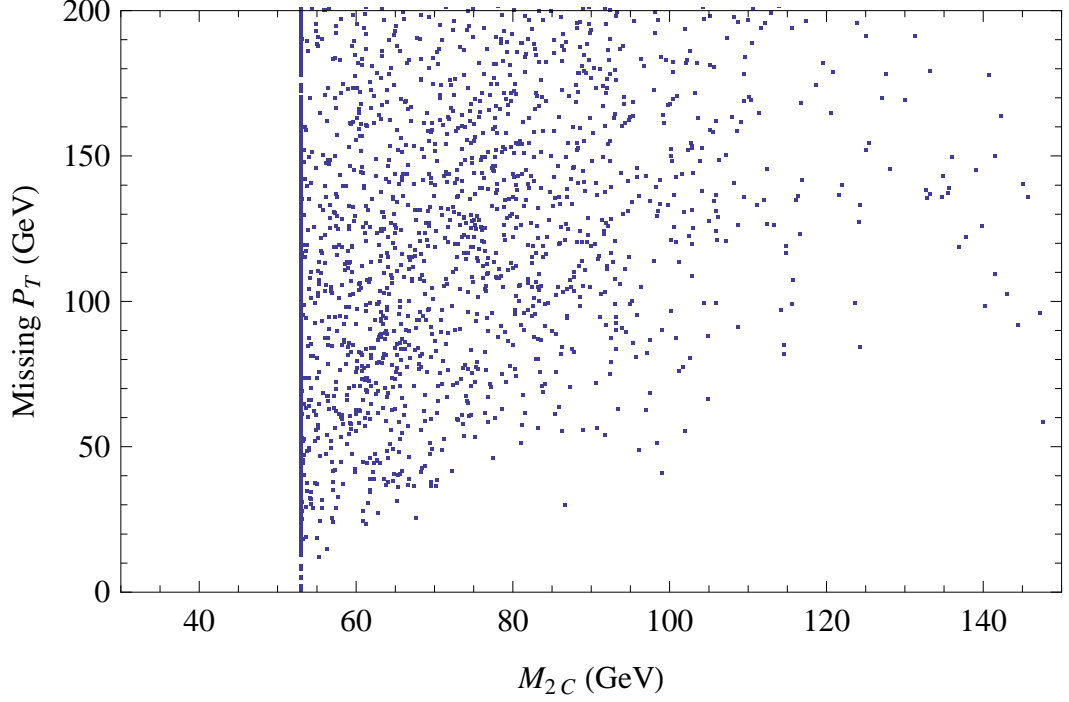


Figure 7.8: The missing transverse momentum vs M_{2C} values for HERWIG data. This shows that a $\cancel{P}_T > 20$ GeV cut would not affect the distribution for $M_{2C} > 65$ GeV.

on this parameter. Fig. 7.8 shows the HERWIG simulation’s missing transverse momentum versus the M_{2C} . A non-trivial M_{2C} requires substantial \cancel{P}_T . Small \cancel{P}_T of less than about 20 GeV only affects the M_{2C} shape below about 65 GeV. The shape of the $M_{2C} < 65$ GeV therefore will require a higher fidelity model from which to train the shapes. Instead, we just choose to not fit bins with $M_{2C} < 65$ GeV.

All events near the end of $M_{2C,UB}$ distribution require significant \cancel{P}_T , therefore \cancel{P}_T cuts will not affect the part of this distribution which we fit. The number of events with no non-trivial upper-bounds will also be affected by \cancel{P}_T cuts. We only fit the $M_{2C,UB}$ distribution up to about 233 GeV.

7.4 Estimated Performance

Determining the mass based on the shape of the distribution enables one to use all the events and not just those near the end point. We fit both upper-bound and lower-bound shapes to the data as described in the Appendix D. As one expects, fitting the lower-bound shape more tightly constrains the mass from below and fitting the upper-bound shape more tightly constrains the mass from above. Combining the two gives approximately even uncertainty. We calculate ideal distributions assuming $M_{\tilde{\chi}_1^0}$ at five values 50, 60, 70, 80, and 90 GeV. We then fit a quadratic

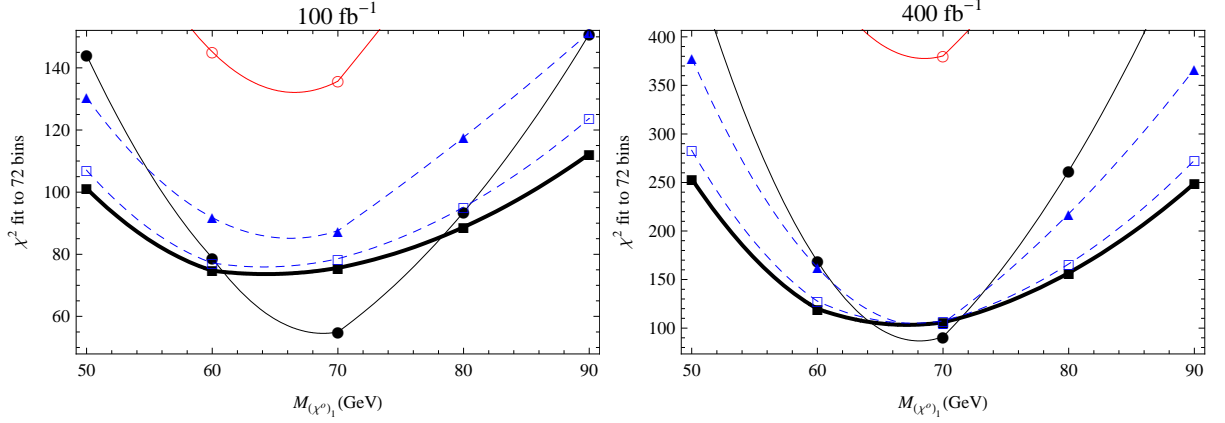


Figure 7.9: The result of χ^2 fits to the data with differing assumptions for 100 fb^{-1} (left panel) and 400 fb^{-1} (right panel). The thick line with filled squares shows the final result with all cuts, resolution error, combinatorics, and backgrounds included and estimated in the shape fitting. This gives us $M_{\tilde{\chi}_1^0} = 63.2 \pm 4.1 \text{ GeV}$ with 700 events (signal or background) representing 100 fb^{-1} . After 400 fb^{-1} this improves to $M_{\tilde{\chi}_1^0} = 66.0 \pm 1.8 \text{ GeV}$. The error-free best case gives $M_{\tilde{\chi}_1^0} = 67.0 \pm 0.9 \text{ GeV}$. The correct value is $M_{\tilde{\chi}_1^0} = 67.4 \text{ GeV}$.

interpolation through the points. Our uncertainties are based on the value where χ^2 increases by 1 from its minimum of this interpolation. This uncertainty estimate agrees with about 2/3 of the results falling within that range after repeated runs. Our uncertainty estimates do not include the error propagated from the uncertainty in the mass difference (see Eq(7.11)).

We present results for an early LHC run, about 100 fb^{-1} , and for the longest likely LHC run before an upgrade, about 400 fb^{-1} . After about 100 fb^{-1} , we have 700 events (about 400 signal and 300 background). After 400 fb^{-1} , we have about 2700 events (about 1600 signal and 1100 background). Only 4 events out of 1600 are from direct pair production. Most of our signal events follow at the end of different decay chains starting from gluinos or squarks. The upstream decay products produce significant UTM against which the two $\tilde{\chi}_2^0$ parent particles recoil.

First for the ideal case. After 400 fb^{-1} , using only signal events and no energy resolution, the χ^2 fits to the predicted shapes give $M_{\tilde{\chi}_1^0} = 67.0 \pm 0.9 \text{ GeV}$ (filled circles in Fig. 7.9). This mass determination can practically be read off from the endpoints seen in Fig. 7.2; the M_{2C} endpoint is near 120 GeV and subtracting the mass differences gives $M_{\tilde{\chi}_1^0} = 120 \text{ GeV} - M_- = 67 \text{ GeV}$. We now explore how well we can do with fewer events and after incorporating the effects listed in Section 7.3.

How does background affect the fit? If we ignore the existence of background in our sample, and we fit all the events to the signal-only shapes, then we find a poor fit shown as the empty circle curve in Fig. 7.9. By poor fit, we mean the χ^2 is substantially larger than the 72 bins being compared (36 bins from each the upper-bound and lower-bound distributions). Despite

this worse fit, the shape fits still give a very accurate mass estimate: $M_{\tilde{\chi}_1^0} = 65.4 \pm 1.8$ GeV after 100 fb^{-1} and $M_{\tilde{\chi}_1^0} = 67.4 \pm 0.9$ GeV after 400 fb^{-1} . At this stage, we still assume perfect energy resolution and no missing transverse momentum cut.

Next, if we create a background model as described in Section 7.3, we are able to improve the χ^2 fit to nearly 1 per bin; the mass estimate remains about the same, but the uncertainty increases by about 20%. We find a small systematic shift (smaller than the uncertainty) in our mass prediction as we increase the fraction of the shape due to the background model vs the signal model. As we increased our fraction of background, we found the mass estimate was shifted down from 66.5 at 0% background to 65.6 when we were at 60% background. The best χ^2 fit occurs with 30% background; which is very close to the 33% we use from the estimate, but farther from the true background fraction of about 40%. With 400 fb^{-1} of data, the systematic errors are all but eliminated with the endpoint dominating the mass estimate. These fits are shown as the triangles with dashed lines and give $M_{\tilde{\chi}_1^0} = 65.1 \pm 2.4$ GeV which after the full run becomes $M_{\tilde{\chi}_1^0} = 67.3 \pm 1.1$ GeV.

Including energy resolution as described in Section 7.3 shows a large increase in the uncertainty. The dashed-line with empty square markers shows the χ^2 fit when we include both a background model and the effect of including energy resolution. These fits are shown as the empty squares with dashed lines and give $M_{\tilde{\chi}_1^0} = 63.0 \pm 3.6$ GeV which after the full run becomes $M_{\tilde{\chi}_1^0} = 66.5 \pm 1.6$ GeV.

The final shape factor that we account for are the cuts associated with the missing transverse momentum. After we apply cuts requiring $\cancel{p}_T > 20$ GeV and fit only $M_{2C} > 65$ GeV we have our final result shown by the thick lines with filled squares. This includes all cuts, resolution error, combinatorics and backgrounds. We find $M_{\tilde{\chi}_1^0} = 63.2 \pm 4.1$ GeV with 700 events (signal or background) representing 100 fb^{-1} , and after 400 fb^{-1} this improves to $M_{\tilde{\chi}_1^0} = 66.0 \pm 1.8$ GeV. The true mass on which the **HERWIG** simulation is based is $M_{\tilde{\chi}_1^0} = 67.4$, so all the estimates are within about 1σ of the true mass.

Fig 7.10 shows the ideal curve expected if $M_{\tilde{\chi}_1^0} = 70$ GeV including all effects from energy resolution, background, combinatoric, and \cancel{p}_T cuts. The χ^2 corresponds to the solid square on the left panel of Fig. 7.9.

The error in mass determination obtained with limited statistics can be estimated using Poisson statistics. In our studies we find that, as one would expect, increasing the number of events by a factor of four, we bring down our error by about a factor of two. This means that one

HERWIG Data and
Ideal Expectation for $M_{(\chi^0)_1}=70$ GeV
701 Events, All Effects

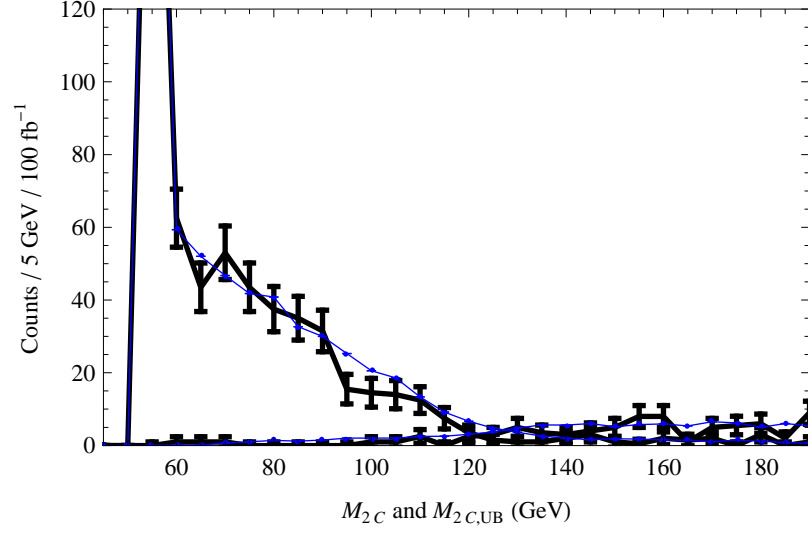


Figure 7.10: HERWIG data for 100 fb^{-1} (thick line) and the smooth ideal expectation assuming $M_{\chi^0_1} = 70 \text{ GeV}$ generated by Mathematica with all resolution, background, and combinatoric effects included (thin line). The χ^2 of this curve to the HERWIG gives the solid-black square on the left frame of Fig. 7.9.

could expect $\pm 8 \text{ GeV}$ after about 25 fb^{-1} which represents 100 signal events and 75 background events.

Chapter Summary

Despite adding some of the complicating effects one would encounter with real data, we have discovered other factors which demonstrate that one could obtain an even better precision than estimated in Chapter 6. There, we used only our simple Mathematica model and neglected most sources of realistic uncertainty. We assumed all the events could be modeled as being direct production without spin-correlations. With these simplifications, we argued the mass could be determined to $\pm 6 \text{ GeV}$ using 250 signal events.

In this chapter, we performed a case study to show that the relevant M_{2C} and $M_{2C,UB}$ shapes can be successfully determined from the mass difference M_- , the m_{ll} distribution observation, the upstream transverse momentum (UTM) distribution observation. We included and accounted for many realistic effects: we modeled the large energy-resolution error of hadronic jets. We also included the effects of backgrounds, \cancel{p}_T cuts, and combinatorics. Our signal and backgrounds were generated with HERWIG. We discussed how a Dalitz-like plot can estimate the background fraction and shape. Observed inputs were used in a simple model to determine ideal

distribution shapes that makes no reference to parton distribution functions, cross sections, or other model-dependent factors that we are not likely to know early in the process.

Despite these extra sources of uncertainty, we found a final mass determination of ± 4.1 GeV with about 400 signal events which is still better than the appropriately scaled result from RS [15]. The sources of the mass determination improvement are twofold: (1) the prediction and fitting of upper-bound distribution, and (2) the sharper end-point in the presence of large UTM. Under equivalent circumstances, the sharper endpoint is enough to give a factor of 2 improvement in the uncertainty over the direct production case assumed in [15]. Fitting the upper bound tends to improve the determination by an additional factor of $\sqrt{2}$. This improvement is then used to fight the large hadronic-jet energy resolution and background uncertainty.

Mass determination using M_{2C} and $M_{2C,UB}$ applies to many other processes. We have focused on cases where the mass difference is given by the end-point of an m_{ll} distribution involving a three-body decay. If there is not a three-body decay, then the mass difference may be found by applying other mass determination techniques like the mass shell techniques (MST) [166, 167, 168] or edges in cascade decays [156, 158, 159] or M_{T2} at different stages in symmetric decay chains [14].

How does our method’s performance compare to previous mass determination methods? Firstly, this technique is more robust than the $\max M_{T2}$ ‘kink’ because in fitting to the shape of the distribution, it does not rely entirely on identification of the events near kinematic boundary. One can view M_{2C} and $M_{2C,UB}$ as variables that event-by-event quantify the ‘kink’. Other than the ‘kink’ technique, the previous techniques surveyed in Chapter 4 apply to cases where there is no three-body decay from which to measure the mass difference directly. However, each of those techniques still constrains the mass difference with great accuracy. The technique of [156, 157, 158, 159] which uses edges from cascade decays determines the LSP mass to ± 3.4 GeV with about 500 thousand events from 300 fb^{-1} . The approach of [167] assumes a pair of symmetric decay chains and assumes two events have the same structure. They reach ± 2.8 GeV using 700 signal events after 300 fb^{-1} , but have a 2.5 GeV systematic bias that needs modeling to remove. By comparison, adjusting to 700 signal events we achieve ± 2.9 GeV without a systematic bias after propagating an error of 0.08 GeV in the mass difference and with all discussed effects. Uncertainty calculations differ amongst groups, some use repeated trial with new sets of Monte Carlo data, and others use χ^2 . Without a direct comparison under like circumstance, the optimal method is not clear; but it is clear that fitting the M_{2C} and $M_{2C,UB}$ distributions can determine

the mass of invisible particles at least as well, if not better than the other known methods in both accuracy and precision.

In summary, we have developed a mass determination technique, based on the constrained mass variables, which is able to determine the mass of a dark-matter particle state produced at the LHC in events with large missing transverse momentum. The M_{2C} method, which bounds the mass from below, was supplemented by a new distribution $M_{2C,UB}$ which bounds the mass from above in events with large upstream transverse momentum. A particular advantage of the method is that it also obtains substantial information from events away from the end point allowing for a significant reduction in the error. The shape of the distribution away from the end-point can be determined without detailed knowledge of the underlying model, and as such, can provide an early estimate of the mass. Once the underlying process and model generating the event has been identified the structure away from the end-point can be improved using, for example, **HERWIG** to produce the process dependent shape. We performed a case-study simulation under LHC conditions to demonstrate that mass-determination by fitting the M_{2C} and $M_{2C,UB}$ distributions survives anticipated complications. With this fitting procedure it is possible to get an early measurement of the mass - with just 400 signal events in our case study we found we would determine $M_{\tilde{\chi}_1^0} = 63.2 \pm 4.1$. The ultimate accuracy obtainable by this method is $M_{\tilde{\chi}_1^0} = 66.0 \pm 1.8$ GeV. We conclude that this technique's precision is as good as, if not better than, the best existing techniques.

Chapter 8

The Variable M_{3C} : On-shell Interlineate States

Chapter Overview

The main concept of the constrained mass variable M_{2C} [15] [16] is that after studying several kinematic quantities we may have well determined the mass difference between two particle states but not the mass itself. We then incorporate these additional constraints in the analysis of the events. We check each event to test the lower bounds and upper bounds on the mass scale that still satisfies the mass difference and the on-shell conditions for the assumed topology. Because the domain over which we are minimizing contains the true value for the mass, the end-points of the lower bounds and upper bounds distributions' give the true mass.

The subject of this chapter is extending the constrained mass variable to the case with three new on-shell states as depicted in Fig 4.3. The constrained mass variable for this case will be called M_{3C} . We structure the chapter around a case study of the benchmark point SPS 1a [3]. In this study, the three new states are identified as $Y = \tilde{\chi}_2^0$, $X = \tilde{l}$ and $N = \tilde{\chi}_1^0$. The visible particles leaving each branch are all opposite-sign same-flavor (OSSF) leptons (μ or e). This allows us to identify any hadronic activity as upstream transverse momentum.

The chapter is structured as follows: Sec. 8.1 introduces the definition of M_{3C} and how to calculate it. Sec. 8.3 discusses the dependence of M_{3C} on complications from combinatorics, large upstream transverse momentum (UTM), \cancel{p}_T cuts, parton distributions, and energy resolution. Sec 8.4 applies M_{3C} variables to HERWIG data from the benchmark supersymmetry spectrum SPS 1a. Finally we summarize the chapter's contributions.

8.1 Introducing M_{3C}

We will now introduce the definition of M_{3C} , how to calculate it, its relationship to previous mass shell techniques.

8.1.1 Definition of M_{3C}

The upper bound and lower bound on the mass of the third lightest new particle state in the symmetric decay chain is the constrained mass variable $M_{3C, LB}$ and $M_{3C, UB}$. This variable applies to the symmetric, on-shell intermediate state, topology from Fig. 4.3 which depicts two partons that collide and produce some observed upstream transverse momentum (UTM) with four momenta k and an on-shell, pair-produced new state Y . On each branch, Y decays to on-shell intermediate particle state X and a visible particle v_1 with masses M_X and m_{v_1} . Then X decays to the dark-matter particle N and visible particle v_2 with masses M_N and m_{v_2} . The four-momenta of v_1 , v_2 and N are respectively α_1 , α_2 and p on one branch and β_1 , β_2 and q in the other branch. The missing transverse momenta \not{P}_T is given by the transverse part of $p + q$.

We initially assume that we have measured the mass differences from other techniques. For an on-shell intermediate state, there is no single end-point that gives the mass difference. The short decay chain gives a kinematic endpoint $\max m_{12}$ described in Eq(4.3) that constrains a combination of the squared mass differences. Unless two of the states are nearly degenerate, the line with constant mass differences lies very close to the surface given by Eq(4.3). The two mass differences are often tightly constrained in other methods. The mass differences are constrained to within 0.3 GeV from studying long cascade decay chains where one combines constraints from several endpoints of different invariant mass combinations [157]. The concepts from Chapter 5 also provide another technique to determine the mass differences. After initially assuming that we know the mass difference, we show that our technique can also find the mass differences. The M_{3C} distribution shape is a function of both the mass scale and mass differences. We can constrain both the mass differences and the mass scale by fitting the $\max m_{12}$ edge constraints and the ideal $M_{3C}(M_N, \Delta M_{YN}, \Delta M_{XN})$ distribution shapes to the observed $M_{3C}(\Delta M_{YN}, \Delta M_{XN})$. To find all three parameters from this fit, we will take M_N , ΔM_{YN} , and ΔM_{XN} as independent variables.

For this first phase of the analysis, let's assume the mass differences are given. For each event, the variable $M_{3C, LB}$ is the minimum value of the mass of Y (third lightest state) after minimizing over the unknown division of the missing transverse energy \not{P}_T between the two dark

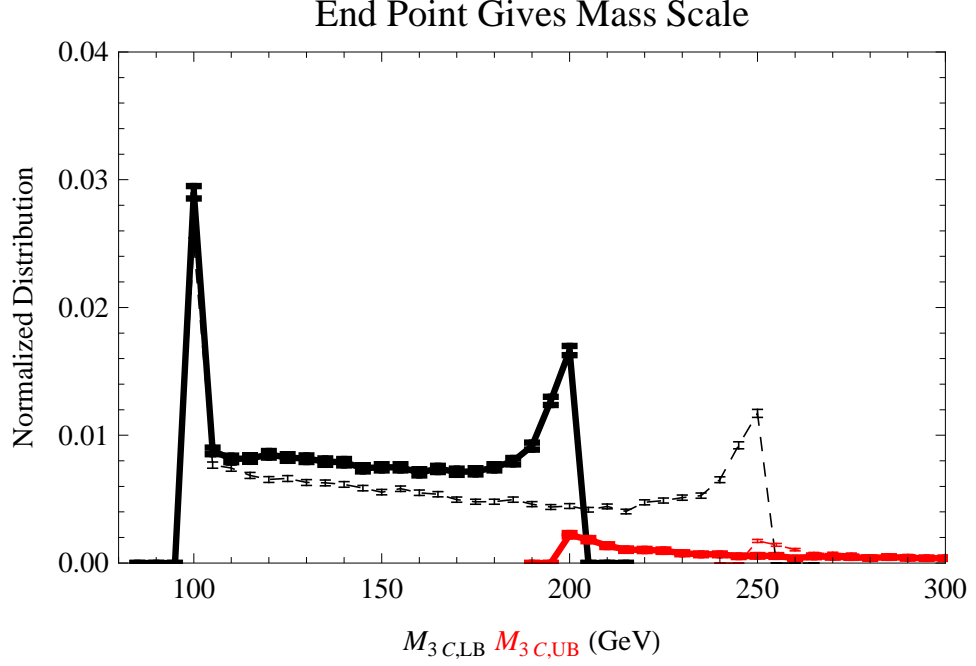


Figure 8.1: Ideal $M_{3C, LB}$ and $M_{3C, UB}$ distribution for 25000 events in two cases both sharing $\Delta M_{YN} = 100$ GeV and $\Delta M_{XN} = 50$ GeV. The solid, thick line shows $M_Y = 200$ GeV, and the dashed, thin line shows $M_Y = 250$ GeV.

matter particles N :

$$m_{3C, LB}^2(\Delta M_{YN}, \Delta M_{XN}) = \min_{p, q} (p + \alpha_1 + \alpha_2)^2 \quad (8.1)$$

Constrained to

$$(p + q)_T = \not{p}_T \quad (8.2)$$

$$\sqrt{(\alpha_1 + \alpha_2 + p)^2} - \sqrt{(p^2)} = \Delta M_{YN} \quad (8.3)$$

$$\sqrt{(\alpha_2 + p)^2} - \sqrt{(p^2)} = \Delta M_{XN} \quad (8.4)$$

$$(\alpha_1 + \alpha_2 + p)^2 = (\beta_1 + \beta_2 + q)^2 \quad (8.5)$$

$$(\alpha_2 + p)^2 = (\beta_2 + q)^2 \quad (8.6)$$

$$p^2 = q^2 \quad (8.7)$$

where $\Delta M_{YN} = M_Y - M_N$ and $\Delta M_{XN} = M_X - M_N$. There are eight unknowns in the four momenta of p and q and seven equations of constraint. Likewise we define $M_{3C, UB}$ as the maximum value of M_Y compatible with the same constraints. We discuss how to numerically implement this minimization and maximization in Sec. 8.2. Because the true p and q are within the domain over which we are minimizing (or maximizing), the minimum (maximum) is guaranteed to be less than (greater than) or equal to M_Y .

Figure 8.1 shows an ideal $M_{3C,LB}$ and $M_{3C,UB}$ distributions for 25000 events in two cases both sharing $\Delta M_{YN} = 100$ GeV and $\Delta M_{XN} = 50$ GeV. The dashed line represents the distributions from events with $M_Y = 250$ GeV, and in the solid line represents the distributions from events with $M_Y = 200$ GeV. One can clearly see sharp end-points in both the upper bound and lower bound distributions that give the value M_Y . The upper-bound distribution is shown in red.

We expect an event to better constrain the mass scale if we are given additional information about that event. In comparison to M_{2C} where Y decays directly to N , the on-shell intermediate state has an additional state X . The extra state X and information about its mass difference ΔM_{XN} enables M_{3C} to make an event-by-event bound on M_Y stronger than in the case of M_{2C} . We will see that this stronger bound is partially offset by greater sensitivity to errors in momentum measurements.

The variable M_{3C} , like other variables we have discussed M_{2C} , M_{T2} , M_T and M_{CT} , is invariant under longitudinal boosts of its input parameters. We can understand this because all the constraint equations are invariant under longitudinal boosts. The unknown p and q are minimized over all possible values fitting the constraints so changing frame of reference will not change the extrema of the Lorentz invariant quantity $(p + \alpha)^2$.

8.2 How to calculate M_{3C}

To find the M_{3C} , we observe that if we assume masses of Y , X , and N to be (χ_Y, χ_X, χ_N) ¹ with the given mass differences then there are eight constraints

$$(p + q)_T = \not{p}_T \quad (8.8)$$

$$(\alpha_1 + \alpha_2 + p)^2 = (\beta_1 + \beta_2 + q)^2 = \chi_Y^2 \quad (8.9)$$

$$(\alpha_2 + p)^2 = (\beta_2 + q)^2 = \chi_X^2 = (\chi_Y - \Delta M_{YN} + \Delta M_{XN})^2 \quad (8.10)$$

$$p^2 = q^2 = \chi_N^2 = (\chi_Y - \Delta M_{YN})^2 \quad (8.11)$$

and eight unknowns, p_μ and q_μ . The spatial momenta \vec{p} and \vec{q} can be found as linear functions of the 0th component of p and q by solving the matrix equation

$$\begin{pmatrix} 1 & 0 & 0 & 1 & 0 & 0 \\ 0 & 1 & 0 & 0 & 1 & 0 \\ -2\alpha_x & -2\alpha_y & -2\alpha_z & 0 & 0 & 0 \\ 0 & 0 & 0 & -2\beta_x & -2\beta_y & -2\beta_z \\ -2(\alpha_2)_x & -2(\alpha_2)_y & -2(\alpha_2)_z & 0 & 0 & 0 \\ 0 & 0 & 0 & -2(\beta_2)_x & -2(\beta_2)_y & -2(\beta_2)_z \end{pmatrix} \begin{pmatrix} p_x \\ p_y \\ p_z \\ q_x \\ q_y \\ q_z \end{pmatrix} = \begin{pmatrix} -(k + \alpha + \beta)_x \\ -(k + \alpha + \beta)_y \\ -2\alpha_o p_o + (\chi_Y^2 - \chi_N^2) - \alpha^2 \\ -2\beta_o q_o + (\chi_Y^2 - \chi_N^2) - \beta^2 \\ -2(\alpha_2)_o p_o + (\chi_X^2 - \chi_N^2) - (\alpha_2)^2 \\ -2(\beta_2)_o q_o + (\chi_X^2 - \chi_N^2) - (\beta_2)^2 \end{pmatrix} \quad (8.12)$$

¹We again use χ to distinguish hypothetical masses (χ_Y, χ_X, χ_N) from the true masses (M_Y, M_X, M_N) .

where $\alpha = \alpha_1 + \alpha_2$ and $\beta = \beta_1 + \beta_2$. We substitute \vec{p} and \vec{q} into the on-shell constraints

$$p_o^2 - (\vec{p}(p_o, q_o))^2 = \chi_N^2 \quad (8.13)$$

$$q_o^2 - (\vec{q}(p_o, q_o))^2 = \chi_N^2 \quad (8.14)$$

giving two quadratic equations for p_o and q_o . These give four complex solutions for the pair p_o and q_o . We test each event for compatibility with a hypothetical triplet of masses $(\chi_Y, \chi_X, \chi_N) = (\chi_Y, \chi_Y - \Delta M_{YN} + \Delta M_{XN}, \chi_Y - \Delta M_{YX})$. If there are any purely real physical solutions where ($p_o > 0$ and $q_o > 0$), then we consider the mass triplet (χ_Y, χ_X, χ_N) viable.

As we scan χ_Y , a solution begins to exist at a value less than or equal to M_Y and then sometimes ceases to be a solution above M_Y . Sometimes there are multiple islands of solutions. To find the M_{3C} , we can test each bin starting at $\chi_Y = \Delta M_{YN}$ along the path parameterized by χ_Y and the mass differences to find the first bin where at least one physical solution exists. This is the lower bound value of M_{3C} for the event.

Likewise for an upper bound. We begin testing at the largest conceivable mass scale we expect for the Y particle state. If a solution exists, we declare this a trivial $M_{3C,UB}$. If no solution exists, then we search downward in mass scale until a solution exists.

A faster algorithm involves a bisection search for a solution within the window that starts at ΔM_{YN} and ends at our highest conceivable mass. We then use a binary search algorithm to find at what χ_Y the solution first appears for $M_{3C,LB}$ or at what χ_Y the solution disappears giving $M_{3C,UB}$. There are rare events where there are multiple islands of solutions. This occurs in about 0.01% of the events with 0 UTM and in about 0.1% for $k_T = 250$ GeV. In our algorithm we neglect windows of solutions more narrow than 15 GeV. We report the smallest edge of the lower-mass island as the lower bound and the upper edge of the larger-mass island as the upper bound. Because of the presence of islands, we are not guaranteed that solutions exist everywhere between $M_{3C,LB}$ and $M_{3C,UB}$. With the inclusion of energy resolution errors and background events, we also find cases where there are no solutions anywhere along the path being parameterized. If there is no solutions anywhere in the domain we make $M_{3C,LB}$ to be the largest conceivable mass scale, and we set $M_{3C,UB} = \Delta M_{YN}$.

8.2.1 Comparison to other Mass Shell Techniques

The variable M_{3C} is a hybrid mass shell technique[168]. In Chapter 4 we reviewed other mass shell technique that measure the mass in the case of three new states. Cheng, Gunion, Han Marandella, McElrath (CGHMM) [166] describe counting solutions at assumed values for the

mass for Y , X , and N . By incorporating a minimization or maximization, we enhance CGHMM's approach because we have a variable whose value changes slightly with slight changes of the inputs instead of the binary on-off that CGHMM has with the existence of a solution². We also incorporate knowledge of the added information from other measurements which accurately determine the mass differences. Finally, the quantity M_{3C} can form a distribution whose shape tells us information about the masses. Because for most events there is only one 'turn-on' point below M_Y , the distribution $M_{3C, LB}$ is very similar to the derivative of the figure 8 of CGHMM[166] to the left of their peak and $M_{3C, UB}$ is similar to the negative of the derivative to the right of their peak. They differ in that there may be multiple windows of solutions; also CGHMM's Fig 8 is not exactly along the line of fixed mass differences; and the effect of backgrounds and energy resolution are dealt with differently.

We also hope to show that the use of the distribution's shape enables us to exploit the essentially non-existent dependence of the distributions on the unknown collision energies and incorporate the dependency on UTM directly. This diminishes the dependence of the measurement on the unknown model while still allowing us to exploit the majority of the distribution shape in the mass determination.

After studying previous MSTs, we were tempted to use Bayes theorem with a parton distribution function as a likelihood function as was done in Goldstein and Dalitz [161] and Kondo, Chikamatsu, Kim [162] (GDKCK). They used the parton distribution function to weight the different mass estimates of the top-quark mass (M_Y in our topology). We found that such a weighting leads to a prediction for M_Y much smaller than the true value. This can be understood because the parton distributions make collisions with smaller center-of-mass energies (small x) more likely, therefore the posterior will prefer smaller values of M_Y which are only possible for smaller values of x . Only if one includes the cross-section for production, i.e. the likelihood of the event existing at all, in the Bayes likelihood function will we have the appropriate factor that suppresses small values of x and therefore small values of M_Y . This balance therefore leads to the maximum likelihood (in the limit of infinite data) occurring at the correct M_Y . Unfortunately, inclusion of the magnitude of the cross section introduces large model dependence. In the case of the top-quarks mass determination, the GDKCK technique gives reasonable results. This is because they were not scanning the mass scale, but rather scanning χ_Y (the top quark mass) while assuming $\chi_N = M_N = 0$ and $\chi_X = M_X = M_W$. The likelihood of solutions as one scans χ_Y rapidly goes to zero below the true top-quark mass M_{top} . The parton distribution

²I am grateful to Chris Lester for pointing out to me the importance of this feature.

suppresses the likelihood above the true M_{top} . The net result gives the maximum likelihood near the true top-quark mass but suffers from a systematic bias [163][164] that must be removed by modeling [165].

8.3 Factors for Successful Shape Fitting

One major advantage of using the M_{3C} distribution (just as the M_{2C} distribution) is that the bulk of the relevant events are used to determine the mass and not just those near the endpoint. To make the approach mostly model independent, we study on what factors the distributions shape depends. We show that there is a strong dependence on upstream transverse momentum (UTM) which can be measured and used as an input and therefore does not increase the model dependency. We show there is no numerically significant dependence on the collision energy which is distributed according to the parton distribution functions. This makes the distribution shape independent of the production cross section and the details of what happens upstream from the part of the decay chain that we are studying. We model these effects with a simple Mathematica Monte Carlo event generator assuming $M_Y = 200$ GeV, $M_X = 150$ GeV, and $M_N = 100$ GeV.

- **Effect of Combinatorics Ambiguities**

Just as in the topology in Fig 4.4 studied earlier, where $\tilde{\chi}_2^0$ decays via a three body decay, the branch assignments can be determined by either distinct OSSF pairs or by studying which OSSF pairs have both $m_{12} \leq \max m_{12}$. In 90% of the events, there is only one combination that satisfies this requirement. This allows us to know the branch assignment of 95% of the four lepton events without ambiguity.

Unlike the three-body decay case, the order of the two leptons on each branch matters. The intermediate mass $M_X^2 = (\alpha_2 + p)^2$ depends on α_2 and does not depend on α_1 . To resolve this ambiguity we consider the four combinations that preserve the branch assignment but differ in their ordering. The $M_{3C, LB}$ for the event is the minimum of these combinations. Likewise the $M_{3C, UB}$ is the maximum of these combinations. As one expects, Fig. 8.2 (Left) shows how the combinatorics ambiguity degrades the sharpness of the cut-off at the true mass. Not all applications share this ambiguity; for example in top-quark mass determination (pair produced with $Y = top$, $X = W^\pm$, $N = \nu$) the b -quark-jet marks α_1 and the lepton marks α_2 .

- **Effect Large Upstream Transverse Momentum**

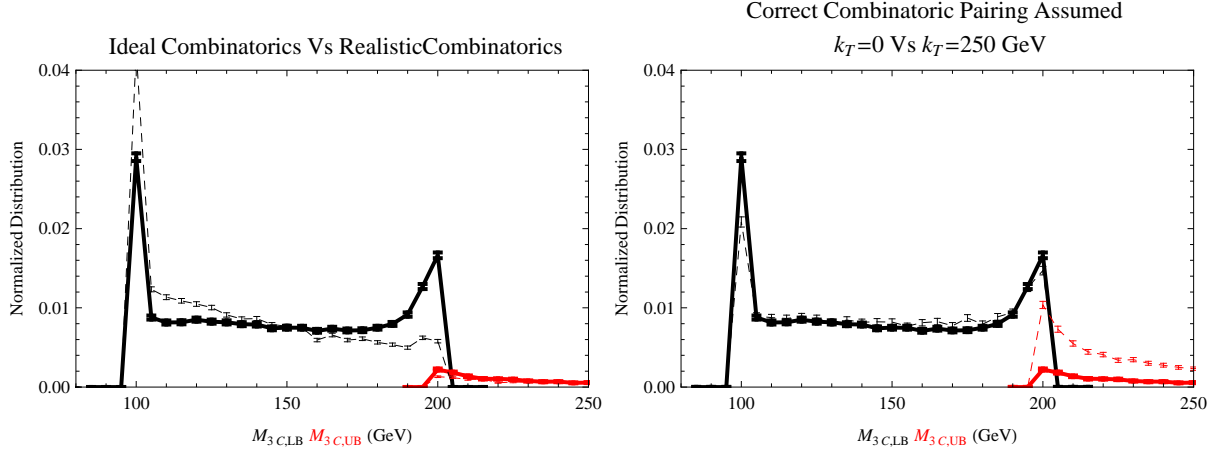


Figure 8.2: (Left) The M_{3C} distributions before (solid) and after (dashed) introducing the combinatoric ambiguity. (Right) The M_{3C} distributions with and without UTM. The no UTM case ($k_T = 0$) is shown by the solid line; the large UTM case with $k_T = 250$ GeV is shown by the dashed line.

In a similar behavior to M_{2C} , the distributions of the variable M_{3C} show a strong dependence on large upstream transverse momentum (UTM). In our case study this is identified as the combination of all the hadronic activity. Fig 8.2 (Right) shows the stronger upper-bound cut-off in the presence of large UTM. Unlike M_{2C} , in M_{3C} with $k_T = 0$ we still have events with non-trivial upper bound values.

We also tested the distribution for different values of k^2 . In Fig 8.2 (Right) we fixed $k^2 = (100 \text{ GeV})^2$. We also performed simulations with $k^2 = (500 \text{ GeV})^2$ and found the difference of the two M_{3C} distributions consistent with zero after 15000 events. In other words, the distribution depends mostly on k_x and k_y and appears independent of k_0 .

• The Effects of Detector Energy Resolution

Compared to M_{2C} , the information about the extra states gives a stronger set of bounds. Unfortunately, the solution is also more sensitive to momentum measurement error. We model the finite energy resolution using Eqs(7.13-7.15). The hadronic energy resolution is larger than the leptonic energy resolution which will increase the uncertainty in the missing transverse momentum.

Fig. 8.3 shows the effect on the M_{3C} distribution of realistic leptonic energy resolution while keeping $k_T = 0$. On the left we show the energy resolution (dashed line) compared to the perfect energy resolution (solid line). The energy resolution washes out the sharp cut-off. On the right we show $M_{3C, LB}$ with perfect energy resolution plotted against the result with realistic energy resolution. This shows that the cut-off is strongly washed out because the events with M_{3C} closer

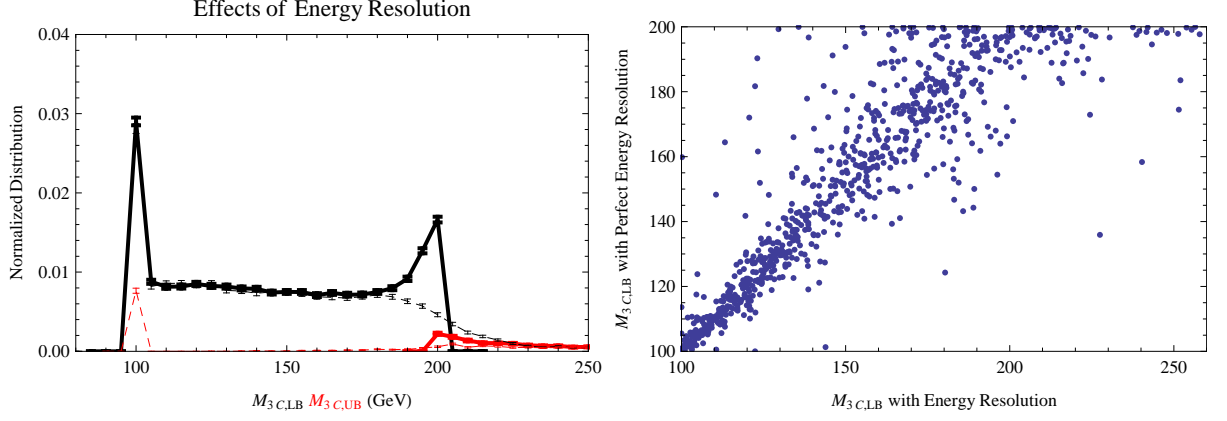


Figure 8.3: The effect of energy resolution on the M_{3C} distribution. (Left) The dotted line shows the energy resolution has washed out the sharp cut-off. (Right) $M_{3C, LB}$ with perfect energy resolution plotted against the result with realistic energy resolutions.

to the true value of M_Y (200 GeV in this case) are more sensitive to energy resolution than the events with M_{3C} closer to ΔM_{YN} . The peak in the upper-bound distribution at $M_{3C, UB} = 100$ GeV comes from events that no longer have solutions after smearing the four momenta.

Because the energy resolution affects the distribution shape, its correct modeling is important. In the actual LHC events the \cancel{P}_T energy resolution will depend on the hadronic activity in the events being considered. Two events with the same $k_T = 0$ may have drastically different \cancel{P}_T resolutions. Modeling the actual detector's energy resolution for the events used is important to predict the set of ideal distribution shapes which are compared against the low-statistics observed data.

• Parton Distribution Function Dependence

For a mostly model-independent mass determination technique, we would like to have a distribution that is independent of the specific production mechanism of the assumed event topology. The parton distributions determine the center-of-mass energy \sqrt{s} of the hard collisions; but the cross section depends on model-dependent couplings and parameters. The events we consider may come from production of different initial states (gluons or squarks) but end in the assumed decay topology. The M_{3C} distribution, like the M_{2C} distribution, shows very little dependence on the underlying collision parameters or circumstances.

Fig 8.4 (Left) shows the dependence of the M_{3C} distributions on the parton collision energy. The solid line shows the M_{3C} distributions of events with collision energy \sqrt{s} distributed according to Eq(7.10), and the dashed line shows the M_{3C} distributions of events with fixed $\sqrt{s} = 600$ GeV. Fig 8.4 (Right) shows the difference of these two distributions with 2σ error

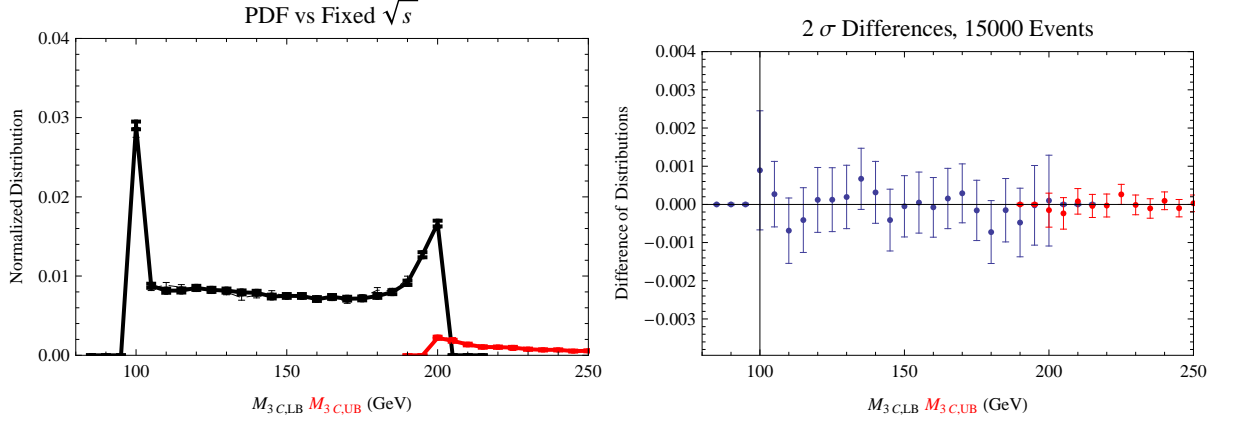


Figure 8.4: The dependence of the M_{3C} distributions on the parton collision energy. The solid line shows the collision distributed according to Eq(7.10), and the dashed line shows the collision energy fixed at $\sqrt{s} = 600$ GeV.

bars as calculated from 15000 events. The two distributions are equal to within this numerical precision.

• Effects of \cancel{p}_T Cuts

As described in [187, 186, 15, 16], the Standard Model four leptons with missing transverse momentum backgrounds are very strongly suppressed after a missing transverse momentum cut. This requires an analysis of what type of an effect a $\cancel{p}_T > 20$ GeV cut will have on the distribution shape. Fig. 8.5 shows that the effect of this cut is dominantly on the smallest M_{3C} bins. On the left we see the $M_{3C, LB}$ result versus the \cancel{p}_T . Unlike the M_{2C} case in Fig 7.8, the M_{3C} solutions in Fig. 8.5 do not correlate with the \cancel{p}_T . The right side of the figure shows difference between the $M_{3C, UB}$ and $M_{3C, LB}$ distributions with and without the cut $\cancel{p}_T > 20$ GeV. The smallest bins of $M_{3C, LB}$ are the only bins to be statistically significantly affected. The left-side suggests this lack of dependence on \cancel{p}_T cuts is somewhat accidental and is due to the nearly uniform distribution of M_{3C} solutions being removed by the cut. The stronger dependence of the smallest M_{3C} bins on the \cancel{p}_T cut means we can either model the effect or exclude the first bins (about 10 GeV worth) from the distribution used to predict the mass. We will choose the latter because we will find that the background events also congregate in these first several bins.

• Spin correlations

In our simulation to produce the ideal curves, we assumed each decay was uncorrelated with its spin in the rest frame of the decaying particle. Spin correlations at production may affect

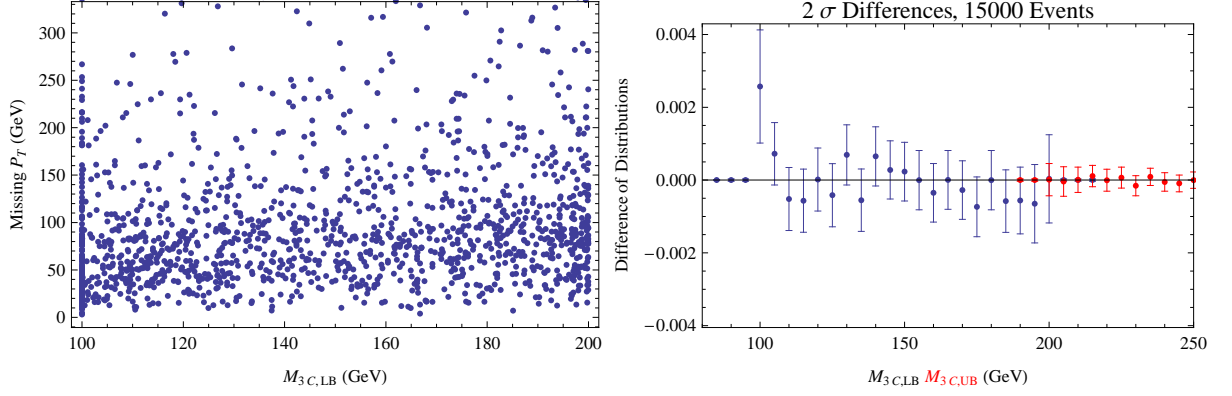


Figure 8.5: The effect of missing transverse momentum cuts on the M_{3C} distributions. (Left) The $M_{3C, LB}$ result versus the \cancel{P}_T . (Right) The difference of the $M_{3C, UB}$ and $M_{3C, LB}$ distributions with and without the cut $\cancel{P}_T > 20$ GeV. The smallest bins of $M_{3C, LB}$ are the only bins to be statistically significantly affected.

this; however, such spin correlations are washed out when each branch of our assumed topology is at the end of longer decay chain. These upstream decays are the source of considerable UTM.

Some spin correlation information can be easily taken into account. The m_{12} (or m_{34}) distribution's shape is sensitive to the spin correlations along the decay chain [150]. The observed m_{12} (or m_{34}) distribution can be used as an input to producing the ideal distribution shape. In this way spin correlations along the decay chain can be taken into account in the simulations of the ideal distributions.

Spin correlations between the two branches can also affect the distribution shape. To demonstrate this, we modeled a strongly spin-correlated direct production process. Fig 8.6 (Left) shows the spin-correlated process that we consider. Fig 8.6 (Right) shows the M_{3C} upper and lower bound distributions from this process compared to the M_{3C} distribution from the same topology and masses but without spin correlations. We compare distributions with perfect energy resolution, $m_{v_1} = m_{v_2} = 0$ GeV, $M_Y = 200$ GeV, $M_X = 150$ GeV, and $M_N = 100$ GeV. Our maximally spin-correlated process involves pair production of Y through a pseudoscalar A . The fermion Y in both branches decays to a complex scalar X and visible fermion v_1 through a purely chiral interaction. The scalar X then decays to the dark-matter particle N and another visible particle v_2 . The production of the pseudoscalar ensures that the Y and \bar{Y} are in a configuration $\sqrt{2}^{-1}(|\uparrow\downarrow\rangle + |\downarrow\uparrow\rangle)$. The particle Y then decays with X preferentially aligned with the spin. The \bar{Y} decays with X^* preferentially aligned against the spin. Because X is a scalar, the particle N decays uniformly in all directions from the rest frame of X . The correlated directions of X causes the two sources of missing transverse momentum to be preferentially parallel. The resulting greater magnitude of missing transverse momentum increases the cases where M_{3C} has

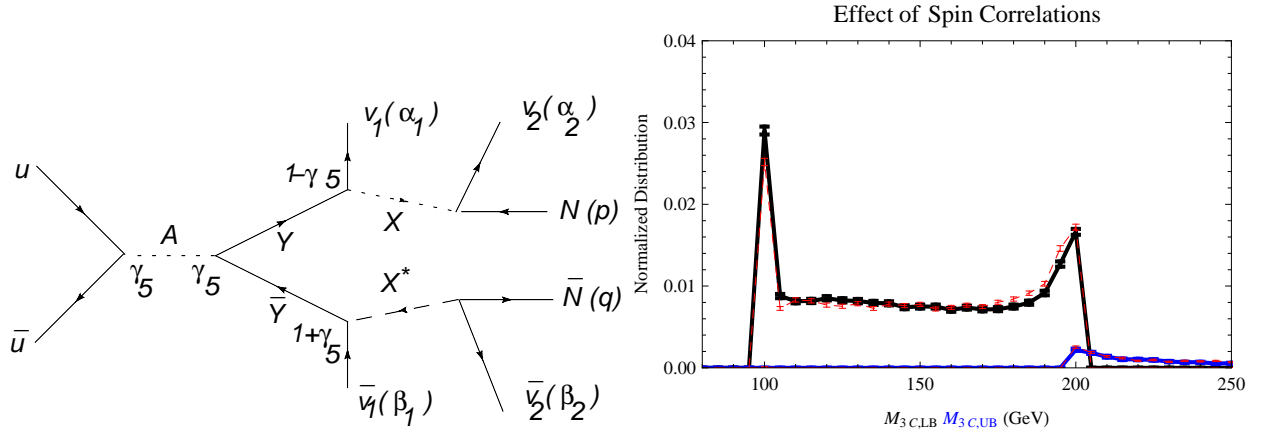


Figure 8.6: Effect of a spin correlated process on the M_{3C} distributions. Modeled masses are $M_Y = 200$ GeV, $M_X = 150$ GeV, and $M_N = 100$ GeV. The thick black and thick blue lines show the distributions of the uncorrelated lower bound and upper bound M_{3C} . The dotted red lines show the distributions of the spin correlated process.

a solution closer to the endpoint. For this reason the spin correlated distribution (red dotted distribution) is above the uncorrelated distribution (black thick lower bound distribution and blue thick upper bound distribution). The upper bound distribution is statistically identical after 25000 events. The lower bound distribution clearly has been changed, but not as much as the M_{2C} distribution in Fig. 6.3. This is due to the subsequent decay of the X particle which lessens the likelihood that the two N s will be parallel. For the remainder of the chapter we assume no such spin correlations are present.

• Backgrounds

The Standard Model backgrounds for four-leptons and missing transverse momentum are studied in [187, 186]. In the two previous chapters we summarized the SM backgrounds and the dominance of SUSY backgrounds for this channel (see also [15][16]). As was mentioned earlier, the Standard Model backgrounds for four leptons with missing transverse momentum are very strongly suppressed after a missing transverse momentum cut.

To improve the quality of the fit, a model for backgrounds can be created based on assumptions about the origin of the events and wedge-box analysis like those described in Bisset *et.al*[160] and references therein. We performed such a model in the previous chapter, and found the distribution shape isolated the correct mass of $\tilde{\chi}_1^0$ to within 1 GeV with versus without the background model. Although the quality of the fit without modeling the backgrounds is decreased, we find that the mass of the LSP associated with the best-fit is tolerant to unknown backgrounds. In the SPS 1a example studied in the next section, SUSY background events form

about 12% of the events. We again see less than a 1 GeV shift in $M_{\tilde{\chi}_1^0}$ with versus without the background events. As such, we do not try to model the background in this M_{3C} study.

8.4 Estimated Performance

With an understanding of the factors affecting the shapes of the M_{3C} distributions, we combine all the influences together and consider the mass determination performance. We follow the same modeling and simulation procedures used in Sec. 7.2 except now we include an on-shell intermediate state and calculate M_{3C} . We use HERWIG [17, 18, 19] to generate events according to the SPS 1a model [3]. This is an mSUGRA model with $m_o = 100$ GeV, $m_{1/2} = 250$ GeV, $A_o = -100$ GeV, $\tan\beta = 10$, and $\text{sign}(\mu) = +$. We initially assume the mass differences $\Delta M_{YN} = 80.8$ GeV and $\Delta M_{XN} = 47.0$ GeV have been previously measured and take them as exact. We later show how the distribution shape with the m_{ll} endpoint also solves for the two mass differences.

Like M_{2C} , the M_{3C} distributions is able to be well-predicted from observations. When we are determining masses based on distribution shapes, the larger the area difference between two distributions representing different masses, the more accurately and precisely we will be able to tell the difference. Unfortunately, the M_{3C} distribution is sensitive to the finite momentum resolution errors and combinatoric errors which have the effect to decrease the large area difference between the distributions of two different masses shown in Figs. 8.1.

Just as in Chapter 7, we model the distribution shape with a simple Mathematica Monte Carlo event generator, and compare the predicted distribution shapes against the HERWIG data modeling the benchmark point SPS 1a. We again use the observed UTM as an input to the Mathematica simulated ideal distributions. By modeling with the Mathematica, which does not use the SUSY cross sections, and comparing to more realistic HERWIG generated data, we hope to test that we understand the major dependencies of the shape of the M_{3C} distributions. The Mathematica event generator produces events based on assumptions uniform angular distribution of the parents in the COM frame, the parent particles decay with a uniform angular distribution in the rest frame of the parent. The particles are all taken to be on shell. $k_T > 0$ is simulated by boosting the event in the transverse plane to compensate a specified k_T .

Figure 8.7 shows the performance. The left side of Fig. 8.7 shows the M_{3C} lower bound and upper bound counts per 5 GeV bin from the HERWIG generated data, and it shows the predicted ideal counts calculated with Mathematica using the observed UTM distribution and assuming $M_{\tilde{\chi}_1^0} = 95$ GeV. The upper bound and lower bound show very close agreement. The background

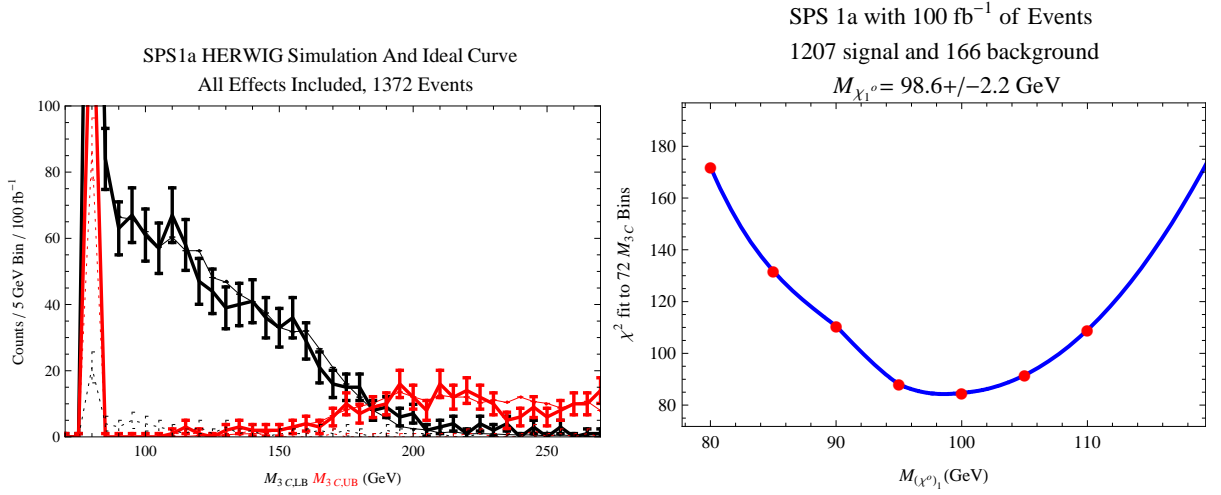


Figure 8.7: Fit of ideal $M_{3C}(M_{\tilde{\chi}_1^0})$ distributions to the HERWIG generated M_{3C} distributions. Includes combinatoric errors, backgrounds, energy resolution, and \cancel{p}_T cuts. (Left) The observed HERWIG counts versus the expected counts for ideal $M_{\tilde{\chi}_1^0} = 95$ GeV. (Right) The χ^2 fit to ideal distributions of $M_{\tilde{\chi}_1^0} = 80, 85, 90, 95, 100, 105, 110$ GeV. The correct mass is $M_{\tilde{\chi}_1^0} = 96.0$ GeV.

events are shown in dotted lines and are seen accumulating in the first few bins. These are the same bins dominantly affected by \cancel{p}_T cuts. For this reason we excluded these first two bins from the distribution fit. The right side of Fig 8.7 shows the χ^2 fit of the HERWIG simulated data M_{3C} distribution to the ideal $M_{3C}(M_{\tilde{\chi}_1^0})$ distribution with $M_{\tilde{\chi}_1^0}$ taken as the independent variable. Ideal distribution shapes are calculated at values of $M_{\tilde{\chi}_1^0} = 80, 85, 90, 95, 100, 105, 110$ GeV. The χ^2 fitting procedure is described in more detail in Appendix D. All effects discussed in this chapter are included: combinatoric errors, SUSY backgrounds, energy resolution, and \cancel{p}_T cuts. Our ideal curves were based on the Mathematica simulations with 25000 events per ideal curve. Despite the presence of backgrounds, the χ^2 is not much above 1 per bin.

The particular fit shown in Fig 8.7 gives $M_{\tilde{\chi}_1^0} = 98.6 \pm 2.2$ GeV where we measure uncertainty by using the positions at which χ^2 is increased by one. We repeat the fitting procedure on nine sets each with ≈ 100 fb⁻¹ of HERWIG data (≈ 1400 events for each set). The mean and standard deviation of these nine fits give $M_{\tilde{\chi}_1^0} = 96.8 \pm 3.7$ GeV. After 300 fb⁻¹ one should expect a $\sqrt{3}$ improvement in the uncertainty giving ± 2.2 GeV. The correct mass is $M_{\tilde{\chi}_1^0} = 96.05$ GeV.

Our technique also enables a combined fit to both the mass differences and the mass scale. The m_{ll} endpoint in Eq(4.3) constrains a relationship between the three masses. Gjelsten, Miller, and Osland estimate this edge can be measured to better than 0.08 GeV [157, 159] using many different channels that lead to the same edge, and after modeling energy resolution and background. In the next several paragraphs we show that by combining this edge with the fits to the M_{3C} upper bound and lower bound distribution shapes, we can constrain all three masses.

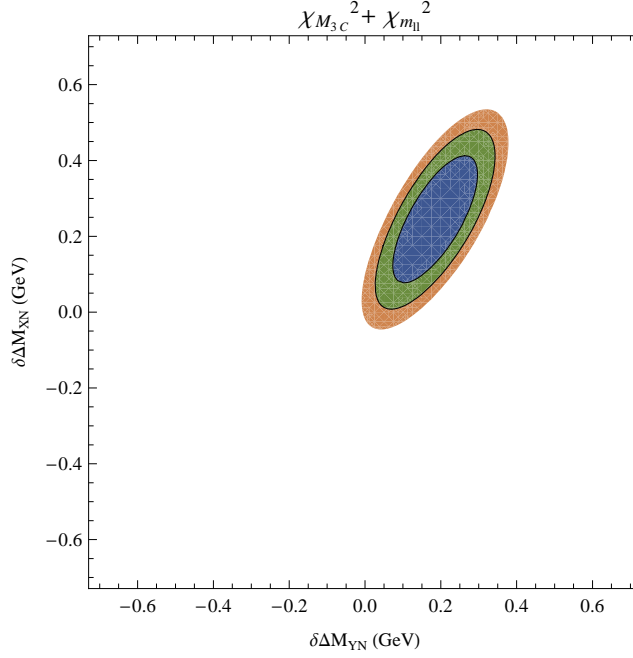


Figure 8.8: Combined constraint from fitting both $\max m_{ll}$ and M_{3C} with the mass difference as free parameters. We parameterized the difference from the true values in the model by $\Delta M_{YN} = 80.8 \text{ GeV} + \delta\Delta M_{YN}$ and $\Delta M_{XN} = 47.0 \text{ GeV} + \delta\Delta M_{XN}$. We shown the $1, 2, 3\sigma$ contours.

We first numerically calculated the effect of errors in the mass differences. We used 300 fb^{-1} of events (about 3600 signal and 450 background) including all the effects discussed. We parameterize the error from the correct mass difference in the model by the variables $\delta\Delta M_{YN}$ and $\delta\Delta M_{XN}$ so that mass differences are given by $\Delta M_{YN} = 80.8 \text{ GeV} + \delta\Delta M_{YN}$ and $\Delta M_{XN} = 47.0 \text{ GeV} + \delta\Delta M_{XN}$. We calculated the $\chi^2_{M_{3C}}$ at 8 points surrounding the correct mass difference by amounts $\delta\Delta M_{YN} = \pm 1 \text{ GeV}$ and $\delta\Delta M_{XN} = \pm 1 \text{ GeV}$. The minimum $\chi^2_{M_{3C}}$ at each of the 9 points gives the value of $M_{\tilde{\chi}_1^0}$ for each mass difference assumed. The position of the minima can be parameterized by a quadratic near the true mass difference. The resulting fit

$$M_{\tilde{\chi}_1^0} = 96.4 + 1.9 (\delta\Delta M_{XN})^2 + 2.5 \delta\Delta M_{YN} \delta\Delta M_{XN} + 3.2 \delta\Delta M_{XN} - 3.8 (\delta\Delta M_{YN})^2 - 8.3 \delta\Delta M_{YN} \quad (8.15)$$

shows in units of GeV how the mass $M_{\tilde{\chi}_1^0}$ is affected by small errors in the mass difference.

The $\chi^2_{M_{3C}}$ at these 9 different values for the mass difference provides another constraint on the mass differences. Fitting the $\chi^2_{M_{3C}}$ to a general quadratic near the true mass difference gives

$$\chi^2_{M_{3C}} = 162 + 38 (\delta\Delta M_{XN})^2 - 8 \delta\Delta M_{YN} \delta\Delta M_{XN} - 5 \delta\Delta M_{XN} - 25 \delta\Delta M_{YN}. \quad (8.16)$$

The $\chi^2_{M_{3C}}$ described by Eq(8.16) shows a sloping valley. The sides of the valley constrain $\delta\Delta M_{XN}$ as seen by the large positive coefficient of $(\delta\Delta M_{XN})^2$. The valley slopes downward

along $\delta\Delta M_{YN}$ as can be seen by the large negative coefficient of $\delta\Delta M_{YN}$ which leaves this axis unbounded within the region studied.

The unconstrained direction along ΔM_{YN} can be constrained by the mass relationships given by the endpoint $\max m_{ll}$ or by M_{T2} as described in Chapter 5. Here we work with $\max m_{ll}$ to provide this constraint. We calculate the $\chi^2_{\max m_{ll}}$ using $\delta \max m_{ll} = 0.08$ GeV, and Eq(4.3) with $M_Y = \Delta M_{YN} + \delta\Delta M_{YN} + M_{\tilde{\chi}_1^o}$ and $M_X = \Delta M_{XN} + \delta\Delta M_{XN} + M_{\tilde{\chi}_1^o}$ where we use $M_{\tilde{\chi}_1^o}$ from Eq(8.15). This $\chi^2_{\max m_{ll}}$ constrains a diagonal path in $(\delta\Delta M_{YN}, \delta\Delta M_{XN})$. The value of the $\chi^2_{\max m_{ll}}$ at the minimum is a constant along this path. The combined constraint $\chi^2_{M_{3C}}$ to $\chi^2_{\max m_{ll}}$ leads to the a minimum at $\delta\Delta M_{YN} = 0.18$ GeV and $\delta\Delta M_{XN} = 0.25$ GeV where $M_{\tilde{\chi}_1^o} = 95.7$ GeV as shown in Fig. 8.8. We have shown the contours where χ^2 increases from its minimum by 1, 2 and 3. The uncertainty in the mass differences around this minimum is about ± 0.2 GeV. The bias from the true mass differences is due to the unconstrained $\chi^2_{M_{3C}}$ along $\delta\Delta M_{YN}$. We can use modeling to back out the unbiased mass differences. Propagating the effects of uncertainty in the mass differences, we estimate a final performance of $M_{\tilde{\chi}_1^o} = 96.4 \pm 2.4$ GeV after 300 fb^{-1} with about 3600 signal events amid 450 background events. We find the mass differences (without bias correction) of $M_{\tilde{\chi}_2^o} - M_{\tilde{\chi}_1^o} = 81.0 \pm 0.2$ GeV and $M_{\tilde{l}_R} - M_{\tilde{\chi}_1^o} = 44.3 \pm 0.2$ GeV. This is to be compared to the HERWIG values of $M_{\tilde{\chi}_1^o} = 96.0$ GeV, $M_{\tilde{\chi}_2^o} - M_{\tilde{\chi}_1^o} = 80.8$ GeV, and $M_{\tilde{l}_R} - M_{\tilde{\chi}_1^o} = 44.3$ GeV.

How does this performance compare to other techniques? Because SPS 1a is commonly used as a test case, we can approximately compare performance with two different groups. The technique of [156, 157, 158, 159] which uses edges from cascade decays determines the LSP mass to ± 3.4 GeV with about 500 thousand events from 300 fb^{-1} . The approach of CEGHM [167] assumes a pair of symmetric decay chains and assumes two events have the same structure. They reach ± 2.8 GeV using 700 signal events after 300 fb^{-1} , but have a 2.5 GeV systematic bias that needs modeling to remove. Both techniques also constrain the mass differences. By comparison we find ± 3.7 GeV after 100 fb^{-1} (1200 signal, 150 background) and estimate ± 2.4 GeV after 300 fb^{-1} (3600 signal, 450 background) and propagating reasonable uncertainties in the mass differences. The uncertainty calculations differ amongst groups. Some groups estimate uncertainty from repeated trials, and others use the amount one can change the mass before χ^2 increases by one. Without careful comparison under like circumstance by the same research group, the optimal method is not clear. What is clear is that fitting the M_{3C} and $M_{3C,UB}$ distributions determines the mass of invisible particles as well if not better than the other known methods in both accuracy and precision.

Chapter Summary

In this chapter, we have extended the constrained mass variable to the case with three new particle states. We assume events with a symmetric, on-shell intermediate-state topology shown in Fig. 4.3. We can either assume that we have measured the mass difference between these new states through other techniques, or combine our technique with the $\max m_{ll}$ edge to find both mass differences and the mass scale. The new constrained mass variables associated with events with these three new particle states are called $M_{3C, LB}$ and $M_{3C, UB}$, and they represent an event-by-event lower bound and upper bound (respectively) on the mass of the third lightest state possible while maintaining the constraints described in Eqs(8.2-8.7). We have shown that most of the M_{2C} distribution properties described in the previous chapter carry through to M_{3C} . The additional particle state and mass difference enable a tighter event-by-event bound on the true mass. The M_{3C} distribution is more sensitive than the M_{2C} distribution to the momentum and energy resolution errors. Studying the performance on the SPS 1a benchmark point, we find that despite the energy resolution degradation, we are able to determine $M_{\tilde{\chi}_1^0}$ to at least the same level of precision and accuracy or possibly even better precision and accuracy than that found by using cascade decays or by using other MSTs.

Chapter 9

Discussions and Conclusions

In this thesis, we have started in Chapter 2 with a study of principles that in the past have successfully predicted the existence and the mass of new particle states. We showed astrophysical evidence for dark matter and discussed properties that make supersymmetry an attractive theory for the dark-matter candidate. We discussed the grand unification of the three gauge couplings, and we introduced the mass-matrix unification suggested by Georgi and Jarlskog. In Chapter 3 we showed how the mass unification is being quantitatively challenged by tighter constraints on the parameters, but that the mass unification hypothesis leads to a favored class of $\tan \beta$ enhanced threshold corrections where $\tan \beta$ is large and the sign of the gluino mass is opposite that of the wino mass. Chapter 4 turns to the task of measuring the masses of new particle states if they are produced with dark matter at hadron colliders. We observed that determining the sign of M_3 , determining spin, and determining the entire sparticle mass spectra are all facilitated by a model-independent measure the mass of the dark-matter particle. We discussed the current techniques to constrain the masses of the new particle states. We developed ideas of how to use M_{T2} in Chapter 5 which enables us to find new constraints between particles in symmetric cascade decays, and we argued that M_{T2} is a better variable to extract this information than M_{CT} . Chapters 6 and 7 discussed the constrained mass variables M_{2C} and $M_{2C,UB}$ which uses a previously measured mass difference to find the maximum and minimum mass of the dark-matter particle on an event-by-event basis. This technique benefits from an M_{2C} and $M_{2C,UB}$ distribution that can be determined from experimental observables and the unknown dark-matter mass. The distribution shape can be fit to the bulk of the data to estimate the mass of the dark-matter particle more accurately than end-point techniques. Chapter 8 discussed the benefits and down-falls of the constraint mass variable M_{3C} . Unlike the edges-from-cascade-decays method [156, 157, 158, 159] and the mass-shell technique of CEGHM[167] each of which require the existence of four new particle states, the constrained mass variables only require two

new particle states for M_{2C} and three new particle states for M_{3C} . Although proper comparisons to other techniques are difficult, it is clear that the constrained mass variables can determine the mass of invisible particles at least as well if not better than the other known model-independent methods in both accuracy and precision.

From here what are the directions for continued research? The origin of the Yukawa mass matrices remains unknown. The Georgi-Jarlskog relations appear to hint at a solution, but only decrease the number of unknowns slightly. The fits to the GUT-scale Yukawa parameters is a starting point for more research on explaining this structure. There are relatively few studies on how to measure the sign of the gluino mass parameter relative to the winos mass parameter; there are even fewer that do not make use of simplifying assumptions about the underlying supersymmetry model. The results of Chapter 5 need to be extended to include the effects of combinatoric ambiguities. In Chapters 7-8 there are several distribution properties which should be better studied. We would like to understand the physics of the invariance of the constrained mass variable distributions to changes in \sqrt{s} and choice of k^2 when $k_T \neq 0$. In Chapter 8 it would also be nice to classify the conditions which determine how many islands of solutions exist for M_{3C} . The M_{3C} method could be tested on top-quark data to remeasure the masses of the t , W and ν . In Chapters 6-8 we have considered two constrained mass variables M_{2C} and M_{3C} where the decay chains are symmetric, but we may find greater statistics for asymmetric events. For example in many models one expects more events where $\tilde{\chi}_2^0$ is produced with $\tilde{\chi}_1^0$ or $\tilde{\chi}^\pm$. The concepts of the constrained mass variable could be extended to deal with these asymmetric event topologies or to cases with both LSPs and neutrinos.

In conclusion, the thesis contributed to predictions of mass properties of new particle states that may be discovered at the LHC and developed the tools to make precision mass measurements that may help falsify or validate this prediction and many others. Modern physics is rooted in an interplay between creating theoretical models, developing experimental techniques, making observations, and falsifying theories. The LHC's results will complete this long-awaited cycle making experimental observations to constrain the growing balloon of theories of which this thesis is a small part.

Appendix A

Renormalization Group Running

This appendix details our use of the Renormalization Group Equations (RGEs) to relate the reported values for observables at low-energy scales to their values the GUT scale. The one-loop and two-loop RG equations for the gauge coupling and the Yukawa couplings in the Standard Model and in the MSSM that we use in this thesis come from a number of sources [113][40][114][110]. We solve the system using the internal differential equation solver in Mathematica 6.0 on a basic Intel laptop. We considered using SoftSUSY or SuSpect to decrease the likelihood of programming errors on our part, but neither met our needs sufficiently. SoftSUSY[191] has only real Yukawa couplings, and SuSpect [183] focuses primarily on the third generation RG evolution.

We assume a model for the neutrino spectrum that does not impact the running of the quark or charged lepton parameters below the GUT scale. This assumption is not trivial; there are neutrino models where Y^ν will affect the ratio y_b/y_τ by as much as 15% [192]. Furthermore due to unitarity constraints, the UV completion of the effective dimension-five neutrino mass operators must take place before the GUT scale [193]. One way to have a UV completion below the GUT scale while making the RGE running independent of the specific model is to set-up a non-degenerate right-handed neutrino spectrum. One then constructs the couplings such that large Yukawa couplings in Y^ν are integrated out with the heaviest right-handed neutrino mass which is at or above the GUT scale. One can then have the remaining right-handed neutrinos considerably below the GUT scale which couple to much smaller values Y^ν that do not affect the running of Y^e or Y^u . The rules for running the neutrino parameters and decoupling the right-handed neutrinos for the U_{MNS} are found in Refs. [113][194] [195] [196] [197]. For our work finding the quark and lepton masses and mixings at the GUT scale, we assume the effects of the neutrinos on the RGE equations effectively decouple at or above the GUT scale.

Our running involves three models at different energy scales. Between M_X to an effective

SUSY scale M_S , we assume the MSSM. Between M_S to M_Z , we assume the Standard Model. Below M_Z , we assume QCD and QED . We do not assume unification, rather we use the low-energy values in Table 3.1 and Eq(3.1) provide our boundary condition. The uncertainty in the final digit(s) of each parameter is listed in parenthesis. For example 123.4 ± 0.2 is written as 123.4(2).

First, we use QCD and QED low-energy effective theories to run the quark and lepton masses from the scales at which the particle data book reports their values to M_Z . The V_{CKM} mixing angles are set at this scale. Next, we run using the Standard-Model parameters, including the Higgs VEV and Higgs self coupling from M_Z to an effective SUSY scale M_S . At an effective SUSY scale M_S , we match the Standard Model Yukawa couplings using the running Higgs VEV $v(M_S)$ onto MSSM Yukawa couplings. In the matching procedure, we convert the gauge coupling constants from \overline{MS} to \overline{DR} as described in [191], and we apply approximate supersymmetric threshold corrections as parameterized in Chapter 3. Details of the RG equations and the matchings are described in the following sections.

A.1 RGE Low-Energy $SU(3)_c \times U(1)_{EM}$ up to the Standard Model

Below M_Z we use QCD and QED RG Equations to move the parameters to the scale reported in the Particle Data Book. We run the light-quark masses between $\mu = M_Z$ to $\mu_L = 2 \text{ GeV}$ with the following factors:

$$\eta_{u,d,s} = (1.75 \pm 0.03) + 19.67 \left(\alpha_s^{(5)}(M_Z) - 0.118 \right) \quad (\text{A.1})$$

$$\eta_c = (2.11 \pm 0.03) + 41.13 \left(\alpha_s^{(5)}(M_Z) - 0.118 \right) \quad (\text{A.2})$$

$$\eta_b = (1.46 \pm 0.02) + 8.14 \left(\alpha_s^{(5)}(M_Z) - 0.118 \right), \quad (\text{A.3})$$

that are calculated with the 4-loop RGE equations using Chetyrkin's RUNDEC software for Mathematica [198]. These factors are used as $m_b(m_b)/\eta_b = m_b(M_Z)$. The uncertainty in the first term is an estimate of the theoretical error from neglecting the five-loop running give by $\delta\eta/\eta \approx \exp(\mathcal{O}(1)\langle\alpha_s\rangle^5 \log \frac{M_Z}{\mu_L}) - 1$. RUNDEC also converts the top quark's pole mass to an \overline{MS} running mass, and applies the small threshold corrections from decoupling each of the quarks. The different η factors take the parameters from a six-quark effective model at $\mu = M_Z$ to their respective scales.

The leptons can be converted from their Pole mass into running masses at M_Z by a similar running factor:

$$\eta_e = 1.046 \quad \eta_\mu = 1.027 \quad \eta_\tau = 1.0167. \quad (\text{A.4})$$

Parameter	At Scale $\mu = M_Z$
m_t	169.6(2.3) GeV
m_c	599(50) MeV
m_u	1.54(50) MeV
m_b	2.87(6) GeV
m_s	57(12) MeV
m_d	3.1(5) MeV

Table A.1: The \overline{MS} values for the running quark masses at M_Z .

We did not incorporate the lepton masses as error sources.

The input values in Table 3.1 lead to the values at M_Z in Table A.1 where we have propagated uncertainty from both the strong coupling constant uncertainty and the uncertainty in the mass at the starting scale. These values for the parameters at M_Z agree with those calculated recently elsewhere in the literature [199].

The gauge coupling constants g_1 and g_2 are determined from e_{EM} , $\sin^2 \theta_W$ at the scale M_Z by

$$g_1^2(M_Z) = \frac{5}{3} \frac{e_{EM}^2(M_Z)}{\cos^2 \theta_W} \quad g_2^2(M_Z) = \frac{e_{EM}^2(M_Z)}{\sin^2 \theta_W}. \quad (\text{A.5})$$

A.2 RGE for Standard Model with Neutrinos up to MSSM

We found using the two-loop vs the one-loop RG equations for the gauge-coupling produced a shift in the low energy parameters of more than 1σ . For this reason, we always use two-loop RG equations for the gauge couplings. For the Yukawa couplings we find the two-loop vs the one-loop RGE equations shift the low-energy parameters much less than the experimental uncertainty. Therefore, we perform our minimizations using the one-loop RG equations for the Yukawa and checked the final fits against the two-loop RG equations.

We reproduce here for reference the two-loop gauge coupling RG equations and the one-loop Yukawa coupling RG equations as this level of detail is sufficient to reproduce our results. We

define $t = \log M$. The equations are compiled from [196], [113], [110].

$$\begin{aligned}
\frac{d}{dt}g_1 &= \frac{1}{16\pi^2} \frac{41}{10} g_1^3 \\
&+ \frac{g_1^3}{(16\pi^2)^2} \left(\frac{199}{50} g_1^2 + \frac{27}{15} g_2^2 + \frac{44}{5} g_3^2 - \frac{17}{10} \text{Tr}(Y^u Y^{u\dagger}) - \frac{1}{2} \text{Tr}(Y^d Y^{d\dagger}) - \frac{3}{2} \text{Tr}(Y^e Y^{e\dagger}) \right) \\
\frac{d}{dt}g_2 &= \frac{1}{16\pi^2} \frac{-19}{6} g_2^3 \\
&+ \frac{g_2^3}{(16\pi^2)^2} \left(\frac{9}{10} g_1^2 + \frac{35}{6} g_2^2 + 12 g_3^2 - \frac{3}{2} \text{Tr}(Y^u Y^{u\dagger}) - \frac{3}{2} \text{Tr}(Y^d Y^{d\dagger}) - \frac{1}{2} \text{Tr}(Y^e Y^{e\dagger}) \right) \\
\frac{d}{dt}g_3 &= \frac{-7}{16\pi^2} g_3^3 \\
&+ \frac{g_3^3}{(16\pi^2)^2} \left(\frac{11}{10} g_1^2 + \frac{9}{2} g_2^2 - 26 g_3^2 - 2 \text{Tr}(Y^u Y^{u\dagger}) - 2 \text{Tr}(Y^d Y^{d\dagger}) \right)
\end{aligned} \tag{A.8}$$

$$T = \text{Tr}(3Y^u Y^{u\dagger} + 3Y^d Y^{d\dagger} + Y^e Y^{e\dagger} + Y^\nu Y^{\nu\dagger}) \tag{A.9}$$

$$\frac{d}{dt}Y^u = \frac{1}{16\pi^2} \left(-\mathbf{I} G^u + \mathbf{I} T + \frac{3}{2} Y^u Y^{u\dagger} - \frac{3}{2} Y^d Y^{d\dagger} \right) \cdot Y^u \tag{A.10}$$

$$\frac{d}{dt}Y^\nu = \frac{1}{16\pi^2} \left(-\mathbf{I} G^\nu + \mathbf{I} T + \frac{3}{2} Y^\nu Y^{\nu\dagger} - \frac{3}{2} Y^e Y^{e\dagger} \right) \cdot Y^\nu \tag{A.11}$$

$$\frac{d}{dt}Y^d = \frac{1}{16\pi^2} \left(-\mathbf{I} G^d + \mathbf{I} T + \frac{3}{2} Y^d Y^{d\dagger} - \frac{3}{2} Y^u Y^{u\dagger} \right) \cdot Y^d \tag{A.12}$$

$$\frac{d}{dt}Y^e = \frac{1}{16\pi^2} \left(-\mathbf{I} G^e + \mathbf{I} T + \frac{3}{2} Y^e Y^{e\dagger} - \frac{3}{2} Y^\nu Y^{\nu\dagger} \right) \cdot Y^e \tag{A.13}$$

where

$$\begin{aligned}
G^u &= \frac{17}{20} g_1^2 + \frac{9}{4} g_2^2 + 8 g_3^2 & G^d &= \frac{1}{4} g_1^2 + \frac{9}{4} g_2^2 + 8 g_3^2 \\
G^e &= \frac{9}{4} g_1^2 + \frac{9}{4} g_2^2 & G^\nu &= \frac{9}{20} g_1^2 + \frac{9}{4} g_2^2.
\end{aligned} \tag{A.14}$$

The Higgs self-interaction λ (following the convention $-\lambda(H^\dagger H)^2 \subset \mathcal{L}$) obeys the RG equation:

$$16\pi^2 \frac{d}{dt} \lambda = 12\lambda^2 - \left(\frac{9}{5} g_1^2 + 9g_2^2 \right) \lambda + \frac{9}{4} \left(\frac{3}{25} g_1^4 + \frac{2}{5} g_1^2 g_2^2 + g_2^4 \right) + 4T\lambda \tag{A.15}$$

$$-4\text{Tr}(3Y^u Y^{u\dagger} Y^u Y^{u\dagger} + 3Y^d Y^{d\dagger} Y^d Y^{d\dagger} + Y^e Y^{e\dagger} Y^e Y^{e\dagger}). \tag{A.16}$$

Between M_Z and M_S , we run the Standard-Model VEV using [40]:

$$16\pi^2 \frac{d}{dt} v = v \left(\frac{9}{4} \left(\frac{1}{5} g_1^2 + g_2^2 \right) - T \right). \tag{A.17}$$

$$\begin{aligned}
16\pi^2 \frac{d}{dt} \kappa &= \left(-\frac{3}{2} Y^e Y^{e\dagger} \kappa - \frac{3}{2} \kappa Y^e Y^{e\dagger} + \frac{1}{2} Y^\nu Y^{\nu\dagger} \kappa + \frac{1}{2} \kappa Y^\nu Y^{\nu\dagger} \right) \\
&+ \mathbf{I} \left(\text{Tr}(2Y^\nu Y^{\nu\dagger} + 2Y^e Y^{e\dagger} + 6Y^u Y^{u\dagger} + 6Y^d Y^{d\dagger}) - 3g_2^2 + 4\lambda \right) \kappa \\
\frac{d}{dt} M_{RR} &= \frac{1}{16\pi^2} \left((Y^{\nu\dagger} Y^\nu)^T M_{RR} + M_{RR} Y^{\nu\dagger} Y^\nu \right).
\end{aligned} \tag{A.18}$$

We normalize g_1 to the $SU(5)$ convention: $g_1^2 = \frac{3}{5} g_Y^2$.

A.3 RGE for the MSSM with Neutrinos up to GUT Scale

The MSSM RG equations are in the \overline{DR} scheme. To convert \overline{MS} running quark masses to \overline{DR} masses at the same scale, we use [111]

$$\delta m_{sch} = \frac{m_{\overline{DR}}}{m_{\overline{MS}}} = \left(1 - \frac{1}{3} \frac{g_3^2}{4\pi^2} - \frac{29}{72} \left(\frac{g_3^2}{4\pi^2} \right)^2 \right). \quad (\text{A.19})$$

No corrections were used for switching lepton running masses from one scheme to the other.

The gauge coupling constants are related via [191]

$$\alpha_{3\overline{DR}}^{-1} = \alpha_{3\overline{MS}}^{-1} + \frac{3}{12\pi} \quad (\text{A.20})$$

$$\alpha_{2\overline{DR}}^{-1} = \alpha_{2\overline{MS}}^{-1} + \frac{2}{12\pi} \quad (\text{A.21})$$

where $\alpha_3 = g_3^2/4\pi$ and $\alpha_2 = g_2^2/4\pi$. We define $t = \log M$. The RG equations are:

$$\begin{aligned} \frac{d}{dt} g_1 &= \frac{1}{16\pi^2} \frac{33}{5} g_1^3 \\ &+ \frac{g_1^3}{(16\pi^2)^2} \left(\frac{199}{25} g_1^2 + \frac{27}{5} g_2^2 + \frac{88}{5} g_3^2 - \frac{26}{5} \text{Tr}(Y^u Y^{u\dagger}) - \frac{14}{5} \text{Tr}(Y^d Y^{d\dagger}) - \frac{18}{5} \text{Tr}(Y^e Y^{e\dagger}) \right) \end{aligned} \quad (\text{A.22})$$

$$\begin{aligned} \frac{d}{dt} g_2 &= \frac{1}{16\pi^2} g_2^3 \\ &+ \frac{g_2^3}{(16\pi^2)^2} \left(\frac{9}{5} g_1^2 + 25 g_2^2 + 24 g_3^2 - 6 \text{Tr}(Y^u Y^{u\dagger}) - 6 \text{Tr}(Y^d Y^{d\dagger}) - 2 \text{Tr}(Y^e Y^{e\dagger}) \right) \end{aligned} \quad (\text{A.23})$$

$$\begin{aligned} \frac{d}{dt} g_3 &= \frac{-3}{16\pi^2} g_3^3 \\ &+ \frac{g_3^3}{(16\pi^2)^2} \left(\frac{11}{5} g_1^2 + 9 g_2^2 + 14 g_3^2 - 4 \text{Tr}(Y^u Y^{u\dagger}) - 4 \text{Tr}(Y^d Y^{d\dagger}) \right) \end{aligned} \quad (\text{A.24})$$

$$\frac{d}{dt} Y^u = \frac{1}{16\pi^2} \left(-\mathbf{I} G^u + \mathbf{I} 3 \text{Tr}(Y^u Y^{u\dagger}) + \mathbf{I} \text{Tr}(Y^\nu Y^{\nu\dagger}) + 3 Y^u Y^{u\dagger} + Y^d Y^{d\dagger} \right) \cdot Y^u \quad (\text{A.25})$$

$$\frac{d}{dt} Y^\nu = \frac{1}{16\pi^2} \left(-\mathbf{I} G^\nu + \mathbf{I} 3 \text{Tr}(Y^u Y^{u\dagger}) + \mathbf{I} \text{Tr}(Y^\nu Y^{\nu\dagger}) + 3 Y^\nu Y^{\nu\dagger} + Y^e Y^{e\dagger} \right) \cdot Y^\nu \quad (\text{A.26})$$

$$\frac{d}{dt} Y^d = \frac{1}{16\pi^2} \left(-\mathbf{I} G^d + \mathbf{I} 3 \text{Tr}(Y^d Y^{d\dagger}) + \mathbf{I} \text{Tr}(Y^e Y^{e\dagger}) + 3 Y^d Y^{d\dagger} + Y^u Y^{u\dagger} \right) \cdot Y^d \quad (\text{A.27})$$

$$\frac{d}{dt} Y^e = \frac{1}{16\pi^2} \left(-\mathbf{I} G^e + \mathbf{I} 3 \text{Tr}(Y^d Y^{d\dagger}) + \mathbf{I} \text{Tr}(Y^e Y^{e\dagger}) + 3 Y^e Y^{e\dagger} + Y^\nu Y^{\nu\dagger} \right) \cdot Y^e \quad (\text{A.28})$$

where

$$G^u = \frac{13}{15} g_1^2 + 3 g_2^2 + \frac{16}{3} g_3^2 \quad G^d = \frac{17}{15} g_1^2 + 3 g_2^2 + \frac{16}{3} g_3^2 \quad (\text{A.29})$$

$$G^e = \frac{9}{5} g_1^2 + 3 g_2^2 \quad G^\nu = \frac{3}{5} g_1^2 + 3 g_2^2.$$

$$\begin{aligned} 16\pi^2 \frac{d}{dt} \kappa &= \left(Y^e Y^{e\dagger} \kappa + \kappa Y^e Y^{e\dagger} + Y^\nu Y^{\nu\dagger} \kappa + \kappa Y^\nu Y^{\nu\dagger} \right) \\ &+ \mathbf{I} \left(2 \text{Tr}(Y^\nu Y^{\nu\dagger}) + 6 Y^u Y^{u\dagger} - \frac{6}{5} g_1^2 - 6 g_2^2 \right) \kappa \end{aligned} \quad (\text{A.30})$$

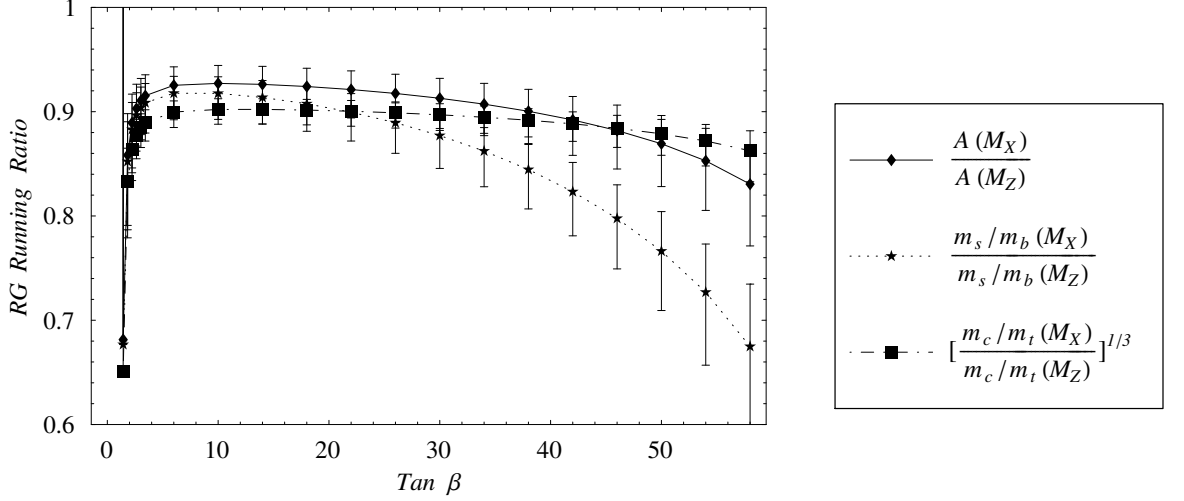


Figure A.1: The impact of RG running parameter ratios with $M_S = 500$ GeV. These ratios determine χ defined in Eq. A.34. If $M_S = M_Z$, all three are degenerate at small $\tan \beta$.

$$\frac{d}{dt} M_{RR} = \frac{1}{16\pi^2} \left(2 (Y^{\nu\dagger} Y^\nu)^T M_{RR} + 2 M_{RR} Y^{\nu\dagger} Y^\nu \right) \quad (\text{A.31})$$

We normalize g_1 to the $SU(5)$ convention: $g_1^2 = \frac{3}{5} g_Y^2$.

A.4 Approximate Running Rules of Thumb

At $\tan \beta < 10$ and when $M_S \sim M_Z$, the running of parameters from M_Z to M_X obey the following relationships exploited in the RRRV [1] study:

$$\frac{\bar{\eta}_o(M_X)}{\bar{\eta}_o(M_Z)} \approx \frac{\bar{\rho}_o(M_X)}{\bar{\rho}_o(M_Z)} \approx \frac{\lambda_o(M_X)}{\lambda_o(M_Z)} \approx 1 \quad \frac{A_o(M_X)}{A_o(M_Z)} \approx \chi \quad (\text{A.32})$$

$$\frac{(m_u/m_c)_o(M_X)}{(m_u/m_c)_o(M_Z)} \approx \frac{(m_d/m_s)_o(M_X)}{(m_d/m_s)_o(M_Z)} \approx 1 \quad \frac{(m_s/m_b)_o(M_X)}{(m_s/m_b)_o(M_Z)} \approx \chi \quad \frac{(m_c/m_t)_o(M_X)}{(m_c/m_t)_o(M_Z)} \approx \chi^3 \quad (\text{A.33})$$

where

$$\chi \approx \exp \left(\int_{t_o}^{t_f} \frac{-y_t^2}{16\pi^2} dt \right) \quad (\text{A.34})$$

and $t_o = \log M_Z$ and $t_f = \log M_X$. Fig. A.1 shows the two-loop results reflecting how the running of these ratios change when we consider $M_S = 500$ GeV and larger values of $\tan \beta$. If we had plotted the $M_S = M_Z$ case, the curves in Fig. A.1 would have been completely degenerate at small $\tan \beta$. As a consistency check, we compare our results to Fusaoka and Koide [110]. They find $\chi \approx 0.851$ at $\tan \beta = 10$ with their choice of $m_t(M_Z) = 180$. Our code also gives $\chi = 0.851$ at $\tan \beta = 10$ if we select $M_S = M_Z$ and omit the conversion to \overline{DR} scheme.

Appendix B

Hierarchical Yukawa couplings and Observables

In this appendix, we find the masses and unitary matrices associated with a general hierarchical Yukawa coupling matrix. We use this expansion to find general expressions for V_{CKM} to the order needed for comparison to current experiments. Consider a general hierarchical Yukawa matrix

$$Y^u = y_t \begin{pmatrix} Y_{11}^u & Y_{12}^u & Y_{13}^u \\ Y_{21}^u & Y_{22}^u & Y_{23}^u \\ Y_{31}^u & Y_{32}^u & 1 \end{pmatrix} \approx Y^u = y_t \begin{pmatrix} \mathcal{O}(\epsilon^4) & \mathcal{O}(\epsilon^3) & \mathcal{O}(\epsilon^3) \\ \mathcal{O}(\epsilon^3) & \mathcal{O}(\epsilon^2) & \mathcal{O}(\epsilon^2) \\ \mathcal{O}(\epsilon^3) & \mathcal{O}(\epsilon^2) & 1 \end{pmatrix} \quad (\text{B.1})$$

where ϵ is a small parameter. Diagonalization of $Y^u Y^{u\dagger}$ leads to the diagonal matrix from $U_L^u Y^u Y^{u\dagger} U_L^{u\dagger} = |D_u|^2$ where $Y^u = U_L^{u\dagger} D_u U_R^u$. The matrix $|D^u|^2$ gives the square of the mass eigenstates.

$$|D_3^u/y_t|^2 = 1 + Y_{23}^u Y_{23}^{u*} + Y_{32}^u Y_{32}^{u*} + \mathcal{O}(\epsilon^5) \quad (\text{B.2})$$

$$|D_2^u/y_t|^2 = Y_{22}^u Y_{22}^{u*} + Y_{12}^u Y_{12}^{u*} + Y_{21}^u Y_{21}^{u*} - Y_{22}^{u*} Y_{23}^u Y_{32}^u - Y_{22}^u Y_{23}^{u*} Y_{32}^{u*} + \mathcal{O}(\epsilon^7) \quad (\text{B.3})$$

$$|D_3^u/y_t|^2 = Y_{11}^u Y_{11}^{u*} - \frac{Y_{11}^{u*} Y_{12}^u Y_{21}^u}{Y_{22}^u} - \frac{Y_{11}^u Y_{12}^{u*} Y_{21}^{u*}}{Y_{22}^{u*}} + \frac{Y_{12}^u Y_{12}^{u*} Y_{21}^u Y_{21}^{u*}}{Y_{22}^u Y_{22}^{u*}} + \mathcal{O}(\epsilon^{10}) \quad (\text{B.4})$$

The resulting approximate expressions for $U_L^{u\dagger}$ are

$$(U_L^{u\dagger})^{13} = Y_{13}^u + Y_{12}^u Y_{32}^{u*} + \mathcal{O}(\epsilon^6) \quad (\text{B.5})$$

$$(U_L^{u\dagger})^{23} = Y_{23}^u + Y_{22}^u Y_{32}^{u*} + \mathcal{O}(\epsilon^6) \quad (\text{B.6})$$

$$(U_L^{u\dagger})^{33} = 1 - \frac{1}{2} Y_{23}^u Y_{23}^{u*} + \mathcal{O}(\epsilon^6) \quad (\text{B.7})$$

$$(U_L^{u\dagger})^{12} = \frac{Y_{12}^u}{Y_{22}^u} \quad (\text{B.8})$$

$$(U_L^\dagger)^{22} = 1 - \frac{1}{2} \left(|Y_{23}^u|^2 + \left| \frac{Y_{12}^u}{Y_{22}^u} \right|^2 \right) + \mathcal{O}(\epsilon^4) \quad (\text{B.9})$$

$$(U_L^\dagger)^{32} = -Y_{23}^{u*} - Y_{22}^{u*} Y_{32}^u - \frac{Y_{12}^u Y_{13}^{u*}}{Y_{22}^u} + \frac{Y_{12}^u Y_{12}^{u*} Y_{23}^{u*}}{2 Y_{22}^u Y_{22}^{u*}} + \mathcal{O}(\epsilon^5) \quad (\text{B.10})$$

$$(U_L^{u\dagger})^{11} = 1 - \frac{1}{2} \left| \frac{Y_{12}^u}{Y_{22}^u} \right|^2 + \mathcal{O}(\epsilon^4) \quad (\text{B.11})$$

$$(U_L^{u\dagger})^{21} = -\frac{Y_{12}^{u*}}{Y_{22}^{u*}} \quad (\text{B.12})$$

$$(U_L^\dagger)^{31} = -Y_{13}^{u*} + \frac{Y_{12}^{u*} Y_{23}^{u*}}{Y_{22}^{u*}} + \mathcal{O}(\epsilon^5). \quad (\text{B.13})$$

These results have been checked numerically including the phase.

If we assume the Y^d Yukawa matrices follow the same form as Eq. B.1, we can obtain parallel expressions for U_L^d . The CKM matrix is then given by $V_{CKM} = U_L^u U_L^{d\dagger}$ and, we obtain these expressions for the individual components:

$$V_{us} = \frac{Y_{12}^d}{Y_{22}^d} - \frac{Y_{12}^u}{Y_{22}^u} + \quad (\text{B.14})$$

$$\begin{aligned} & \frac{-Y_{12}^{d2} Y_{12}^{d*}}{2 Y_{22}^{d2} Y_{22}^{d*}} - \frac{Y_{12}^d Y_{21}^d Y_{21}^{d*}}{Y_{22}^{d2} Y_{22}^{d*}} + \frac{Y_{11}^d Y_{21}^{d*}}{Y_{22}^d Y_{22}^{d*}} - \frac{Y_{13}^d Y_{32}^d}{Y_{22}^d} + \frac{Y_{12}^d Y_{23}^d Y_{32}^d}{Y_{22}^{d2}} + \frac{Y_{12}^d Y_{12}^{d*} Y_{12}^u}{2 Y_{22}^d Y_{22}^{d*} Y_{22}^u} \\ & + \frac{Y_{12}^{u2} Y_{12}^{u*}}{2 Y_{22}^{u2} Y_{22}^{u*}} + \frac{Y_{12}^u Y_{21}^u Y_{21}^{u*}}{Y_{22}^{u2} Y_{22}^{u*}} - \frac{Y_{12}^d Y_{12}^u Y_{12}^{u*}}{2 Y_{22}^d Y_{22}^u Y_{22}^{u*}} - \frac{Y_{11}^u Y_{21}^{u*}}{Y_{22}^u Y_{22}^{u*}} + \frac{Y_{13}^u Y_{32}^u}{Y_{22}^u} - \frac{Y_{12}^u Y_{23}^u Y_{32}^u}{Y_{22}^{u2}} + \mathcal{O}(\epsilon^5) \\ V_{cd} &= -\frac{Y_{12}^{d*}}{Y_{22}^{d*}} + \frac{Y_{12}^{u*}}{Y_{22}^{u*}} \quad (\text{B.15}) \end{aligned}$$

$$\begin{aligned} & -\frac{Y_{12}^u Y_{12}^{u*2}}{2 Y_{22}^u Y_{22}^{u*2}} - \frac{Y_{12}^{u*} Y_{21}^u Y_{21}^{u*}}{Y_{22}^u Y_{22}^{u*2}} + \frac{Y_{12}^{d*} Y_{12}^u Y_{12}^{u*}}{2 Y_{22}^{d*} Y_{22}^u Y_{22}^{u*}} + \frac{Y_{11}^{u*} Y_{21}^u}{Y_{22}^u Y_{22}^{u*}} - \frac{Y_{13}^{u*} Y_{32}^u}{Y_{22}^{u*}} + \frac{Y_{12}^{u*} Y_{23}^u Y_{32}^u}{Y_{22}^{u*2}} \\ & \frac{Y_{12}^d Y_{12}^{d*2}}{2 Y_{22}^d Y_{22}^{d*2}} + \frac{Y_{12}^{d*} Y_{21}^d Y_{21}^{d*}}{Y_{22}^d Y_{22}^{d*2}} - \frac{Y_{11}^d Y_{21}^{d*}}{Y_{22}^d Y_{22}^{d*}} + \frac{Y_{13}^{d*} Y_{32}^d}{Y_{22}^{d*}} - \frac{Y_{12}^{d*} Y_{23}^d Y_{32}^d}{Y_{22}^{d*2}} - \frac{Y_{12}^d Y_{12}^{d*} Y_{12}^u}{2 Y_{22}^d Y_{22}^{d*} Y_{22}^u} + \mathcal{O}(\epsilon^5) \end{aligned}$$

$$V_{ub} = Y_{13}^d - Y_{13}^u - \frac{Y_{23}^d Y_{12}^u}{Y_{22}^u} + \frac{Y_{12}^u Y_{23}^u}{Y_{22}^u} + \mathcal{O}(\epsilon^5) \quad (\text{B.16})$$

$$V_{td} = -Y_{13}^{d*} + Y_{13}^{u*} + \frac{Y_{12}^{d*} Y_{23}^{d*}}{Y_{22}^{d*}} - \frac{Y_{12}^{d*} Y_{23}^{u*}}{Y_{22}^{d*}} + \mathcal{O}(\epsilon^5) \quad (\text{B.17})$$

$$V_{cb} = -Y_{23}^u + Y_{23}^d + \mathcal{O}(\epsilon^4) \quad (\text{B.18})$$

$$V_{ts} = Y_{23}^{u*} - Y_{23}^{d*} + \mathcal{O}(\epsilon^4) \quad (\text{B.19})$$

In the above equations, we have included enough terms to achieve experimental accuracy for the Yukawa couplings.

For completeness, we include the diagonal entries

$$V_{ud} = 1 - \frac{Y_{12}^d Y_{12}^{d*}}{2 Y_{22}^d Y_{22}^{d*}} + \frac{Y_{12}^{d*} Y_{12}^u}{Y_{22}^{d*} Y_{22}^u} - \frac{Y_{12}^u Y_{12}^{u*}}{2 Y_{22}^u Y_{22}^{u*}} \quad (\text{B.20})$$

$$V_{cs} = 1 - \frac{Y_{12}^d Y_{12}^{d*}}{2 Y_{22}^d Y_{22}^{d*}} + \frac{Y_{12}^d Y_{12}^{u*}}{Y_{22}^d Y_{22}^{u*}} - \frac{Y_{12}^u Y_{12}^{u*}}{2 Y_{22}^u Y_{22}^{u*}} \quad (\text{B.21})$$

$$V_{tb} = 1 + Y_{23}^d Y_{23}^{u*} - \frac{Y_{23}^d Y_{23}^{d*}}{2} - \frac{Y_{23}^u Y_{23}^{u*}}{2} \quad (\text{B.22})$$

To express the Wolfenstein A and λ terms to experimental accuracy, one needs the lengthy expression for V_{us} . Because the Wolfenstein parameters are redundant with the V_{CKM} elements from which they are based, we will omit explicit expressions for A and λ . The Wolfenstein parameters $\bar{\rho} + i\bar{\eta}$ represent a phase convention independent expression for the CP violation and can be expressed compactly:

$$\bar{\rho} + i\bar{\eta} = - \frac{Y_{13}^{d*} - Y_{13}^{u*} - \frac{Y_{23}^{d*} Y_{12}^{u*}}{Y_{22}^{u*}} + \frac{Y_{12}^{u*} Y_{23}^u}{Y_{22}^{u*}}}{\left(-\frac{Y_{12}^{d*}}{Y_{22}^{d*}} + \frac{Y_{12}^{u*}}{Y_{22}^{u*}}\right) (Y_{23}^{d*} - Y_{23}^{u*})}. \quad (\text{B.23})$$

The Jarlskog CP Invariant is given by

$$J_{CP} = \text{Im} \left(- \frac{\left(\frac{Y_{12}^{d*}}{Y_{22}^{d*}} - \frac{Y_{12}^{u*}}{Y_{22}^{u*}}\right) \left(- (Y_{23}^d Y_{12}^u) + Y_{13}^d Y_{22}^u - Y_{13}^u Y_{22}^d + Y_{12}^u Y_{23}^u\right) (Y_{23}^{d*} - Y_{23}^{u*})}{Y_{22}^u} \right). \quad (\text{B.24})$$

Appendix C

Verifying M_{T2} in Eq(5.4)

We derived the M_{T2} side of Eq(5.4) by following the analytic solution given by Barr and Lester in [170]. In this appendix, we outline how to verify that M_{T2} is indeed given by

$$M_{T2}(\chi = 0, \alpha, \beta, \vec{P}_T = -\alpha_T - \beta_T) = 2(\alpha_T \cdot \beta_T + |\alpha_T| |\beta_T|) \quad (\text{C.1})$$

when $\alpha^2 = \beta^2 = 0$ and $p^2 = q^2 = \chi^2 = 0$ and $g_T = 0$. To do this we note that M_{T2} can also be defined as the minimum value of $(\alpha + p)^2$ minimized over p and q subject to the conditions $p^2 = q^2 = \chi^2$ (on-shell dark-matter particle state), and $(\alpha + p)^2 = (\beta + q)^2$ (equal on-shell parent-particle state), and $(\alpha + \beta + p + q)_T = 0$ (conservation of transverse momentum) [15].

The solution which gives Eq(C.1) has $p_T = -\beta_T$ and $q_T = -\alpha_T$ with the rapidity of $p(q)$ equal to the rapidity of α (β). We now verify that this solution satisfies all these constraints. Transverse momentum conservation is satisfied trivially: $(\alpha + \beta + p + q)_T = (\alpha + \beta - \alpha - \beta)_T = 0$. The constraint to have the parent particles on-shell can be verified with $2|\alpha_T||p_T| - 2\vec{p}_T \cdot \vec{\alpha}_T = 2|\beta_T||q_T| - 2\vec{q}_T \cdot \vec{\beta}_T = 2|\beta_T||\beta_T| + 2\vec{\alpha}_T \cdot \vec{\beta}_T$.

Now all that remains is to show that the parent particle's mass is at a minimum with respect to ways in which one splits up p and q to satisfy $p_T + q_T = \vec{P}_T$ while satisfying the above constraints. We take p and q to be a small deviation from the stated solution $p_T = -\beta_T + \delta_T$ and $q_T = -\alpha_T - \delta_T$ where δ_T is the small deviation in the transverse plane. We keep p and q on shell at $\chi = 0$. The terms p_o, p_z, q_o, q_z are maintained at their minimum by keeping the rapidity of p and q equal to α and β . The condition $(p + \alpha)^2 = (q + \beta)^2$ is satisfied for a curve of values for δ_T . The deviation tangent to this curve near $|\delta_T| = 0$ is given by $\delta_T(\lambda) = \lambda \hat{z} \times (\alpha_T |\beta_T| + \beta_T |\alpha_T|)$ where \times is a cross product, \hat{z} denotes the beam direction, and we parameterized the magnitude by the scalar λ . Finally, we can substitute p and q with the deviation $\delta_T(\lambda)$ back into the expression $(\alpha + p)^2$ and verify that $2(\alpha_T \cdot \beta_T + |\alpha_T| |\beta_T|)$ at $\lambda = 0$ is indeed the minimum.

Appendix D

Fitting Distributions to Data

In order to determine M_N (which is $M_{\tilde{\chi}_1^0}$ in our case studies) we perform a χ^2 fit between ideal constrained mass variable distributions and the HERWIG data or other low-statistics data. Because the mass difference is a given, it does not matter whether we work with M_N or M_Y as the independent variable.

First we illustrate the procedure if there is only one distribution being fit as in Chapter 6. We work with the constrained mass variable M_{2C} using M_Y as the independent variable. To do this we define a χ^2 distribution by computing the number of events, C_j , in a given range, j , (bin j) of M_{2C} . The variable N is the total number of events in bins that will be fit. Assuming a Poisson distribution, we assign an uncertainty, σ_j , to each bin j given by

$$\sigma_j^2 = \frac{1}{2} (N f(M_{2Cj}, M_Y) + C_j). \quad (\text{D.1})$$

Here the normalized distribution of ideal events is $f(M_{2C}, M_Y)$, and the second term has been added to ensure that the contribution of bins with very few events, where Poisson statistics does not apply¹, have a reasonable weighting. Then χ^2 is given by

$$\chi^2(M_Y) = \sum_{\text{bin } j} \left(\frac{C_j - N f(M_{2Cj}, M_Y)}{\sigma_j} \right)^2. \quad (\text{D.2})$$

The minimum $\chi^2(M_Y)$ is our estimate of M_Y . The amount M_Y changes for an increase of χ^2 by one gives our 1σ uncertainty, δM_Y , for M_Y [200]. As justification for this we calculate ten different seed random numbers to generate ten distinct groups of 250 events. We check that the M_Y estimates for the ten sets are distributed with about 2/3 within δM_Y of the true M_Y as one would expect for 1σ error bars. One might worry that with our definition of χ^2 , the value of χ^2 per degree of freedom is less than one. However this is an artifact of the fact that the bins with very few or zero events are not adequately described by Poisson statistics and if we

¹By this we mean that $N f(M_{2Cj}, M_Y)$ has a large percent error when used as a predictor of the number of counts C_j when $N f(M_{2Cj}, M_Y)$ is less than about 5.

remove them we do get a reasonable χ^2 per degree of freedom. The determination of M_Y using this reduced set gives similar results.

In Chapters 7 and 8 we determine the mass with two distributions (the upper and the lower bound distributions). We treat these two distributions separately and add the resulting χ^2 to form a final χ^2 . In these chapters we choose $M_{\tilde{\chi}_1^0}$ as the independent variable. We illustrate with $M_{2C, LB}$ and $M_{2C, UB}$, but the procedure is the same for M_{3C} .

First we update the definitions for this case. We define N_{LB} as the number of M_{2C} events in the region to be fit, and likewise N_{UB} is the number of $M_{2C, UB}$ events in the region to be fit. The M_{2C} of the events are grouped into bins, C_j , in a given range, j . The variable $f_{LB}(M_{2C}, M_{\tilde{\chi}_1^0})$ is the normalized M_{2C} distribution of ideal events expected in bin j as calculated with an assumed $M_{\tilde{\chi}_1^0}$, the measured M_- , the observed m_{ll} distribution, the observed UTM distribution, and the appropriate detector simulator. We likewise define the upper bound distribution to be $f_{UB}(M_{2C, UB}, M_{\tilde{\chi}_1^0})$. We also define the background distribution for lower-bound and upper-bound distributions to be $f_{B, LB}(M_{2C})$ and $f_{B, UB}(M_{2C, UB})$ and the fraction of the total events we estimate are from background λ .

Again, we assign an uncertainty, σ_j , to each bin j given by

$$\sigma_{LB, j}^2(M_{\tilde{\chi}_1^0}) = \frac{1}{2} (N_{LB} ((1 - \lambda) f_{LB}(M_{2Cj}, M_{\tilde{\chi}_1^0}) + \lambda f_{B, LB}(M_{2Cj})) + C_j), \quad (D.3)$$

and likewise for the upper-bound distribution. The second term has been added to ensure an appropriate weighting of bins with very few events that does not bias the fit towards or away from this end-point. In bins with few counts, normal Poisson statistics does not apply².

The χ^2 is given by

$$\begin{aligned} \chi^2(M_{\tilde{\chi}_1^0}) = & \sum_{\text{bin } j} \left(\frac{C_j - N_{LB} (1 - \lambda) f_{LB}(M_{2Cj}, M_{\tilde{\chi}_1^0}) - N_{LB} \lambda f_{B, LB}(M_{2Cj}, M_{\tilde{\chi}_1^0})}{\sigma_{LB, j}} \right)^2 \\ & + \sum_{\text{bin } j} \left(\frac{C_{UB, j} - N_{UB} (1 - \lambda) f_{UB}(M_{2C, UBj}, M_{\tilde{\chi}_1^0}) - N_{UB} \lambda f_{B, UB}(M_{2C, UBj}, M_{\tilde{\chi}_1^0})}{\sigma_{UB, j}} \right)^2. \end{aligned} \quad (D.4)$$

We calculate ideal distributions for $M_{\tilde{\chi}_1^0} = 50, 60, 70, 80, 90$ GeV. We fit quadratic interplant through the points. The minimum $\chi^2(M_{\tilde{\chi}_1^0})$ of the interplant is our estimate of $M_{\tilde{\chi}_1^0}$. The amount $M_{\tilde{\chi}_1^0}$ changes for an increase in χ^2 by one gives our 1σ uncertainty, $\delta M_{\tilde{\chi}_1^0}$, for $M_{\tilde{\chi}_1^0}$ [200].

The M_{3C} fits in Chapter 8 were performed following this same procedure. In this case we choose $M_{\tilde{\chi}_1^0} = 80, 85, 90, 95, 100, 105, 110$ GeV. For the M_{3C} studies we did not create a

²By this we mean that $N f(M_{2Cj}, M_{\tilde{\chi}_1^0})$ has a large percent error when used as a predictor of the number of counts C_j when $N f(M_{2Cj}, M_{\tilde{\chi}_1^0})$ is less than about 5.

background model and therefore fixed the background parameter to $\lambda = 0$. The studies involving nine different choices of $(\Delta M_{YN}, \Delta M_{XN})$ were done using $M_{\tilde{\chi}_1^0} = 90, 100, 110$ GeV.

Some subtleties for which we should check. If the bin size is not large enough, the artificially large variations in the distribution sometimes bias the fits to place the endpoint near a fluctuation. The bin size should be made large enough so that this does not happen. This can be checked for by testing if the results are invariant with respect to changing the bin size by a small amount. Because of the larger number of lower bound events, the optimal bin size may be different for the upper-bound and the lower-bound distributions.

Appendix E

Uniqueness of Event Reconstruction

In the Chapters 6 and 8 we claim that the events near an endpoint of M_{2C} and M_{3C} distributions (events that nearly saturate the bound) are nearly reconstructed. This appendix offers a proof of the claim. To prove uniqueness, we need to establish that as M_{3C} or M_{2C} of an event (lower bound or upper bound) approach the endpoint of the distributions, the solutions with different values of q and p approach a common solution.

We begin with M_{3C} . Sec. 8.2 shows that there are at most four solutions given M_N , M_X and M_Y formed by the intersection of two ellipses in (p_o, q_o) defined by Eqs(8.13-8.14) as shown in Fig E.1. Consider the case that an event has a lower bound M_{3C} near M_Y . We are guaranteed that a solution occurs at the true mass scale when we choose the correct combinatoric assignments. As one varies the mass scale downward, the two ellipses drift and change shape and size so that four solutions become two solutions and eventually, at the value of M_{3C} for the event, become one single solution. When the disconnection of the two ellipses occurs near the true mass scale, the value of M_{3C} will be near the endpoint. The unique solutions for p and q given at M_{3C} are nearly degenerate with the true values of p and q found when one uses the true masses to solve for p and q . The closer M_{3C} is to the endpoint the closer the two ellipses are to intersecting at a single point when the true masses are used and to giving a unique reconstruction. The example pictured in Fig. E.1 show an event with M_{3C} within 1% of the endpoint and where the p and q are reconstructed to within 4%. This shows that for M_{3C} events that are near the endpoint allowing for any choice of combinatorics then nearly reconstruct the true values for p and q . If there are combinatoric ambiguities, one need to test all combinatoric possibilities. If the minimum combinatoric option has a lower bound at the end-point, the above arguments follow unchanged. The above arguments can be repeated to show $M_{3C,UB}$ near the endpoint also reconstructs the correct p and q .

Next we turn to M_{2C} . For every event the lower-bounds satisfy $M_{2C}(M_Y - M_N) \leq M_{3C}(M_Y -$

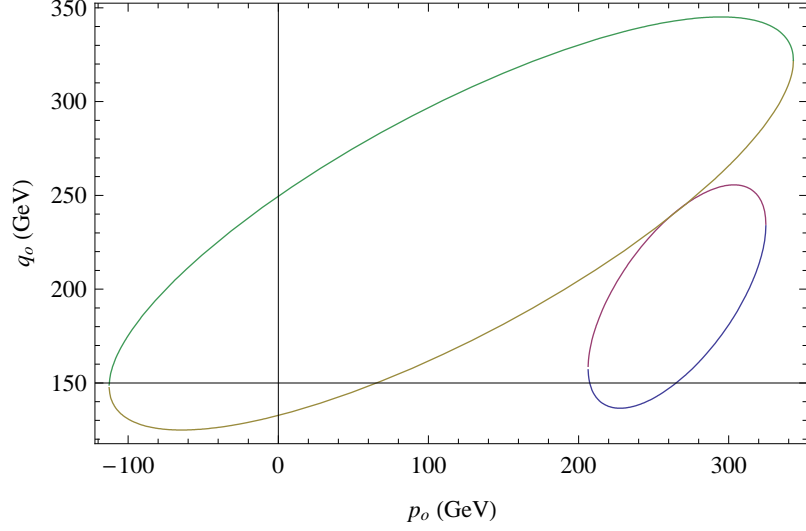


Figure E.1: Shows the ellipses defined for p_o and q_o in Eqs(8.13-8.14) using the correct mass scale for an event that nearly saturates the M_{3C} endpoint. For this event, the M_{3C} lies within 1% of the endpoint and reconstructs p and q to within 4%. Perfect error resolution and combinatorics are assumed.

$M_N, M_X - M_N$). With M_{2C} the propagator $(p + \alpha_2)^2$, which we can equate with χ_X^2 , is not fixed. The kinematically allowed values for χ_X are $M_N^2 < \chi_X^2 < M_Y^2$ assuming the visible states α_1 and α_2 are massless. Eq(8.12) shows that \vec{p} and \vec{q} solutions are linear in χ_X^2 with no terms dependent on χ_X alone or other powers of χ_X . Including χ_X^2 as a free parameter in Eqs(8.13-8.14) leads to two ellipsoids (or hyperboloids) in the space (p_o, q_o, χ_X^2) . We will assume without loss of generality that these are ellipsoids. Again, at the true mass scale we are guaranteed the two ellipsoids intersect at an ellipse. Now as one varies the mass scale the two ellipsoids drift and change shape and size. The M_{2C} value then corresponds to the mass scale where the two ellipsoids are in contact at one point. As we select events with a value of M_{2C} that approaches the true mass scale the intersection of the two ellipsoids shrink to a point giving a unique reconstruction of p and q . The combinatoric ambiguities for M_{2C} are avoided by selecting events with two distinct OSSF pairs. Events that saturate the upper bound of M_{2C} also reconstruct p and q by the same logic as above.

Appendix F

Acronyms List

- Λ CDM Λ (Cosmological Constant) Cold Dark Matter
- CKM Cabibbo-Kobayashi-Maskawa
- CMB Cosmic Microwave Background
- \overline{DR} Dimensional Reduction (Renormalization Scheme)
- GIM Glashow-Iliopoulos-Maiani
- GJ Georgi-Jarlskog
- GUT Grand Unified Theory
- ISR Initial State Radiation
- KK Kaluza Klein
- LHC Large Hadron Collider
- LKP Lightest Kaluza Klein particle
- LSP Lightest supersymmetric particle
- \overline{MS} Minimal Subtraction (Renormalization Scheme)
- MACHO MAssive Compact Halo Objects
- OSSF Opposite-Sign Same Flavor
- QFT Quantum Field Theory
- REWSB Radiative Electroweak Symmetry Breaking
- RG Renormalization Group
- RGE Renormalization Group Equations
- SM Standard Model
- SSB Spontaneous Symmetry Breaking
- SUSY Supersymmetry
- UED Universal Extra Dimensions
- UTM Upstream Transverse Momentum
- VEV Vacuum Expectation Value

Bibliography

- [1] R. G. Roberts, A. Romanino, G. G. Ross, and L. Velasco-Sevilla, *Precision test of a fermion mass texture*, *Nucl. Phys.* **B615** (2001) 358–384, [[hep-ph/0104088](#)].
- [2] W. Vandelli, *Prospects for the detection of chargino-neutralino direct production with ATLAS detector at the LHC*. PhD dissertation, Universita Degli Studi Di Pavia, Dipartimento Di Fisica, 2006.
- [3] B. C. Allanach *et. al.*, *The snowmass points and slopes: Benchmarks for susy searches*, [hep-ph/0202233](#).
- [4] R. Boyle, *A Free Enquiry into the Vulgarly Received Notion of Nature*. Cambridge University Press, 1685. Introduction of 1996 edition.
- [5] F. Wilczek, *From “not wrong” to (maybe) right*, *Nature* **428** (2004) 261.
- [6] G. D’Agostini, *From observations to hypotheses: Probabilistic reasoning versus falsificationism and its statistical variations*, [physics/0412148](#).
- [7] CDF Collaboration, *Luminosity web page*, http://www-cdf.fnal.gov/~konigsb/lum_official_page.html (June, 2008).
- [8] W.-M. Yao, *Review of Particle Physics*, *Journal of Physics G* **33** (2008) 1+.
- [9] A. Collaboration, *ATLAS computing : Technical design report*, CERN, *ATLAS-TDR-017, CERN-LHCC-2005-022* (2005).
- [10] G. Ross and M. Serna, *Unification and Fermion Mass Structure*, *Phys. Lett.* **B664** (2008) 97–102, [[0704.1248](#)].
- [11] H. Georgi and C. Jarlskog, *A new lepton - quark mass relation in a unified theory*, *Phys. Lett.* **B86** (1979) 297–300.
- [12] C. G. Lester and D. J. Summers, *Measuring masses of semi-invisibly decaying particles pair produced at hadron colliders*, *Phys. Lett.* **B463** (1999) 99–103, [[hep-ph/9906349](#)].
- [13] A. Barr, C. Lester, and P. Stephens, *$m(T_2)$: The truth behind the glamour*, *J. Phys.* **G29** (2003) 2343–2363, [[hep-ph/0304226](#)].
- [14] M. Serna, *A short comparison between m_{T_2} and m_{CT}* , *JHEP* **06** (2008) 004, [[0804.3344](#)].
- [15] G. G. Ross and M. Serna, *Mass Determination of New States at Hadron Colliders*, *Phys. Lett.* **B665** (2008) 212–218, [[0712.0943](#)].
- [16] A. J. Barr, G. G. Ross, and M. Serna, *The Precision Determination of Invisible-Particle Masses at the LHC*, *Phys. Rev.* **D78** (2008) 056006, [[0806.3224](#)].
- [17] G. Corcella *et. al.*, *HERWIG 6.5 release note*, [hep-ph/0210213](#).

- [18] S. Moretti, K. Odagiri, P. Richardson, M. H. Seymour, and B. R. Webber, *Implementation of supersymmetric processes in the HERWIG event generator*, *JHEP* **04** (2002) 028, [[hep-ph/0204123](#)].
- [19] G. Marchesini *et. al.*, *HERWIG: A Monte Carlo event generator for simulating hadron emission reactions with interfering gluons. Version 5.1 - April 1991*, *Comput. Phys. Commun.* **67** (1992) 465–508.
- [20] A. J. Barr, A. Pinder, and M. Serna, *Precision Determination of Invisible-Particle Masses at the CERN LHC: II*, *Phys. Rev.* **D79** (2009) 074005, [[0811.2138](#)].
- [21] P. A. M. Dirac, *The Quantum theory of electron*, *Proc. Roy. Soc. Lond.* **A117** (1928) 610–624.
- [22] C. D. Anderson, *The positive electron*, *Phys. Rev.* **43** (Mar, 1933) 491–494.
- [23] E. Lane, *Harvard’s Nima Arkani-Hamed Ponders New Universes, Different Dimensions, AAAS: Advancing Science Serving Society* (May, 2005).
- [24] J. D. Jackson, *Weisskopf tribute*, *Cern Courier* (Dec, 2002).
- [25] V. F. Weisskopf, *On the self-energy and the electromagnetic field of the electron*, *Phys. Rev.* **56** (Jul, 1939) 72–85.
- [26] M. Gell-Mann, *The Eightfold Way: A Theory of strong interaction symmetry*, . CTSL-20.
- [27] Y. Ne’eman, *Derivation of strong interactions from a gauge invariance*, *Nucl. Phys.* **26** (1961) 222–229.
- [28] T. Ne’eman, *In remembrance of yuval ne’eman (1925-2006)*, *Physicsapplus* (2006). <http://physicsapplus.org.il>.
- [29] e. . Fraser, G., *The particle century*, . Bristol, UK: IOP (1998) 232 p.
- [30] V. E. Barnes, P. L. Connolly, D. J. Crennell, B. B. Culwick, W. C. Delaney, W. B. Fowler, P. E. Hagerty, E. L. Hart, N. Horwitz, P. V. C. Hough, J. E. Jensen, J. K. Kopp, K. W. Lai, J. Leitner, J. L. Lloyd, G. W. London, T. W. Morris, Y. Oren, R. B. Palmer, A. G. Prodell, D. Radojčić, D. C. Rahm, C. R. Richardson, N. P. Samios, J. R. Sanford, R. P. Shutt, and J. R. Smith, *Observation of a hyperon with strangeness minus three*, *Phys. Rev. Lett.* **12** (Feb, 1964) 204–206.
- [31] **BABAR** Collaboration, B. Aubert *et. al.*, *Measurement of the spin of the Omega-hyperon at BABAR*, *Phys. Rev. Lett.* **97** (2006) 112001, [[hep-ex/0606039](#)].
- [32] S. Okubo, *Note on unitary symmetry in strong interactions*, *Prog. Theor. Phys.* **27** (1962) 949–966.
- [33] S. Weinberg, *Quantum Theory of Fields*. Cambridge University Press, 1996.
- [34] T.-P. Cheng and L.-F. Li, *Gauge theory of elementary particle physics*. Oxford University Press, 1984.
- [35] M. K. Gaillard and B. W. Lee, *Rare Decay Modes of the K-Mesons in Gauge Theories*, *Phys. Rev.* **D10** (1974) 897.
- [36] T. D. Lee, *ANALYSIS OF DIVERGENCES IN A NEUTRAL SPIN 1 MESON THEORY WITH PARITY NONCONSERVING INTERACTIONS*, *Nuovo Cim.* **A59** (1969) 579–598.

- [37] S. L. Glashow, J. Iliopoulos, and L. Maiani, *Weak Interactions with Lepton-Hadron Symmetry*, *Phys. Rev.* **D2** (1970) 1285–1292.
- [38] V. I. Borodulin, R. N. Rogalev, and S. R. Slabospitsky, *CORE: COmpendium of RElations: Version 2.1*, [hep-ph/9507456](#).
- [39] M. Srednicki, *Quantum field theory*, . Cambridge, UK: Univ. Pr. (2007) 641 p.
- [40] P. Ramond, *Journeys beyond the standard model*, . Reading, Mass., Perseus Books, 1999.
- [41] W.-M. Yao, *Review of Particle Physics*, *Journal of Physics G* **33** (2006) 1+.
- [42] S. Weinberg, *A Model of Leptons*, *Phys. Rev. Lett.* **19** (1967) 1264–1266.
- [43] O. W. Greenberg, *Spin and Unitary Spin Independence in a Paraquark Model of Baryons and Mesons*, *Phys. Rev. Lett.* **13** (1964) 598–602.
- [44] O. W. Greenberg, *The color charge degree of freedom in particle physics*, 0805.0289.
- [45] D. J. Gross and F. Wilczek, *Asymptotically Free Gauge Theories. 1*, *Phys. Rev.* **D8** (1973) 3633–3652.
- [46] H. D. Politzer, *RELIABLE PERTURBATIVE RESULTS FOR STRONG INTERACTIONS?*, *Phys. Rev. Lett.* **30** (1973) 1346–1349.
- [47] C. H. Llewellyn Smith and J. F. Wheeler, *Electroweak Radiative Corrections and the Value of $\sin^2\theta_W$* , *Phys. Lett.* **B105** (1981) 486.
- [48] **UA1** Collaboration, G. Arnison *et. al.*, *Experimental observation of isolated large transverse energy electrons with associated missing energy at $\sqrt{s} = 540\text{-GeV}$* , *Phys. Lett.* **B122** (1983) 103–116.
- [49] **UA1** Collaboration, G. Arnison *et. al.*, *Experimental observation of lepton pairs of invariant mass around $95\text{-GeV}/c^2$ at the CERN SPS collider*, *Phys. Lett.* **B126** (1983) 398–410.
- [50] G. Bertone, D. Hooper, and J. Silk, *Particle dark matter: Evidence, candidates and constraints*, *Phys. Rept.* **405** (2005) 279–390, [[hep-ph/0404175](#)].
- [51] H. Baer and X. Tata, *Dark matter and the LHC*, 0805.1905.
- [52] J. Oortz, *The force exerted by the stellar system in the direction perpendicular to the galactic plane and some related problems*, *Bulletin of the Astronomical Institutes of the Netherlands* **VI** (1932) 249.
- [53] Y. Sofue and V. Rubin, *Rotation Curves of Spiral Galaxies*, *Annual Reviews Astronomy and Astrophysics* **39** (2001) 137–174, [[arXiv:astro-ph/0010594](#)].
- [54] D. Russeil, O. Garrido, P. Amram, and M. Marcelin, *Rotation curve of our Galaxy and field galaxies*, in *Dark Matter in Galaxies* (S. Ryder, D. Pisano, M. Walker, and K. Freeman, eds.), vol. 220 of *IAU Symposium*, pp. 211–+, July, 2004.
- [55] F. Swicky, *On the masses of nebulae and of clusters of nebulae*, *The Astrophysical Journal* **86** (1937) 217.
- [56] R. Bottema, J. L. G. Pestana, B. Rothberg, and R. H. Sanders, *MOND rotation curves for spiral galaxies with Cepheid- based distances*, *Astron. Astrophys.* **393** (2002) 453–460, [[astro-ph/0207469](#)].

- [57] D. Clowe *et. al.*, *A direct empirical proof of the existence of dark matter*, *Astrophys. J.* **648** (2006) L109–L113, [[astro-ph/0608407](#)].
- [58] D. Spergel, *Particle Dark Matter*, [astro-ph/9603026](#).
- [59] J. B. Hartle, *An introduction to Einstein’s general relativity*, . San Francisco, USA: Addison-Wesley (2003) 582 p.
- [60] J. Frieman, M. Turner, and D. Huterer, *Dark Energy and the Accelerating Universe*, 0803.0982.
- [61] **CDMS** Collaboration, Z. Ahmed *et. al.*, *A Search for WIMPs with the First Five-Tower Data from CDMS*, 0802.3530.
- [62] **XENON** Collaboration, J. Angle *et. al.*, *First Results from the XENON10 Dark Matter Experiment at the Gran Sasso National Laboratory*, *Phys. Rev. Lett.* **100** (2008) 021303, [[0706.0039](#)].
- [63] **DAMA** Collaboration, R. Bernabei *et. al.*, *On a further search for a yearly modulation of the rate in particle dark matter direct search*, *Phys. Lett.* **B450** (1999) 448–455.
- [64] **DAMA** Collaboration, R. Bernabei *et. al.*, *First results from DAMA/LIBRA and the combined results with DAMA/NaI*, 0804.2741.
- [65] H. Baer, A. Mustafayev, E.-K. Park, and X. Tata, *Target dark matter detection rates in models with a well- tempered neutralino*, *JCAP* **0701** (2007) 017, [[hep-ph/0611387](#)].
- [66] J. R. Ellis, K. A. Olive, Y. Santoso, and V. C. Spanos, *Update on the direct detection of supersymmetric dark matter*, *Phys. Rev.* **D71** (2005) 095007, [[hep-ph/0502001](#)].
- [67] S. Arrenberg, L. Baudis, K. Kong, K. T. Matchev, and J. Yoo, *Kaluza-Klein Dark Matter: Direct Detection vis-a-vis LHC*, 0805.4210.
- [68] W. de Boer, C. Sander, V. Zhukov, A. V. Gladyshev, and D. I. Kazakov, *EGRET excess of diffuse galactic gamma rays as tracer of dark matter*, *Astron. Astrophys.* **444** (2005) 51, [[astro-ph/0508617](#)].
- [69] **CDMS** Collaboration, D. S. Akerib *et. al.*, *First results from the cryogenic dark matter search in the Soudan Underground Lab*, *Phys. Rev. Lett.* **93** (2004) 211301, [[astro-ph/0405033](#)].
- [70] M. Tegmark, *Cosmological neutrino bounds for non-cosmologists*, *Phys. Scripta* **T121** (2005) 153–155, [[hep-ph/0503257](#)].
- [71] N. Arkani-Hamed, S. Dimopoulos, and G. R. Dvali, *The hierarchy problem and new dimensions at a millimeter*, *Phys. Lett.* **B429** (1998) 263–272, [[hep-ph/9803315](#)].
- [72] T. Appelquist, H.-C. Cheng, and B. A. Dobrescu, *Bounds on universal extra dimensions*, *Phys. Rev.* **D64** (2001) 035002, [[hep-ph/0012100](#)].
- [73] G. Servant and T. M. P. Tait, *Is the lightest Kaluza-Klein particle a viable dark matter candidate?*, *Nucl. Phys.* **B650** (2003) 391–419, [[hep-ph/0206071](#)].
- [74] M. Battaglia, A. Datta, A. De Roeck, K. Kong, and K. T. Matchev, *Contrasting supersymmetry and universal extra dimensions at the CLIC multi-TeV $e^+ e^-$ collider*, *JHEP* **07** (2005) 033, [[hep-ph/0502041](#)].

- [75] R. Haag, J. T. Lopuszanski, and M. Sohnius, *All Possible Generators of Supersymmetries of the s Matrix*, *Nucl. Phys.* **B88** (1975) 257.
- [76] F. Gliozzi, J. Scherk, and D. I. Olive, *Supersymmetry, Supergravity Theories and the Dual Spinor Model*, *Nucl. Phys.* **B122** (1977) 253–290.
- [77] D. Stockinger, *The muon magnetic moment and supersymmetry*, [hep-ph/0609168](#).
- [78] S. P. Martin, *A supersymmetry primer*, [hep-ph/9709356](#).
- [79] H. Baer and X. Tata, *Weak scale supersymmetry: From superfields to scattering events*, . Cambridge, UK: Univ. Pr. (2006) 537 p.
- [80] S. J. Gates, M. T. Grisaru, M. Rocek, and W. Siegel, *Superspace, or one thousand and one lessons in supersymmetry*, *Front. Phys.* **58** (1983) 1–548, [[hep-th/0108200](#)].
- [81] J. Wess and J. Bagger, *Supersymmetry and supergravity*, . Princeton, USA: Univ. Pr. (1992) 259 p.
- [82] K. E. Cahill, *Elements of supersymmetry*, [hep-ph/9907295](#).
- [83] I. J. R. Aitchison, *Supersymmetry and the MSSM: An elementary introduction*, [hep-ph/0505105](#).
- [84] L. E. Ibanez and G. G. Ross, *Supersymmetric Higgs and radiative electroweak breaking*, *Comptes Rendus Physique* **8** (2007) 1013–1028, [[hep-ph/0702046](#)].
- [85] L. E. Ibanez and G. G. Ross, *$SU(2)_L \times U(1)$ symmetry breaking as a radiative effect of supersymmetry breaking in guts*, *Phys. Lett.* **B110** (1982) 215–220.
- [86] K. Inoue, A. Kakuto, H. Komatsu, and S. Takeshita, *Aspects of Grand Unified Models with Softly Broken Supersymmetry*, *Prog. Theor. Phys.* **68** (1982) 927.
- [87] L. Alvarez-Gaume, J. Polchinski, and M. B. Wise, *Minimal Low-Energy Supergravity*, *Nucl. Phys.* **B221** (1983) 495.
- [88] S. Raby, *SOME THOUGHTS ON THE MASS OF THE TOP QUARK*, *Nucl. Phys.* **B187** (1981) 446.
- [89] S. L. Glashow, *WHERE IS THE TOP QUARK?*, *Phys. Rev. Lett.* **45** (1980) 1914.
- [90] K. T. Mahanthappa and M. A. Sher, *THE MASS OF THE TOP QUARK IN $SU(5)$* , *Phys. Lett.* **B86** (1979) 294.
- [91] T. Yanagida, *HORIZONTAL SYMMETRY AND MASS OF THE TOP QUARK*, *Phys. Rev.* **D20** (1979) 2986.
- [92] B. Pendleton and G. G. Ross, *Mass and mixing angle predictions from infrared fixed points*, *Phys. Lett.* **B98** (1981) 291.
- [93] W. A. Bardeen, M. Carena, S. Pokorski, and C. E. M. Wagner, *Infrared fixed point solution for the top quark mass and unification of couplings in the mssm*, *Phys. Lett.* **B320** (1994) 110–116, [[hep-ph/9309293](#)].
- [94] S. Dimopoulos, S. Raby, and F. Wilczek, *Supersymmetry and the scale of unification*, *Phys. Rev. D* **24** (Sep, 1981) 1681–1683.

- [95] L. E. Ibanez and G. G. Ross, *Low-Energy Predictions in Supersymmetric Grand Unified Theories*, *Phys. Lett.* **B105** (1981) 439.
- [96] S. Dimopoulos and H. Georgi, *Softly Broken Supersymmetry and SU(5)*, *Nucl. Phys.* **B193** (1981) 150.
- [97] N. Sakai, *Naturalness in Supersymmetric Guts*, *Zeit. Phys.* **C11** (1981) 153.
- [98] W. de Boer and C. Sander, *Global electroweak fits and gauge coupling unification*, *Phys. Lett.* **B585** (2004) 276–286, [[hep-ph/0307049](#)].
- [99] S. Willenbrock, *Tripllicated trinification*, *Phys. Lett.* **B561** (2003) 130–134, [[hep-ph/0302168](#)].
- [100] H. Georgi and S. L. Glashow, *Unity of all elementary particle forces*, *Phys. Rev. Lett.* **32** (1974) 438–441.
- [101] J. C. Pati and A. Salam, *Lepton number as the fourth color*, *Phys. Rev.* **D10** (1974) 275–289.
- [102] G. G. Ross, *GRAND UNIFIED THEORIES*, . Reading, Usa: Benjamin/cummings (1984) 497 P. (Frontiers In Physics, 60).
- [103] A. J. Buras, J. R. Ellis, M. K. Gaillard, and D. V. Nanopoulos, *Aspects of the Grand Unification of Strong, Weak and Electromagnetic Interactions*, *Nucl. Phys.* **B135** (1978) 66–92.
- [104] S. F. de Medeiros Varzielas and G. G. Ross, *SU(3) family symmetry and bi-tri maximal mixing*, *Nuclear Physics B* **733** (2006) 31 – 47, [[hep-ph/0507176](#)].
- [105] T. Appelquist and J. Carazzone, *Infrared Singularities and Massive Fields*, *Phys. Rev.* **D11** (1975) 2856.
- [106] A. Pich, *Effective field theory*, [hep-ph/9806303](#).
- [107] B. V. Martemyanov and V. S. Sopov, *Light quark mass ratio from dalitz plot of $\eta \rightarrow \pi^+ \pi^- \pi^0$ decay*, *Phys. Rev.* **D71** (2005) 017501, [[hep-ph/0502023](#)].
- [108] T. E. W. Group, *A combination of cdf and d0 results on the mass of the top quark*, [hep-ex/0703034](#).
- [109] D. Groom, *Review of Particle Physics*, *The European Physical Journal* **C15** (2000) 1+.
- [110] H. Fusaoka and Y. Koide, *Updated estimate of running quark masses*, *Phys. Rev.* **D57** (1998) 3986–4001, [[hep-ph/9712201](#)].
- [111] H. Baer, J. Ferrandis, K. Melnikov, and X. Tata, *Relating bottom quark mass in \overline{dr} -bar and \overline{ms} -bar regularization schemes*, *Phys. Rev.* **D66** (2002) 074007, [[hep-ph/0207126](#)].
- [112] V. Lubicz, *Lattice qcd, flavor physics and the unitarity triangle analysis*, [hep-ph/0702204](#).
- [113] P. H. Chankowski and S. Pokorski, *Quantum corrections to neutrino masses and mixing angles*, *Int. J. Mod. Phys.* **A17** (2002) 575–614, [[hep-ph/0110249](#)].
- [114] V. D. Barger, M. S. Berger, and P. Ohmann, *Supersymmetric grand unified theories: Two loop evolution of gauge and yukawa couplings*, *Phys. Rev.* **D47** (1993) 1093–1113, [[hep-ph/9209232](#)].

- [115] S. M. Barr and I. Dorsner, *Atmospheric neutrino mixing and $b - \tau$ unification*, *Phys. Lett.* **B556** (2003) 185–191, [[hep-ph/0211346](#)].
- [116] J. L. Diaz-Cruz, H. Murayama, and A. Pierce, *Can supersymmetric loops correct the fermion mass relations in $su(5)$?*, *Phys. Rev.* **D65** (2002) 075011, [[hep-ph/0012275](#)].
- [117] D. M. Pierce, J. A. Bagger, K. T. Matchev, and R.-j. Zhang, *Precision corrections in the minimal supersymmetric standard model*, *Nucl. Phys.* **B491** (1997) 3–67, [[hep-ph/9606211](#)].
- [118] T. Blazek, S. Raby, and S. Pokorski, *Finite supersymmetric threshold corrections to ckm matrix elements in the large $\tan \beta$ regime*, *Phys. Rev.* **D52** (1995) 4151–4158, [[hep-ph/9504364](#)].
- [119] M. Carena, D. Garcia, U. Nierste, and C. E. M. Wagner, *Effective lagrangian for the anti- $t b h$ interaction in the mssm and charged higgs phenomenology*, *Nucl. Phys.* **B577** (2000) 88–120, [[hep-ph/9912516](#)].
- [120] M. Carena and H. E. Haber, *Higgs boson theory and phenomenology. $((v))$* , *Prog. Part. Nucl. Phys.* **50** (2003) 63–152, [[hep-ph/0208209](#)].
- [121] K. Tobe and J. D. Wells, *Revisiting top-bottom-tau yukawa unification in supersymmetric grand unified theories*, *Nucl. Phys.* **B663** (2003) 123–140, [[hep-ph/0301015](#)].
- [122] K. Hagiwara, A. D. Martin, D. Nomura, and T. Teubner, *Improved predictions for $g-2$ of the muon and $\alpha(qed)(m(z)^{**2})$* , [[hep-ph/0611102](#)].
- [123] L. L. Everett, G. L. Kane, S. Rigolin, and L.-T. Wang, *Implications of muon $g-2$ for supersymmetry and for discovering superpartners directly*, *Phys. Rev. Lett.* **86** (2001) 3484–3487, [[hep-ph/0102145](#)].
- [124] L. Randall and R. Sundrum, *Out of this world supersymmetry breaking*, *Nucl. Phys.* **B557** (1999) 79–118, [[hep-th/9810155](#)].
- [125] L. J. Hall, R. Rattazzi, and U. Sarid, *The top quark mass in supersymmetric $so(10)$ unification*, *Phys. Rev.* **D50** (1994) 7048–7065, [[hep-ph/9306309](#)].
- [126] S. Komine and M. Yamaguchi, *Bottom-tau unification in susy $su(5)$ gut and constraints from $b - \bar{c} s$ gamma and muon $g-2$* , *Phys. Rev.* **D65** (2002) 075013, [[hep-ph/0110032](#)].
- [127] C. Pallis, *$b - \tau$ unification and sfermion mass non-universality*, *Nucl. Phys.* **B678** (2004) 398–426, [[hep-ph/0304047](#)].
- [128] M. R. Ramage and G. G. Ross, *Soft susy breaking and family symmetry*, *JHEP* **08** (2005) 031, [[hep-ph/0307389](#)].
- [129] S. F. King and M. Oliveira, *Yukawa unification as a window into the soft supersymmetry breaking lagrangian*, *Phys. Rev.* **D63** (2001) 015010, [[hep-ph/0008183](#)].
- [130] T. Blazek, R. Dermisek, and S. Raby, *Predictions for higgs and susy spectra from $so(10)$ yukawa unification with $\mu \neq 0$* , *Phys. Rev. Lett.* **88** (2002) 111804, [[hep-ph/0107097](#)].
- [131] T. Blazek, R. Dermisek, and S. Raby, *Yukawa unification in $so(10)$* , *Phys. Rev.* **D65** (2002) 115004, [[hep-ph/0201081](#)].
- [132] D. Auto, H. Baer, C. Balazs, A. Belyaev, J. Ferrandis, and X. Tata, *Yukawa coupling unification in supersymmetric models*, *JHEP* **06** (2003) 023, [[hep-ph/0302155](#)].

- [133] C. Balazs and R. Dermisek, *Yukawa coupling unification and non-universal gaugino mediation of supersymmetry breaking*, *JHEP* **06** (2003) 024, [[hep-ph/0303161](#)].
- [134] R. Gatto, G. Sartori, and M. Tonin, *Weak selfmasses, cabibbo angle, and broken $su(2) \times su(2)$* , *Phys. Lett.* **B28** (1968) 128–130.
- [135] K. Matsuda and H. Nishiura, *Can four-zero-texture mass matrix model reproduce the quark and lepton mixing angles and cp violating phases?*, *Phys. Rev.* **D74** (2006) 033014, [[hep-ph/0606142](#)].
- [136] C. T. Hill, *Are There Significant Gravitational Corrections to the Unification Scale?*, *Phys. Lett.* **B135** (1984) 47.
- [137] J. R. Ellis and M. K. Gaillard, *Fermion Masses and Higgs Representations in $SU(5)$* , *Phys. Lett.* **B88** (1979) 315.
- [138] S. Antusch and M. Spinrath, *Quark and lepton masses at the GUT scale including SUSY threshold corrections*, 0804.0717.
- [139] S. Mrenna, G. L. Kane, and L.-T. Wang, *Measuring gaugino soft phases and the LSP mass at Fermilab*, *Phys. Lett.* **B483** (2000) 175–183, [[hep-ph/9910477](#)].
- [140] Baer and Tata, *Supersymmetry Phenomenology*. Cambridge University Press, 1996.
- [141] **D0** Collaboration, B. Abbott *et. al.*, *Spin correlation in $t\bar{t}$ production from $p\bar{p}$ collisions at $\sqrt{s} = 1.8$ TeV*, *Phys. Rev. Lett.* **85** (2000) 256–261, [[hep-ex/0002058](#)].
- [142] R. Devenish and A. Cooper-Sarkar, *Deep inelastic scattering*, . Oxford, UK: Univ. Pr. (2004) 403 p.
- [143] F. Maltoni, T. McElmurry, R. Putman, and S. Willenbrock, *Choosing the factorization scale in perturbative QCD*, [hep-ph/0703156](#).
- [144] J. Alwall *et. al.*, *Madgraph/madevent v4: The new web generation*, *JHEP* **09** (2007) 028, [[arXiv:0706.2334](#) [[hep-ph](#)]].
- [145] **CompHEP** Collaboration, E. Boos *et. al.*, *Comphep 4.4: Automatic computations from lagrangians to events*, *Nucl. Instrum. Meth.* **A534** (2004) 250–259, [[hep-ph/0403113](#)].
- [146] The Durham HEP Databases, *Parton Distribution Functions*, . <http://durpdg.dur.ac.uk/HEPDATA/PDF>.
- [147] J. L. Feng, T. Moroi, L. Randall, M. Strassler, and S.-f. Su, *Discovering supersymmetry at the Tevatron in Wino LSP scenarios*, *Phys. Rev. Lett.* **83** (1999) 1731–1734, [[hep-ph/9904250](#)].
- [148] N. V. Krasnikov, *SUSY model with R-parity violation, longlived charged slepton and quasistable matter*, *JETP Lett.* **63** (1996) 503–509, [[hep-ph/9602270](#)].
- [149] K. Jedamzik, *The cosmic $6Li$ and $7Li$ problems and BBN with long-lived charged massive particles*, *Phys. Rev.* **D77** (2008) 063524, [[0707.2070](#)].
- [150] C. Athanasiou, C. G. Lester, J. M. Smillie, and B. R. Webber, *Distinguishing spins in decay chains at the Large Hadron Collider*, *JHEP* **08** (2006) 055, [[hep-ph/0605286](#)].
- [151] D. J. Phalen and A. Pierce, *Sfermion interference in neutralino decays at the LHC*, *Phys. Rev.* **D76** (2007) 075002, [[arXiv:0705.1366](#) [[hep-ph](#)]].

- [152] M. Drees, W. Hollik, and Q. Xu, *One-loop calculations of the decay of the next-to-lightest neutralino in the mssm*, *JHEP* **02** (2007) 032, [[hep-ph/0610267](#)].
- [153] B. C. Allanach, C. G. Lester, M. A. Parker, and B. R. Webber, *Measuring sparticle masses in non-universal string inspired models at the LHC*, *JHEP* **09** (2000) 004, [[hep-ph/0007009](#)].
- [154] B. C. Allanach, J. P. Conlon, and C. G. Lester, *Measuring Smuon-Selectron Mass Splitting at the CERN LHC and Patterns of Supersymmetry Breaking*, *Phys. Rev.* **D77** (2008) 076006, [[0801.3666](#)].
- [155] C. Lester, *Model independent sparticle mass measurements at ATLAS*. PhD dissertation, University of Cambridge, Department of Physics, December, 2001. CERN-THESIS-2004-003.
- [156] H. Bachacou, I. Hinchliffe, and F. E. Paige, *Measurements of masses in sugra models at lhc*, *Phys. Rev.* **D62** (2000) 015009, [[hep-ph/9907518](#)].
- [157] B. K. Gjelsten, D. J. Miller, and P. Osland, *Measurement of SUSY masses via cascade decays for SPS 1a*, *JHEP* **12** (2004) 003, [[hep-ph/0410303](#)].
- [158] C. G. Lester, *Constrained invariant mass distributions in cascade decays: The shape of the 'm(ql)-threshold' and similar distributions*, *Phys. Lett.* **B655** (2007) 39–44, [[hep-ph/0603171](#)].
- [159] B. K. Gjelsten, D. J. Miller, P. Osland, and A. R. Raklev, *Mass determination in cascade decays using shape formulas*, *AIP Conf. Proc.* **903** (2007) 257–260, [[hep-ph/0611259](#)].
- [160] M. Bisset, N. Kersting, and R. Lu, *Improving SUSY Spectrum Determinations at the LHC with Wedgebox and Hidden Threshold Techniques*, [0806.2492](#).
- [161] G. R. Goldstein, K. Sliwa, and R. H. Dalitz, *Observing top-quark production at the Fermilab Tevatron*, *Phys. Rev.* **47** (1993) 967–972.
- [162] K. Kondo, T. Chikamatsu, and S. H. Kim, *Dynamical likelihood method for reconstruction of events with missing momentum. 3: Analysis of a CDF high p(T) e mu event as t anti-t production*, *J. Phys. Soc. Jap.* **62** (1993) 1177–1182.
- [163] R. Raja, *On measuring the top quark mass using the dilepton decay modes*, *ECONF* **C960625** (1996) STC122, [[hep-ex/9609016](#)].
- [164] R. Raja, *Remark on the errors associated with the Dalitz-Goldstein method*, *Phys. Rev.* **D56** (1997) 7465–7465.
- [165] O. Brandt, *Measurement of the mass of the top quark in dilepton final states with the D0 detector*, . FERMILAB-MASTERS-2006-03.
- [166] H.-C. Cheng, J. F. Gunion, Z. Han, G. Marandella, and B. McElrath, *Mass Determination in SUSY-like Events with Missing Energy*, *JHEP* **12** (2007) 076, [[0707.0030](#)].
- [167] H.-C. Cheng, D. Engelhardt, J. F. Gunion, Z. Han, and B. McElrath, *Accurate Mass Determinations in Decay Chains with Missing Energy*, *Phys. Rev. Lett.* **100** (2008) 252001, [[0802.4290](#)].

- [168] M. M. Nojiri, G. Polesello, and D. R. Tovey, *A hybrid method for determining SUSY particle masses at the LHC with fully identified cascade decays*, *JHEP* **05** (2008) 014, [0712.2718].
- [169] **D0** Collaboration, V. M. Abazov *et. al.*, *Improved W boson mass measurement with the $D\bar{O}$ detector*, *Phys. Rev.* **D66** (2002) 012001, [hep-ex/0204014].
- [170] C. Lester and A. Barr, *MTGEN : Mass scale measurements in pair-production at colliders*, *JHEP* **12** (2007) 102, [0708.1028].
- [171] W. S. Cho, K. Choi, Y. G. Kim, and C. B. Park, *Measuring superparticle masses at hadron collider using the transverse mass kink*, *JHEP* **02** (2008) 035, [0711.4526].
- [172] W. S. Cho, K. Choi, Y. G. Kim, and C. B. Park, *Measuring the top quark mass with m_{T2} at the LHC*, 0804.2185.
- [173] K. Hamaguchi, E. Nakamura, and S. Shirai, *A Measurement of Neutralino Mass at the LHC in Light Gravitino Scenarios*, 0805.2502.
- [174] W. S. Cho, K. Choi, Y. G. Kim, and C. B. Park, *Gluino Stransverse Mass*, *Phys. Rev. Lett.* **100** (2008) 171801, [0709.0288].
- [175] B. Gripaios, *Transverse observables and mass determination at hadron colliders*, arXiv:0709.2740 [hep-ph].
- [176] A. J. Barr, B. Gripaios, and C. G. Lester, *Weighing Wimps with Kinks at Colliders: Invisible Particle Mass Measurements from Endpoints*, *JHEP* **02** (2008) 014, [0711.4008].
- [177] M. M. Nojiri, Y. Shimizu, S. Okada, and K. Kawagoe, *Inclusive transverse mass analysis for squark and gluino mass determination*, 0802.2412.
- [178] D. R. Tovey, *On measuring the masses of pair-produced semi-invisibly decaying particles at hadron colliders*, *JHEP* **04** (2008) 034, [0802.2879].
- [179] *Atlas m_{T2} wiki c++ library*, <https://twiki.cern.ch/twiki/bin/view/Atlas/StransverseMassLibrary>.
- [180] G. A. Moortgat-Pick, H. Fraas, A. Bartl, and W. Majerotto, *Polarization and spin effects in neutralino production and decay*, *Eur. Phys. J.* **C9** (1999) 521–534, [hep-ph/9903220].
- [181] G. A. Moortgat-Pick and H. Fraas, *Implications of cp and cpt for production and decay of majorana fermions*, hep-ph/0012229.
- [182] S. Y. Choi, B. C. Chung, J. Kalinowski, Y. G. Kim, and K. Rolbiecki, *Analysis of the neutralino system in three-body leptonic decays of neutralinos*, *Eur. Phys. J.* **C46** (2006) 511–520, [hep-ph/0504122].
- [183] A. Djouadi, J.-L. Kneur, and G. Moultaka, *Suspect: A fortran code for the supersymmetric and higgs particle spectrum in the mssm*, hep-ph/0211331.
- [184] C. Collaboration, *CMS physics : Technical Design Report*. CERN Report No: CERN-LHCC-2006-001 ; CMS-TDR-008-1, 2006.
- [185] A. De Roeck *et. al.*, *Supersymmetric benchmarks with non-universal scalar masses or gravitino dark matter*, *Eur. Phys. J.* **C49** (2007) 1041–1066, [hep-ph/0508198].

- [186] M. Bisset, N. Kersting, J. Li, F. Moortgat, and Q. Xie, *Pair-produced heavy particle topologies: Mssm neutralino properties at the lhc from gluino / squark cascade decays*, *Eur. Phys. J.* **C45** (2006) 477–492, [[hep-ph/0501157](#)].
- [187] D. K. Ghosh, R. M. Godbole, and S. Raychaudhuri, *Signals for r-parity-violating supersymmetry at a 500-gev $e^+ e^-$ collider*, [hep-ph/9904233](#).
- [188] J. Tanaka, *Discovery potential of the Standard Model Higgs at the LHC*, *Nuclear Physics B Proceedings Supplements* **144** (July, 2005) 341–348.
- [189] F. E. Paige, S. D. Protopopescu, H. Baer, and X. Tata, *ISAJET 7.69: A Monte Carlo event generator for $p p$, anti- $p p$, and $e^+ e^-$ reactions*, [hep-ph/0312045](#).
- [190] **ATLAS** Collaboration, S. Akhmadalev *et. al.*, *Hadron energy reconstruction for the ATLAS calorimetry in the framework of the non-parametrical method*, *Nucl. Instrum. Meth.* **A480** (2002) 508–523, [[hep-ex/0104002](#)].
- [191] B. C. Allanach, *Softsusy: A c++ program for calculating supersymmetric spectra*, *Comput. Phys. Commun.* **143** (2002) 305–331, [[hep-ph/0104145](#)].
- [192] B. Bajc, G. Senjanovic, and F. Vissani, *$b - \tau$ unification and large atmospheric mixing: A case for non-canonical see-saw*, *Phys. Rev. Lett.* **90** (2003) 051802, [[hep-ph/0210207](#)].
- [193] B. A. Campbell and D. W. Maybury, *Triviality and the supersymmetric see-saw*, [hep-ph/0605144](#).
- [194] A. Dighe, S. Goswami, and W. Rodejohann, *Corrections to tri-bimaximal neutrino mixing: Renormalization and planck scale effects*, [hep-ph/0612328](#).
- [195] F. Vissani and A. Y. Smirnov, *Neutrino masses and $b - \tau$ unification in the supersymmetric standard model*, *Phys. Lett.* **B341** (1994) 173–180, [[hep-ph/9405399](#)].
- [196] S. Antusch, J. Kersten, M. Lindner, and M. Ratz, *Neutrino mass matrix running for non-degenerate see-saw scales*, *Phys. Lett.* **B538** (2002) 87–95, [[hep-ph/0203233](#)].
- [197] G. K. Leontaris, S. Lola, and G. G. Ross, *Heavy neutrino threshold effects in low-energy phenomenology*, *Nucl. Phys.* **B454** (1995) 25–44, [[hep-ph/9505402](#)].
- [198] K. G. Chetyrkin, J. H. Kuhn, and M. Steinhauser, *Rundec: A mathematica package for running and decoupling of the strong coupling and quark masses*, *Comput. Phys. Commun.* **133** (2000) 43–65, [[hep-ph/0004189](#)].
- [199] I. Dorsner, P. F. Perez, and G. Rodrigo, *Fermion masses and the uv cutoff of the minimal realistic $su(5)$* , [hep-ph/0607208](#).
- [200] P. Bevington and K. Robinson, *Data Reduction and Error Analysis in the Physics Sciences*. McGraw Hill, second edition ed., 1992.